Alma Mater Studiorum – Università di Bologna

DOTTORATO DI RICERCA IN

SCIENZE DELLA TERRA, DELLA VITA E DELL'AMBIENTE

Ciclo 34

Settore Concorsuale: 04/A2 - GEOLOGIA STRUTTURALE, GEOLOGIA STRATIGRAFICA, SEDIMENTOLOGIA E PALEONTOLOGIA

Settore Scientifico Disciplinare: GEO/03 - GEOLOGIA STRUTTURALE

INTEGRATED STUDY OF THE TECTONIC EVOLUTION OF THE MID-NORWEGIAN PASSIVE MARGIN

Presentata da: Giulia Tartaglia

Coordinatore Dottorato

Prof.ssa Maria Giovanna Belcastro

Supervisore

Prof. Giulio Viola

Co-Supervisore

Prof. Thomas Scheiber

Esame finale anno 2022

Savoir s'étonner à propos est le premier pas fait sur la route de la découverte.

Louis Pasteur (1822-1895)

Acknowledgments

I would first like to thank my supervisor Prof. Giulio Viola, for his mentoring, guidance, and patience during my work on this PhD thesis. His insightful feedback pushed me to sharpen my thinking. He always advices the new PhD students to "enjoy the doctoral path, because it is a unique moment of your life". Thanks to his stimulating approach, the scientific opportunities he offered me, I can say that I enjoyed a lot this path.

I would like to acknowledge my co-supervisor Prof. Thomas Scheiber for his collaboration, good days on the field and fruitful feedbacks on my research.

I wish to thank all the colleagues of NGU, Jochen Knies, Ola Fredin, Marco Brönner, Roelant van der Lelij, Jasmin Schönenberger and Annina Margreth for the stimulating annual meetings, the data and constructive feedbacks.

I would like to offer my special thanks to Prof. Stefano Bernasconi, for the time he dedicated to the geochemical side of this research, and for his guidance in a new scientific world for me.

Alberto Ceccato is thanked for the good and instructive days in the field, his essential collaboration and his helpful feedbacks.

I wish to thank all the members of the Deformation Fluid Tectonic group of Bologna, professors, researchers, PhD students. From each of them, I learned something than now it is expressed in this final dissertation.

My heartful thanks are for Lisa Carrera and Sharon Pittau, my friends and PhD colleagues, for their patience with me, for all the laughs, beers and sometimes tears sheared together. Without you, girls, these three years would not have been the same.

A special thanks is for my best friend, Bea, the only person who always understands how I feel and who I am. She is the safe haven of my life.

And now, I have to switch in Italian. Ho bisogno di ringraziare la mia famiglia. Ringrazio i miei zii, Noemi e Michele, per esserci sempre nonostante la distanza. Li ringrazio per averci donato due pupi, Alberto e Leonardo, meravigliosi, felici e simpatici, che, mi spiace per tutti, ma sono le prime persone che voglio vedere appena torno a casa.

Mamma, Papà, a voi un grazie enorme e infinito per esserci e per avere un cuore grande.

Last but not least, ringrazio Corrado, per l'amore, la pazienza, le attenzioni che mi regala. Grazie per il supporto incondizionato da sempre. Grazie per la vita felice e la famiglia che stiamo costruendo insieme.

Abstract

This PhD thesis investigates the brittle tectonic evolution of the Mid-Norwegian Passive Margin (MNPM) in time and through space. A multidisciplinary and multiscalar workflow has been conceptualised, developed and applied to collect relevant data at several scales of observations and to interpret the many structural, mineralogical, geochemical and petrophysical features that characterise the long and complex brittle evolution of the margin.

The thesis first presents a high-resolution structural-geochronological study of a regional fault zone, the Lærdal-Gjende Fault in southwestern Norway. This case study helped define a scientifically sound workflow and test the possibility of structurally and geochronologically resolving multiple reactivations within a single fault. Through the definition, characterisation and dating of "Brittle Structural Facies" within the Lærdal-Gjende Fault, i.e, tightly juxtaposed, although not coeval, structural domains, a time-constrained conceptual model for the evolution of the fault was generated. Specifically, five Brittle Structural Facies have been characterised and dated by illite K-Ar within the fault core. The obtained ages constrain four periods of faulting, associated with strain accommodation induced by the hyperextension of the Norwegian margin down to recent reactivations in the Paleogene. The alternating widening and narrowing of the active fault zone in response to varying deformation mechanisms, including coseismic rupturing, has been resolved. As a result, this study highlights the importance of Brittle Structural Facies characterisation as part of a multidisciplinary workflow to investigate the diachronic evolution of fault zones. In turn, this may assist when aiming at the reconstruction of the structural brittle evolution of large areas, such as the MNPM.

The PhD thesis thus moves on to presenting an integrated reconstruction of the polyphase brittle evolution of the MNPM. The conceptualised and tested multidisciplinary and multiscalar workflow made it possible to reconstruct the evolution of the margin while dealing with the significant complexity of its polyphasic fracture network. The applied approach relied on remote sensing detection of lineaments along the entire MNPM, meso- and microstructural analysis of selected representative faults and fractures, paleostress inversion and K-Ar dating of fault gouges and altered rocks coupled with their mineralogical characterisation. The obtained results, particularly the sixty-two new K-Ar ages, helped to partially fill in the knowledge gap due to the

lack of absolute time constraints on the phases of brittle deformation and alteration affecting the margin. The proposed structural-geochronological model of the MNPM includes six time-constrained tectonic events: i) a Palaeozoic NE-SW compression forming WNW-ESE-trending and N(NE)-dipping thrust faults; ii) a Palaeozoic transpression with a NW-SE-oriented maximum stress axis, forming conjugate NW-SE and E-W strike slip faults; iii) a Carboniferous faulting event associated with rift initiation that formed NW-SE and NE-SW, variably dipping, faults; iv) a Late Triassic-Early Jurassic overall E-W extension that formed epidote and quartz-coated, N-S striking, normal faults, and coeval alteration of the host rock due to faulting-enhanced fluid circulation; v) an Early Cretaceous NW-SE extension, forming quartz-, calcite-, prehnite- and zeolite coated normal, transtensional NE-SW and N-S striking faults; vi) a Late Cretaceous (K-Ar ages <100 Ma) extension episode that reactivated pre-existing, suitably oriented faults, with extensive synkinematic precipitation of mainly prehnite and zeolite.

In addition, this thesis has tested an innovative research theme, by providing the first clumped isotopic constraints on calcite veins and calcite slickensides from basement rocks and faults and by proposing their interpretation through time and in space in the context of the polyphase evolution of the margin. Clumped isotope thermometry has been applied on calcite veins and mineralisations associated with brittle structures, collected in the MNPM and in the North Sea Margin, on the island of Bømlo. The wide range of documented fluid temperature (21 – 186 °C) and of carbon and oxygen isotopic values proves that calcite precipitated at varying thermal conditions from marine and meteoric fluids during a multiphase evolution. Structural data integrated with geochemical results suggest a trend of decreasing fluid temperature in time. In addition, the comparison of results from the MNPM and North Sea margins indicates that MNPM calcites mainly derive from highly mixed meteoric and marine fluids, locally circulating within paleosols in surficial environments, while North Sea calcites derive from seawater and mixed seawater fluids, probably at greater depth and with higher fluid temperature.

Lastly, the thesis also contains the results of the 3D modelling of the petrophysical properties and fracture distribution of fractured, weathered, dated basement outcrops on Bømlo island. These outcrops are thought to be analogues of the offshore, fractured and weathered, structural highs that host the main hydrocarbon reserves of unconventional plays in the Norwegian territory (e.g., Utsira High). Structural analysis of Virtual Outcrop Models integrated with Discrete Fracture Network modelling assisted the investigation of the relationships between sub-seismic and seismic-resolution fractures and the bulk permeability of the fractured and weathered basement volumes. Results indicate that a strongly oblate permeability tensor may be expected within a sub-seismic resolution fault, in which the maximum permeability component (K_1) is controlled by the intersection direction of the dominant meso-scale fracture sets associated with the fault. Finally, the results of *in-situ* unconfined compressive strength and permeability measurements on fractured and weathered crystalline basement of Bømlo are presented. Structural, petrophysical and geomechanical analyses permitted to build a model of the fractured basement reservoir, where the highly permeable fracture network is then "compartmentalised" into subdomains bounded by faults with lower permeability, which act as relative seals and local fluid-barriers.

In conclusion, studying at different scales the brittle fracture network along the MNPM has permitted to obtain a new integrated tectonic evolutionary model of the margin. The generated model and the workflow behind it may be applied in a multiscalar fashion, whereby observations and results are applicable during both up- and down-scaling processes. Also, they may assist with further 3D modelling of fractured (and weathered) rock volumes, which are to be studied and understood for their potential as reservoirs for the extraction or storage of georesources.

Contents

Chapter 1 - Introduction

1.1 General background

Passive margins are major morphotectonic features of our planet and are widespread around the world (Fig. 1.1). With a current aggregate length of c. 105.000 km, they represent an important exploration domain (Levell et al., 2010) as they host significant hydrocarbon reserves. As such, they have been explored and exploited for many decades (e.g., Bugge et al., 2002; Levell et al., 2010; Samakinde et al., 2020). Almost 75% of discovered conventional hydrocarbons were sourced from passive margins (Levell et al., 2010). Due to their global distribution, their geodynamic role in the Earth's fundamental processes, and their role as major reservoirs and exploration frontiers, they continue to attract the attention of researchers worldwide and to catalyse important research efforts.

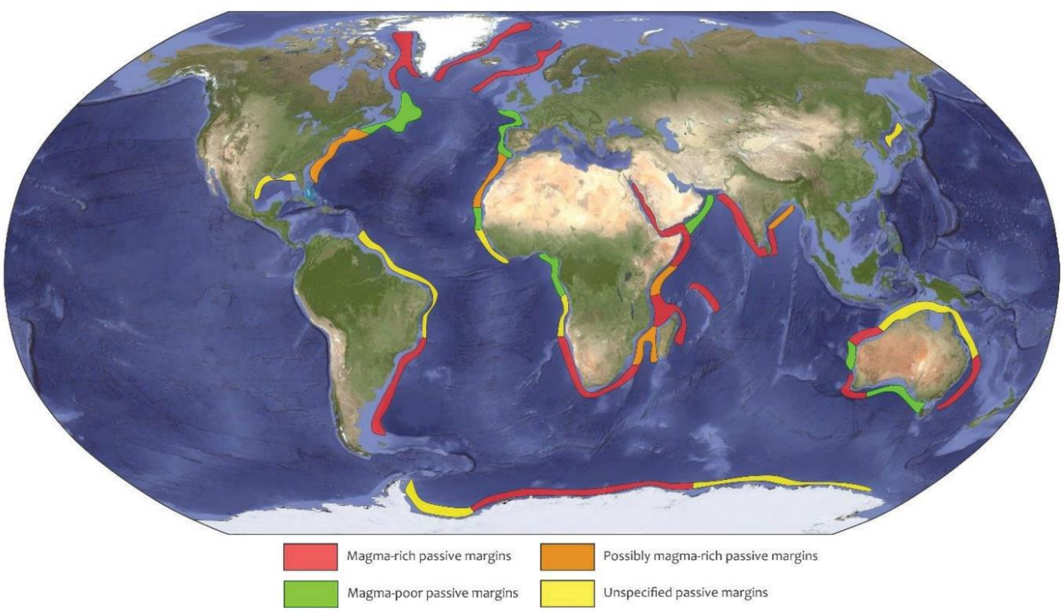

Figure 1.1 - Distribution of passive margins around the world sorted according to their recognised different types (Zastrozhnov, 2020, modified after Berndt et al., 2019).

The formation of passive margins is commonly explained in the framework of the existing geodynamic models for rifting. Conceptual models for the development of passive continental margins have been proposed starting in the late 70's (McKenzie, 1978; Wernicke et al., 1985; Keen and Beaumont, 1990). The "pure shear" model by McKenzie (1978), for example, suggests that extension associated with rifting results in the symmetric thinning of the continental crust leading to the formation of tilted blocks in the upper crust (Fig. 1.2). The “simple shear” model of Wernicke (1985), on the other hand, does not imply a tectonic framework based upon symmetrical deformation and proposes, instead, the existence of a lithospheric detachment fault crossing the crust and reaching into the upper mantle along which crustal thinning, exhumation and magmatism take place leading to asymmetric rifting causing margin geometry (Fig. 1.2, Berndt et al., 2019).

Most modern models of rifting and break-up include several evolutionary stages comprising discrete phases of both pure shear and simple shear as well as the complex interaction between the thinning crust and the upwelling mantle, lithospheric necking, and diffuse faulting, rifting localisation and exhumation of mantle material (Keen and Beaumont, 1990; Lavier and Manatschal, 2006; Reston, 2007; Huismans and Beaumont, 2011 and references therein).

As to the presence and amount of volcanism that may accompany rifting, two major types of divergent rifted margins have been identified: volcanic and magma-poor margins (Fig. 1.1, 1.2, Berndt et al., 2019). Magma-poor margins exhibit wide zones of continental thinning by diffuse faulting and the subsequent formation of numerous, large, tilted blocks, and are frequently associated with slow extension (Manatschal, 2004; Reston, 2007; Péron-Pinvidic and Manatschal, 2019). These margins may be referred to as “hyper-extended” when the crust, in response to extreme stretching, becomes very thin and embrittled, with fluids penetrating to mantle depth along fault zones and serpentinising the upper mantle material (Manatschal, 2004; Beltrando et al., 2014; Doré and Lundin, 2015).

Volcanic margins, on the other hand, are characterised by large amounts of syn-rift extrusive and intrusive bodies and exhibit significant crustal thinning in a relatively narrow zone (c. 20 km) (Geoffroy et al., 2015).

From a geometrical point of view, it is possible to identify a third group of margins, i.e., the transform margins that bound part of the Atlantic Ocean and along which the main movement of plates is oblique shear instead of extensional (Biari et al., 2021). Oblique shearing within transform margins might be one of the main mechanisms for the breakup of continents as less force is required to break obliquely through cratonic crust (Lundin and Doré, 2019; Biari et al., 2021). One characteristic feature of many transform margins is the existence of marginal ridges parallel to the transform margin (Biari et al., 2021).

Today, it is widely accepted that rifting is a complex process and generally polyphasic in its evolution and reflects the interplay of numerous factors, among which complex crust-mantle interactions (Péron-Pinvidic and Manatschal, 2019). Moreover, it has been long noticed that most rifted margins around the world developed on former orogens, and particularly on former suture zones (Will and Frimmel, 2018; Phillips et al., 2019; Osmundsen et al., 2021). Based on plate kinematic calculations and on the position of the continent-ocean transition, modern studies propose that most margins open in an oblique manner, with more than 70% of all known rift segments exceeding an obliquity of 20% (e.g., Brune et al., 2014).

In summary, because of their polyphase nature and their tendency to develop on pre-existing suture zones (by which they are significantly influenced; Rotevatn et al., 2018; Schiffer et al., 2019; Will and Frimmel, 2018), passive margins are all characterised by some individual peculiarities in addition to their first-order, long wavelength features.

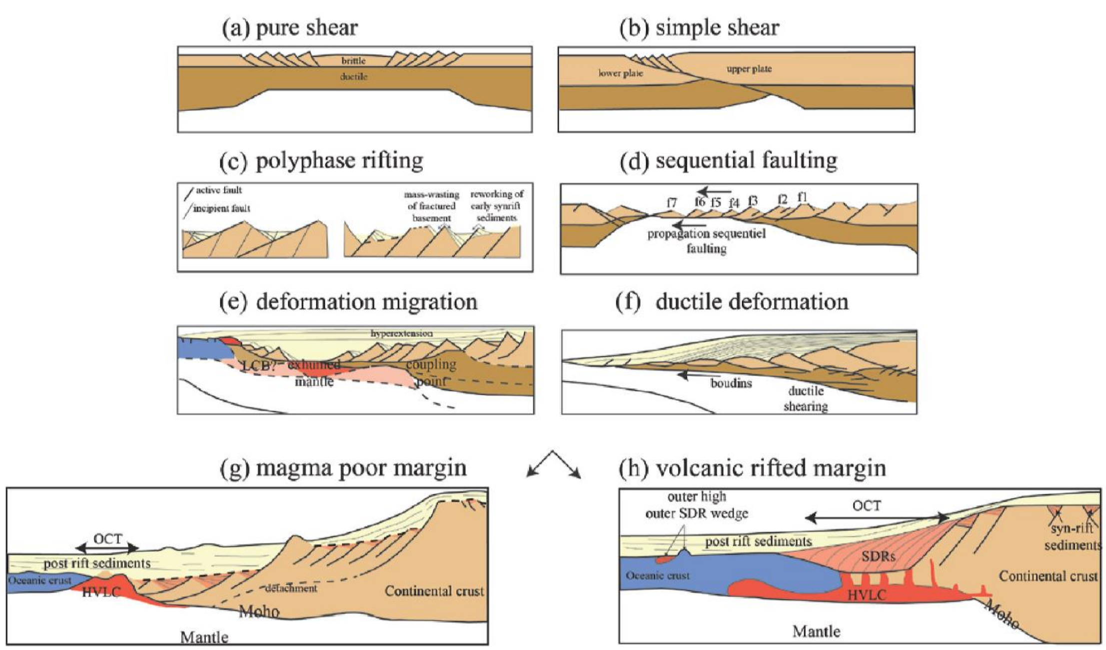

Figure 1.2 - Schematic representation of the progress of knowledge from top to bottom: the early view of (a) Mackenzie (1978) and (b) Wernicke (1985), new concepts of (c) Reston (2005), (d) Ranero and Perez-Gussinye (2010), (e) Péron-Pinvindic et al. (2013) and (f) Clerc et al. (2018); (g) and (h) show schematic representation of the architecture of a slowly extended magma-poor margin and a rapidly extended magma-rich margin (Biari et al., 2021).

1.2 Rationale of the study

The Mid-Norwegian Passive Margin (MNPM) is a volcanic, polyphase, oblique rifted margin formed from the collapse of the Scandinavian Caledonides in the Devonian and the formation of the NE Atlantic Ocean in the Eocene (Faleide et al., 2008; Theissen-Krah et al., 2017). This margin is oblique compared to the adjacent, N-S striking North Sea Margin, which represents its southern continuation (Fig. 1.3). The MNPM and the North Sea margin both experienced two main rifting stages that led to a diachronous breakup in the Eocene, which tends to be younger northwards (Gernigon et al., 2020). The two sectors thus developed diachronically, with the North Sea recording older rifting in the Permo-Triassic and in the Late Triassic-Jurassic, with some discrete Cretaceous extensional episodes (Scheiber and Viola, 2018; Gernigon et al., 2020; Fossen et al., 2021). The MNPM recorded the two rifting phases in the Late Permian-Early Triassic and in the Late Triassic-Jurassic, but also a relevant rifting in the Cretaceous, coeval to the formation of the main offshore basins of the MNPM (Gernigon et al., 2020; Zastrozhnov et al., 2020).

The MNPM and the North Sea margin both spatially interfere with major ductile and brittle-ductile lineaments of tectonic origin, which significantly influenced the margins evolution. Examples are the Møre-Trøndelag Fault Complex (MTFC) and the Høybakken Detachments along the MNPM, and the Hardangerfjord Shear Zone and the Nordfjord-Sogn Detachment along the North Sea margin (Fig. 1.4). They developed during the Devonian accommodating extension due to the orogenic collapse of the Scandinavian Caledonides. In particular, the MTFC is an ENE-WSW regional fault complex composed of sub-parallel fault strands (e.g., Hitra-Snåsa and Verran Faults; Grønlie and Roberts, 1989; Séranne, 1992; Redfield et al., 2005; Lundberg et al., 2012). Its penetrative brittle-ductile ENE-WSW-trending structural grain governed and influenced the orientation of the MNPM that is now subparallel to the MTFC. The MTCF experienced multiple episodes of ductile and brittle reactivation since the Devonian, with dominant strike-slip kinematics and a minor dip-slip component, and, quite remarkably, it is still seismically active (Grønlie and Roberts, 1989; Grønlie et al., 1991; Bungum et al., 1991; Séranne, 1992; Kendrick et al., 2004; Redfield et al., 2004, 2005; Gordon et al., 2016; Nasuti et al., 2011, 2012; Lundberg et al., 2012).

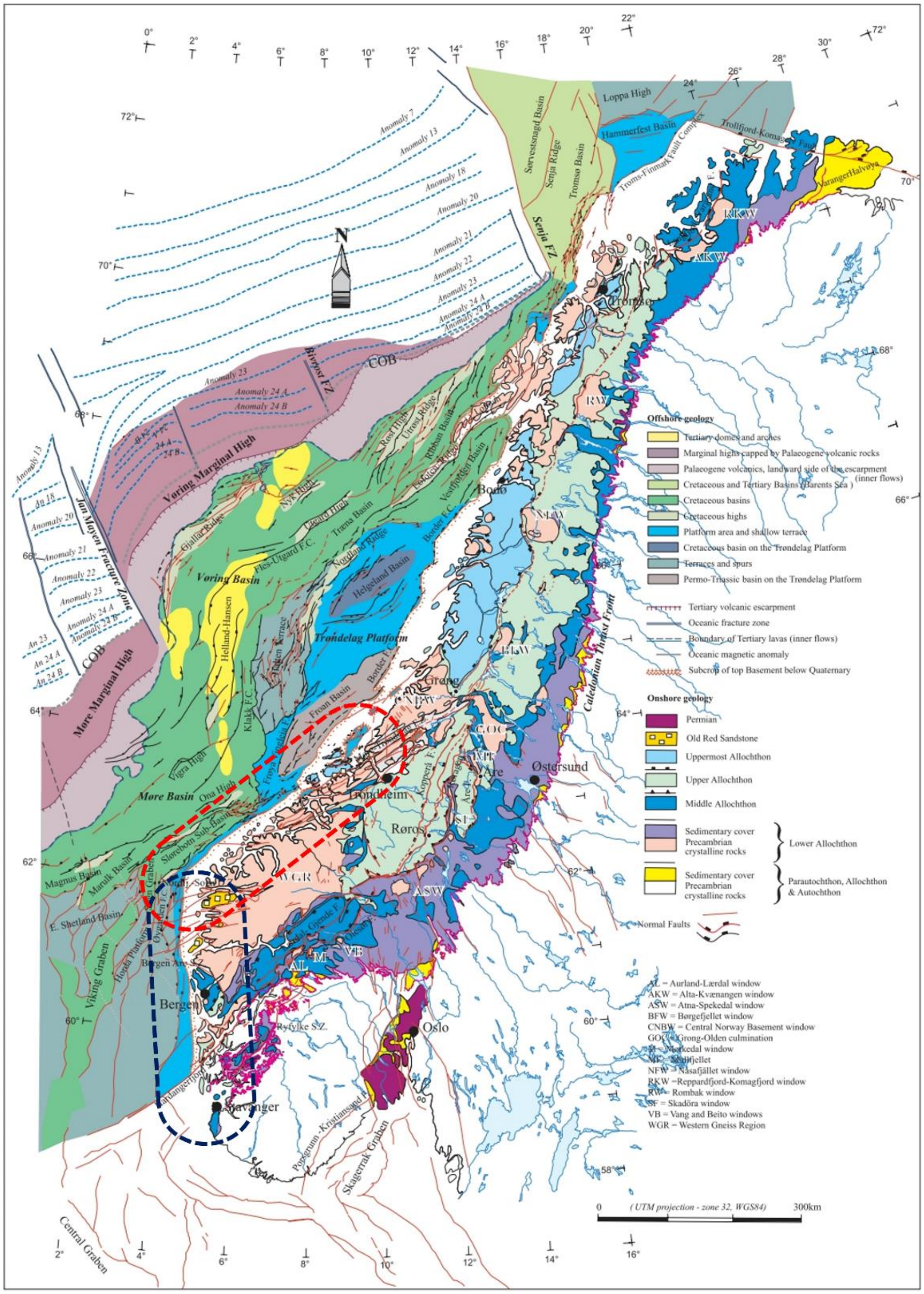

Figure 1.3 - Geological map of Norway. In red it is shown the indicative extent of the studied portion of the onshore Mid-Norwegian Passive Margin and in dark blue that of the North Sea Margin (modified after Mosar et al., 2002).

The Hardangerfjord Shear Zone (HFZ) is a top-to-the-NW extensional shear zone, active in the Devonian (Fossen and Hurich, 2005). The Høybakken and Nordfjord-Sogn Detachments are low-angle, extensional shear zones that favoured the formation of Devonian sedimentary basins, with a top-to-the-SW and top-to-the-W sense of shear, respectively (Osmundsen et al., 2006; Milnes and Corfu, 2011; Fossen et al., 2016).

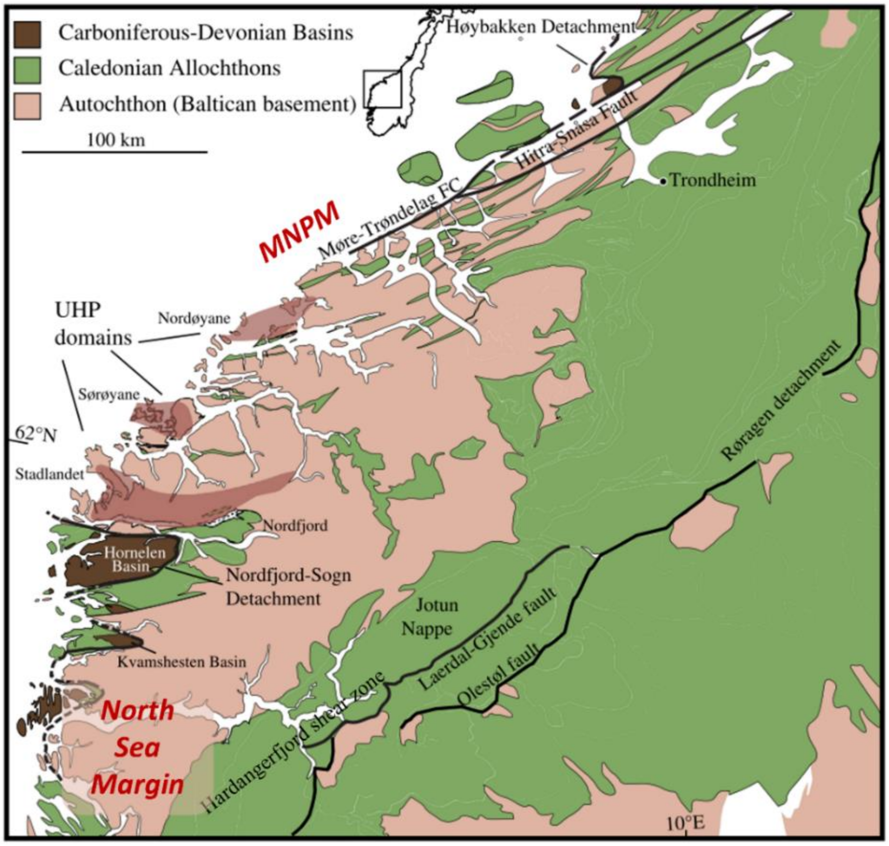

Figure 1.4 - Geologic map of the northern part of the North Sea Margin and of the MNPM, showing the main regional lineaments: from South to North these are the Hardangerfjord Shear Zone, the Nordfjord-Sogn Detachment, the Møre-Trøndelag Fault Complex (MTFC) and the Høybakken Detachment (Modified after Walsh et al., 2013).

Both sectors of the Norwegian margin are characterised by a dense network of faults and fractures developed during their long brittle evolution (Fig. 1.5; Gabrielsen et al., 2002; Scheiber and Viola, 2018; Gernigon et al., 2021). This brittle network is well exposed in the crystalline basement along the onshore domain of the margin (Gabrielsen et al., 2002; Scheiber and Viola, 2018). In the offshore domain, the exhumed crystalline basement blocks also recorded and preserved an analogous brittle deformation pattern (Fig. 1.5). The onshore and offshore domains differ for the presence or lack of a sedimentary cover. In fact, the offshore fractured basement is covered by thick Meso-Cenozoic sedimentary sequences, which are no more preserved onshore due to the evolution of the margin and the stripping effects of numerous recent glaciations (Fig. 1.6) (Faleide et al., 2008; Zastrozhnov et al., 2020).

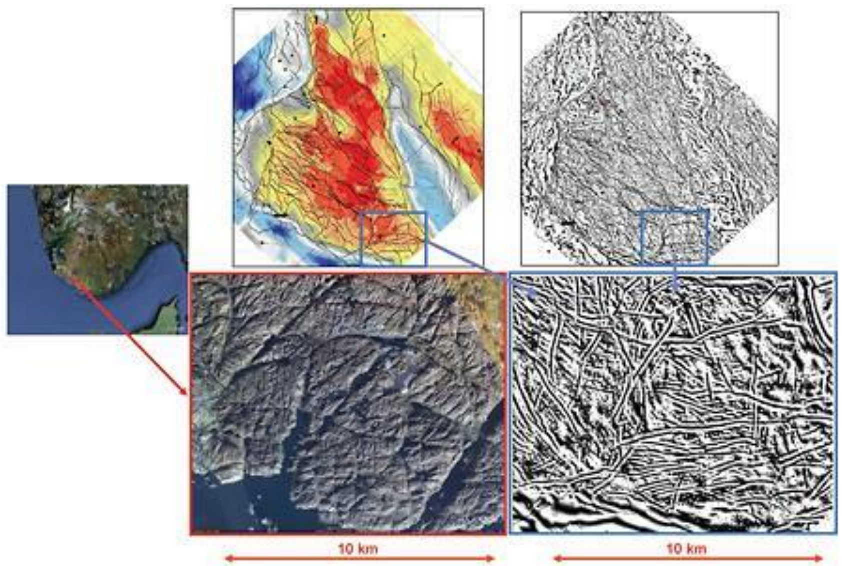

Figure 1.5 - Comparison of satellite image of onshore Southwestern Norway and a seismic image of the top of the basement on Utsira High, North Sea (courtesy of Lundin Norway AS). The two images show a similar fracture pattern affecting the basement.

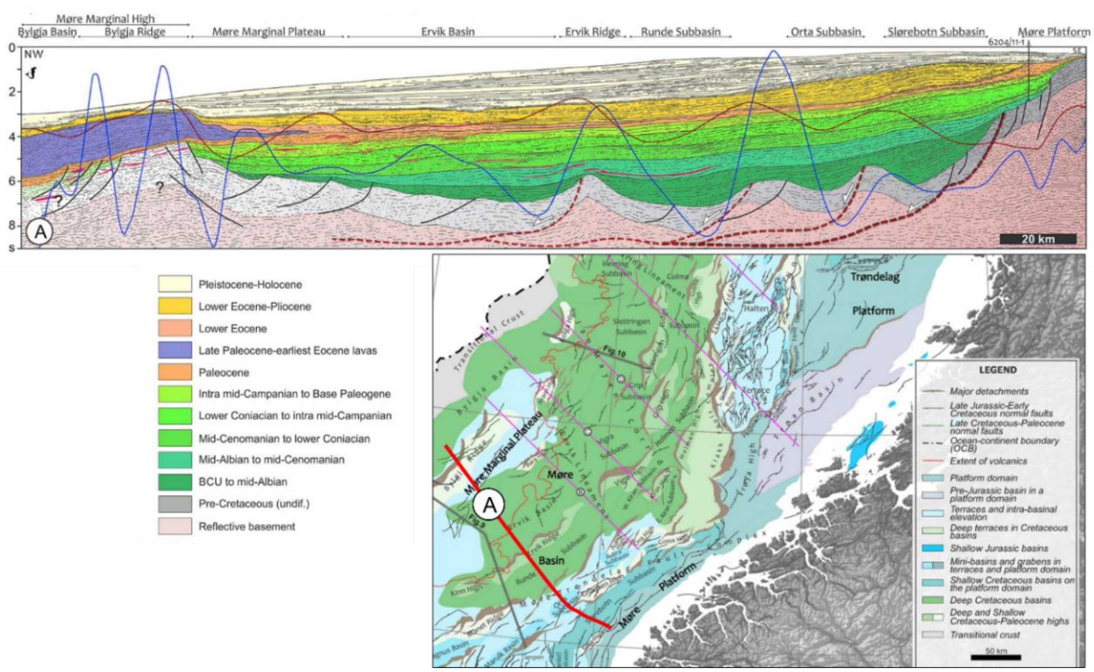

Figure 1.6 - Geological cross-section across the Møre Basin. The main detachment faults are shown by thick dashed red lines (Modified after Zastrozhnov et al., 2020).

1.2.1 Hydrocarbon reserves

The Norwegian offshore domain is a mature hydrocarbon province that has been extensively mapped since the discovery of conventional oil and gas reserves therein in the late 1960's (Rønnevik et al., 1983; Riber et al., 2015; Gernigon et al., 2021). The volcanic MNPM has since been the site of unprecedented geological and geophysical investigations, research, exploration and hydrocarbon production (Blystad, 1995; Brekke, 2000; Faleide et al., 2010 and references therein; Nasuti et al., 2011, 2012).

The offshore domain of the MNPM and the North Sea Margin also host unconventional hydrocarbon plays. These hydrocarbon reserves are hosted within "fractured and weathered" basement volumes (Fig. 1.7; Trice, 2014; Riber et al., 2015; 2017; Fredin et al., 2017a). In detail, the offshore fractured crystalline basement is locally irregularly draped by variable thicknesses of highly weathered rocks, called saprolites, which are the direct expression of deep weathering under aggressive climatic conditions. Recent studies have shown that those saprolitic layers are genetically associated with the main phases of brittle deformation that have affected the Norwegian basement during its long evolution (Fig. 1.7; Trice, 2014; Riber et al., 2015, 2017; Fredin et al., 2017a). Indeed, these highly weathered uncoherent layers, which can host significant oil and gas reserves, are in general intimately associated with faults and fractures (Trice; 2014; Riber et al., 2015; 2017; Fredin et al., 2017a). Since the discovery of significant unconventional hydrocarbon reserves within exhumed offshore fractured and weathered crystalline basement blocks of North Sea (e.g., Petford and McCaffrey, 2003; Riber et al., 2015, 2017; Trice et al., 2019), a surge of interest in the geometry, petrophysical properties and development of intra-basement fracture networks in the context of passive margin evolution has, therefore, developed (e.g., Fossen, 2010; Breivik et al., 2011; Riber et al., 2015; Fredin et al., 2017a; Scheiber and Viola, 2018; Trice et al., 2019; Fazlikhani et al., 2020; Ceccato et al., 2021a, b).

Previous studies on the MNPM predominantly focused on determining the crustal architecture, the geometry and evolution of the complex margin system since the collapse of the Caledonian orogen. Only a few, instead, focused on studying the onshore domain and, in detail, the focus of the scientific community has been the geometry and evolution of the MTFC (e.g., Séranne, 1992; Redfield et al., 2005; Osmundsen et al., 2006; Lundberg et al., 2012; Nasuti et al., 2012). All these decades of studies notwithstanding, the reconstruction of the onshore and offshore evolution of the MNPM still lacks absolute time constraints on the many evolutionary stages that have been documented.

Considering that brittle fracture patterns and the associated weathered rocks are present both in the offshore domain beneath the thick Mesozoic sedimentary cover (e.g., references), and in their onshore basement analogues, studying the geometrical, kinematic, and absolute temporal components of the onshore MNPM is pivotal to the understanding of the entire margin evolution and to continue exploration activities offshore in highly inaccessible domains.

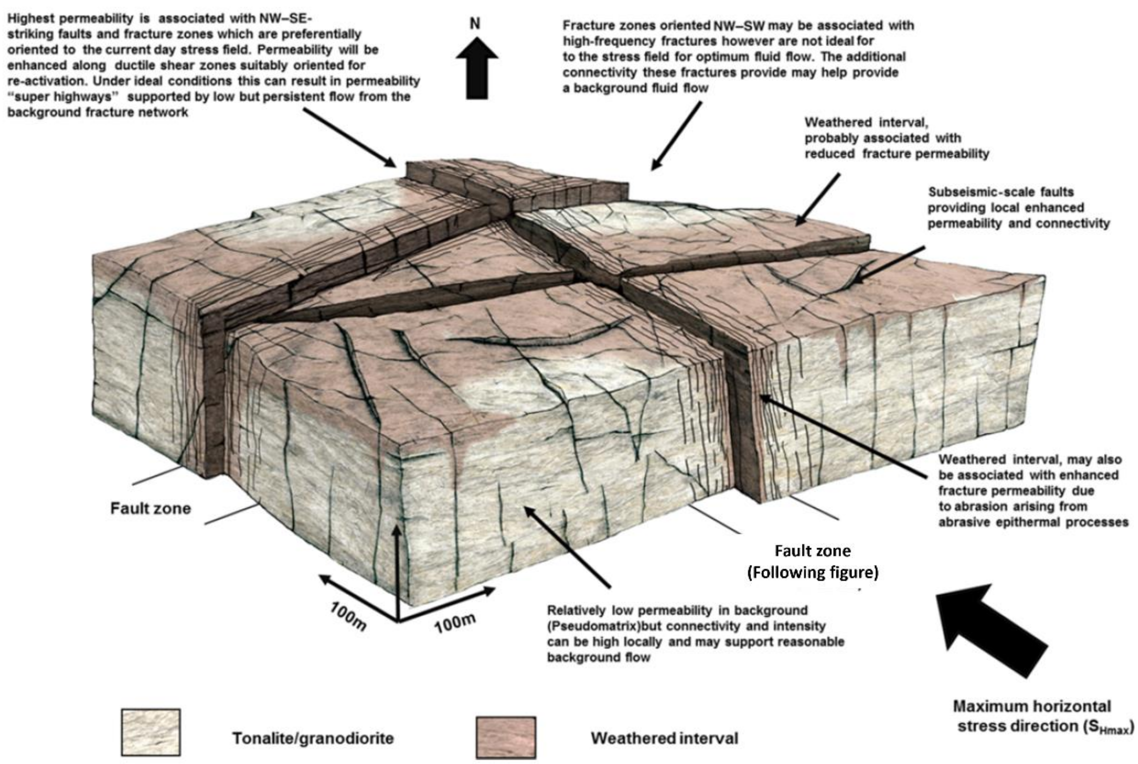

Figure 1.7 - Conceptual model of a basement reservoir. Case study of Lancaster Discovery in West of Shetlands. The model highlights the presence of an inhomogeneous layer of weathered rock, whose depth is influenced by the presence and orientation of faults and fractures (modified after Trice, 2014).

Structural and textural features at the reservoir scale are commonly defined through seismic geophysical investigations which, at the current analytical resolution, allow us to detect structures with thickness or throws > 4-10 m (Tanner et al., 2019; Gernigon et al., 2021). However, sub-seismic-resolution scale (SSRS) features (thickness/throw <4-10 m; Damsleth et al., 1998; Walsh et al., 1998) within basement rocks also affect the basement bulk structural, petrophysical and mechanical properties (Ceccato et al., 2021a). Hence, the mesoscale, *in-situ* study of onshore fractured basement volumes provides the unique opportunity to characterise the details of local brittle fracture patterns, and to understand the relationships with larger, reservoir-scale structures in the inaccessible offshore domain.

From a structural geological point of view, the main interests in studying the MNPM lie in i) characterising and understanding its full kinematic evolution and geometrical obliquity with respect to the adjacent North Sea Margin to the south and extrapolating the consequences thereof upon the modalities of rifting and strain localisation; ii) reconstructing its long-lived and polyphase evolution, which is characterised by the activation and repeated reactivation of major tectonic lineaments and by the development of pervasive brittle fracture networks, whose origin is not yet completely unravelled and whose presence is key to the reconstruction of the details of margin evolution and to constraining the petrophysical properties of fractured and weathered basement; iii) filling the knowledge gap due to the lack of absolute time constraints on the margin's many phases of brittle deformation; and, last but not least, iv) better understanding the occurrence of large hydrocarbon unconventional plays within fractured, weathered basement blocks.

1.3 Objectives and organisation of the thesis

This thesis is part of the project "Basement fracturing and weathering on- and offshore Norway - Genesis, age, and landscape development" (BASE2), which is a research agreement between a consortium of oil industries active on the Norwegian margin, the Geological Survey of Norway, and the University of Bologna. The main aim of this project is to study the genesis, age, and landscape development of fractured and weathered basement on- and offshore Norway.

The detailed structural-geochronological study of the onshore fracture network of the MNPM offers the potential to refine the better understanding of the regional structural evolution. This PhD thesis aims to add more and better constraints to resolve the brittle fracture pattern of the Norwegian margin by means of a multidisciplinary and multiscale approach that combines structural, geochronological, and mineralogical analyses. In addition, it aims to compare the pre-existing time-constrained tectonic models of the North Sea with a new proposed evolutionary model for the evolution of the MNPM sector. Finally, this thesis also proposes a multidisciplinary and multiscale toolbox to study complexly fractured basement rocks.

The *fil rouge* of this thesis resolves around the structural evolution in time of brittle structures. As such, the thesis first deals with a high-resolution study of a single fault zone that was necessary to define a scientifically sound workflow and approach to the issue and to test the possibility of resolving structurally and geochronologically multiple reactivation events even within a single fault. The thesis moves then onto the project core, i.e., the multidisciplinary and multiscalar study carried out to build a time-constrained tectonic model for the evolution of the MNPM. This thesis tests then an innovative research theme, by providing the first clumped isotopic constraints on calcite veins from basement rocks and by attempting their interpretation in terms of fault evolution through time and in space in the context of the long structural evolution of the margin. Lastly, the thesis also contains the results of models of the petrophysical properties and fracture distribution of fractured, weathered, dated basement outcrops onshore to be used as analogues of the offshore structural highs that host the main hydrocarbon reserves of the above-mentioned unconventional plays.

In more detail, Chapter 2 sets the scene by expanding on the geological setting of the study area. It describes the known evolution of the MNPM and of the MTFC. It also briefly describes existing evolutionary tectonic models of the North Sea margin.

Chapter 3 describes the main steps of the applied multidisciplinary and multiscale workflow. The presented workflow includes remote sensing detection of lineaments, meso- and microstructural characterisation of faults and fractures, paleostress inversion, K-Ar dating of fault rocks coupled with mineralogical analysis, clumped isotope thermometry performed on calcite mineralisations, and finally, petrophysical measurements on fractured, weathered outcrops, combined with Virtual Outcrop Models and Discrete Fracture Network (DFN) modelling.

Chapters 4 to 7 report core of the obtained results. Chapter 4 is dedicated to testing and improving the workflow by describing the detailed structural analysis of a single fault zone, the Lærdal-Gjende Fault (LGF, southwestern Norway, Fig. 1.5). This chapter presents the paper *“Brittle structural facies” analysis: A diagnostic method to unravel and date multiple slip events of long-lived faults* by Tartaglia et al. (2020), published on Earth and Planetary Science Letters. In this paper the “Brittle Structural Facies” (BSF) concept was used and improved to discriminate different structural domains within the Lærdal-Gjende Fault core, characterised by varying microstructures, mineralogical compositions, kinematics, and absolute age. Their detailed structural analysis integrated with K-Ar dating of the fault rock assemblage helped to identify several tightly juxtaposed, although not coeval, structural domains (the BSF) within the LGF. BSF are demonstrated to be key to understanding the structural heterogeneity of fault zones, the diachronic formation of geometrically and kinematically complex fault cores and to reconstructing fault evolution in time and through space. In fact, five BSF have been identified and sampled. They have been characterised structurally, mineralogically and dated, allowing us to constrain four distinct time periods of faulting from the Jurassic to the Paleogene.

Chapter 5 is a paper in review for GSA Bulletin titled *“Time-constrained multiphase brittle tectonic evolution of the onshore mid-Norwegian Passive Margin”* by Tartaglia et al.. It applies a multidisciplinary and multiscale workflow aiming to unravel the evolution of the brittle structural network along the MNPM. By means of remote sensing lineament detection, field work, microstructural analysis, paleostress inversion, mineralogical characterisation and K-Ar dating of fault rocks, six tectonic events have been identified, from Caledonian compression down to Late Cretaceous extensional pulses (< 100 Ma). This study represents the core of the project, and sheds light onto the structural evolution of MNPM and confirms the active role of the MTFC during the rifting stages. Sixty-two new radiometric K-Ar ages from structurally carefully characterised fault rocks are presented. These represent a major step forward the erection of a fully time-constrained evolutionary model for the MNPM.

Chapter 6 deals with an innovative approach to the reconstruction of the brittle evolution of crystalline basement rocks in the absence of sedimentary covers that may help with regional correlations. Calcite veins, slickenfibers and mineralisations are commonly associated with the MNPM brittle structures. They derive from different events of crystallisation during brittle evolution and fluid ingress. Clumped palaeothermometry on “tectonic carbonates” within basement rocks has been applied, in collaboration with Prof. Bernasconi from ETH (Zurich, Switzerland), to better understand the origin of fluids and, if possible, to discriminate different generations of calcite crystallisation events. This chapter presents a paper in preparation, which deals with the isotopic results from calcite samples collected on the MNPM and North Sea margin. These new data add innovative constraints on the evolutionary tectonic models of the two segments of the Norwegian margin.

In order to link the structural analysis of onshore fractured outcrops to the offshore basement fracture pattern, modelling of geometrical, mechanical and permeability properties of fractured and weathered outcrops, considered as analogues of offshore crystalline basement highs, was performed. After the definition of the structural evolution in time of the margin, this thesis reports the petrophysical characterisation of selected fractured, weathered basement blocks. Chapter 7 summarises the results of two studies, in which I am one of the authors, *Constraints upon fault zone properties by combined structural analysis of virtual outcrop models and discrete fracture network modelling* (Ceccato et al., 2021a, Journal of Structural Geology) and *In-situ quantification of mechanical and permeability properties on outcrop analogues of offshore fractured and weathered crystalline basement: Examples from the Rolvsnes granodiorite, Bømlo, Norway* (Ceccato et al., 2021b, Marine and Petroleum Geology). To understand the relationships between sub-seismic and seismic-resolution fracturs and the bulk permeability of the fractured rock, a regional-scale fault zone in the North Sea Margin was studied by means of structural analysis of Virtual Outcrop Models integrated with Discrete Fracture Network (DFN) modelling. Fracture geometrical and spatial characteristics allowed us to constrain the variability of the structural permeability tensor as a function of the mesoscopic fracture pattern. This chapter also presents the results of *in-situ* unconfined compressive strength and permeability measurements on fractured and weathered crystalline basement of Bømlo (North Sea Margin). Data analysis permits to build a model of the fractured basement reservoir, where the highly permeable fracture network is then "compartmentalised" into polyhedral fault-bounded domains with low permeability, acting like local fluid-barriers.

Chapter 2 - Geological Setting

2.1 Scandinavian Caledonides

From southwestern Norway to the Barents Sea in the north, the territory of Norway is shaped by the backbone of the Scandinavian Caledonides, an orogenic belt formed in response to the Late Silurian-Early Devonian continental collision between Baltica and Laurentia (Fossen and Dunlap, 1998; Corfu et al., 2014). The convergence of Baltica and Laurentia led to a Himalaya-type collision, with the NW-directed subduction of the Baltican margin beneath Laurentia (Labrousse et al., 2010). This episode, the so-called Scandian orogeny, led to metamorphism up to peak conditions of 3.6 GPa and 800 °C between c. 420 to 400 Ma ago (e.g., Kylander-Clark et al., 2009; Walsh et al., 2013).

Shortening and subduction formed a complex stack of nappes of the Baltic autochthonous basement overlain by sequences of the Baltic Shield, the ancient Iapetus Ocean and Laurentian basement cover units (Corfu et al., 2014), classically grouped in the literature in the Lower, Middle and Upper Caledonian Allochthons (Fig. 2.1). In detail, the Lower Allochthon consists of Baltican basement and its upper Proterozoic to Lower Palaeozoic metasedimentary cover (Fossen and Hurich, 2005; Corfu et al., 2014). The Middle Allochthon includes continental, crystalline Proterozoic rocks with their Late Proterozoic cover, not related to the Baltican shield, among which the Jotun Nappe in southwestern Norway is a remarkable example (Fossen and Hurich, 2005). The Upper Allochthon includes exotic nappes, such as Ordovician-Silurian ophiolites and island-arc complexes. Some of these complexes may have originated as distinct terranes of the Iapetus Ocean, subsequently accreted onto the Baltican margin during the closure of the ocean and the continental collision (Fossen and Hurich, 2005; Corfu et al., 2014).

The currently exposed MNPM is mainly shaped within the Western Gneiss Region (WGR), which is a window of Baltican Proterozoic orthogneiss exposed beneath a stack of allochthon units emplaced onto the Baltican margin at c. 430-415 Ma (Fig. 2.1; Walsh et al., 2013). The WGR exhibits a northwest-ward increase of the Scandian metamorphic grade, climaxing with the exposure of UHP rocks along the coast of the MNPM (Walsh et al., 2013). Above the WGR, the nappe sequence along the MNPM includes the Upper Allochthon in the form of ophiolitic rocks from the oceanic terranes and sedimentary and crystalline rocks of the rifted and hyperextended margin of Baltica, and the Uppermost Allochthon composed of ophiolitic and metasedimentary rocks Laurentian affinity (Andersen et al., 2012; Walsh et al., 2013).

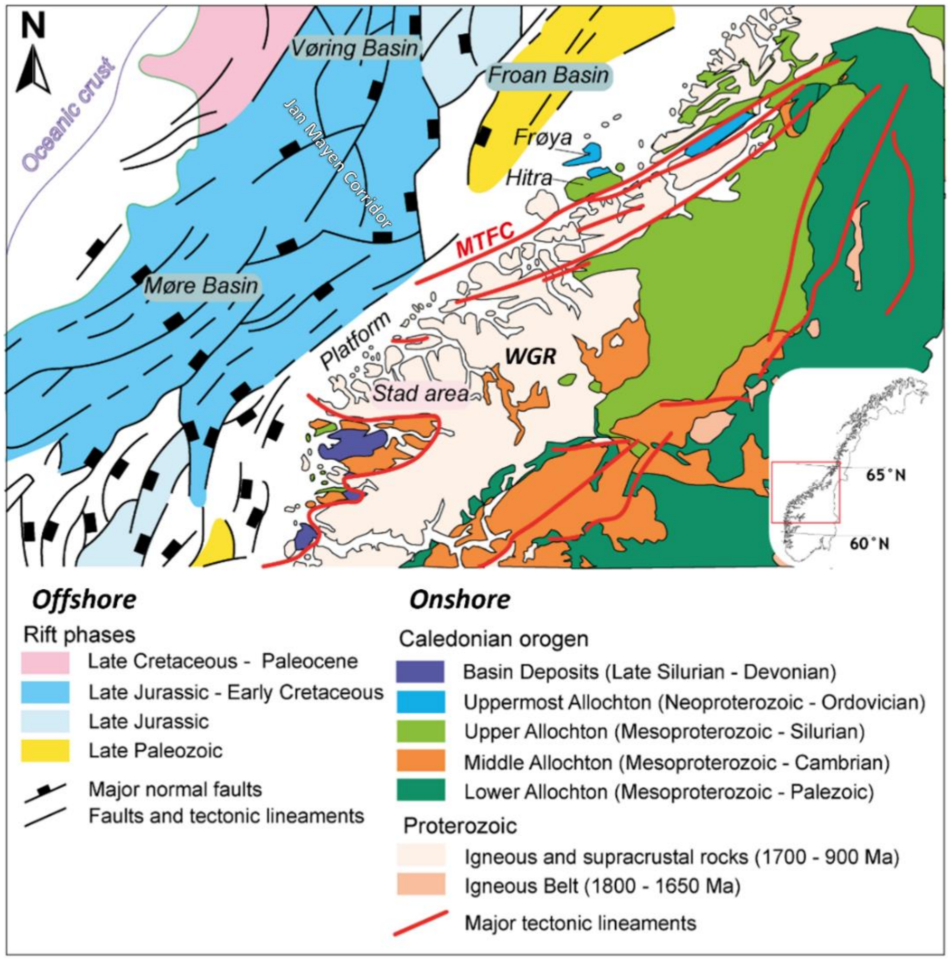

Figure 2.1 - Simplified geological map of the intersection between MNPM and North Sea Margin, showing the distribution of the tectonic nappes.

The Caledonian collisional tectonics led to the formation of an over-thickened orogenic pile that collapsed during the Early Devonian (c. 408-402 Ma; Fossen and Dunlap, 1998). The collapse was favoured by the nucleation and reactivation of orogen-scale extensional detachments (Fossen and Hurich, 2005). Overall NW-SE extension caused the exhumation of the deeply seated orogenic roots to shallow crustal levels. The progressive accommodation of deformation from the ductile to the brittle regime led to the nucleation of major faults and brittle fault zones, which overprinted earlier ductile detachments (Fossen et al., 2016). Remarkable examples of these Devonian extensional detachments are the Hardangerfjord Shear Zone, the Nordfjord-Sogn detachment zone and the Møre-Trøndelag Fault Complex (Fig. 1.4, 2.2; Corfu et al., 2014; Fossen et al., 2016).

2.2 Evolution of the Mid-Norwegian Passive Margin

The MNPM is one of the most studied volcanic rifted margins in the world (Osmundsen et al., 2005, 2006, 2010; Péron-Pinvidic and Osmundsen, 2016; Theissen-Krah et al., 2017; Péron-Pinvidic et al., 2020; Gernigon et al., 2020, 2021), and its detailed characterisation began with magnetic and gravity data acquisition in the 1960s-1970s (Grønlie and Ramberg, 1970; Talwani and Eldholm, 1972). The MNPM is composed of two large offshore segments, which, from SW to NE, include the Møre and the Vøring segments of the margin (Fig. 2.1). Discrete, NW-SE-trending tectonic structures, such as the Jan Mayen Corridor, separate these segments (Faleide et al., 2008; Gernigon et al., 2020), each of which is composed of an inner platform, the Møre, and Vøring Platforms, and a system of outer basins, the Møre-Trøndelag and the Vøring Basins (Fig. 2.1).

The MNPM is a polyphasic rift system, which developed after the orogenic collapse of the Caledonides up to crustal breakup in the early Eocene (Doré et al., 1999; Faleide et al., 2008; Fossen, 2010; Nasuti et al., 2011, 2012; Gernigon et al., 2020, 2021; Osmundsen et al., 2021). The first evidence of incipient extension is a number of intra-continental basins distributed onshore that formed during the Devonian (Braathen et al., 2002; Fossen, 2010; Osmundsen et al., 2021). They formed by extensional reactivation of low-angle Caledonian thrusts. The Devonian maximum extension concentrated in the central and southern part of the Caledonides, in the area between the WGR and East Greenland (Fossen, 2010). It is believed that the first rifting phase affecting the MNPM was in the mid-Carboniferous time, based on structural observations onshore East Greenland, but it remains poorly constrained along the Norwegian margin (e.g., Stemmerik et al., 1993; Stemmerik, 2000). However, undifferentiated Palaeozoic basins (Devonian-Carboniferous?) have been identified in the deepest part of the Trøndelag Platform (Zastrozhnov et al., 2018; Péron-Pinvidic et al., 2020), and they may support the hypothesis of early increments of rifting in the MNPM already in Carboniferous times.

The main rifting phases experienced by the MNPM were in Late Permian-Early Triassic, Late Jurassic-Early Cretaceous and Late Cretaceous-Early Paleogene times (e.g., Brekke, 2000; Osmundsen et al., 2021). Permo-Triassic extension is well documented in the Trøndelag Platform by seismic evidence and has been interpreted to culminate in the Early Triassic (Müller et al. 2005; Zastrozhnov et al., 2018). The Middle to Late Triassic and earliest Jurassic represents a post-rift phase with relative tectonic quiescence (Brekke, 2000; Müller et al., 2005; Gernigon et al., 2021), followed by intermittent and moderate Early and Middle Jurassic stretching events (Blystad, 1995; Gernigon et al., 2021).

The Late Jurassic-Early Cretaceous rifting event is characterised by a drastic kinematic and tectonic change in the North Atlantic, related to the northward propagation of the Atlantic rifting and reflects major extension and crustal thinning in the NE Atlantic (Lundin and Doré, 2011; Stoker et al., 2017). The stretching of the crust and block faulting favoured the development of up to 10 km deep Cretaceous basins along the MNPM, where significant syn-rift deposits accumulated (Gernigon et al., 2020; Zastrozhnov et al., 2018). There is no general consensus today on how long the regional extension continued into the Early Cretaceous (e.g., Blystad, 1995; Brekke, 2000; Osmundsen and Ebbing, 2008; Zastrozhnov et al., 2018, 2020; Gernigon et al., 2021).

A further distinct extensional rifting phase is documented in the Late Cretaceous-Palaeocene (Doré et al., 1999; Faleide et al., 2008; Stoker et al., 2016; Péron-Pinvidic and Osmundsen, 2020), followed by continental breakup and associated magmatism in the MNPM. The final breakup was diachronous and initiated at 57-58 Ma in the Møre segment and later propagated to the outer Vøring Margin at 56-55 Ma (Gernigon et al., 2019; Zastrozhnov et al., 2020).

The post-breakup period is mainly characterised by cooling, regional subsidence and relative tectonic quiescence (Brekke, 2000; Faleide et al., 2008), although a series of compressional events is known to have affected the Vøring Basin in the mid-Eocene, Oligocene, mid-Miocene and Pleistocene (Lundin and Doré, 2002; Doré et al., 2008). This compressional tectonics is expressed by localised basin inversion and selective reactivation of the structural highs along the Fles Fault Complex and in the proximal domain (Nordland Ridge; Zastrozhnov et al., 2018). The geodynamic reason for these compressional events remains highly debated and ridge push, coeval spreading reorganisation in the oceanic domain, far-field orogenic stress or mantle drag have all been proposed and potential causes (Lundin and Doré, 2002; Mosar et al., 2002; Doré et al., 2008; Zastrozhnov et al., 2018; Gernigon et al., 2021).

In the Quaternary, large and thick ice masses expanded over the Norwegian Sea and affected the recent more evolution of the MNPM. This period was also associated with neotectonic activity characterised by large landslides and vertical movements of Scandinavia caused by the isostatic response to ice sheet build-up and melting during and after the glacial phases (Medvedev et al., 2019; Gernigon et al., 2021).

2.2.1 Møre-Trøndelag Fault Complex (MTFC)

The Møre-Trøndelag Fault Complex is an ENE-WSW-oriented regional fault complex. It extends onshore for more than 300 km in central-mid Norway and continues into the Norwegian Sea (Fig. 2.2; Gabrielsen et al., 1999; Redfield et al., 2005; Lundberg et al., 2012; Nasuti et al., 2012). This structure has been related to similarly oriented faults in the Scottish Highlands, such as the Highland Boundary Fault (e.g., Séranne, 1992; Fossen, 2010).

In the offshore domain, the MTFC separates basins of different ages, i.e., the Jurassic-Cretaceous North Sea basin system to the south from the wider and deeper Cretaceous basins of the MNPM to the north (Fig. 2.1; Redfield et al., 2005). Onshore, the MTFC crosscuts the Precambrian autochthonous basement and the overlying Caledonian nappes (Fig. 2.2; Corfu et al., 2014).

The MTFC consists of different fault strands, such as the Hitra-Snåsa Fault and the Verran Fault, and an enveloping volume of rock deformed by second-order fault zones (Bering, 1992; Séranne, 1992; Grønlie and Roberts, 1989; Redfield et al., 2004, 2005; Osmundsen et al., 2006; Redfield and Osmundsen, 2009; Nasuti et al., 2011; Lundberg et al., 2012). Each fault strand is defined by a several meter thick, medium to low-grade mylonitic zone, superimposed and reworked by brittle fault rocks (Kendrick et al., 2004; Redfield et al., 2005). The Hitra-Snåsa Fault exposes a pervasive ductile fabric with a horizontal stretching lineation oriented 060°N, with superimposed sets of quartz and epidote coated faults, striated fault planes and green cataclasites (Séranne, 1992; Osmundsen et al., 2006). The Verran Fault is a splay of the Hitra-Snåsa Fault, characterised by sequences of mylonites with a prominent sub-horizontal stretching lineation (Séranne, 1992).

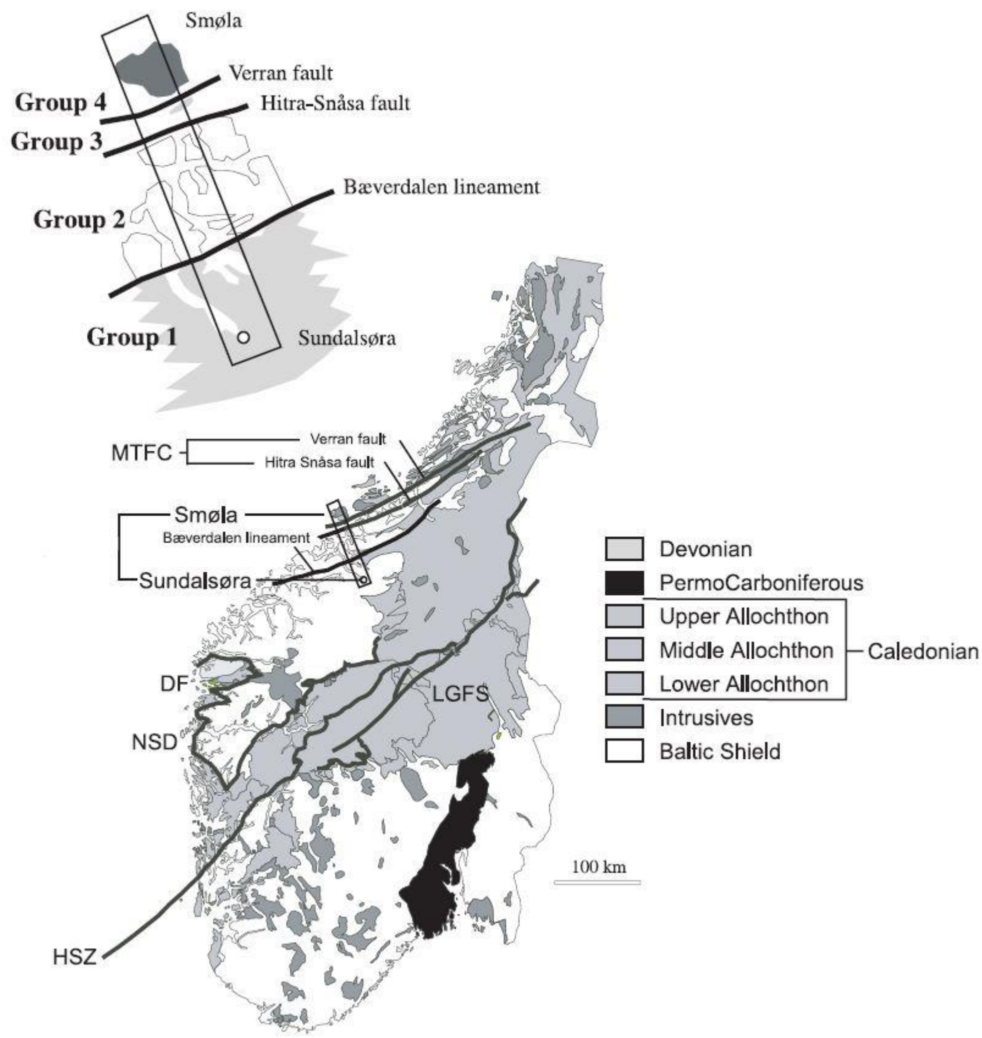

Figure 2.2 - Geological schematic map of southern Norway, showing the principal regional structures, such as Møre Trøndelag Fault Complex (MTFC) and its main strands (Redfield et al., 2004). (HSZ: Hardangerfjord Shear Zone; LGFS: Lærdal-Gjende Fault System; NSD: Nordfjord-Sogn Detachment).

The MTFC has been repeatedly reactivated in response to varying stress regimes through time, resulting in a complex finite deformation pattern (e.g., Bering, 1992; Séranne, 1992; Gabrielsen et al., 1999; Redfield et al., 2005; Osmundsen et al., 2006; Nasuti et al., 2011; Lundberg et al., 2012). A possible initial dextral transpression along the MTFC was likely accommodated in the Early to Middle Devonian (Séranne, 1992; Gabrielsen et al., 1999). However, the dominant kinematics of the MTFC is overall sinistral, accommodated under ductile conditions in the Early to Middle Devonian. An up to 2 km thick mylonitic shear zone documents the sinistral shear at that time as documented by the $^{40}Ar/^{39}Ar$ dating of synkinematic white micas (Kendrick et al., 2004). From the Devonian onward, progressive regional exhumation led to the transition into a shallower, brittle deformation regime. Previous studies propose multiple oblique reactivations of the MTFC during the Late Devonian, Permo-Triassic, and Jurassic (e.g., Grønlie and Roberts, 1989; Grønlie et al., 1991; Séranne, 1992; Redfield et al., 2004, 2005). In addition, pseudotachylytes from the Hitra-Snåsa Fault have been dated to the Late Carboniferous-Early Permian by Sherlock et al. (2004). The MTFC also accommodated normal faulting in the Late Jurassic-Early Cretaceous, as well as possible Quaternary post-glacial reactivation (Redfield et al., 2005). The area is still seismically active in a transtensional mode (Gabrielsen and Færseth, 1988; Bungum et al., 1991).

2.3 Evolution of the North Sea Passive Margin

The evolution of the North Sea Margin has been characterised in detail by means of structural and geochronological analysis of the fault and fracture network exposed on Bømlo, North Sea, by Scheiber and Viola (2018) and its tectonic evolutionary model is reported in Fig. 2.3. This reconstruction integrates and is supported by other authors' studies of the North Sea Margin (Færseth, 1996; Ksienzyk et al., 2016; Phillips et al., 2019; Fossen et al., 2016, 2021).

The latest stages of Caledonian compression during the Mid-Ordovician-Silurian are recorded by ENE-WSW-striking thrusts and kinematically consistent conjugate sets of strike-slip shear fractures and minor faults accompanied by the emplacement of greisen dykes (i.e., veins filled with quartz, K-feldspar, and muscovite), and mineralised veins (Scheiber et al., 2016).

A first phase of NW-SE extension occurred during the Devonian in response to the Caledonian orogenic collapse, as recorded by the development of minor, NE-SW-striking normal faults. The North Sea Margin experienced two main rifting phases: in the Permo-Triassic and in the Jurassic-Early Cretaceous (Scheiber and Viola, 2018; Gernigon et al., 2020; Fossen et al., 2021). The first main North Sea rifting stage in the Permo-Triassic is recorded by widespread NE-dipping normal faults that formed during overall ENE-WSW extension (Fig. 2.3; Viola et al., 2016; Scheiber and Viola, 2018). This rifting event led to the formation of the most prominent structural highs and basins of the North Sea, namely the Stord Basin, Utsira High, and the Viking Graben (Scheiber and Viola, 2018).

Rifting and crustal stretching continued during the Late Triassic and Jurassic leading to the formation of ENE-dipping normal faults associated with the deepening and development of the offshore Viking Graben (Scheiber and Viola, 2018) and the progressive reactivation of the previously formed NE- and E-dipping normal faults (Viola et al., 2016).

Far-field stress fields related to the Early Cretaceous rifting stage of the northern North Sea and the MNPM subsequently led to the development of N-S trending faults and fractures as well as the reactivation of N-S and NE-SW suitably oriented faults during an overall NW-SE extension (Fig. 2.3; Viola et al., 2016; Scheiber and Viola, 2018).

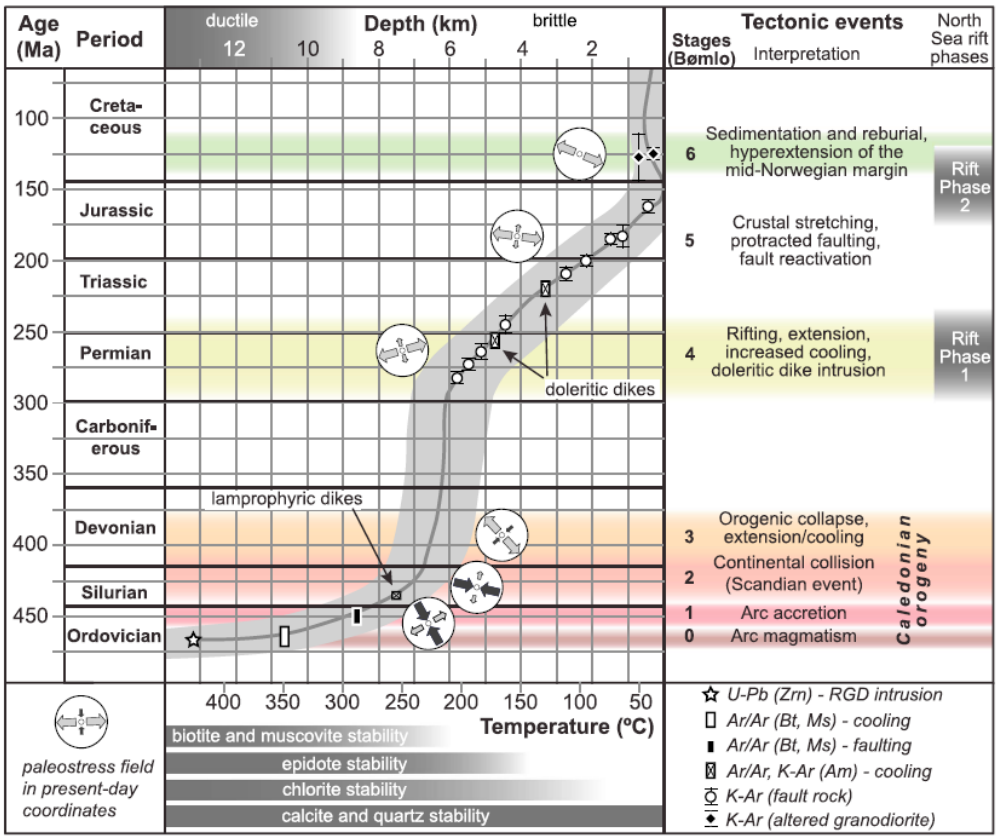

Figure 2.3 - Diagram showing the tectonic evolution of North Sea Margin. Depth increase affects the temperature according to a geothermal gradient of 30 °C/km. Cooling path constructed based on radiometric and thermochronological data (see references in Scheiber and Viola, 2018). Am = amphibole; Bt = biotite; Ms = muscovite; Zrn = Zircon (Scheiber and Viola, 2018).

During the brittle deformation related to rifting evolution, the exhuming crystalline basement was fractured and altered/weathered within time periods of sub-aerial exposure (Viola et al., 2016; Fredin et al., 2017a; Scheiber and Viola, 2018). Altered/weathered basement rocks are invariably found as lenses along fractures and altered volumes within high-fracture density deformation zones. K-Ar dating of alteration-related authigenic illite has revealed the occurrence of multiple alteration/weathering events during this prolonged and multi-phased brittle deformation history (Viola et al., 2016; Fredin et al., 2017a; Scheiber and Viola, 2018) with a significant, regional event dated to the Late Triassic (c. 220-200 Ma, Fredin et al., 2017a). Further alteration events likely occurred in the Permian, Jurassic and Early Cretaceous (Viola et al., 2016; Scheiber and Viola, 2018).

Chapter 3 - Methodology

The applied workflow is multidisciplinary and multiscalar. It includes seven main steps, as shown in Fig. 3.1. Each used methodology will be briefly described in the following paragraphs. The ultimate goal of this workflow is the generation of an "absolute time"-constrained tectonic evolutionary model for the MNPM that considers all the geological information gathered through the various applied methodologies of investigation, such as structural geology, geochronology, remote sensing, mineralogical analysis, and isotope geology.

3.1 Lineament detection by remote sensing analysis

The analysis at the regional scale of the brittle fracture network of the Norwegian margin in the study area has been performed by remote sensing of lineaments at the 1:10.000 and 1:100.000 scales. This step aims to obtain the orientations of the lineament main trends as detectable at the regional scale, and also to identify and select areas along the margin with a high density of faults and fractures suitable for detailed mesoscale structural analysis and the ground-truthing of the remotely sensed data.

The high-resolution (1x1m-pixel) georeferenced LiDAR (Light Detection And Ranging) dataset of the MNPM and North Sea margins has been processed, to obtain hill-shaded relief models of the ground (Fig. 3.2a). The light orientation in the hillshade is standard at N315°. The hillshaded DEMs of the Norwegian margins exhibit lineaments at different scales. These lineaments are mainly the ground expression of faults and fractures accumulated during the local long-lived brittle history (Gabrielsen et al., 2002; Scheiber et al., 2015; Scheiber and Viola, 2018; Fig. 3.2b, c).

Two different methods to do an automated picking of lineaments were tested: (i) Hough Transform algorithm with GRASS GIS (see Rocchini et al., 2017) and (ii) FRACPAQ with MATLAB (see Healy et al., 2017). They both detect lineaments, and FRACPAQ also allows to automatically perform a statistical analysis. However, the automatically mapped lineaments did not always have a real geological meaning, resulting in the need of a systematic verification of the results. It was thus eventually decided to do a completely manual mapping of lineaments (fractures and faults) from the LiDAR datasets (Fig. 3.3).

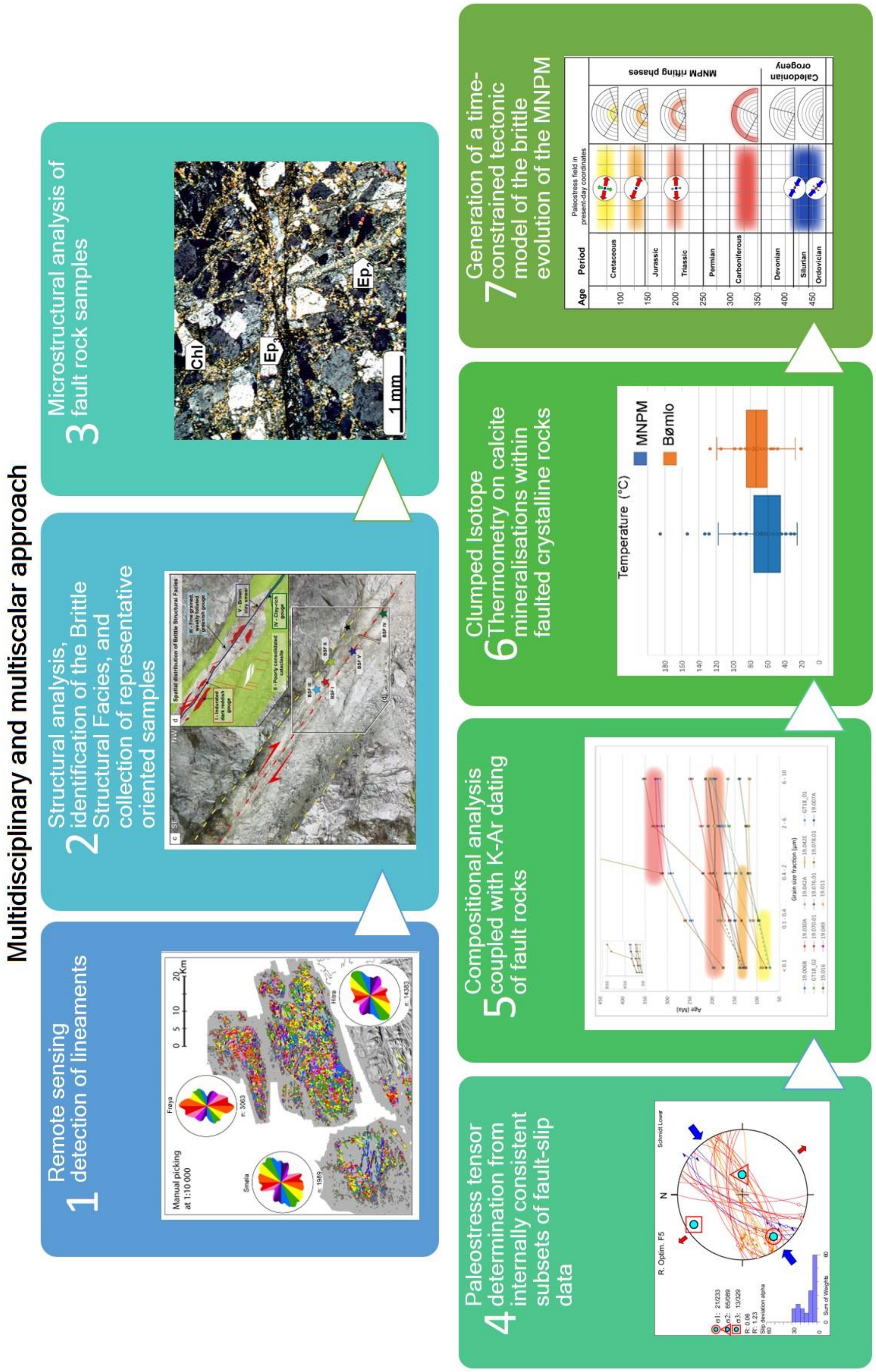

Figure 3.1 - Schematic representation of the applied workflow.

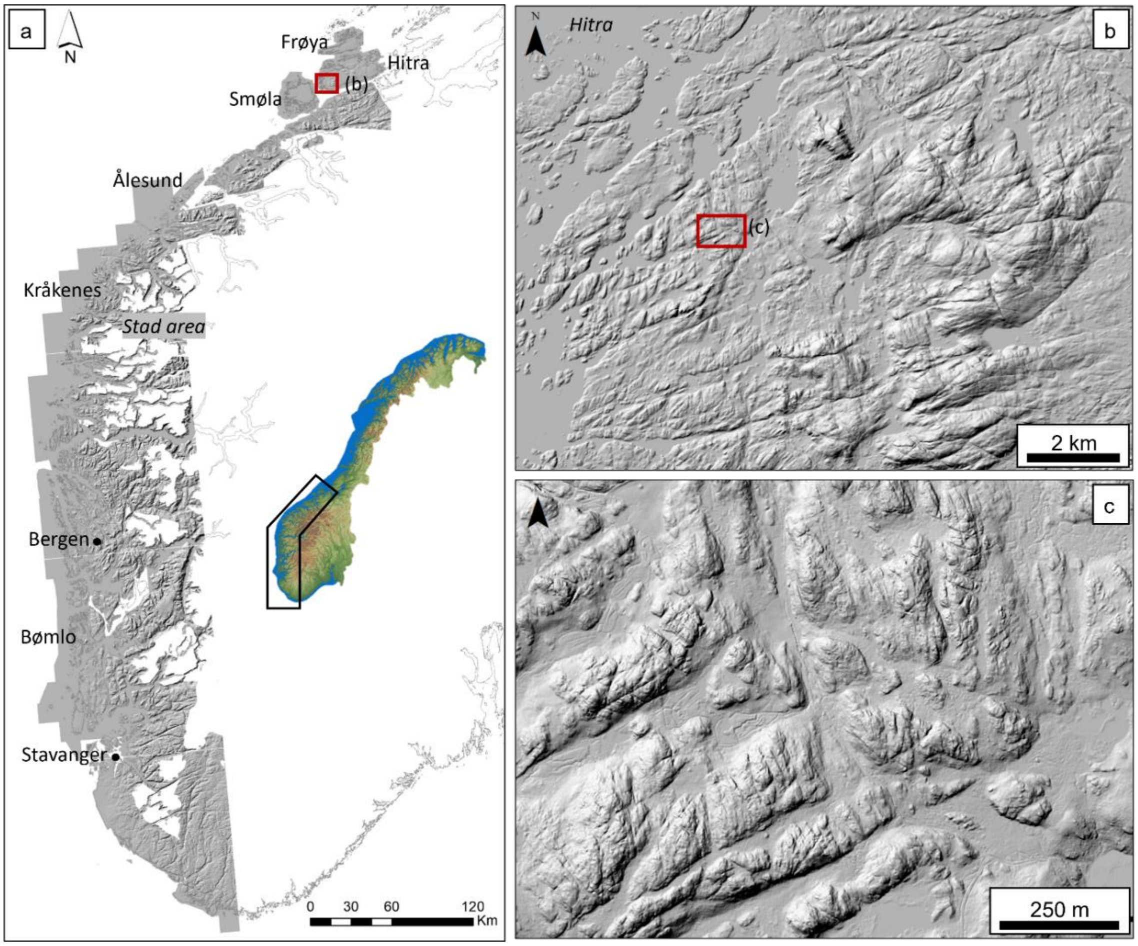

Figure 3.2 - a) LiDAR dataset of onshore MNPM and North Sea coastline; b-c) detail of high resolution hillshaded DEMs of Hitra island at different scales showing surface lineaments.

The measured strike of lineaments has been plotted in rose diagrams by using the MARD (Moving Average Rose Diagram) application by Munro and Blenkinsop (2012) (Fig. 3.3). MARD conducts a moving average smoothing, a form of signal low-pass filter processing, on the raw data according to a set of pre-defined conditions selected by the user. This form of signal processing filter smooths the angular dataset, emphasising significant circular trends whilst reducing background noise. Customisable parameters include the angular range (or aperture) over which the data is averaged, and whether an unweighted or weighted moving average is to be applied (Munro and Blenkinsop, 2012). The vector mean, mean resultant (or length), circular standard deviation and circular variance can be calculated. The plotted rose diagrams in this thesis are bidirectional, equal area stereoplots, with angular range of 13° and weighting factor of 0.90.

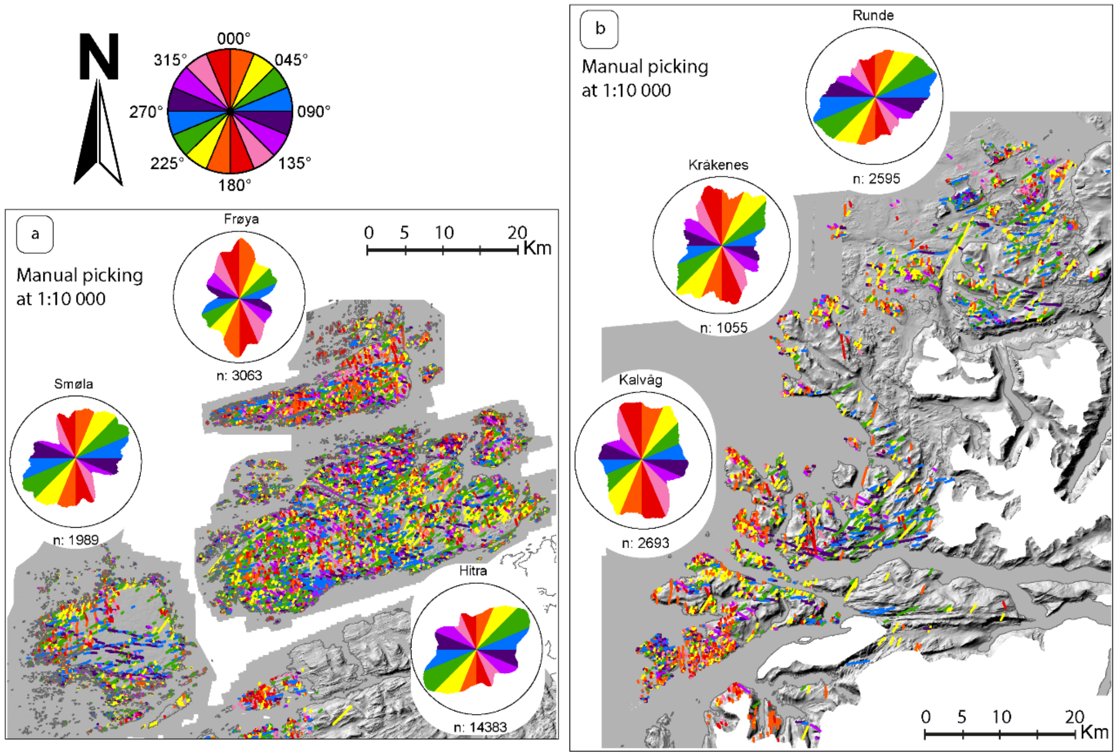

Figure 3.3 - Remote sensing lineaments mapped in the area of Hitra, Frøya and Smøla islands (a) and in the Stad area (b, southern MNPM) at the 1:10.000 scale of observation. Lineaments' strikes are plotted in rose diagrams using the by MARD application

3.2 Structural analysis

Field structural analysis represents the main step of the study of the brittle fracture network at the mesoscopic scale. It has been conducted onshore and along the coast of the MNPM, from Hitra in the North to the Stad area in the south (Fig. 3.2). Fieldwork made it possible to ground truth the remotely detected sets of lineaments. 86 different structural sites were studied from selected key areas of the MNPM (Fig. 3.3). In each site fault-slip data were collected, each of which includes information on fracture or fault orientation, slip direction and sense of movement, lithotype, fault rock type and fracture mineralogy. In some cases, the spatial persistence/extension of fractures and faults and their throw were also measured. As a result, a comprehensive structural dataset has been compiled for a significant part of the MNPM. This fault-slip dataset represents the input data for the paleostress inversion.

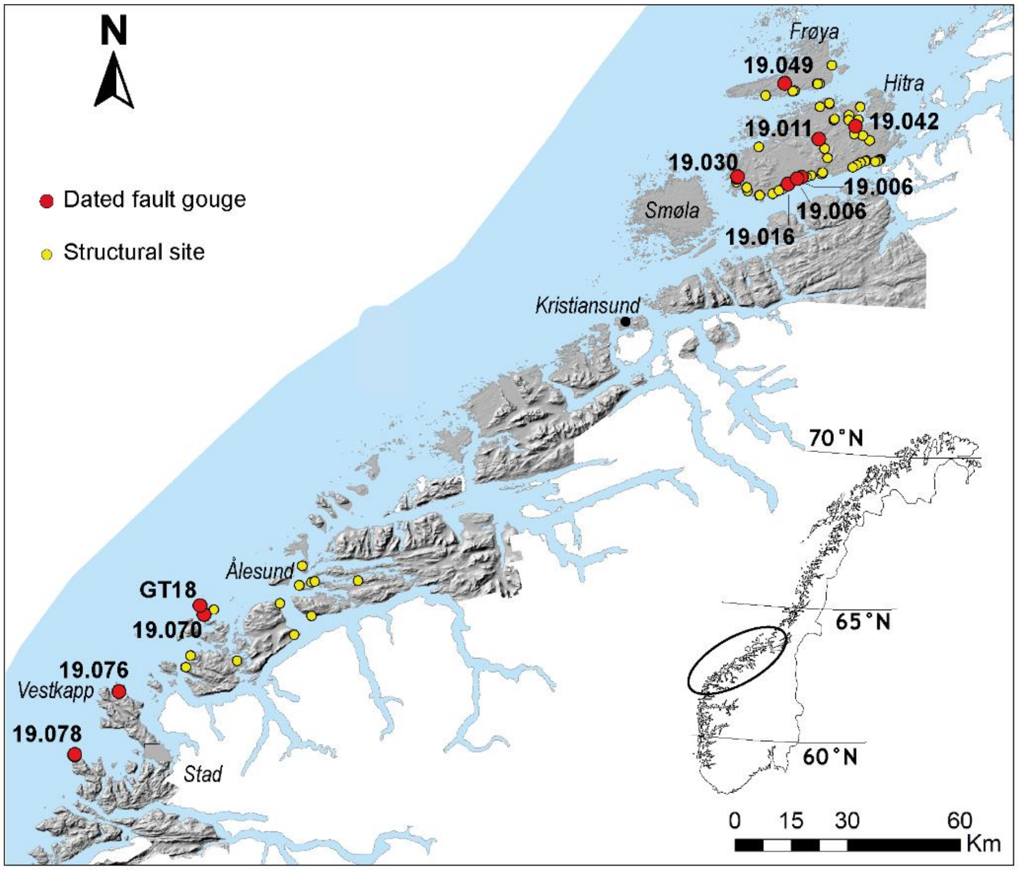

Figure 3.4 - Structural sites studied along the MNPM (in yellow). The red dots indicate the sampling sites of fault gouges.

During fieldwork, samples of cohesive and uncohesive fault rocks and mineral decorations along faults have been collected (Fig. 3.4). Cohesive fault rocks and associated mineral coatings from discrete fault slip surfaces were collected to study their structures and petrography at the microscale. Uncohesive fault rocks, such as fault gouge, were collected for K-Ar dating coupled with mineralogical analysis. Calcite veins and mineralisations were collected to study their isotopic composition, and origin and temperature of the source fluids by clumped thermometry.

3.2.1 Brittle Structural Facies: A conceptual tool of the adopted toolbox

Fault zones are typically heterogeneous from a geometrical and spatial point of view. They can contain multiscalar domains characterised by varying (micro)-structures and mineralogical compositions. These domains result from differential strain partitioning during the multiple recorded faulting stages, and, as a result, can preserve the isotopic and kinematic signature of different slip periods. These juxtaposed, although not coeval, domains are referred to in here as “Brittle Structural Facies” (BSF).

In geology, the concept of *facies* has traditionally been applied to descriptions of sedimentary and metamorphic rocks (e.g., Winkler, 1976). To a lesser extent, the term *facies* has been applied to ductile deformed rocks (Tikoff and Fossen, 1999), to geochemistry, and in the interpretation of well logs (Braathen et al., 2009). In all these cases, *facies* refers to the assemblage of specific characteristics of a rock volume. These characteristics can be sedimentological features, or mineral assemblages that are typical of specific P-T conditions (Braathen et al., 2009).

The term “structural facies” was introduced by Tveranger et al. (2005) and it is becoming widely used in petroleum geology, where it refers to “any feature or rock body deriving its present properties from tectonic deformation” (Tveranger et al., 2005). They stressed that as the term "facies" is not linked to any specific scale or feature, it allows a high degree of flexibility when building models with varying levels of detail. They also state that the main advantage of the concept of fault facies is that it implies that deformational features have a volumetric extent and impact on rock properties (Tveranger et al., 2005). This term was introduced to build stochastic models of tectonised rock volumes, by subdividing the fault zone in discrete blocks with defined dimensions and property ranges related to strain.

A more rigorous definition of *fault facies* was proposed by Braathen et al., 2009. They refer to the general and flexible definition of Tveranger et al (2005), highlighting the sedimentary characteristics of each facies and proposing a hierarchical scheme of description of fault facies. They applied this term within the branch of hydrocarbon and groundwater reservoir modelling. Since then, the approach has remained in use in petroleum geology modelling. It remains a flexible approach, which has also been modified by subsequent authors and different research groups (e.g., Grant, 2019).

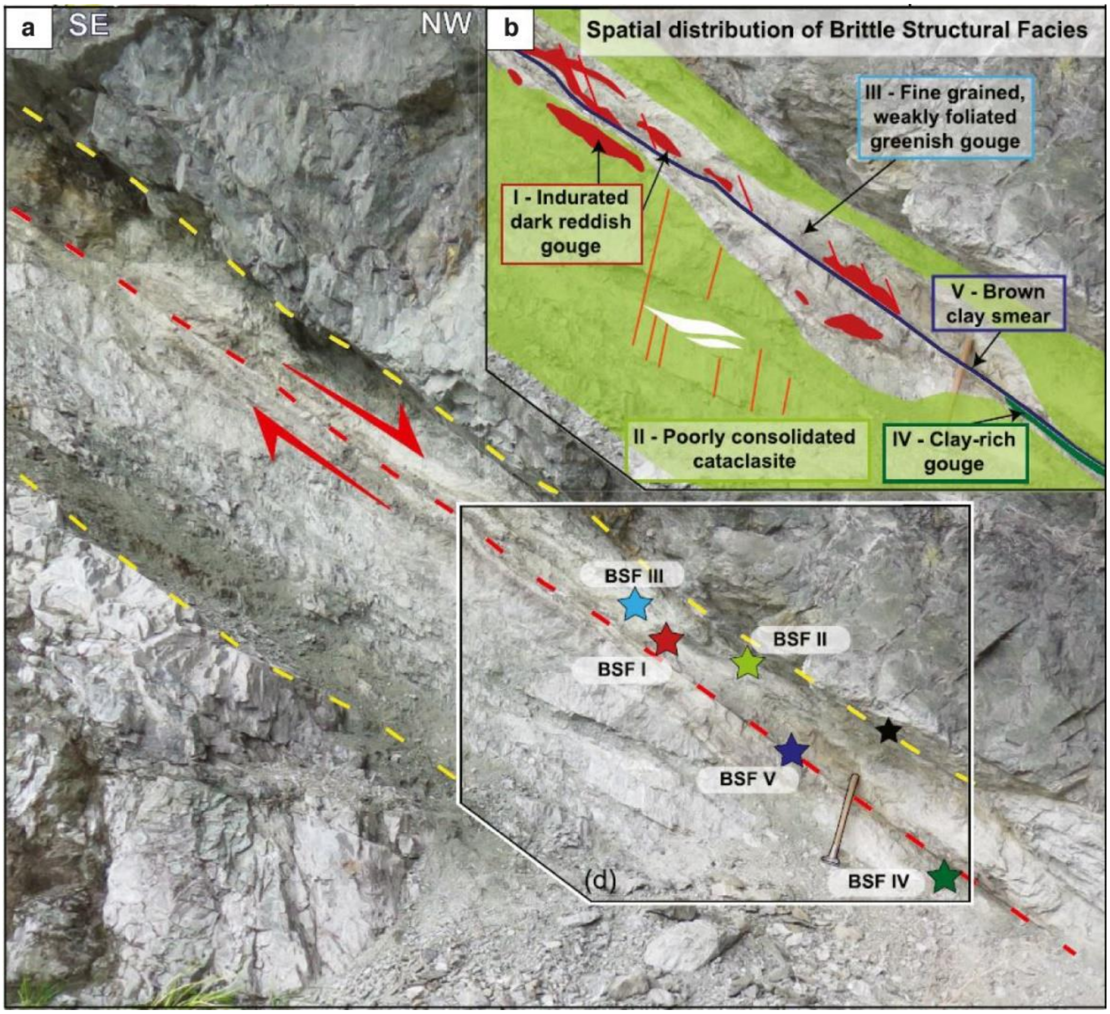

Figure 3.5 - a) Lærdal-Gjende fault core. Stars indicate the recognised and sampled different BSF within the fault core; b) simplified scheme of the BSF distribution within the fault core (modified after Tartaglia et al., 2020).

Although existing studies implementing the concept of fault facies have declined this term in a rather flexible fashion, the main strength of "fault facies" is that it invariably implies an assemblage of characteristics typical for a rock volume, or, in our case, a deformed rock volume. Our contribution to this term is its application to the field of structural geology, in the detailed analysis of fault internal architecture. We decided to use the term Brittle Fault Facies (BSF) to refer to a deformed volume of rock characterised by a specific fault rock type, texture, colour, clay content, composition, and age of formation. BSF can be described by means of a multidisciplinary approach, from the detailed mapping at the outcrop to the microstructural analysis of fault rocks, passing through detailed compositional analysis and dating in the laboratory. This means that a BSF is not only a deformed lithon in a fault core, but it is the remnant of a fault rock developed during a specific tectonic/faulting event. This faulting episode may be kinematically and temporally different from the event that formed the surrounding BSF in the fault core. Therefore, BSF analysis can help with proving that fault cores do not necessarily develop during a single event, and, in turn, to reconstruct their complex evolution through space and in time.

The BSF concept has been tested and applied to the Lærdal-Gjende Fault case study, presented in Chapter 4 (Fig. 3.5), before being regularly used to study and sample fault zones along the entire MNPM.

3.3 Microstructural analysis

Oriented thin sections of selected cohesive fault rock samples and mineral decorations, cut parallel to the transport direction (fault slip lineation) and perpendicular to the fault plane, were prepared for optical microscopy and petrographic analysis. Microstructural analysis permits to investigate deformation processes, to reconstruct relative crosscutting relationships of faulting and/or veining, and to define PT conditions at the time of faulting.

3.4 Paleostress inversion

The paleostress inversion technique searches for the state of stress that best accounts for a given fault-slip dataset, according to geometric and kinematic compatibility criteria (Bott, 1956). When studying a multiply reactivated and complexly deformed area, paleostress inversion analysis can help to distinguish and reconstruct how the stress field orientation varied in time, during different deformation events.

By applying inversion techniques, one calculates the reduced stress tensor that best accounts for an internally homogeneous set of faults. This method requires several assumptions to be made for it to be successfully applied (Wallace, 1951; Bott, 1959; and Unruh, 1998; Pollard, 2000; Lacombe, 2012; Lacombe et al., 2013): 1) the observed slip direction on the fault surface is parallel to the resolved shear traction on the fault plane; 2) the faulted volume of rock is physically homogeneous and isotropic and, if pre-fractured, also mechanically isotropic, i.e., the orientation of fault planes on which slip occurs is random; 3) the studied rock volume has to be large compared to the dimension of the studied faults and in it stress is distributed homogenously; 4) the faulted medium responds to applied stresses as a rheologically linear material; 5) faults do not mutually interact, i.e. they slip independently of each other, and 6) at the time of faulting no block rotation occurred.

In the case of multiple faulting events affecting a given region, the identification of internally consistent subsets of faults through the sorting of the total and heterogeneous regional dataset is, therefore, a fundamental step to fulfil the requirements above. A homogeneous set of faults is a group of faults and fractures in any given area that are compatible from a geometric, kinematic, and dynamic perspective and, therefore, share similar or kinematically compatible orientations and/or fault rock assemblages and mineral coatings. The internally homogeneous sets of faults of this study have been sorted from the total structural dataset derived from the analysis of the MNPM, compiled after several weeks of field work. Pivotal to the identification of these homogeneous sets was data collected from remote sensing, field work and microstructural analysis.

The software WinTensor was used to invert the collected fault-slip data and compute the reduced paleostress tensors (Delvaux and Sperner, 2003). This software iteratively applies an inversion algorithm to search for the state of stress that best accounts for the input fault-slip dataset (e.g., Angelier, 1984; Delvaux and Sperner, 2003). The goodness of the optimisation process is measured by the fit between the theoretical slip vectors and those measured in the field (Delvaux and Sperner, 2003). This is achieved by analysing for all faults belonging to the inverted set the misfit angle α, which is defined as the acute angle between the theoretical maximum shear traction vector and the measured slip vector on an individual fault plane (i.e., the stria). A set of faults can be considered as homogeneous if the slip deviation for all faults (their α value) is lower or equal to 30°, a condition that implies that all processed faults are compatible with the calculated stress tensor. If the α value for any given fault is >30°, then that fault is incompatible with the computed reduced tensor, suggesting that it belongs to a different set and that it formed in a different stress field and, thus, during a different deformation episode (Delvaux and Sperner, 2003).

The calculated reduced stress tensor is defined by the orientation of the three principal stress axes (σ_1, σ_2, and σ_3, with $\sigma_1 \geq \sigma_2 \geq \sigma_3$) and by the stress ratio R, calculated as (Angelier, 1984; Lacombe, 2012):

$$R = \frac{\sigma 2 - \sigma 3}{\sigma 1 - \sigma 3}$$

To visualise in a clearer way the stress ratio and the resulting stress regime, we rely on the R’ index, which is calculated by R’ = R, when σ_1 is vertical (extensional stress regime), R’ = 2 - R, when σ_2 is vertical (strike-slip stress regime) and R’ = 2 + R, when σ_3 is vertical (compressional stress regime; Fig. 3.6 and 3.7; Delvaux and Sperner, 2003). R’ ranges between 0 and 3. R’ = 0.5 describes a pure extensional regime, R’ = 1.5 describes a pure strike slip regime and R’ = 2.5 indicates a pure compressional regime. All the intermediate values indicate a mixed regime, e.g., R’ = 1.0 means a transtensional regime. Finally, the inverted stress tensors are correlated with specific tectonic events in the regional framework.

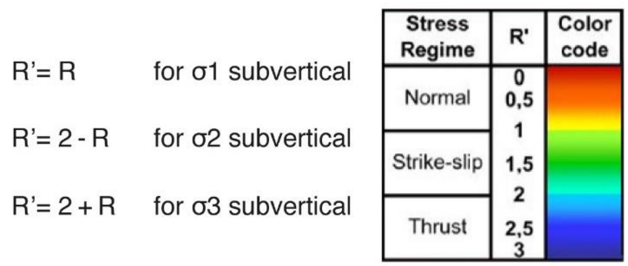

Figure 3.6 - R’ range values and corresponding stress regimes. Colour code applied by WinTensor software (modified after Delvaux, 2012).

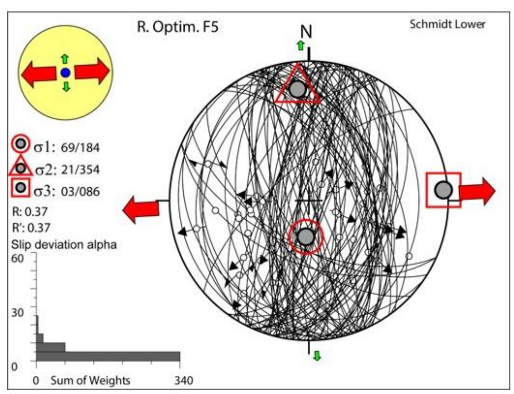

Figure 3.7 - Example of an extensional reduced stress tensor computed from a homogeneous subset of faults, including the orientation of the principal stress axes and of R and R’.

3.5 K-Ar fault rock dating

The time dimension of a fault is a key element for a comprehensive reconstruction of its evolution. Dating faults is important for regional and tectonic studies, for instance, when dealing with the timing of continental breakup and rifting, intra-continental deformation or evolution of basins, as well as for the estimation of the recurrence interval of seismicity and discriminate active faults from quiescent ones (Tagami, 2012). However, there are objective difficulties when attempting to obtain absolute and relative time constraints on deformation events and to unambiguously associate deformation ages with specific kinematics, mineral assemblages, and mechanical properties of a fault zone.

The K-Ar ($^{40}K/^{40}Ar$) methodology is a dating technique based on the natural decay of ^{40}K into ^{40}Ar, which has a decay constant of 0.581×10^{-10} yr^{-1} (e.g., Dalrymple and Lanphere, 1969; Tagami, 2012). K-Ar radiometric dating has been firstly applied to the dating of low-temperature, fine-grained illite-type separates (Wasserburg et al., 1956). Later, K-Ar dating has shown to also be a powerful methodology for the dating of authigenic, synkinematic clay minerals (mainly illite, as the K bearing clay) in fault rocks (van der Pluijm et al., 2001; Zwingmann and Mancktelow, 2004; Tagami, 2012; Pleuger et al., 2012; Clauer, 2013; Davids et al., 2013; Torgersen et al., 2015a; Viola et al., 2016; Vrolik et al., 2018; Mottram et al., 2020).

3.5.1 Illite mineralogy

Illite and muscovite both belong to the phyllosilicate group. The basic structure of phyllosilicates is based on interconnected six member rings of SiO_4^{-4} tetrahedra that extend outward in infinite sheets (Fig. 3.8a). Three out of the 4 oxygens from each tetrahedra are shared with other tetrahedra, leading to the basic structural unit of $Si_2O_5^{-2}$. Most phyllosilicates contain the hydroxyl ion, OH^-, with the OH located at the centre of the 6 membered rings (Fig. 3.8b).

Two identical and opposing sheets of linked tetrahedra form a composite layer, with a sheet of octahedrally coordinated M cations (mainly Al, Mg, Fe) sandwiched in-between (Fig. 3.8c). The octahedral sheets in both cases are held together by weak Van der Waals bonds (Deer et al., 2013).

Two sheets of tetrahedra are superimposed and are linked by a plane of M cations. Hydroxyl ions together with the apical oxygen of the tetrahedra complete the octahedral coordination of the central sheet of cations. Two different types of phyllosilicate can be discriminated:

1. The trioctahedral sheet silicates where each O or OH ion is surrounded by 3 divalent cations, like Mg or Fe;

2. The dioctahedral sheet silicates where each O or OH ion is surrounded by 2 trivalent cations, usually Al.

Muscovite is a dioctahedral sheet silicate (Fig. 3.8d), whose general chemical formula is $KAl_2(AlSi_3O_{10})(OH)_2$. The general formula of illite is $K_{0.65}Al_{2.0}[Al_{0.65}Si_{3.35}O_{10}](OH)_2$. Illites are structurally related to muscovite, because of the dioctahedral structure and the presence of K as interlayer cation (Deer et al., 2013). Illite differs from muscovite chemically in having more silica and less potassium, and physically in occurring with clay-size particles (< 2µm, Deer et al., 2013).

The hexagonal unit cell of sheet silicates allows to superimpose the different layers creating a structure wherein each is related to the next by a rotation through 0° or by a multiple of 60°. Various sequences of layer rotations are possible, and if they are repeated regularly these build up unit cells with one, two, three or more layers. The most common stacking sequences lead to either one- or two-layered monoclinic polytypes (1M, $2M_1$), a different two-layered monoclinic ($2M_2$) or a three-layered trigonal (3T) polytype. Polytype 1M involves layer shifts parallel to one *x* axis, $2M_1$ and $2M_2$ along two, and 3T along all three *x* axes (Deer et al., 2013).

The most common illite polytype is 1Md, with a disordered one-layered monoclinic cell. The $2M_1$ and $2M_2$ polytypes are more common for muscovite, but they are also known for illite (Meunier et al., 2004; Deer et al., 2013). Another illite polytype is $1M_d$ that exhibits a variable degree of disorder in the stacking sequence. Disorder derives from the presence of stacking defects in the 1M sequence due to non-rational rotations between two adjacent layers (Meunier et al., 2004).

Naturally, illite may contain smectite layers, which can be regularly or randomly stratified. An illite/smectite (I/S) mixed layer aggregate is the most abundant clay mineral of sedimentary rocks (Deer et al., 2013). Illites mainly form because of diagenetic/low-grade metamorphic processes acting upon smectites. With increasing temperatures, the grain size of the <2µm grain size fraction increases, the proportion of interlayered expandable material decreases and the ratio of $2M_1$ to 1M polytype increases (Deer et al., 2013). Finally, illites may also form from alteration of feldspars in weathering zones.

During faulting, fracturing and cataclastic flow lead to grain comminution that results in the systematic reduction of the average grain size and forms a fractal (i.e., power-low) grain-size distribution within a fault gouge layer (Zwingmann and Mancktelow, 2004; Tagami, 2012). Brittle faulting is dilatational and may enhance the ingress of fluids into the actively deforming rock volume (Caine et al., 1996). Hence, fluid circulation commonly favours the synkinematic formation of new phases and/or recrystallisation of pre-existing minerals in the active fault zone

(Solum et al., 2005; Haines and van der Pluijm, 2008; Tagami, 2012; Vrolijk et al., 2018). Fault gouges generally contain a variety of clay minerals, deriving from i*n-situ* clay mineralisation or from mechanical incorporation of protolith clays from the wall rock (Tagami, 2012).

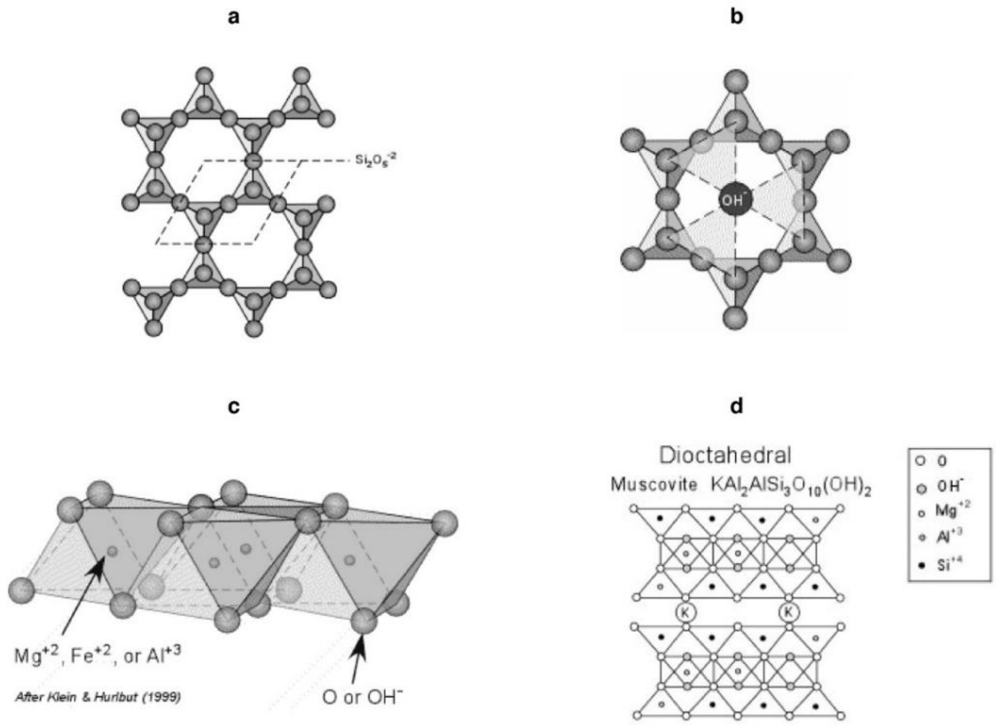

Figure 3.8 - a) Schematic basic structure of phyllosilicates, made of sheets of rings of SiO_4^{-4} tetrahedra; b) the basic group contains the hydroxyl ion, OH^-, located at the centre of rings; c) octahedral layers containing cations such as Mg, Fe or Al; d) schematic representation of muscovite, a dioctahedral mica (modified after https://www.tulane.edu/~sanelson/eens211/phyllosilicates.htm).

In detail, two mineralogical reactions have been widely utilised for K-Ar dating applications: the illitisation of illite/smectite (I/S) and the neocrystallisation of authigenic 1M/1Md illite (Fig. 3.9; Haines and van der Pluijm, 2008; Zwingmann et al., 2010). These reactions are both kinetically controlled. For example, the smectite to illite reaction is a function of temperature, K-concentration and time (Grathoff et al., 2001). Hence, it is likely that these reactions are favoured and accelerated by hydrothermal flow episodes. The temperature required for the reactions (i.e., c. 150 °C) can be generally attained at depths of c. 5 km under normal geothermal gradients (c. 25-30 °C/km) (Tagami, 2012).

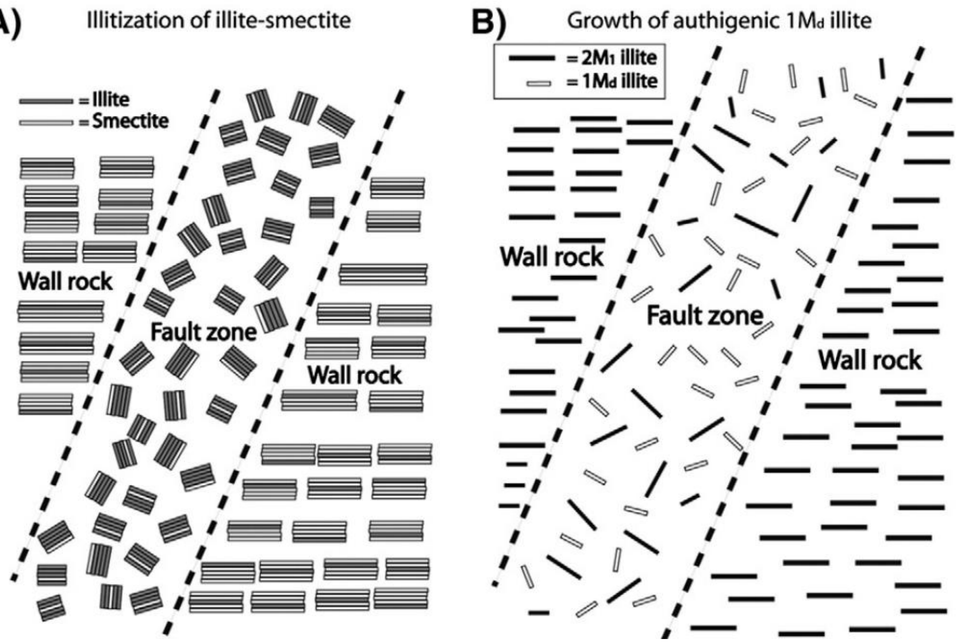

Figure 3.9 - Two types of mineral transformations within fault gouges to form illites suitable for K-Ar dating. (A) Illitisation of illite-smectite in clay-rich fault gouges, which results in higher contents of illite in illite-smectite compared to the wall rocks. (B) Neocrystallisation of authigenic discrete $1M_d$ illite in fault gouges (Tagami, 2012).

3.5.2 Theoretical background of the K-Ar systematics applied to fault rock dating

In the '60s, Hower and co-workers found that there is a relationship between K-Ar age and grain size in shales, wherein the age increases with the size of the dated fraction (Hower et al., 1963), a relationship referred to as 'inclined spectrum' by Pevear (1999). This trend is commonly interpreted to result from the physical mixing of different populations of illites (van der Pluijm et al., 2001), or the contamination by inherited K-bearing minerals (Zwingmann and Mancktelow, 2004) or being a consequence of grain size-dependent Ar loss (Verdel et al., 2012).

Care must be taken when dealing with the reliability of obtained K-Ar ages in relation to the temperature of the system during deformation. The closure temperature of illite K-Ar is empirically estimated to c. 260 °C for an ordinary grain size of 2μm (Fig. 3.10; Hunziker et al., 1986; Tagami, 2012), whereas the temperature of *in-situ* illite formation is estimated as c. 100-150 °C (Zwingmann and Mancktelow, 2004). Hence, the K-Ar age of authigenic illite records the time of its formation within a fault, unless any subsequent heating episode causes the partial or complete opening of the illite K-Ar system (Zwingmann and Mancktelow, 2004; Haines and van der Pluijm, 2008; Tagami, 2012; Torgersen et al. 2015b).

Decay system	Mineral	Closure temperature (°C)	Activation energy (kJ/mol)
(K–Ar)	Biotite	350–400	210
	Muscovite	300–350	180
	Illite[a]	~260	220
	K-feldspar	150–350	170–210

[a] Grain size of 2 μm is assumed.

Figure 3.10 - Closure temperatures for K-Ar system (modified after Tagami, 2012).

Heating episodes could be also responsible for thermally activated volume diffusion and consequent partial loss of radiogenic ^{40}Ar (Verdel et al., 2012; Torgersen et al., 2015a.) Modelling of Ar volume diffusion on illites of three different grain size fractions (10, 2 and 0.1 µm) at transient high temperatures of between 190 and 370 °C, has shown that during heating-cooling pulses of 5 and 10 Ma to temperatures of 230-240 °C, even very fine-grained illites (<0.1 µm) do not experience more than a 10% resetting of their initial K-Ar age (Fig. 3.11; Torgersen et al., 2015a). For the same thermal evolution, larger grains (10 µm) are essentially unaffected. At 300-310 °C, the Ar isotopic system of both 0.1 and 2 µm grains is completely reset, whereas the modelled age of 10 µm grains is fully reset only above temperatures of c. 350 °C (Torgersen et al., 2015a). Therefore, Ar loss by volume diffusion is believed to only be important in cases of anomalously high temperatures maintained over significantly long-time intervals (Torgersen et al., 2015a).

To deal with the mixing of protolithic/inherited clay minerals, different generations of illites or other K-bearing mineral phases potentially present in the dated samples, X-Ray Diffraction (XRD) analysis is applied on the dated grain size fractions. This technique helps to characterise the mineralogical composition of each fraction. Additionally, XRD helps to identify and even quantify different clay minerals, illite/smectite mixed layers and potential non-clay contaminants in separates, such as inherited K-bearing phases (Tagami, 2012; Viola et al., 2016). Lastly, it can also identify the polytypes of illites.

The $2M_1$ illite polytype is generally assigned to a detrital (high temperature) origin and the 1M polytype to an authigenic origin at lower temperature (at T < 200 °C, Pevear, 1999). The discrimination of illite polytypes is therefore crucial to the isotopic dating of clay-sized fractions.

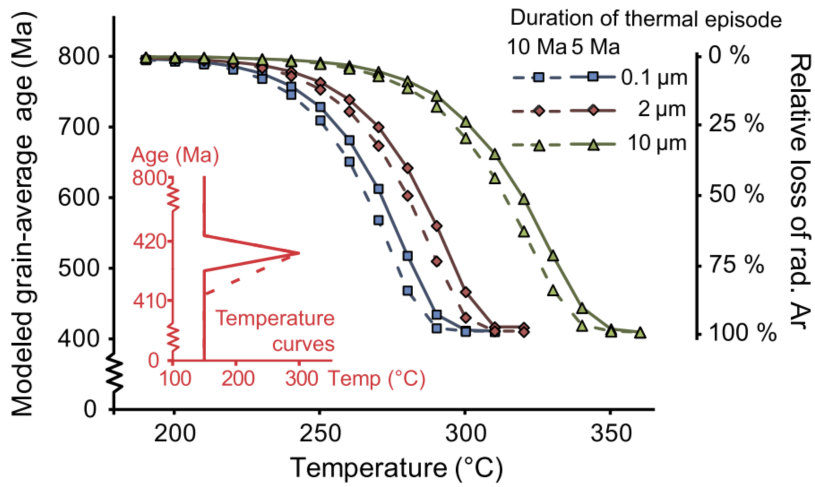

Figure 3.11 - Results of Ar diffusion modelling, with modelled age and percentage of radiogenic Ar loss plotted against temperature. The diagram shows the impact on 800 Ma old illite (grain sizes: 0.1, 2 and 10 µm) of transient elevated temperatures peaking at 418 Ma. Color-coding reflects the different grain sizes, whereas solid and striped lines mark 5 and 10 Ma long thermal episodes, respectively. The red inset diagram shows the modelled temperature curves, in which solid and striped lines correspond to those in the main diagram (Torgersen et al., 2015a).

The interpretation of K-Ar dates from clay minerals may be also supported by examination of crystal morphology and typology by scanning (SEM) and transmission (TEM) electron microscopy, and comparison of the observed shapes with the XRD data. The origin of illite can be inferred by the habit of the crystals and its aspect. Fibrous (lath) crystals are more likely to be synkinematic/authigenic in respect to platy ones (Pevear, 1999; Torgersen et al., 2015b; Viola et al., 2018; Mottram et al., 2020). Moreover, straight particle edges are commonly considered to be typical for authigenic sheet silicates, whereas irregular edges are rather identifying detrital particles variously affected by dissolution and erosional processes (e.g., Hunziker et al., 1986; Haines and Van der Pluijm, 2012).

The Illite Age Analysis approach (IAA) of Pevear (1999) is a method to deal with the mixing of different populations of illites. This approach calculates authigenic vs detrital endmember ages based on the different illite polytypes dated within one sample (Pevear, 1999; Grathoff et al., 2001). The IAA approach has been successfully applied only in a limited number of fault dating studies (e.g., van der Pluijm et al., 2001; Aldega et al., 2019; Curzi et al., 2020). Torgersen and co-authors (2015a) demonstrated that the IAA cannot be used when the authigenic illite/muscovite is 2M1 (e.g., Zwingmann et al., 2010), when the wall rock contains diagenetic 1M/1Md illite (Haines and van der Pluijm, 2010) or when fault reactivation causes neocrystallisation of illite of the same polytype as that formed during earlier faulting episodes. On the other hand, fault-rock-derived inclined spectra can be produced by multiple faulting episodes during structural reactivation without the need for changes in mineralogy or clay polytypes (Torgersen et al., 2015a).

A recent conceptual model for the interpretation of K-Ar ages is the Age Attractor Model (Fig. 3.12; Torgersen et al., 2015a; Viola et al., 2016). It interprets the inclined curves on K-Ar ages vs grain size fraction diagrams (Fig. 3.13) as mixing of authigenic and inherited illites. Newly crystallised minerals (authigenic/synkinematic illite) are expected to be the most abundant in the finer grain size fractions. Hence, the age of the finest grain size fraction (<1 μm) dates the timing of the last faulting increment recorded by the fault and thus acts as an age attractor toward which the curve converges (Fig. 3.13c, f, h; Torgersen et al., 2015a). Even the finest grain size fraction, however, may still include inherited protolithic minerals or different generations of authigenic phases reworked during multiple stages of deformation. Ages obtained from the finest grain size fractions should thus be still considered as maximum ages, although they provide the best available constraint on the timing of the most recent faulting event recorded by the fault rock (van der Pluijm et al., 2001; Zwingmann and Mancktelow, 2004; Torgersen et al., 2015a; Viola et al., 2016).

The coarser grain size fractions, on the contrary, are enriched in protolithic (inherited) minerals, such as, for example, older generations of illites or inherited K-feldspar. The ages of the intermediate size fractions reflect the combined action of authigenic growth of younger rims on inherited crystals and physical mixing of authigenic with comminuted protolithic illite (Torgersen et al., 2015a; Viola et al., 2016, 2018), and are, therefore, commonly devoid of a real geological meaning.

According to the Age Attractor Model, the ages of more than one faulting/fluid ingress event may only be constrained if the tectonic events (e.g., fault reactivations) occur at successively lower temperatures (Torgersen et al., 2015a). When a fault is reactivated repeatedly at either the same (Fig. 3.11f) or higher temperatures (Fig. 3.11h) only the age of the last faulting event can be constrained.

The model also describes the possibility that different grain size fractions yield the same age within the analytical error. In this case the age-grain size curves are horizontal (Fig. 7d, e), and it is reasonable to conclude that they constrain a common high temperature event (above c. 250 °C) for authigenic crystallisation or thermal reset of inherited crystals, or the fault gouge does not contain any protolithic K-bearing phases, and all the dated K-bearing minerals are authigenic (Torgersen et al., 2015a).

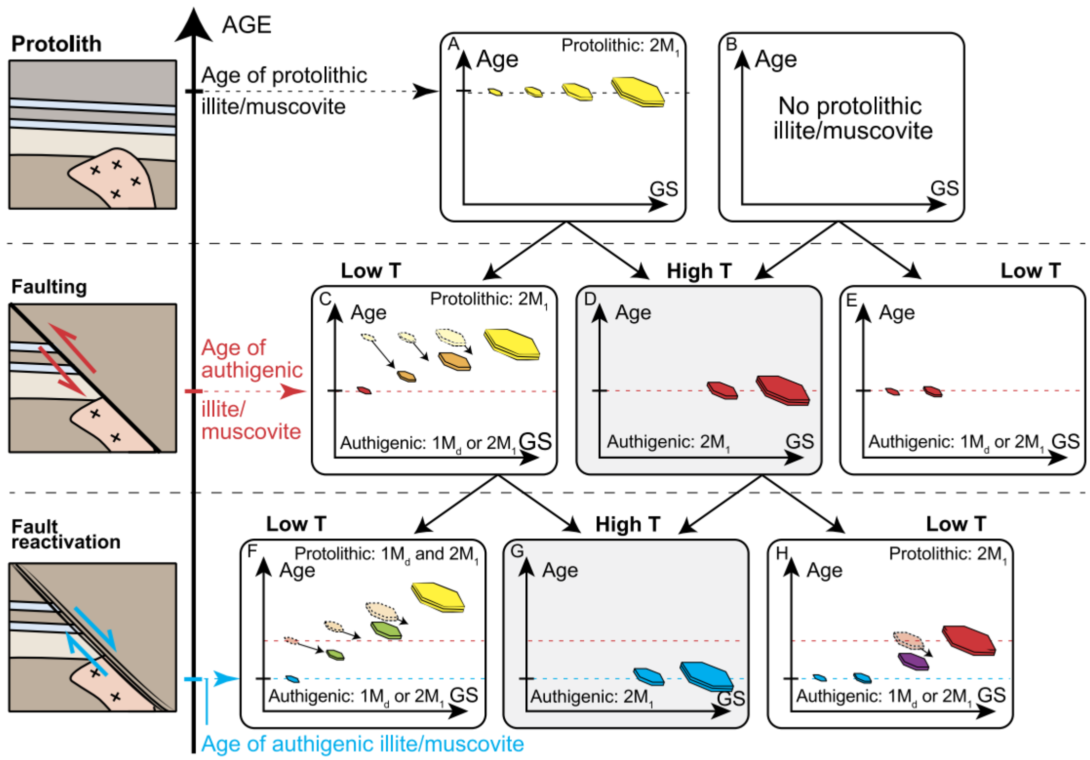

Figure 3.12: Conceptual model for the interpretation of K-Ar age-grain size patterns as mixing curves, wherein the slope is controlled by the age difference between protolithic (i.e., inherited) and synkinematic, authigenic illite/muscovite. The finest size fraction dates the timing of the last faulting increment and represents the age attractor towards which the mixing line converges. Panels A to H are schematic age vs. grain-size (GS) diagrams illustrating the progression of protolithic and authigenic illite/muscovite from protolith (A-B) through fault initiation (C-E) to fault reactivation (F-H), as well as the impact of temperature during deformation on grain-size and age distribution (high T > c. 250 °C > low T). Arrows in C, F and H indicate the shift in age and grain size of protolithic grains as a consequence of overgrowth of younger authigenic illite/muscovite (Torgersen n et al., 2015a).

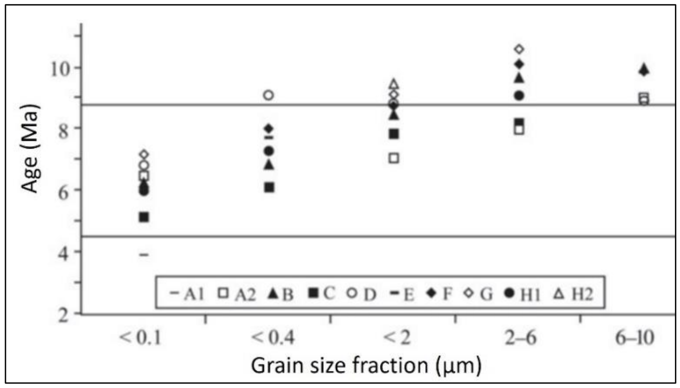

Figure 3.13 - Example of "inclined spectrum" showing K-Ar age vs. grain size data. Note clear trend of decreasing age with decreasing grain size (Zwingmann et al., 2010).

3.5.2 Technical procedure

The characterised and dated samples have been prepared and dated at the laboratories of the Geological Survey of Norway (Trondheim). The analytical procedures followed by the NGU laboratories are described in detail in Viola et al. (2018). A summary of the main steps of the methodology is presented.

C. 400-500 g of fault sample material were collected at the outcrop. The untreated sample was weighed and loaded into plastic bottles and submerged in water. Bottles were sealed and placed in a Julabo F38-ME cryostatic bath filled with ethylene glycol and subjected to at least one month of more than 100 cyclic temperature oscillations between -12 and +25 °C with a 2-hr hold time at each temperature. This method causes water to infiltrate between the particles and disaggregate them gently by gelifraction, without causing artificial grain size reduction.

Subsequently, the < 2 µm material of the disaggregated samples was separated by using Stokes' law in order to obtain the <2 µm, 2-6 µm, and 6-10 µm fractions. The <2 µm suspensions were centrifuged with a Beckman-Coulter Avanti J-26S XP centrifuge to separate 0.1-0.4 µm and <0.1 µm fractions. The obtained five grain size fractions (<0.1 µm, 0.1-0.4 µm, 0.4-2 µm, 2-6 µm, and 6-10 µm) were then dried in an oven at 45 ± 10 °C. Air-dried, homogenised clay materials and standards were wrapped in folded molybdenum microcapsules, and the net mass of the aliquots was determined using a Mettler Toledo XPE26DR microbalance equipped with an antistatic ionizer. The microbalance has a resolution of 2 µg and a measured uncertainty of 4 µg(1σ) for the total weighing procedure. Sample aliquots and standards were left overnight in a drying oven and weighed again to determine the dry weight and relative humidity loss. Finally, to eliminate the excess water, the molybdenum envelopes were loaded into an ultrahigh vacuum extraction line and baked at a maximum temperature of 120 °C.

Argon was extracted from the samples in a Pond Engineering double vacuum resistance furnace at 1400 °C for 20 min. During heating, bulk sample gas was expanded directly into a stainless-steel vessel housing a freshly activated Titanium Sublimation Pump, to strip the sample gas from a majority of reactive gases including H_2O, N, O2, CO, and CO_2. A known molar amount of approximately 2×10^{-13} moles of pure ^{38}Ar spike was prepared and was equilibrated with the purified sample gas.

Argon isotopes were determined on an IsotopX NGX multicollector noble gas mass spectrometer in multicollector mode. Furnace blanks were run regularly between samples and had $^{40}Ar/^{36}Ar$ compositions close to atmospheric argon (Lee et al., 2006). Instrument mass discrimination was determined using aliquots of argon purified from air and compared with the reference value of 298.56 ± 0.31 (Lee et al., 2006).

K concentration was determined by digesting a sample aliquot of ~5.5-50 mg in Li2B4O7 flux at a temperature of 1000 ± 50 °C in Pd crucibles. The resulting glass was subsequently dissolved in HNO_3 and analysed on a Perkin Elmer Optima 4300 DV ICP-OES. 1σ uncertainties were estimated from the reproducibility of a range of standards with K concentrations between 0.19% K and 8.3% K and take into account the signal strength of K during analysis.

K-Ar ages were calculated using the ^{40}K decay constants, abundance, and branching ratio of Steiger and Jäger (1977). Atmospheric Ar corrections were performed using the relative abundances of argon isotopes of Lee et al. (2006). Age uncertainties were estimated using the error equation for multicollector isotope dilution measurements from Hałas and Wójtowicz (2014).

X-ray diffraction (XRD) analyses were performed on a Bruker D8 Advance with LynxEye detector. Measurement parameters were used as follows: Cu Kα radiation, 40 kV/40 mA, scan range 3-75 °2θ (2-40 °2θ for clays), step size 0.02 °2θ, time/step 1 s, fixed divergence slit 0.6 mm (1 mm for clays), primary and secondary soller slits 2.5 °, Ni-filter, knife edge, and sample rotation 1/30 s. Randomly prepared specimens were used for semiquantification, whereas oriented specimens on glass slide were studied for clay identification. These were prepared by letting 1 ml of sample suspension dry out on a glass slide. The slides were analysed at room temperature, after 24 hr glycolysation and after heat treatment at 500 °C for 1 hr.

3.6 Clumped isotope thermometry

Carbonate clumped isotope thermometry is a relatively new geochemical method that can determine the formation temperature of a carbonate mineral (Eiler, 2007; Bernasconi et al., 2018, 2021). The study of clumped isotopes started at Caltech, by Eiler's team in 2004 (Eiler and Schauble, 2004). This methodology relies on the concept of *isotopologues* that are variants of a molecule that differ in the isotopic identity of one or more of their constituent atoms (Fig. 3.14). Multiply substituted isotopologues, commonly called *clumps*, are isotopologues that contains two or more rare isotopes, i.e., they are produced by 'clumping' rare isotopes together (Eiler, 2007). Rare isotopes are ones which are in very low abundance. For example, the rare isotopes of C and O are the heavy ones, i.e., ^{13}C and ^{18}O (Fig. 3.14).

Isotopic substitution of a heavy for a light isotope (e.g., ^{13}C for ^{12}C and 18O for ^{16}O) in a chemical bond reduces the vibration frequencies of that bond and, therefore, influences thermodynamic stabilities of molecules and rates of kinetically controlled reactions (Eiler, 2007). As a consequence, multiply substituted isotopologues (e.g., $^{13}C^{18}O^{16}O$ for CO_2), generally have lower zero-point energies, are slower-vibrating than their singly substituted analogues and, therefore, their stability increases with decreasing temperature (Schmid and Bernasconi, 2010).

In carbonates, at low temperatures multiply substituted isotopologues are present at higher abundances than expected if the isotopes were stochastically distributed among all isotopologues (Eiler, 2007, 2011; Schmid and Bernasconi, 2010). These isotope exchange reactions are temperature-dependent and involve a homogeneous equilibrium (Schmid and Bernasconi, 2010). In detail, the carbonate clumped isotope thermometry is based on the determination of temperature-dependent excess abundance of the ^{13}C-^{18}O bonds in the carbonate lattice above a theoretical random distribution (Schauble et al., 2006; Eiler, 2007; Bernasconi et al., 2018, 2021). This method is independent of the $\delta^{18}O$ of the fluid in which the mineral grew. Consequently, the fluid $\delta^{18}O$ and the stable isotopic ratio of oxygen of the carbonate are measured simultaneously and can be reconstructed using clumped isotope thermometry (Bernasconi et al., 2018).

Carbonate clumped isotope compositions are reported as an excess abundance of the CO_2 isotopologue of cardinal mass 47 (dominantly the isotopologues $^{13}C^{18}O^{16}O$) compared to a stochastic distribution according to the formula (Bernasconi et al., 2021):

$$\Delta 47 = \frac{R47}{R47*} - 1$$

where R47 is the ratio of the abundances of the set of minor isotopologues with mass 47 (mostly $^{13}C^{18}O^{16}O$ and trace amounts of $^{12}C^{17}O^{18}O$ and $^{13}C^{17}O_2$) divided by the abundance of the most abundant isotopologue with mass 44 ($^{12}C^{16}O_2$). The stochastic ratio R47* is calculated using the measured abundance of ^{13}C and ^{18}O and measured or calculated abundance of ^{17}O in the sample (Bernasconi et al., 2021). Δ47 reflects an internal state of isotope distribution within the carbonate mineral phase, thus it can be used to calculate mineral formation temperature as well as the $\delta^{18}O$ of the precipitating fluid. Theoretically, the Δ47 for CO2 varies from approximately 0% at c. 1000 °C, meaning that a stochastic distribution is achieved, to about 0.94% at 0 °C (Schmid and Bernasconi, 2010).

The variance observed in repeated measurements of a sample during clumped isotope thermometry measurements is relatively large compared to the total range of natural variations (Fernandez et al., 2017). For instance, typical errors associated with a single measurement (about 15-30 ppm; 1 standard deviation) are approximately 5-10 times larger than the signal expected for a 1 °C temperature change (c. 3 ppm at 25 °C; Fernandez et al., 2017; Muller et al., 2017). For a proper evaluation of the error associated with the analysis of clumped isotopes it is, therefore, necessary to obtain multiple replicate measurements.

To summarise, the clumped isotope thermometry retrieves the temperature of the fluid from which calcite crystallised, the carbon and oxygen stable isotope ratios and the fluid $\delta^{18}O$. The possibility to determine both the mineral formation temperature as well as the $\delta^{18}O$ of the precipitating fluid has demonstrated to be key to many geoscience issues. In fact, carbonate clumped isotope thermometer has been applied to different sectors of geology, to deal with the temperature and oxygen isotope composition of ocean waters in deep time (e.g., Rodríguez-Sanz et al., 2017), terrestrial paleotemperature (e.g., Meckler et al., 2015), uplift rates of continents and basin thermochronology (e.g., Ghosh et al., 2006), diagenetic evolution of carbonate sequences (e.g., Millán et al., 2016), and formation of carbonate deposits during fault movement (e.g., Bergman et al., 2013; Huntington and Lechler, 2015). In structural geology this technique is useful to unravel fluid sources and syntectonic fluid flow during faulting in sedimentary rocks (e.g., Luetkemeyer et al., 2016; Curzi et al., 2020; Salomon et al., 2020; Smeraglia et al., 2020). In these cases, the comparison between stable isotopic values of the veins and the host rock, permits also to constrain if the geochemical system was open at the time of fluid circulation. By now, therefore, it has not been applied on carbonate veins within crystalline rocks.

Stochastic abundances of isotologues of common gases

Mass [a]	Isotopologue	Relative abundance
N_2 [b]		
28	$^{14}N_2$	99.30%
29	$^{15}N^{14}N$	0.73%
30	$^{15}N_2$	13.4 ppm
O_2 [c]		
32	$^{16}O_2$	99.50%
33	$^{17}O^{16}O$	756 ppm
34	$^{18}O^{16}O$	0.40%
	$^{17}O_2$	0.144 ppm
35	$^{18}O^{17}O$	1.52 ppm
36	$^{18}O_2$	4.00 ppm
CO_2 [d]		
44	$^{12}C^{16}O_2$	98.40%
45	$^{13}C^{16}O_2$	1.11%
	$^{12}C^{17}O^{16}O$	748 ppm
46	$^{12}C^{18}O^{16}O$	0.40%
	$^{13}C^{17}O^{16}O$	8.4 ppm
	$^{12}C^{17}O_2$	0.142 ppm
47	$^{13}C^{18}O^{16}O$	44.4 ppm
	$^{12}C^{17}O^{18}O$	1.50 ppm
	$^{13}C^{17}O_2$	1.60 ppb
48	$^{12}C^{18}O_2$	3.96 ppm
	$^{13}C^{17}O^{18}O$	16.8 ppb
49	$^{13}C^{18}O_2$	44.5 ppb

[a] Nominal cardinal mass in AMU.
[b] Asuming a $^{15}N/^{14}N$ ratio equal to atmospheric N_2.
[c] Assuming $^{17}O/^{16}O$ and $^{18}O/^{16}O$ ratios equal to the VSMOW standard.
[d] Assuming $^{17}O/^{16}O$ and $^{18}O/^{16}O$ ratios equal to the VSMOW standard and $^{13}C/^{12}C$ ratio equal to the PDB standard.

Figure 3.14 - Stochastic abundances of isotopologues of common gases (Eiler, 2007).

3.6.1 Technical procedure

Calcite veins and slickenfibers have been collected along the MNPM, together with their spatial orientation and, if present, the trend and plunge of the slickenlines, as well as the spatial orientation of the associated fault plane. Samples have been drilled with a mini-drill to obtain at least 2 mg of powder. Carbonate isotopologue measurements were performed at ETH Zurich, thanks to the collaboration with Prof. Stefano Bernasconi. The detailed procedure is described by Schmid and Bernasconi (2010), Meckler et al. (2014) and Müller et al. (2017). The main steps of the procedure are herein described.

Carbon and clumped isotope compositions of carbonates were determined using a Thermo Scientific Kiel IV carbonate preparation device (Thermo Fisher Scientific, Bremen, Germany) to produce CO_2 for isotope analysis from carbonate samples by phosphoric acid digestion, coupled to a Thermo Scientific 253Plus isotope ratio mass spectrometer. The spectrometer is operated at an electron energy of 150V and an acceleration voltage of about 9.5 kV. The mass spectrometer has a precision of 5 to 10 parts per million (ppm) in D47, which corresponds to an error in temperature of 1.2 to 2.48 °C. The Kiel IV device includes a custom built PoraPakQ trap held a -40 °C to eliminate potential organic contaminants, such as halocarbon or hydrocarbon contaminants (Schmid and Bernasconi, 2010; Meckler et al., 2014; Müller et al., 2017).

Prior to each sample run, the pressure-dependent backgrounds are determined on all beams to correct for non-linearity effects in the mass spectrometer. During each run, 22 replicates of 90-110 µg of different samples and 5 replicates of each carbonate standards, ETH-1, ETH-2, and 10 replicates of ETH-3, are analysed for data normalisation. Two replicates of the international standard, IAEA C2, is analysed to monitor the long-term reproducibility of the method. For each sample, 8-12 replicate analyses of 90-120 µg aliquots of carbonate powder are performed. The individual analyses take approximately 30 min (Schmid and Bernasconi, 2010; Meckler et al., 2014; Müller et al., 2017).

All instrumental and data corrections were carried out with the software Easotope (John and Bowen, 2016) using the revised IUPAC parameters for ^{17}O correction (Daëron, 2021). The results are presented in the I-CDES (Intercarb Carbon dioxide equilibration scale) according to Bernasconi et al. (2021). Temperatures are calculated using the Anderson et al. 2021 universal calibration.

3.7 Virtual Outcrop Models (VOMs) and Discrete Fracture Network (DFN) Modelling

In order to correlate the structural analysis of onshore fractured outcrops to the offshore basement fracture pattern, we collected data on the geometrical, mechanical and permeability properties of fractured and weathered outcrops considered to be analogues of offshore crystalline basement highs.

The field and Virtual Outcrop Model (VOM) structural analysis of the Goddo Fault zone on Bømlo island was performed to constrain the relationship between meso-scale fracture patterns and the bulk permeability of this complex, spatially heterogeneous fault zone. The VOM analysis recovers the geometrical characteristics and the spatial variation of fracture intensity. These structural, geometrical, and spatial data represent the input to build stochastic Discrete Fracture Network (DFN) models of selected portions of the fault, with the main goal of evaluating the variation of shape and magnitude of the permeability tensor though the fault zone (Ceccato et al., 2021a).

In addition, petrophysical and geomechanical properties have been measured on selected fractured and weathered outcrops. The modelling of fracture spatial patterns by means of DFN and the characterisation of petrophysical properties of fractured, weathered crystalline rocks have been carried out in collaboration with Dr. Alberto Ceccato, a post-doctoral researcher in the framework of the project BASE2. Most of the work of the attached papers was done by him and my contribution consisted in the data collection during the field work, the investigation, and the reviewing of the proposed conceptual models.

3.7.1 UAV imagery acquisition and Virtual Outcrop Model elaboration

Georeferenced VOMs of the Goddo Fault Zone outcrop were generated using UAV-drone imagery (Unmanned Aerial Vehicles). UAV-drone image acquisition was carried out with a DJI Phantom 4 drone, equipped with a 20 MP camera (CMOS-1 sensor, 24 mm lens) using Ground Station Pro software on an iPad (Fig. 3.15a). Two flights were flown on the fault outcrop: (i) an overview survey, acquiring images at low-resolution (1 cm/pxl), (ii) a high-resolution (1-3 mm/pxl) survey, specifically covering the fault cores. Point clouds, orthophotos and digital surface models were generated through the analysis of the drone imagery in ContextCapture (Bentley Systems Inc.).

The interpretation of fractures and the structural analysis of the generated VOMs were performed in CloudCompare, by plotting the VOMS as point clouds. The point clouds of the two VOMs generated from the two drone flights were combined to build a single, high-resolution VOM of the fault zone (Ceccato et al., 2021a)

Fracture extraction from the VOMs required the segmentation of exposed fracture surfaces and the analysis of fracture traces on the outcrop surface adopting the structural analysis toolkits Facets (Dewez et al., 2016) and Compass (Thiele et al., 2017) implemented in CloudCompare. The Facets tool is designed to retrieve the planar 3D polygon that best fits the points of a manually selected portion of the point cloud (Fig. 3.15b). The Compass tool allows to either fit a square plane to a selected region of defined radius around a selected point of a point cloud (Plane tool), or to retrieve the plane that best fits the trace of a fracture on the outcrop surface (Trace tool). The accuracy of both analytical tools in retrieving reliable orientation data depends on the resolution of the point cloud and the dimension of the segmented fracture plane: the smaller the fracture surface/trace, the fewer the points that can be fitted by the interpretation tools, and thus, the less accurate the retrieved plane orientation (Dewez et al., 2016; Thiele et al., 2017). The interpreted planar or linear trace expression of fractures ranges between 10 cm and 5 m. The structural orientation data exported from Facets and Compass tools were then analysed and plotted with Stereonet v.11.2.2 (Fig. 3.15c). Fracture trace length distributions were analysed with an ad-hoc MATLAB script adopting the functions for distribution fitting made available by FracPaQ (Healy et al., 2017; Rizzo et al., 2017).

The interpreted fracture traces and segmented polygons were then exported as meshes and imported into MOVE (Petex) to identify the dominant fracture sets, analyse their spatial distribution and the related fracture intensity. The imported meshes were converted in rectangular fracture planes displaying the same orientation and horizontal length dimension of the polygons interpreted from the VOM. In MOVE, the entire fracture plane database was sorted into different orientation sets through manual segmentation of point clusters formed by the poles to the fracture planes in the stereographic projections. The linear fracture intensity (P_{10}) was computed for each set on virtual cross-sections across the fault with the aid of virtual scanlines (Fig. 3.15d). Then, several cross-sections were traced through the outcrop, oriented perpendicularly to the average strike of the selected fracture set and cutting across the areas of the VOM populated by the largest density of polygons-fractures. Virtual scanlines were traced perpendicular to the main dip angle of projected fractures on each section (Fig. 3.15e). The length of scanlines drawn on each section was limited to a few meters (<2-5 m). Fracture intensities were then computed by counting the number of fractures intersected and/or occurring in proximity (1-2 m above or below) to the virtual scanline. Finally, to compare results from different scanlines and cross-sections, we projected the virtual scanlines on a single cross-section to track the variation of fracture intensity for each set across the profile (Fig. 3.15f).

3.7.2 Discrete Fracture Network modelling

The quantification of the structural permeability related to meso-scale fracture networks was performed by stochastic DFN modelling in FracMan 7.9 (Golder Associates). FracMan allows to compute the permeability related to a specific fracture network in a rock mass through numerical modelling based on Discrete Fracture Network methods. The fracture network in the DFN models has been generated using a stochastic approach by the obtained parameters from the analysis of VOMs describing the statistical distribution of geometrical fracture properties (Fig. 3.15g). The input parameters for stochastic DFN modelling include: (i) the average orientation and orientation variability; (ii) the target volumetric fracture intensity P_{32}; (iii) a function describing the shape of the cumulative distribution of some fracture size (length, height, radius); (iv) the fracture shape (Ceccato et al., 2021a).

The input P_{32} for each fracture set in each model was calculated from the measured P_{10} intensity retrieved from the virtual scanlines following the approach suggested by Antonellini et al. (2014). The detailed methodology is reported in Ceccato et al., 2021a.

Each DFN model consists of a 100 × 100 × 100 m (106 m^3) volume domain composed of 8000 Representative Elementary Volume (REV) of 125 m^3 (5x5x5 m) each (Fig. 3.15g). Each REV was populated stochastically with selected assemblages of fracture sets. The computed volumetric grid, therefore, represents 8000 possible configurations of a 125 m^3 REV of a rock mass populated by a specific assemblage of fracture sets with specific fracture parameters. By doing so we aimed at analysing the statistical variation of the permeability tensor properties among the 8000 REV in the 106 m^3 modelled volume domain. The permeability computation in the DFN models follows the approach of Oda (1985). The approach of Oda retrieves the magnitude and orientation of the permeability tensor principal components (K_1, K_2, K_3 with $K_1>K_2>K_3$) from the "crack tensor" describing the geometrical properties of the fractures-discontinuities occurring within a REV of fractured rock mass. Comparing the magnitude and orientation of the tensor principal components computed for each of the 8000 REV within the same DFN model, we have retrieved the statistical variability of **K** components of structural permeability (Fig. 3.15h, i).

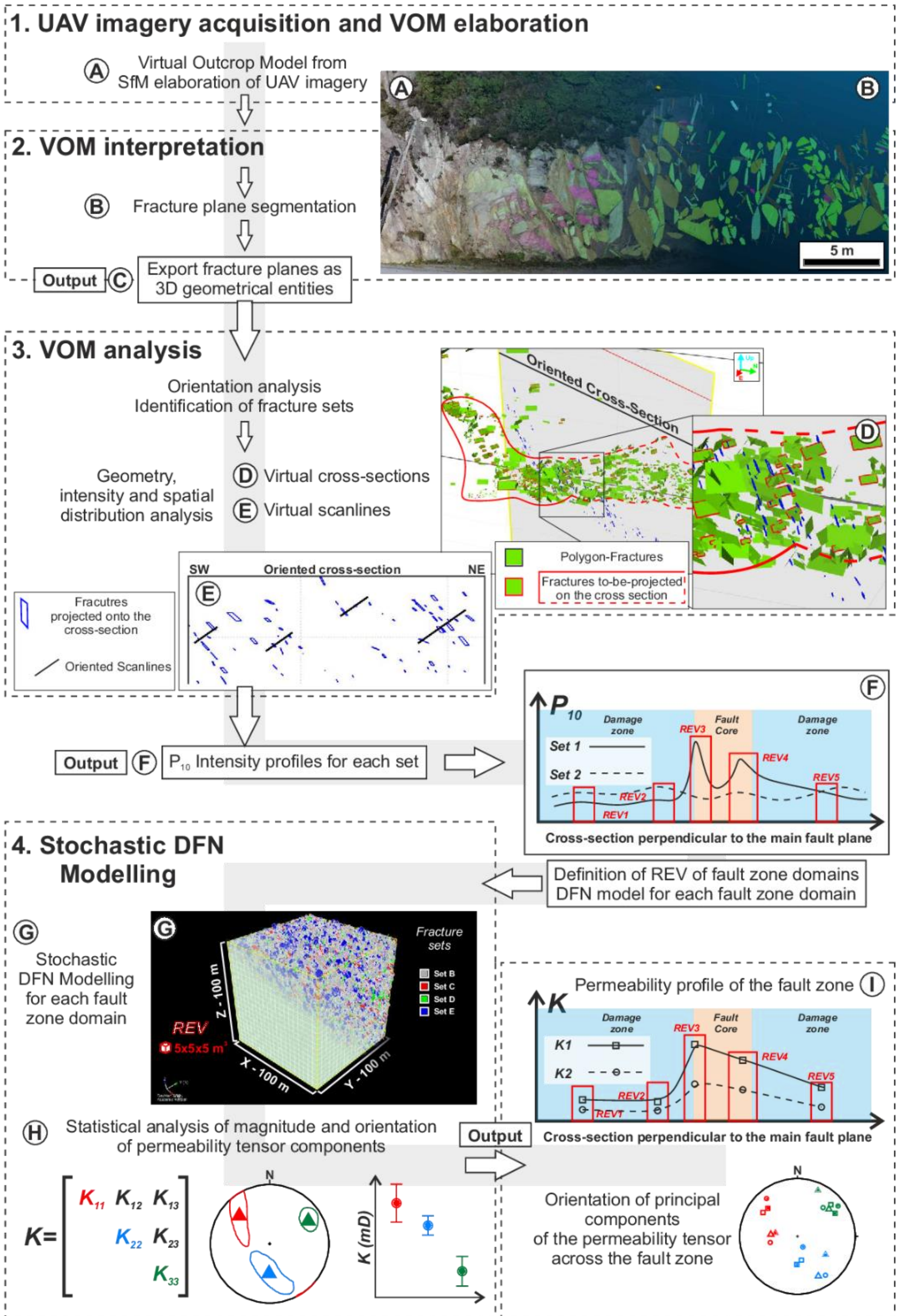

Figure 3.15 - Methodological workflow from VOMs structural analysis to DFN modelling (Ceccato et al., 2021a).

3.8 Petrophysical properties

The investigation of petrophysical (permeability) and geomechanical (Uniaxial Compressive Strength, UCS) properties has been carried out directly in the field on selected representative outcrops of fractured and weathered basement.

3.8.1 Permeability

In-situ permeability measurements have been carried out with a New England Research TinyPerm-3 air-minipermeameter on fault rocks and alteration products related to basement weathering (Ceccato et al., 2021b). The minipermeameter is calibrated by the manufacturer with known standards. The instrument allows a reliable field investigation of rock permeability within small volumes (1-1.5 cm^3) in the 10^{-3}-10 D range, even though controlled laboratory tests have demonstrated its capability to measure permeability values as low as 10^{-5} D (Filomena et al., 2014). In the bulk-rock permeability mode, the instrument directly estimates of the permeability based on the outgoing air flow rate from the built-in compression vessel. Permeability values obtained from air-minipermeametry need to be corrected and standardised in order to be comparable with permeability values obtained from laboratory tests on rock plugs or image analysis (Filomena et al., 2014; Torabi et al., 2018).

Care must be taken when using absolute gas permeability values to analyse the flow of a liquid. In fact, in the same porous medium permeability estimates from permeametry tests adopting a gas as permeating fluid (as in air-minipermeametry) can be significantly larger than the estimates from permeability tests relying on a liquid as permeating fluid as a consequence of possible slip-flow effects (Klinkenberg effect) (van Noort and Yarushina, 2018).

3.8.2 Uniaxial Compressive Strength (UCS)

The geomechanical characterisation has been carried out with a L-type Schmidt hammer (DRC GeoHammer) calibrated according to international standards (ASTM D5873-00; EN 12 504-2; ASTM C 805-02). The reliability range of the instrument extends between 10 MPa and 300 MPa of UCS (Aydin and Basu, 2005).

UCS values were calculated from the analysis of Schmidt hammer rebound values (Aydin and Basu, 2005). Schmidt hammer measurements were carried out perpendicularly to clear, fresh rock surfaces (wherever possible), parallel to the horizontal direction (Ceccato et al., 2021b). Schmidt hammer rebound values obtained from the *in-situ* measurement was converted into

UCS by following the hammer orientation-dependent calibration curves provided by the manufacturer. Horizontal rebound values were converted into UCS by the following equation:

$$UCS = 0.0232*R^{2.2637} \text{ (MPa)}$$

3.8.3 Procedure

Petrophysical and geomechanical analyses have been performed on compositionally and texturally homogeneous volumes of the outcrops, as representative of the bulk rock properties, and along transects. Where rock textural anisotropies were present, petrophysical analysis have been performed both perpendicular and parallel to the dominant planar rock fabric, aiming at evaluating the potential anisotropy of properties. Transects constrain the variation of the analysed properties across weathering fronts and high-density fracture zones. Surface spot analyses for both permeability and UCS analyses have been done by probing representative outcrop surfaces with at least 10 measurements. Selected measuring spots were at least 10-15 cm away from mesoscopic fractures wherever possible (Aydin and Basu, 2005). Both permeability and Schmidt hammer rebound analyses were repeated twice in the immediate surroundings of the selected spot along transects, for a total of three measurements. The replicates were not exactly on the same point to avoid results biased by subtle rock modifications (e.g., compaction and microfracturing) due to the previous measurements. Each measure spot was kept at c. 5-10 cm from the nearest measuring point both along transects and within selected areas and taken to be representative of a 5 cm-radius hemispherical volume below it (ASRM standards; Aydin and Basu, 2005).

Chapter 4

"Brittle structural facies" analysis: A diagnostic method to unravel and date multiple slip events of long-lived faults

Giulia Tartaglia, Giulio Viola, Roelant van der Lelij, Thomas Scheiber, Alberto Ceccato, Jasmin Schönenberger

Earth and Planetary Science Letters 545, (2020), 116420

doi: 10.1016/j.epsl.2020.116420

Abstract

Regional-scale faults typically experience complex, long-lasting histories, commonly recording evidence of multiple reactivation events. Therefore, they contain multiscalar structural domains characterised by varying microstructures, mineralogical compositions, and kinematics. These domains result from differential strain partitioning during the recorded faulting stages, and, as a result, can preserve the isotopic and kinematic signature of the different slip periods. Their detailed structural analysis integrated with K-Ar dating of the fault rock assemblage can help to identify these commonly tightly juxtaposed, although not coeval, domains, which we refer herein to as "Brittle Structural Facies" (BSF). BSF analysis is pivotal (i) to understand the structural heterogeneity of fault zones, (ii) the diachronic formation of geometrically and kinematically complex fault cores and (iii) to reconstruct faults' evolution in time and through space. Following this approach, this study relies on meso-and microstructural analysis, chemical characterisation and K-Ar dating to unravel the evolution of the Lærdal-Gjende Fault (LGF, southwestern Norway). The LGF is a multiply reactivated top-to-the-NW extensional fault with a 1 m thick poorly consolidated core. We recognised, sampled, and characterised five BSF: I) Indurated dark reddish gouge, (II) Poorly consolidated cataclasite, (III) Weakly foliated greenish gouge, (IV) Clay-rich gouge and (V) A few mm-thick clay smear decorating the principal slip surface. Samples were separated into five grain size fractions (from <0.1 to 6-10µm) and analysed by X-Ray Diffraction, Transmission Electron Microscopy and K-Ar geochronology. A c. 180 Ma age cluster defined by 10 ages of the coarsest grain size fractions (2-10µm) likely documents fault nucleation during Jurassic rifting in the North Sea. The ages of the finest fractions, enriched in synkinematic K-bearing minerals (illite, smectite and K-feldspar), constrain four periods of faulting at c. 121 ±3, 87 ±2, 78 ±2 and 57 ±1 Ma. Ages indicate that the LGF accommodated strain due to hyperextension of the Mid-Norwegian margin down to the Late Cretaceous and finally slipped again during the Paleogene. The alternating widening and narrowing of the active fault zone in response to varying deformation mechanisms, including coseismic rupturing, formed the present complex fault architecture. This study highlights the importance of BSF characterisation as part of a multidisciplinary workflow to derive structural and temporal datasets of complex fault zones. BSF analysis, moreover, is demonstrated to be key for investigating the diachronic evolution of fault cores and to resolve multiple slip events of faults.

4.1 Introduction and aims of the study

Fault zones are expression of brittle deformation in the Earth upper crust, where slip localises in response to stresses that exceed the rock strength. Their nucleation and progressive growth lead to the formation of fault cores and surrounding damage zones (Chester and Logan, 1986; Caine et al., 1996). Different fault-related rocks, such as cataclasite, breccia, gouge and pseudotachylyte, may commonly coexist within the same fault zone. Their juxtaposition reflects the temporal and spatial evolution of the fault system, including its deformation mechanisms and physical conditions at the time of initial faulting, as well as of possible re-activations.

Many brittle faults can be interpreted as the summation of multiple deformation events through time. During each faulting episode, slip and strain localisation lead to progressive comminution of the host rock and synkinematic crystallisation of new minerals, such as clays and phyllosilicates. Importantly, *in situ* synkinematic neoblastesis offers the possibility to radiometrically date a given faulting event as well as later multiple reactivations (e.g., van der Pluijm et al., 2001; Pleuger et al., 2012; Bense et al., 2013; Davids et al., 2013; Yamasaki et al., 2013; Torgersen et al., 2015a; Ksienzyk et al., 2016; Viola et al., 2016, 2018; Aldega et al., 2019 et al., 2019; Scheiber et al., 2019).

Unravelling the relationships between mineral assemblages, age, and kinematic framework of all recorded slip events within a fault remains, however, an arduous task (Clauer, 2013; Torgersen et al., 2015a; Viola et al., 2016; Scheiber et al., 2019). The intrinsic complexity of faults and the spatial arrangement of fault rocks reflect the interplay of fluid-rock interaction and the ease of reactivation of brittle structures. The reactivation of suitably oriented faults (Holdsworth, 2004) may lead to the partial or total obliteration of any inherited evidence of earlier deformation events (Viola et al., 2013). Due to these complexities, conceptual evolutionary models of fault zones do not always consider the absolute temporal dimension of faulting, and thus become rather static snapshots of what is instead a dynamic evolution. The lack of details on the temporal dimension of faulting may lead to oversimplifications of the evolution of faults, which, in turn, can lead to a misinterpretation of their possible seismic behaviour and overall tectonic role in the regional framework.

The necessity of a time-constrained reconstruction of faults' evolution has therefore led structural geologists to study in detail their internal architecture (e.g., Caine et al., 1996; Aydin, 2000), which often contains juxtaposed domains characterised by different fault rocks, mineralogical composition, texture, and kinematics. Multiple faulting events cause deformation to preferentially localise into weaker volumes and along slip surfaces, whereas lithons representing remnants of former slip events can be preserved. These domains generally exhibit sharp boundaries and complex crosscutting relationships whose unravelling is crucial to establish a relative temporal sequence of (de)formation. We apply inhere the term "Brittle Structural Facies" (BSF) to refer to such domains (cf. Braathen et al., 2009). In this paper, BSF specifically refers to a deformed volume of rock characterised by a given fault rock type, texture, colour, composition, and age of formation. The identification, structural analysis, mineralogical characterisation, and radiometric dating of BSF are key to (i) understand the structural heterogeneity of fault zones, (ii) decipher the diachronic formation of geometrically and kinematically complex fault cores and (iii) resolve the evolution of multiply reactivated faults.

To document our approach and the usefulness of the BSF concept, we present a structural-geochronological workflow that serves as an example of general validity when aiming to unravel the evolution of long-lived faults. We studied the Lærdal-Gjende Fault (LGF), a multiply reactivated extensional fault in southwestern Norway (Andersen et al., 1999; Fossen and Hurich, 2005; Fossen et al., 2016). The detailed structural analysis of the fault core allowed us to identify five distinct BSF, and to sort out their mutual geometric and relative temporal relationships. Samples from each brittle fault facies were characterised by optical and Scanning Electron Microscopy (SEM). K-bearing phases from fault rock samples were identified, quantified, and characterised by X-Ray Diffraction (XRD) and Transmission Electron Microscopy (TEM) and, finally, dated by the K-Ar technique. This comprehensive structural, compositional, and geochronological dataset has been used to propose an evolutionary scheme of LGF that accounts for all dated faulting stages.

4.2 Geological framework

The study area is in southwestern Norway, near the town of Lærdal (Fig. 4.1a). There, the Baltic autochthonous basement is overlain by Caledonian Allochthons (Corfu et al., 2014) thrusted south-eastward during the Late Silurian-Early Devonian Caledonian collision between Baltica and Laurentia (Fossen and Dunlap, 1998). The autochthonous basement is mainly composed of Mesoproterozoic migmatites that were only marginally affected by Caledonian deformation (Fossen and Hurich, 2005). The Allochthons are tectonic nappes derived from the cover sequences of the Baltic Shield, the ancient Iapetus Ocean and Laurentian basement cover units. The allochthonous unit at the Lærdal site is formed by the Laurentia-derived Jotun Nappe Complex. It is composed of a series of thrust sheets of variously deformed plutonic rocks metamorphosed under amphibolite facies conditions during the Proterozoic Sveconorwegian orogeny (Milnes and Corfu, 2011; Corfu et al., 2014). The Jotun Nappe Complex comprises monzonitic and mangeritic orthogneiss, metagabbroic slivers and anorthositic suites (Milnes and Corfu, 2011).

Caledonian collisional tectonics led to an over-thickened orogenic pile that collapsed during the Early Devonian (408-402 Ma; Fossen and Dunlap, 1998) through the nucleation and reactivation of orogen-scale extensional detachments. NW-SE extension caused the exhumation of the orogenic roots to shallow crustal levels. The progressive accommodation of deformation in the brittle regime led to the nucleation of major faults and brittle fault zones, which overprinted earlier ductile detachments (Fossen et al., 2016). One of these Devonian extensional detachments is the Hardangerfjord Shear Zone (HSZ), which is exposed in the study area (Fig. 4.1a, Fossen et al., 2016). The HSZ is a gently oblique, top-to-the-NW shear zone (Fossen and Hurich, 2005), which is composed at the Lærdal site of tens of meter thick mylonites separating the autochthonous basement from the overlying Jotun Nappe Complex (Fig. 4.1a). The Lærdal-Gjende Fault strikes NE-SW, and at its most representative outcrop in Lærdal it partially reworked and overprinted the mylonitic fabric of the HSZ (Fig. 4.1a, Fossen and Hurich, 2005).

Thermochronological studies indicate that two main episodes of enhanced, rapid exhumation affected southwestern Norway in the Permo-Triassic and in the late Cretaceous-Cenozoic (Johannessen et al., 2013; Walsh et al., 2013; Ksienzyk et al., 2014, 2016). During the Cretaceous, exhumation generated a high relief that was later periodically rejuvenated by brittle faulting (Johannessen et al., 2013).

Two studies have focused on the age of brittle deformation along the LGF. Andersen et al. (1999) studied the greenish epidote-rich cataclasite in the damage zone and constrained Early Triassic up to Early Cretaceous slip by paleomagnetic techniques. Fossen et al. (2016) used K-Ar radiometric dating on synkinematic illite from two fault core gouge samples reporting dates between 200 and 64 Ma. In general, previous authors agree that the LGF nucleated and developed as the shallow crustal brittle expression of the ductile HSZ during the Devonian (although direct geochronological constraints on this episode are not reported), and continued its activity until the Cretaceous, to around 120 Ma. Hence, according to published data, the LGF was active during the post-collisional collapse of the Caledonides and during the Mesozoic North Sea rifting evolution (Andersen et al., 1999; Fossen and Hurich, 2005; Fossen et al., 2016). These studies, however, did not aim at linking the different fault structural facies to their ages, and a time-constrained evolutionary model of the LGF has not yet been proposed.

4.3 Methods

Our study is based on a combined structural-geochronological approach (Viola et al., 2016) wherein a detailed structural analysis of the fault was done by identifying, describing, and characterising different BSF. Characterisation of the BSF and structural analysis were performed along the entire LGF outcrop exposed in Lærdal (Fig. 4.1). Sample collection was from the central part of the LGF outcrop, in a well exposed c. 1 m2portion of the fault core (Fig. 4.1c). C. 400 g of variably consolidated fault rock material was collected for each BSF (Fig. 4.1d). Special care was taken to avoid mixing between different BSF. Oriented samples of consolidated fault rock and wall rock were collected for microstructural analysis. Thin sections oriented parallel to the transport direction and perpendicular to the planar fabric were prepared from the poorly consolidated samples of cataclasite and indurated gouge. They were studied by optical and scanning electron microscopy integrated with energy dispersive X-ray analyser (SEM-EDS) at the University of Padua (Italy) to investigate microstructure and mineralogical composition of the fault rocks.

Characterisation of the samples for K-Ar radiometric dating was performed at the laboratories of the Geological Survey of Norway (Trondheim, Norway) following the routines described by Viola et al. (2018). Samples from each BSF were disintegrated by repeated freezing and thawing cycles. This method avoids artificial grain size reduction of coarse-grained minerals and their contamination in the finer fractions. Samples were separated in five grain size fractions (<0.1, 0.1-0.4, 0.4-2, 2-6 and 6-10µm). Grain size fractions of <2, 2-6 and 6-10µm were separated in distilled water using Stokes' law, whereas the finer fractions (<0.1, 0.1-0.4 and 0.4-2µm) were obtained by high-speed centrifugation of the <2µm fraction.

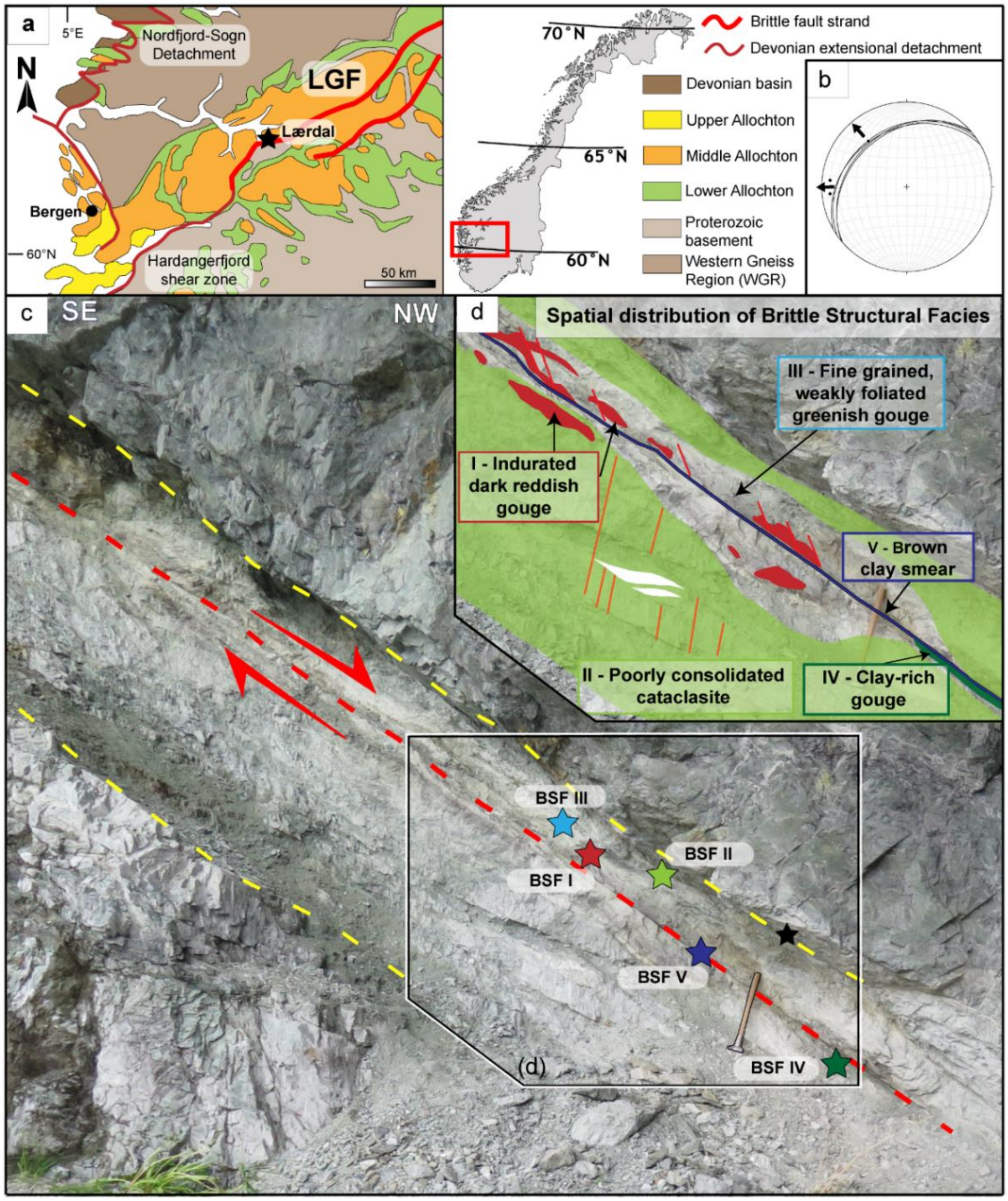

Figure 4.1 - a) Simplified geological map of southwestern Norway with the main structural features of the area. Black star: Lærdal study site; b) Schmidt projection (lower hemisphere) of the principal and secondary slip surfaces of the fault and their associated striae. The arrows show the direction of slip of the hanging wall; c) detailed view to the southwest of the studied LGF outcrop. The principal slip surface (red dashed line) is represented by a thin, laterally continuous smear of dark gouge, while two subparallel secondary slip surfaces (yellow dashed lines) frame the fault core. Stars indicate sample locations. All samples were dated by K-Ar. 40 cm long hammer for scale in the lower part of the outcrop; d) simplified scheme of the BSF of the fault core.

The mineralogical composition of each grain size fraction for each sample was obtained by XRD analysis (with a Bruker D8 Advance diffractometer). Mineral quantification was carried out on randomly prepared specimens using Rietveld modelling with the TOPAS 5 software. Refined parameters include crystallite size, unit cell dimensions, sample displacement, preferred orientation, and background coefficients. The lower limit of quantification and accuracy are mineral-dependent but are generally 1 wt% and 2-3 wt%, respectively. The finest <0.1μm grain size fractions could not be analysed by XRD due to too low sample mass being recovered from these fractions. Detection and imaging of K-bearing phases therein were thus carried out with a TEM (JEOL JEM-2100) equipped with an energy dispersive X-ray analyser (EDS) at the NORTEM laboratory of the Norwegian University of Science and Technology (NTNU). After the structural characterisation of the BFS, and the identification of the K-bearing phases, all grain size fractions were dated by K-Ar technique. Readers are referred to Appendix A for further details on the analytical procedure.

4.4 Results

4.4.1 Fault anatomy and sample location

The LGF is a composite brittle structure defined by a 1-1.5 m thick fault core and an up to 200 m thick asymmetric damage zone. The damage zone is mainly composed of grey-pale green cohesive cataclasite and is thicker in the hanging wall. A dense and complex network of 1-3 cm thick epidote and quartz veins cuts across the hanging wall (Fig. 4.2a) but is not present in the immediate proximity of and within the fault core. Towards the upper part of the hanging wall, metasyenite and metamonzogranite are exposed. In the footwall mylonites, the damage zone is up to 30 m thick.

The fault core is a tabular structure containing a principal slip surface that dips 35° to the NW and bears W-plunging slickenlines (Fig. 4.1b). It is defined by a laterally continuous and only a few mm thick smear of dark gouge (Fig. 4.1d). Secondary slip surfaces, subparallel to the principal slip surface, occur above and below it, bounding the fault core (Fig. 4.1b, c). They contain two sets of lineations, defined by NW-and W-plunging slickenlines (Fig. 4.1b, 4.2b). Riedel shears and bookshelf structures (Fig. 4.2e, f), together with the bending of foliated gouge and sigmoidal lenses of indurated cataclasite (Fig. 4.2c, d), are consistent with a normal top-to-the-NW sense of shear. The principal slip surface cuts across all other structural features (Fig. 4.1d), indicating that its sinistral transtensional W-directed kinematics is related to the youngest recorded increment of faulting.

The fault core contains juxtaposed discrete brittle domains delimited by sharp boundaries, each corresponding to one of the identified BSF of the LGF (Fig. 4.1d). Every BSF contains a distinct fault rock type, each characterised by a different degree of consolidation, colour, clay content (with various degrees of plasticity in hand specimen) and geometric relationships. Five BSF (BSF I to BSF V) were recognised at the outcrop (Fig. 4.1d) and sampled for mineralogical characterisation and K-Ar dating.

Crosscutting relationships at the outcrop allowed to define the relative temporal sequence of BSF formation, from the oldest (BSF I) to the youngest (BSF V). The fault core contains competent and internally fractured lenses of a dark reddish grey indurated gouge (BSF I, Fig. 4.3a) preserved all along a tabular domain in the central portion of the core. These lenses are a few to tens of cm long and locally exhibit sigmoidal shapes (Fig. 4.2d). They are embedded within two other brittle structural facies: a poorly consolidated cataclasite (BSF II) and a weakly foliated gouge (BSF III, Fig. 4.1d). BSF II defines the most external portion of the core and is formed by a poorly consolidated pale green cataclasite (Fig. 4.3b). It is the most abundant structural facies in the fault core. Inside the green cataclasite there occur smaller sigmoidal lenses of whitish cataclasite (identical in thin section to the greenish cataclasite of BSF II), whose asymmetric shape suggests top-to-the-NW extensional shearing (Fig. 4.1d, 2c). The green cataclasite is cut across by narrowly spaced, subvertical, NNE-SSW striking fractures with sporadic calcite coatings. These subvertical fractures are found exclusively within this cataclastic BSF and do not crosscut the younger gouges (BSF III, IV and V). The fine-grained, weakly foliated greenish gouge (BSF III, Fig. 4.3c) cuts the green cataclasite (BSF II) and the associated system of fractures.

White, undulating zeolite veins are sub-parallel to the principal slip surface (Fig. 4.2f). These veins are spatially associated with the dark reddish grey gouge (BSF I), cutting the lenses thereof and the weakly foliated gouge around it (BSF III). Both lenses and veins are, in turn, crosscut by sub-vertical fractures, whose geometrical arrangement is consistent with top-to-the-NW extensional shearing.

Two other distinct types of clay-rich gouge occur in the inner part of the core. A green-grey and plastic gouge variety is preserved exclusively at the north-western exposed termination of the fault, geometrically below the principal slip surface (BSF IV, Fig. 4.3d). Finally, the BSF V is represented by the smear of dark, clay-rich gouge along the principal slip surface (Fig. 4.3e), which forms a laterally continuous 2-3 mm-thick layer and cuts all the BSF described above (Fig. 4.3f).

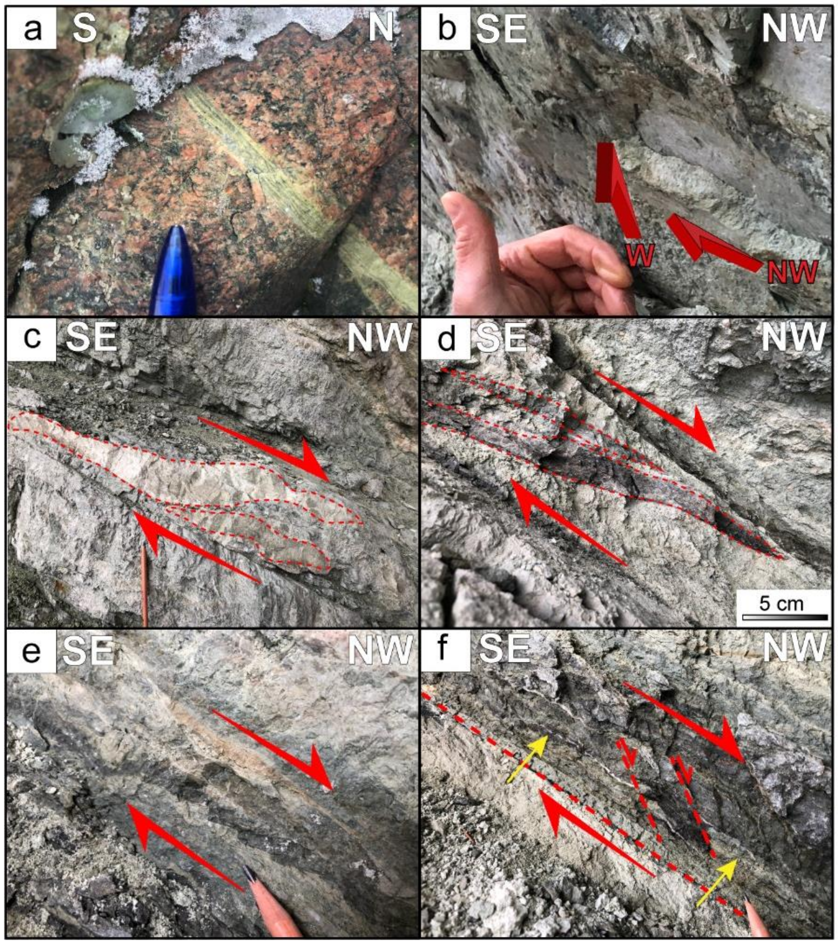

Figure 4.2 - Structural features of the LGF. a) Cm-thick epidote and quartz vein cutting across the hanging wall monzogranite; b) upper secondary slip surface. The red arrows represent the direction of slip of the missing block, i.e., the footwall, according to the slickenlines; c) white sigmoidal lenses of cataclasite embedded by the pale green cataclasite (BSF II) constraining a top-to-the-NW sense of shear; d) top-to-the-NW sigmoidal lens of dark reddish grey indurated gouge (BSF I) embedded within a weakly foliated gouge (BSF III); e) extensional top-to-the-NW bookshelf structures within dark competent reddish grey gouge (BSF I); f) lens of dark reddish grey indurated gouge (BSF I) cut by Riedel fractures. Both the reddish gouge and the host fault rock contain white, undulate zeolite veins subparallel to the principal slip surface, marked by yellow arrows.

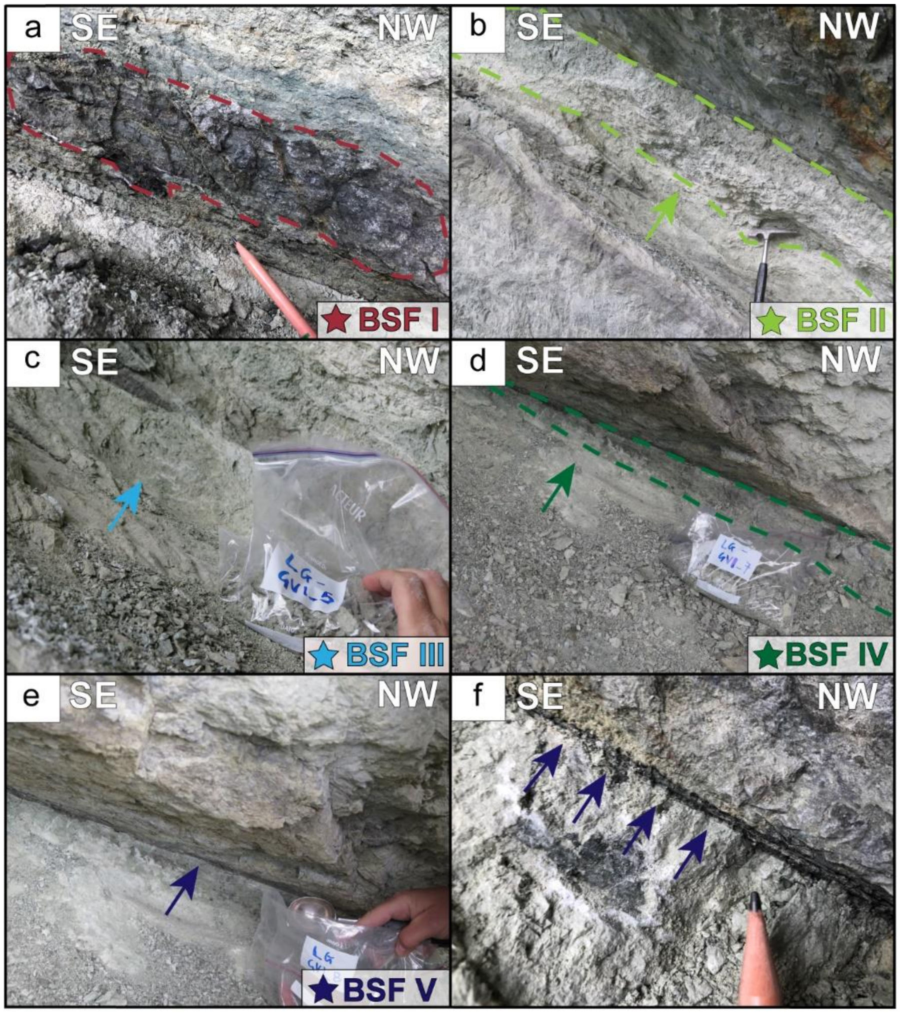

Figure 4.3 - Different brittle structural facies of the fault core and their representative samples for K-Ar dating. The colours of the labels from "a" to "e" are the same of Fig. 4.2. a)BSF I, lens of dark reddish grey indurated gouge; b) BSF II, pale green cataclastic brittle domain representing the most common portion of the fault core; c) BSF III, green, weakly foliated gouge embedding a lithon of BSF I; d) BSF IV, clay-rich gouge preserved just below the principal slip surface of "e" and "f"; e) BSF V, dark smear of black gouge representing a laterally continuous, only a few mm-thick layer along the principal slip surface (f).

4.4.2 Microstructural analysis

The damage zone in the hanging wall is mainly composed of proto-cataclastic to ultracataclastic rocks (Fig. 4.4b). They are formed at the expense of a mylonitic gneiss (Fig. 4.4a) made of quartz-feldspar ribbons wrapped around by chlorite and epidote-rich layers along the foliation (Fig. 4.4a, b). Quartz grains in the mylonitic domains are a few to tens of µm in size, have lobate boundaries and diffuse undulose extinction. Feldspars are commonly altered to sericite. Relict nuclei of K-feldspar with exsolution lamellae occur in the centre of sigmoidal lithons, embedded within the foliation (Fig. 4.4a). An early generation of coarse epidote is overprinted by a subsequent finer-grained generation. The evidence of brittle deformation intensifies toward the core as documented by increased fracture density and the occurrence of discrete gouge levels composed of fine-grained epidote, clay, and opaque minerals (Fig. 4.4b).

Rocks in the fault core form a heterogeneous fault rock assemblage from a microstructural point of view. The dark reddish grey indurated gouge (BSF I) is mainly composed of ultrafine-grained feldspar and clay minerals. Additionally, it exhibits rounded glassy and microcrystalline domains, containing spherulites varying in diameter from 5 to 10µm (Fig. 4.4c). Consistent with the common interpretation of spherulites as diagnostic textures of frictional melts (e.g., Lin, 1994; Di Toro and Pennacchioni, 2004), we interpret these domains as heavily reworked and transposed clasts of pseudotachylyte veins, now preserved in the reddish gouge (BSF I).

The pale green cataclasite (BSF II), which forms the thickest portion of the LGF core, is composed of different domains and types of clasts (Fig. 4.4d, e). These clasts are embedded within an ultracataclastic and locally weakly foliated matrix (Fig. 4.4e) consisting of plagioclase, quartz, epidote, smectite and titanite. All clasts are invariably cut by Fe-chlorite and K-feldspar veins (Fig. 4.4f), themselves transposed and reworked in the ultracataclastic matrix. Some clasts are foliated and made of tightly spaced bands enriched in quartz and feldspars alternated with epidote-rich layers (Fig. 4.4d). The foliation in these clasts and the evidence of crystal-plastic deformation suggest that they are derived from the host rock mylonite.

Other clasts within the pale green cataclasite are, instead, remnants of earlier generations of brittle fault rocks. Dark reddish, very fine-grained clasts are interpreted to be derived from BSF I. Some clasts in the pale green cataclasite, moreover, contain a fine-grained matrix embedding variably sized, reworked sub-rounded quartz and plagioclase (Fig. 4.4d, f). Tiny K-feldspars, smectite, smectite-illite, plagioclase, apatite, quartz, oxides, and Fe-sulphides form the matrix (Fig. 4.4d, f).

1 to 5 mm-thick zeolite veins cut across the fault core (BSF I, II and III) but are absent in the gouges along the principal slip surface. Zeolite forms either euhedral or stretched fibres elongated perpendicular or at high angle to the vein walls. Randomly oriented laumontite crystals are found in dilatant domains around angular clasts of earlier generations of fault rocks (Fig. 4.4g).

Vertical and sub-vertical calcite veins strike NE-SW and have a variable thickness between 10µm, and a few mm. Fibrous calcite crystals are oriented WSW-ENE/W-E, at high angle to the vein boundaries (Fig. 4.4h). In some veins, they exhibit tabular, thin twins (type I), indicating deformation temperatures $<200^{\circ}$C (Ferrill et al., 2004). A second episode of calcite crystallisation occurred after the formation of the zeolite veins, i.e., after the formation of the weakly foliated gouge (BSF III), and before the last slip event along the principal slip surface.

In summary, microstructural observations constrain an increasing intensity of brittle deformation toward the LGF core. Mylonite-and different generations of reworked cataclasite/gouge clasts indicate a polyphase deformation history. Clasts of pseudotachylyte reworked within the indurated fault gouge prove the coseismic character of at least one of the early deformation events.

Microstructural analysis and the observed crosscutting relationships permit constraining the following temporal sequence of veining, from old to young: 1) Pervasive chaotic system of epidote and quartz veins within the damage zone (Fig. 4.2a). Fault rocks of the LGF core contain fractured and transposed lenses of these epidote-rich domains.; 2) Chlorite and feldspar-rich veins cutting across an early generation of fault gouge, now only preserved as clasts in the fault core rocks (Fig. 4.4f); 3) Calcite and zeolite veins not affecting the youngest generations of unconsolidated clay-rich gouge (BSF IV and V), and thus predating the last stages of LGF slip (see below).

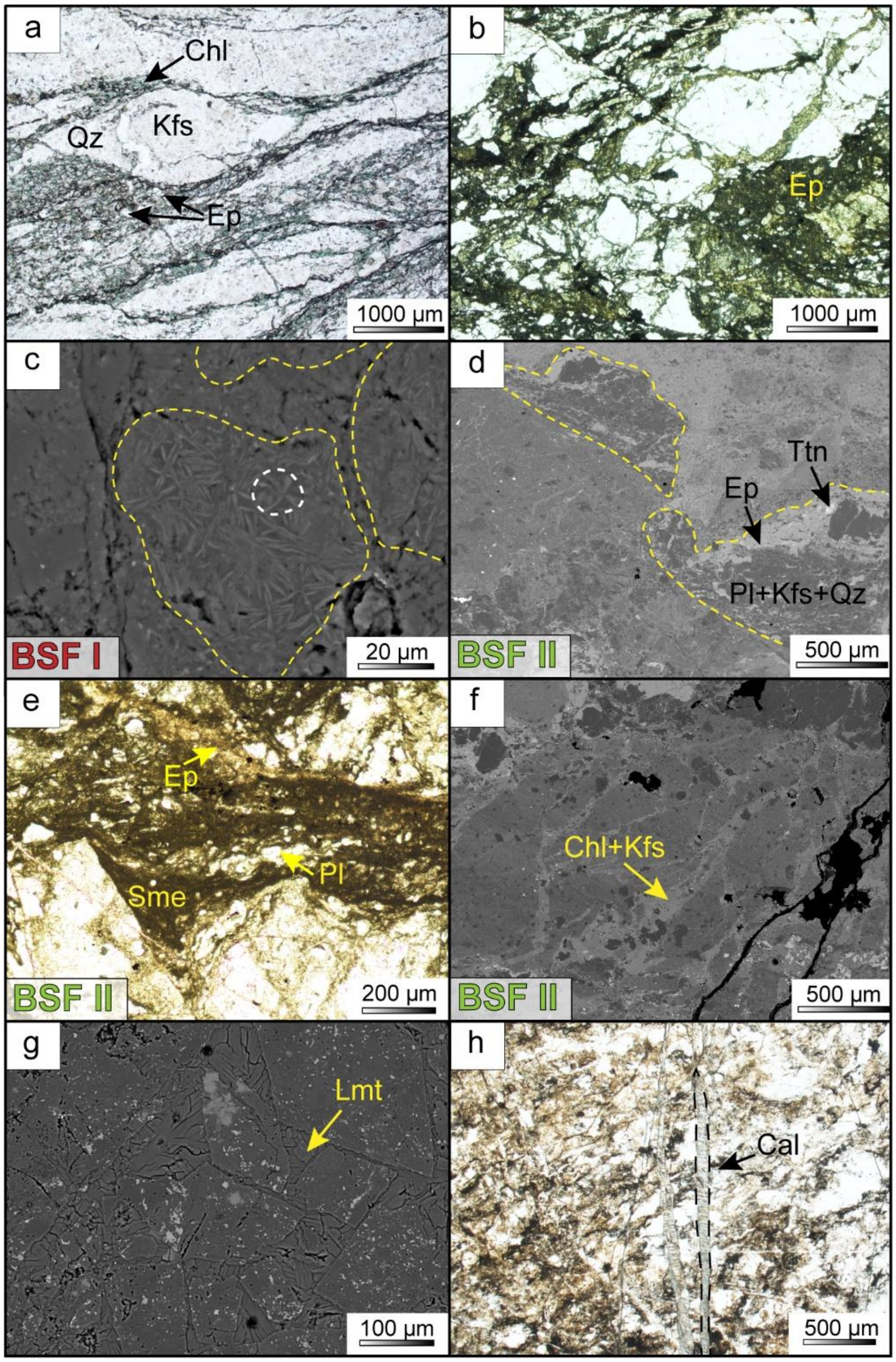

Figure 4.4 - Microphotographs of representative microstructures of the main LGF fault rocks. a) View of thin section cut perpendicular to the foliation and parallel to the stretching lineation. Mylonitic gneiss from the hanging wall of the LGF with quartz-feldspar domains within an epidote and chlorite-defined foliation. A feldspar sigmoidal lens indicates simple shear deformation; b) cataclasite, enriched in epidote, resulting from the hanging wall protolith; note widespread fracturing and the presence of poorly sorted, angular clasts; c-h) views of thin sections cut perpendicular to the fault and parallel to slickenlines; c) SEM image of clasts (in yellow) of spherulites (in white) in a fault gouge matrix, representing heavily transposed and recrystallised pseudotachylyte fragments; d) SEM

image of clasts of different fault rock domains and mylonites (in yellow) embedded within an ultracataclastic matrix within the pale green cataclasite (BSF II); e) microphotograph of the same ultracataclastic matrix of (d) with flow structures; f) SEM image of a gouge clast in BSF II made of feldspars, smectite, quartz and oxides. The clast is cut by Fe-chlorite and K-feldspar veins; g) laumontite crystals around clasts of an early generation of indurated fault gouge; h) fibrous calcite veins parallel to the NW-SE striae. Mineral abbreviations after Whitney and Evans (2010).

4.4.3 Fault rock compositional data

Samples from all the studied BSF have different mineralogical compositions. The relative abundance of mineral phases varies with grain size within the same sample. K-feldspar, epidote, chlorite and smectite occur in all structural facies (Table 4.1). XRD analysis documents a gradual increase of clay minerals towards the finest fractions from a minimum of 4 to a maximum of 44 wt% in the 0.1-0.4µm fractions (e.g., in BSF V the concentration of clay minerals quadruples, Fig. 4.5e). The most abundant clay minerals in the fault core are smectite and illite. TEM analysis confirms the presence of K-bearing phases also in the finest fractions where we could not carry out XRD analysis due to the lack of sufficient material. Illite, mostly Fe-illite, smectite and K-smectite were detected in <0.1µm grain size fraction (Fig. 4.5a-c). K-feldspar is an additional K-bearing phase that is present in all grain size fractions of all samples. At the TEM, euhedral K-feldspar crystals have been documented to also occur in the <0.1µm fraction of BSF I to IV (Fig. 4.5d). XRD and TEM analysis do not document illite in any grain size fractions of BSF III, which, instead, contains smectite and K-feldspar.

In all samples, except that from BSF II, the percentage of K-feldspar decreases towards the finer grain size fractions (Fig. 4.5). In BSF I, K-feldspar ranges between 50 wt% in the coarser and 30 wt% in the 0.1-0.4µm grain size fraction. Similarly, the most clay-rich gouges (BSF IV and V) contain relatively high amounts of K-feldspar, which is still between 27 and 22 wt% in the finest fractions (Fig. 4.5e).

Chlorite is present in all dated fractions and its content tends to increase with decreasing grain size. Plagioclase is not ubiquitous in the samples, but it is one of the main components in BSF II and III. Epidote is a common phase in all BSF, but its content generally decreases with decreasing grain size. It is very abundant (c. 45 wt%) in the foliated greenish gouge of BSF III. Quartz is only sporadically found in BSF III, IV and V, and its concentration decreases steadily with grain size. Two zeolite types occur with different relative abundance, stilbite and laumontite (Table 4.1).

Pyroxene does 1.35not exceed 6% and it is absent in BSF IV, and V. Calcite occurs as an accessory phase.

Table 4.1 - XRD data. Mineral concentrations are given in wt%. GOF represents "Goodness of Fit". "x": unquantified amount.

Sample	Size fraction (µm)	Quartz	K-feldspar	Plagioclase	Illite/Muscovite	Chlorite	Smectite	Stilbite	Laumontite	Heulandite	Epidote	Pyroxene	Calcite	GOF
BSF I	0.1-0.4	-	30	-	-	32	26	-	2	-	4	6	trace?	1.76
	0.4-2	-	40	-	-	27	18	-	2	-	7	6	trace?	1.51
	2-6	-	47	-	-	23	13	-	2	-	10	5	trace?	1.47
	6-10	-	50	trace	-	22	12	-	2	-	9	4	1	1.43
BSF II	0.4-2	-	12	30	trace?	20	8	4	6	trace	16	4	-	1.51
	2-6	-	11	26	-	10	5	8	17	trace	20	3	-	1.46
	6-10	-	10	24	-	8	4	12	21	trace	18	3	-	1.47
BSF III	<0.1	-	-	-	x?	x	x	-	-	-	x	x	-	-
	0.1-0.4	-	9	10	-	36	22	-	trace	-	18	5	-	1.65
	0.4-2	trace	9	17	-	15	11	-	trace	-	43	4	1	1.43
	2-6	1	9	17	-	12	9	-	2	-	45	4	1	1.41
	6-10	1	10	20	-	12	8	-	2	-	42	3	2	1.38
BSF IV	<0.1	-	x	-	x	x	x	-	-	-	x	-	-	-
	0.1-0.4	2	22	-	14	21	29	-	-	-	8	-	3	1.56
	0.4-2	4	33	-	15	13	20	-	-	-	13	-	2	1.42
	2-6	11	37	-	5	11	16	-	-	-	19	-	1	1.37
	6-10	14	35	-	4	11	15	-	-	-	19	-	2	1.35
BSF V	0.1-0.4	-	27	4	30	21	14	-	-	-	4	-	-	1.40
	0.4-2	-	25	5	30	20	15	-	-	-	5	-	-	1.40
	2-6	6	38	6	8	8	5	1	trace	-	28	-	-	1.34
	6-10	7	39	5	5	9	7	1	2	-	25	-	-	1.35

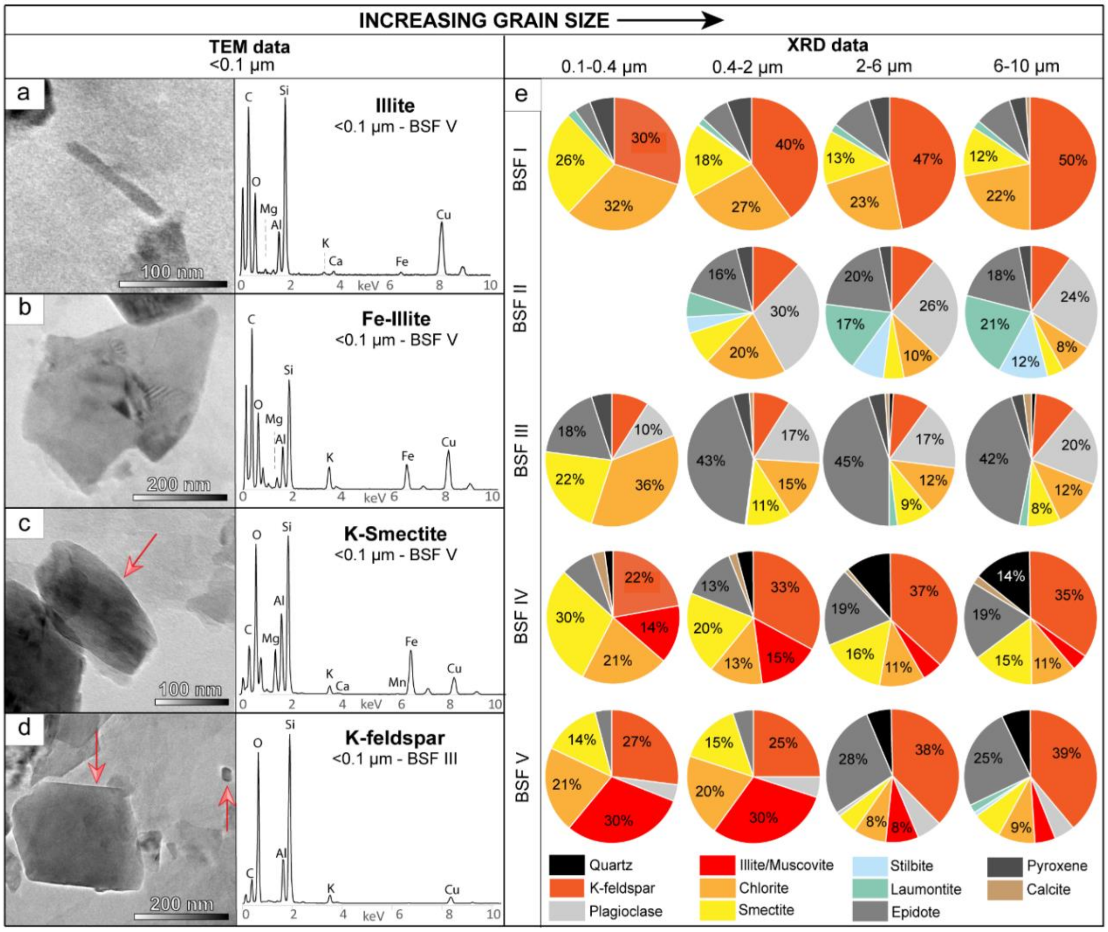

Figure 4.5 - Mineralogical composition of each BSF. a-d) Photos and EDS spectra of K-bearing phases in the <0.1µm fraction by TEM analysis; e) XRD compositional data for each of the studied fractions.

In summary, the general trend of decreasing quartz, epidote, and K-feldspar contents in the finer grain-size fractions (0.1-0.4 and 0.4-2µm) is compensated by the increase of illite, smectite and chlorite. This trend suggests that quartz and epidote are protolithic minerals that did not crystallise during deformation. Pyroxene is a high temperature phase and is thus considered to be inherited in all BSF. The euhedral habit of K-feldspar in the <0.1µm grain size fraction (Fig. 4.5d), however, allows us to deduce that K-feldspar also grew authigenically during faulting. Moreover, the presence of zeolites in BSF I, II and III, which correspond to the most competent rocks in the fault core, allows us to constrain a maximum deformation temperature during faulting of c. 200◦C (Weisenberger and Bucher, 2010). At that temperature, K-feldspar is indeed capable to grow authigenically and synkinematically (Mark et al., 2008; Sasseville et al., 2008; Brockamp and Clauer, 2013).

4.4.4 K-Ar radiometric data

K-Ar ages range from 195 ±4 Ma to 57 ±1 Ma (Table 4.2). Radiometrically determined "age vs. grain size" plots of the dated samples define inclined curves (Fig. 4.6), where the finest grain size fractions yield invariably the youngest ages, and the coarsest fractions (2-6, 6-10 µm) yield the oldest. All the ten ages of the 2-6 and 6-10 µm fractions define a cluster with a mean age of 179 ±2 Ma (MSWD =7.4). The ages of the <0.1µm fraction are 121 ±3, 87 ±2, 78 ±2 Ma, and 57 ±1 Ma. BSF I yielded the oldest <0.1 µm K-Ar age of 121 ±3 Ma; its coarsest grain size fraction (6-10µm) yielded an age of 186 ±4 Ma. The weakly foliated gouge yielded dates between 87 ±2 Ma for the <0.1µm fraction, and of 167 ±3 Ma for the 6-10 µm. The greenish clay-rich gouge yielded dates between 78 ±2 Ma and 184 ±4 Ma for the <0.1 and 6-10 µm fractions, respectively. In BSF V, the <0.1µm fraction yielded the youngest age of the entire dataset at 57 ±1 Ma.

For the greenish cataclasite (BSF II) we could not date the <0.1µm fraction; the 0.1-0.4µm fraction yielded a date of 132 ±3 Ma, which progressively increases towards the 6-10µm fraction and represents the oldest age of the entire dataset at 195 ±4 Ma. In the "age vs. grain size fraction" diagram of Fig. 4.6 the pale green line referring to BSF II can be traced between 121 and 87 Ma for the finest grain size. This age extrapolation does not follow any analytical constraints. The meso- and microstructural data from BSF II and the crosscutting relationships with the other structural facies allow us to conclude that the pale green cataclasite could be of Late Cretaceous age, i.e., an age between the formation of the reddish indurated- (BSF I) and of the weakly foliated gouge (BSF III).

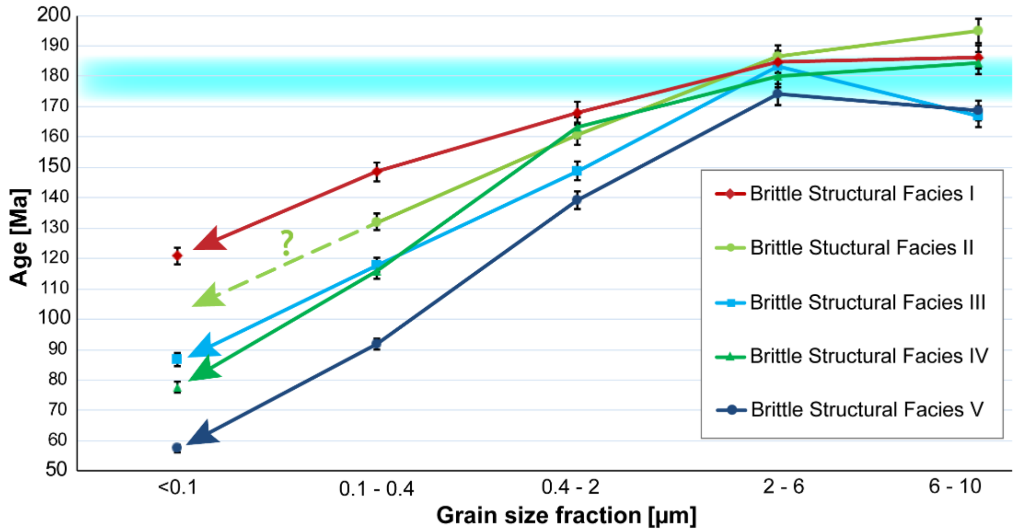

Figure 4.6 - K-Ar age vs. grain size diagram, showing inclined age curves for all samples. A mean age of c. 179 ± 2 Ma is computed for the two coarsest fractions of all samples, highlighted by the light blue bar.

Table 4.2 - K-Ar radiometric data and ages for each grain size fraction of the samples.

Sample Parameters			$^{40}Ar^*$			K		Age Data	
Sample	Size fraction (µm)	Mass (mg)	$^{40}Ar^*$ (mol/g)	σ (%)	$^{40}Ar^*$ (%)	K (wt %)	σ (%)	Age (Ma)	σ (Ma)
BSF I	<0.1	0.72	2.73E-10	0.99	62.1	1.261	2.00	120.8	2.7
	0.1-0.4	2.50	6.58E-10	0.34	87.8	2.452	2.00	148.5	3.0
	0.4-2	3.25	1.18E-09	0.31	92.5	3.877	2.00	168.1	3.4
	4-6	4.36	1.58E-09	0.30	97.8	4.685	2.00	184.8	3.7
	6-10	3.73	1.76E-09	0.31	98.5	5.171	2.00	186.3	3.8
BSF II	0.1-0.4	1.92	2.44E-10	0.48	93.6	1.028	2.00	132.0	2.7
	0.4-2	2.23	3.95E-10	0.38	78.4	1.356	2.00	160.7	3.3
	4-6	7.56	4.51E-10	0.29	96.3	1.324	2.00	186.4	3.8
	6-10	8.72	4.46E-10	0.29	93.9	1.250	2.00	194.9	3.9
BSF III	<0.1	2.23	4.89E-11	1.44	18.4	0.318	2.00	86.6	2.1
	0.1-0.4	3.69	1.66E-10	0.39	59.2	0.789	2.00	117.7	2.4
	0.4-2	3.30	2.77E-10	0.35	80.6	1.029	2.00	148.8	3.0
	4-6	2.04	3.45E-10	0.40	86.1	1.031	2.00	183.2	3.7
	6-10	3.39	3.39E-10	0.34	91.2	1.119	2.00	166.8	3.4
BSF IV	<0.1	1.32	1.14E-10	1.07	20.2	0.830	2.00	77.7	1.8
	0.1-0.4	3.13	3.2E-10	0.35	57.0	1.543	2.00	115.8	2.4
	0.4-2	3.23	9.09E-10	0.31	81.4	3.071	2.00	163.0	3.3
	4-6	5.61	1.29E-09	0.29	93.6	3.927	2.00	179.8	3.6
	6-10	3.46	1.28E-09	0.31	92.1	3.793	2.00	184.3	3.7
BSF V	<0.1	1.32	1.29E-10	0.96	49.4	1.278	2.00	57.4	1.3
	0.1-0.4	1.70	4.32E-10	0.42	78.3	2.639	2.00	91.9	1.9
	0.4-2	1.79	9.99E-10	0.37	91.5	3.983	2.00	139.1	2.8
	4-6	4.73	1.28E-09	0.30	97.5	4.034	2.00	174.1	3.5
	6-10	2.62	1.26E-09	0.33	96.4	4.115	2.00	168.7	3.4

4.5 Discussion

4.5.1 Interpretations of the new K-Ar dates

The “age vs. grain size” curves obtained during this study (Fig. 4.6) are conceptually identical to those produced by other K-Ar geochronological studies of fault-related rocks (Pevear, 1999; Zwingmann and Mancktelow, 2004; Bense et al., 2013; Davids et al., 2013; Yamasaki et al., 2013; Torgersen et al., 2015a; Viola et al., 2016; Aldega et al., 2019). Such inclined curves are generally interpreted as recording variable contamination of the authigenic and synkinematic mineral phase separates by inherited protolithic minerals, mixing of different generations of authigenic minerals, and grain-size-dependent 40Ar loss (van der Pluijm et al., 2001; Verdel et al., 2012; Torgersen et al., 2015a, b; Viola et al., 2016; Vrolijk et al., 2018).

Since brittle faulting is dilatational and may thus enhance the ingress of fluids into the actively deforming rock volume, synkinematic formation of new phases and/or recrystallisation of pre-existing minerals (or parts thereof) is common (Haines and van der Pluijm, 2008; Tagami, 2012; Vrolijk et al., 2018). Newly crystallised minerals will be the most abundant in the finer grain size fractions. Even the finest grain size fractions, however, may still include inherited protolithic minerals or different generations of authigenic phases reworked during multiple stages of deformation. Ages obtained from the finest grain size fractions should thus be still considered as maximum ages, although they provide the best available constraint on the timing of the most recent faulting event the rock recorded (van der Pluijm et al., 2001; Zwingmann and Mancktelow, 2004; Torgersen et al., 2015b; Viola et al., 2016).

The coarser grain size fractions, on the contrary, are enriched in protolithic (inherited) minerals, such as, for example, older generations of K-feldspar. If the coarser grain sizes of different samples from one single fault zone yield the same age, it is reasonable to conclude that they constrain a common thermal or faulting event. Such an early event likely occurred at higher temperature than the more recent ones recorded by the finer fractions (e.g., Viola et al., 2016; Vrolijk et al., 2018; Scheiber et al., 2019). The intermediate grain size fractions (0.4-2 and 2-6µm) generally define a trend of decreasing age with decreasing grain size, as they result from the mixing of different (synkinematic and protolithic) grains with varying isotopic signatures and are, therefore, commonly devoid of a real geological meaning.

In agreement with our compositional data, we adopt the Age Attractor Model (Torgersen et al., 2015a, b; Viola et al., 2016) and thus rely on the concept of progressively increasing amounts of authigenic and synkinematic K-bearing phases with decreasing grain size, such that we consider the finest fractions as mainly composed of authigenic, synkinematic minerals.

In this study, the ages of all BSF of the fault core span the c. 195 to 57 Ma time interval. Interestingly, there are no ages older than 195 ±4 Ma (Jurassic). The Jurassic mean age of 179 ±2 Ma calculated from all the 2-6 and 6-10μm grain size fractions cannot be related to the age of the host rock, because the youngest host rock in Lærdal is Cambrian (Milnes and Corfu, 2011; Corfu et al., 2014). The c. 180 Ma age might, therefore, be interpreted as resulting from a major deformation event and be related to the initiation of brittle faulting along the LGF. The Jurassic and Early Cretaceous activity of the LGF was already constrained by previous authors by different dating techniques (Andersen et al., 1999; Fossen et al., 2016). Our obtained range of ages is comparable with results of Fossen et al. (2016), who documented ages between 191 and 64 Ma for the 2-6μm and <0.2μm fractions from the fault core of the LGF. From the common Jurassic age cluster of Fig. 4.6, each dated BSF follows a different "age vs. grain size" path. Post-Jurassic deformation and/or fluid ingress did thus not cause pervasive illite recrystallisation up to the coarsest fractions, which still yield their original Jurassic age, but instead synkinematic growth of illite up to the <2μm grain size fractions. These results document therefore the evolution of rocks, which, from a single initial radiometric signature recorded at higher temperature, responded differentially during several later episodes of deformation. In fact, each BSF tracks one of the subsequent deformation events with their specific compositional, structural, and isotopic signatures (see Viola et al., 2016, their Fig. 5).

The K-Ar dating approach to brittle faults is generally applied on clays separated from fault rocks (van der Pluijm et al., 2001; Zwingmann and Mancktelow, 2004; Tagami, 2012; Vrolijk et al., 2018). TEM analysis is crucial to identify all K-bearing phases present in the finest fractions, such as illite, smectite and K-feldspar as they could either be simply inherited from the host rock and isotopically reset during faulting or be of authigenic, synkinematic origin (Mark et al., 2008; Sasseville et al., 2008; Surace et al., 2011; Torgersen et al., 2015b). Microstructural, compositional, and thermochronological data from the LGF suggest that the temperature did not exceed 200◦C during the Cretaceous (Ferrill et al., 2004; Weisenberger and Bucher, 2010;

Johannessen et al., 2013). The Ar closure temperature for 1µm illite/muscovite and K-feldspar grains is generally c. 210-250 °C (Kelley, 2002; Verdel et al., 2012; Torgersen et al., 2015a). Thus, thermally induced volume diffusion effects, which could have reset the isotopic clock of the finest grain size fractions, are not considered in our interpretative model. Moreover, TEM images document the presence of authigenic Late Cretaceous K-feldspar, proving that it is indeed a synkinematic phase in the finest grain size fractions (see Torgersen et al., 2015a).

4.5.2 Fault evolution

In order to reconstruct the LGF evolution, being able to assign a K-Ar date to each recognised BSF allows us to correlate the age of K-bearing mineral authigenesis with a specific brittle deformation event. Microstructural observations indicate that the LGF grew in response to widespread cataclastic flow and fracturing superposed on an earlier ductile precursor. The presence of mylonite clasts and multiple generations of cataclasite/gouge support the interpretation of a polyphase deformation history. Additionally, the different composition of each BSF suggests that the LGF has deformed different lithologies and units during its multiple reactivations.

In the following, we deconvolve the LGF deformation history and propose a time-constrained conceptual model for the fault (Fig. 4.7). The brittle fault partially reworked a precursor ductile shear zone (Fig. 4.7a). Deformation was likely associated with diffuse seismicity, generating pseudotachylytes. Crustal-scale extension caused the exhumation of deep crustal blocks and their progressive transition, while *en-route* to the surface, to colder and shallower conditions. Syndeformational fluid circulation created a pervasive network of epidote and quartz veins cutting through the mylonites and the proto-cataclasite that, by then, had formed mainly at the expense of the hanging wall sequence (Fig. 4.7a). Cross-cutting relationships visible at the outcrop permit to conclude that the c. 121 Ma old dark reddish grey and indurated gouge (BSF I) represents the oldest BSF preserved in the fault core. Its composition, with up to 50% K-feldspar in the coarsest grain size fraction, suggests that it formed at the expense of a K-feldspar-rich rock. Deformation and the ingress of fluid allowed the crystallisation of a clay-rich gouge with smectite, illite and chlorite, also embedding clasts of reworked pseudotachylyte (Fig. 4.7b). The remarkable hardness of the preserved lenses of this gouge, compared to the surrounding parts of the fault core, could be due to early induration processes by, for example, zeolite crystallisation (Table 4.1, Fig. 4.4g, Olsen et al., 1998). The early induration likely induced mechanical hardening of the fault core, requiring further deformation to affect a progressively wider volume of the rock by propagating into the hanging wall and footwall mylonites (Fig. 4.7c). A renewed episode of deformation formed the pale green cataclasite (BSF II), composed of heterogeneous clasts of older fault rocks (Fig. 4.7c). The finest grain size fraction (<0.1µm) of the pale green cataclasite contained insufficient material for K-Ar analysis, but relative chronological constraints at the outcrop and microstructural evidence suggest that this BSF formed in the Late Cretaceous (Fig. 4.6, see Section §4.4.4). This BSF is cut by NNE-SSW striking fractures, locally filled with calcite. The orientation of these fractures and veins constrains WNW-ESE extension, which is in agreement with the dominant normal kinematics of the fault. These fractures do not crosscut the younger gouges (BSF III, IV and V), indicating that BSF III to V postdate fracturing and the associated early calcite veining.

At c. 87 Ma a weakly foliated gouge formed in the centre of the fault core (BSF III, Fig. 4.7d). This Cretaceous and the following episodes of slip, up to the probable locking and healing of LGF at c. 57 Ma, were characterised by the narrowing of the active deformation zone. Fault narrowing was likely due to the progressive accumulation of clays in the core, and to the decreasing deformation temperature (Rutter et al., 2001; Scheiber et al., 2019). Slip was accommodated by the formation of a weakly foliated gouge and by the nucleation of Riedel shears in the consolidated fault facies (BSF I and II). BSF II and III contain plagioclase, K-feldspar, and pyroxene, such that they probably derive from a mangeritic protolith of the Jotun Nappe Complex (Milnes and Corfu, 2011; Corfu et al., 2014). Interestingly, the foliated gouge of BSF III does not contain illite but smectite and K-feldspar. Almost identical amounts of K-feldspar are documented in all grain size fractions (c. 9-10%), because of its relative enrichment due to synkinematic neoblastesis.

In agreement with the discussed scenario of decreasing temperature through time, the progressive evolution of the fault caused the formation of unconsolidated, extremely localised fault gouges (BSF IV and V) in the centre of the core. BSF IV and V are distinctly different from the older brittle facies as they include significant amounts of smectite and illite. A green-grey gouge enriched in synkinematic illite, smectite and chlorite formed at 78 Ma (Fig. 4.7e). Finally, a thin, laterally continuous smear of dark gouge cut across all BSF, constraining a last transtensional top-to-the-W increment of faulting of the LGF at 57 Ma (Fig. 4.7f). The likely very low permeability of clay-rich gouge (Evans et al., 1997; Faulkner and Rutter, 2003) suggests that crystallisation of illite and smectite occurred during faulting and not during post-deformational alteration. There is no evidence of other significant deformation episodes affecting the Paleogene clay-rich smear, and we conclude that the LGF ceased its (recorded) activity c. 57 Ma ago.

4.5.3. Regional implications

Our new dataset has also implications for the regional geological framework. The obtained LGF geochronological results do not record any evidence of fault activity prior to the Jurassic (Table 4.2), questioning whether this fault is indeed a Devonian structure (Corfu et al., 2014; Fossen et al., 2016). Lack of Palaeozoic ages in the studied BSF could be due to (1) selective sampling that would have missed potential pre-Jurassic domains, (2) Ar-loss or thermal effects, or (3) obliteration of any pre-Jurassic isotopic signal in all grain size fractions. Our structural characterisation, however, was detailed and thorough and we sampled all BSF recognised at the main LGF outcrop. The LGF is a very long brittle structure (Andersen et al., 1999) and we cannot exclude the possibility that Pre-Jurassic ages, if present, may be preserved elsewhere along the fault strike. Ar-loss or thermal effects can be considered unlikely in a system that underwent progressive cooling to below 250◦C from the Devonian onwards (Johannessen et al., 2013; Walsh et al., 2013; Ksienzyk et al., 2014, 2016 and references therein). As previous studies demonstrate, even in very highly strained and multiply activated faults, earlier slip events are not completely obliterated, and they may be resolved by K-Ar dating of the coarser grain size fractions (Viola et al., 2016). As a consequence, Devonian to pre-Jurassic K-Ar ages, if ever present, would have most probably been preserved in the fault and detected during this study (cf. Torgersen et al., 2015a). However, if the brittle LGF did accommodate a Palaeozoic history, it is likely that the structural and isotopic evidence thereof is preserved only in the cohesive cataclasites and proto-cataclasites of the damage zone, which we did not date, and not in the fault core (e.g., Scheiber et al., 2019).

The LGF preserves evidence of at least five geological significant (re)activation episodes (from the Jurassic to the Paleogene), with indications of coseismic rupturing. Pseudotachylyte developed likely during the Jurassic or the possible earlier localisation history of the LGF. The oldest recorded event at c. 180 Ma could represent crustal stretching associated with the second phase of the North Sea rifting (Gabrielsen et al., 1999; Fossen et al., 2016; Viola et al., 2016). The Cretaceous events at c. 121, 87 and 78 Ma can be related to the hyperextension accommodation along the Mid-Norwegian margin during progressive cooling and exhumation (cf. Fossen et al., 2016; Ksienzyk et al., 2016; Scheiber and Viola, 2018, their Fig. 13). The last recorded Paleogene event (c. 57 Ma), documented by the laterally continuous clay smear along the principal slip surface, likely sealed the fault. The tectonic phase expressed by this geological feature remains, however, poorly constrained, even though other K-Ar Paleogene faulting ages are reported from southwestern Norway (Fossen et al., 2016; Scheiber et al., 2019).

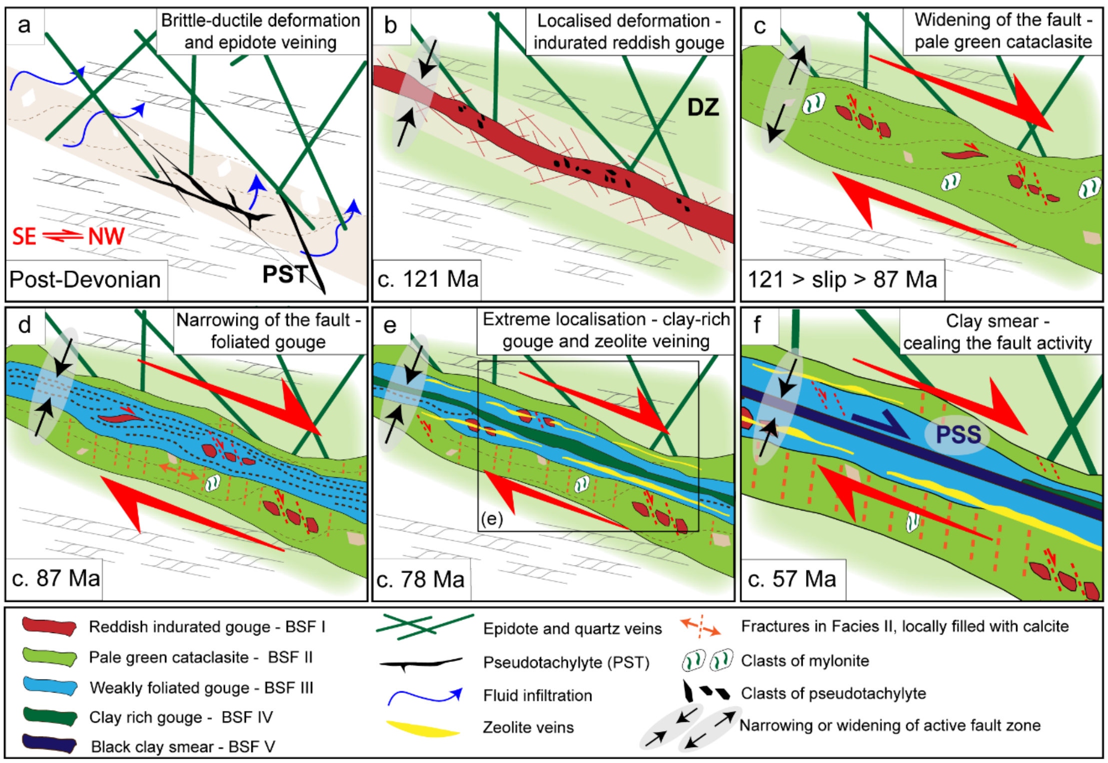

Figure 4.7 - Conceptual model of LGF evolution through time. a) Pseudotachylyte formed during coseismic rupturing, and an earlier fault zone formed at the expense of a mylonitic shear zone. Fluid infiltration created a network of epidote and quartz veins; b) deformation and fluid ingress led to the formation of a dark reddish grey, indurated gouge and caused overall strengthening of the fault core. The gouge embeds clasts of pseudotachylyte; a fracture-rich damage zone (DZ) formed; c) renewed cataclasis affected the previously formed BSF and the host rock leading to the widening of the active fault zone and the formation of the pale green cataclastic facies in the Late Cretaceous; d) at c. 87 Ma a weakly foliated gouge developed in the inner part of the fault core, leading to the progressive narrowing of the active zone; e) extreme localisation led to the formation of a green-grey gouge highly enriched in clay minerals; f) a thin, laterally continuous smear of dark gouge cut across all the other BSF, accommodating a last transtensional top-to-the-W increment of faulting at c. 57 Ma.

4.6 Conclusions

We have presented a methodological approach that is of general validity and that can aid when reading geological archives stored in brittle faults. The present-day LGF core exposes the tight juxtaposition of several BSF. Each BSF is defined by specific fault rocks and is characterised by a unique isotopic signature, fully resolvable by K-Ar geochronology. This study also confirms that extreme localisation of strain, associated with synkinematic (re)crystallisation is indeed a common process within brittle faults (cf. Torgersen et al., 2015a; Viola et al., 2016; Scheiber et al., 2019). The concept of BSF can thus be very useful when characterising complex faults, because BSF can help resolve the spatial and temporal deformation history of fault zones in multiply deformed bedrock terranes, which have experienced both ductile and brittle deformation. Additionally, BSF can be an important tool to investigate and constrain in time the diachronic and heterogeneous evolution of fault cores.

Appendix A

The mineralogical composition of all grain size fractions was studied with X-ray diffraction (XRD). Randomly oriented samples were prepared by side-loading and analysed with a Bruker D8 Advance X-ray diffractometer operating with a Cu X-ray tube (40 kV/40 mA) and Lynxeye XE detector. XRD scanning was performed from 3 to 75° 2θwith a step size of 0.02°2θ, a measurement time of 1 s per step, and rotation speed of 30◦per minute. Fixed divergence had an opening of 0.6 mm and primary and secondary soller slits were 2.5◦. A knife edge was used to reduce scatter radiation. Mineral identification was carried out with the automatic and/or manual peak search-match function of Bruker's Diffrac.EVA V4.2 software using both Crystallographic Open Database (COD) as well as the PDF 4 Minerals database from the International Centre for Diffraction Data (ICDD). For further clay minerals study, oriented mounts of fractions 2-6µm were prepared by letting 1 ml of sample suspension dry out on a glass slide. These slides were measured from 2 to 40°2θat room temperature, after treatment with ethylene glycol for 24 h, and after heating at 550 °C for 1 h.

The procedure followed to perform K-Ar dating of each grain size fractions starts with packing aliquots of air-dry clay samples in molybdenum foil. They are weighed using a Mettler Toledo XPE26DR microbalance, with a resolution of 2µg and a combined weighing uncertainty of 4µg. Samples are degassed at 1400 °C for 10 minutes. The evolved gas is spiked with a known amount of isotopically pure 38Ar and purified in two stages with a Titanium Sublimation Pump and a combination of two SAES GP50 ST101 getters, one at 300◦C and one at 22 °C. The purified argon is analysed in static vacuum in an IsotopX NGX multicollector noble gas mass spectrometer using faraday cups with 1012Ω amplifiers for 38Ar and 36Ar and a 1111Ω amplifier for 40Ar; the gas is analysed for 600 integrations of 1 second. Baseline corrected volts are regressed back to inlet time using an exponential best fit regression function. Blanks are run periodically. Mass bias corrections are performed using a power law on blank corrected intercept values by using within batch air analyses compared with the atmospheric 40Ar/36Ar composition of 298.56 ±0.31 (Lee et al., 2006). The 38Ar spike is calibrated using HD-B1 biotite (Fuhrmann et al., 1987) with a 40Ar* concentration of 3.351 ×10-11mol/g (Charbit et al., 1998). Long term reproducibility of many aliquots of HD-B1 biotite is better than 0.3% RSD.

Potassium concentrations are determined by fluxing approximately 50 mg of clay sample in lithium tetraborate. The resulting glass is dissolved in HNO3spiked with a known concentration of Rh as internal standard. The K concentration is analysed using a Perkin Elmer Optima 4300DV ICP-OES. The uncertainty of K determination is estimated from evaluating the accuracy of several whole rock standards with similar K concentration range and is better than 2%.

Radiogenic 40Ar* concentrations, relative uncertainties, and K-Ar ages are calculated using the equation of Hałas and Wójtowicz, (2014), using the decay constants of Renne et al. (2011).

Chapter 5

Time-constrained multiphase brittle tectonic evolution of the onshore mid-Norwegian Passive Margin

Giulia Tartaglia, Alberto Ceccato, Thomas Scheiber, Roelant van der Lelij, Jasmin Schönenberger, Giulio Viola

Under review in GSA Bulletin

Abstract

The mid-Norwegian Passive Margin (MNPM) is a multiphase rifted margin developed since the Devonian. Its geometry is affected by the long-lived activity of the Møre-Trøndelag Fault Complex (MTFC), an ENE-WSW oriented regional tectonic structure. We propose a time-constrained evolutionary scheme for the MNPM brittle history. By means of remote sensing lineament detection, field work, microstructural analysis, paleostress inversion, mineralogical characterisation and K-Ar dating of fault rocks, six tectonic events have been identified: i) Palaeozoic NE-SW compression forming WNW-ESE striking thrust faults; ii) Palaeozoic NW-SE transpression forming conjugate strike-slip faults; iii) Carboniferous proto-rifting forming NW-SE and NE-SW striking faults; iv) Late Triassic-Jurassic (c. 202 and 177 Ma) E-W extension forming ca. N-S striking epidote and quartz-coated normal faults and widespread alteration; v) renewed rifting in the Early Cretaceous (c. 122 Ma) with a NW-SE extension direction; vi) Late Cretaceous extensional pulses (c. 71, 80, 86, 91 Ma ago) reactivating pre-existing faults and crystallizing prehnite and zeolite. Our multidisciplinary and multiscalar study sheds light onto the structural evolution of the MNPM and confirms the active role of the MTFC during the rifting stages. Our sixty-two new radiometric K-Ar ages define discrete episodes of faulting along the MNPM. The proposed workflow may assist the interpretation of the structural framework of the MNPM offshore domain and also help to better understand fault patterns of fractured passive margins elsewhere.

5.1 Introduction and aims of the study

Passive margins are major morpho-tectonic features of the Earth resulting from extension within continents and the eventual tearing of continental lithosphere to form plate margins and oceanic basins. In addition to the first-order general features common to all margins around the globe, some passive margins may also exhibit remarkable local geological complexities and peculiarities that reflect i) their generally complex polyphase faulting history, with strain and deformation variably distributed in space and through time (Reston, 2005; Duffy et al., 2015; Will and Frimmel, 2018; Phillips et al., 2019; Zastrozhnov et al., 2020); ii) the effects of variably oriented and diachronic subsidiary rifting pulses that pre- and postdate the main rifting phase (Doré et al., 1999; Ren et al., 2003); iii) the effects of the spatial orientation of old, inherited structures, which generally represent zones of mechanical weakness within the crust and tend to preferentially localize rifting (Phillips et al., 2019; Schiffer et al., 2019).

The mid-Norwegian Passive Margin (MNPM) is an archetypal multiphase rifted margin that underwent a progressive evolution from the late orogenic collapse of the Caledonian belt in the Early Devonian down to the Late Eocene (Faleide et al., 2008; Theissen-Krah et al., 2017; Péron-Pinvidic and Osmundsen, 2020). It trends c. NE-SW and its southwestern termination intersects the N-S North Sea margin. Its distinctive oblique geometry compared to the North Sea margin is mainly due to the inherited structural grain of the Møre-Trøndelag Fault Complex (MTFC), an ENE-WSW trending crustal-scale shear zone in mid-Norway (e.g., Bering, 1992; Séranne, 1992; Redfield et al., 2004; Osmundsen et al., 2006; Schiffer et al., 2019; Gernigon et al., 2020; Péron-Pinvidic et al., 2020). While the details of the shear zone's complex faulting history are still being studied and discussed, it is widely accepted that the MTFC has been active at least from the Late Silurian-Early Devonian to the present-day (Séranne, 1992; Braathen et al., 1999, 2002; Osmundsen et al., 2005; Redfield et al., 2005; Sherlock et al., 2004; Nasuti et al., 2011).

The discovery of significant unconventional hydrocarbon reserves within exhumed offshore fractured and weathered crystalline basement blocks of the MNPM (e.g., Petford and McCaffrey, 2003; Riber et al., 2015, 2017; Trice et al., 2019) has caused a surge of interest in the geometry, petrophysical properties and development of intra-basement fracture networks and weathering in the context of passive margin evolution (e.g., Fossen, 2010; Breivik et al., 2011; Riber et al., 2015; Fredin et al., 2017; Scheiber and Viola, 2018; Trice et al., 2019; Fazlikhani et al., 2020; Ceccato et al., 2021a, b). The MNPM is indeed characterized by a dense network of lineaments that are the expression of brittle fault and fracture zones cumulated during the margin's long and multiphase brittle evolution (Gabrielsen et al., 2002). They occur within both on- and offshore basement units (Fredin et al., 2017; Trice et al., 2019). The structural brittle template of the offshore domain has been mainly studied by seismic imaging and drilling. Currently available geophysical techniques permit to only detect fracture and fault zones characterized by minimum detectable throws >5-20 m, the so-called seismic-resolution scale features (Tanner et al., 2019). On the other hand, onshore structural analysis permits to also study smaller brittle features at a sub-seismic resolution scale (Braathen et al., 2004; Redfield and Osmundsen, 2009; Ksienzyk et al., 2016; Scheiber and Viola, 2018; Scheiber et al., 2019; Ceccato et al., 2021a), which are key to the definition of the structural permeability of basement blocks. A detailed study of the brittle fault network exposed on onshore domains and of the related brittle deformation history can, therefore, assist the reconstruction and interpretation of the regional geological framework and evolution of the offshore domain, leading to high-resolution integrated models for the structural evolution recorded by passive margins (e.g., Redfield and Osmundsen, 2009; Ksienzyk et al., 2016; Gabrielsen et al., 2018; Scheiber and Viola, 2018) and better exploration predictive tools.

While decades of petroleum exploration have unveiled the fine details of the regional structure of the offshore domain of the MNPM (e.g., Theissen-Krah et al., 2017; Gernigon et al., 2020; Zastrozhnov et al., 2020 and references therein), so far only a few studies have focused on its onshore counterpart, with the notable exception of the MTFC (e.g., Gabrielsen et al., 1999; Kendrick et al., 2004; Redfield et al., 2004; Osmundsen et al., 2006; Nasuti et al., 2011). Furthermore, although the polyphase evolution of the MNPM is quite well known and established, absolute age constraints on its brittle faulting events are still largely missing, thus preventing detailed reconstructions and correlations along and across the margin.

The intricated network of brittle fractures and faults affecting the offshore MNPM and the lack of well dated sedimentary markers makes retrieving an absolute time sequence for its deformation history a challenging task. All these difficulties notwithstanding, some studies have demonstrated that it is possible to unravel complex brittle histories by studying the details of geometric, kinematic, and geochronological brittle deformation features (e.g., Wilson et al., 2006; Viola et al., 2009; Saintot et al., 2011; Lacombe et al., 2013; Mattila and Viola, 2014; Scheiber and Viola, 2018; Nordbäck et al., 2022). A significant contribution in this respect stems from the possibility to radiometrically date fault rocks associated with key structural features of the margins so as to add absolute time constraints to brittle structural reconstructions (van der Pluijm et al., 2001; Zwingmann and Mancktelow, 2004; Davids et al., 2013; Torgersen et al., 2015; Ksienzyk et al., 2016; Vrolijk et al., 2018; Tartaglia et al., 2020; Fossen et al., 2021).

Aiming at better constraining the evolution of the MNPM, we present the results of a combined multidisciplinary and multiscalar structural-geochronological study focusing on the post-Caledonian evolution of the onshore MNPM and, for the first time, propose a time-constrained evolutionary scheme for its brittle history based on sixty-two new K-Ar ages obtained from some of its representative onshore fault zones. Our conceptual and analytical approach is of general validity and may be useful to unravel complex brittle histories of similar tectonic settings elsewhere.

5.2 Geological Setting

The MNPM forms a 350-500 km wide sector of rifted and hyperextended continental crust facing the Norwegian-Greenland Sea (Northeastern Atlantic Ocean; Fig. 5.1). The studied offshore part of the MNPM is composed of two large segments, which, from SW to NE, include the Møre and the Vøring margins (Fig. 5.1). Discrete, NW-SE-trending tectonic structures, such as the Jan Mayen Corridor, separate these segments (Faleide et al., 2008; Gernigon et al., 2020), each of which contains an inner platform, the Møre, and Vøring Platforms, and a system of outer basins, the Møre and the Vøring Basins (Fig. 5.1). The studied onshore portion of the MNPM between 61° 54' N and 63° 55' N is mainly located within the Western Gneiss Region (WGR), (Fig. 5.1), which is, generally composed of pervasively foliated Proterozoic gneisses locally hosting micaschist, amphibolite and eclogite lenses (Krabbendam and Dewey, 1998; Corfu et al., 2014). The formation of the MNPM results from a long extensional history that started with the collapse of the Scandinavian Caledonides in the Late Silurian-Devonian and continued by deformation localized during discrete tectonic pulses down to the breakup of Greenland from Scandinavia in the early Eocene (Doré et al., 1999; Stemmerik et al., 2000; Faleide et al., 2008; Gernigon et al., 2020). Based on sedimentary and structural observations onshore East Greenland, the initiation of rifting is constrained to the mid-Carboniferous, while it is poorly constrained in the MNPM (e.g., Stemmerik et al., 2000; Rotevatn et al., 2018). By this time, the WGR was exhumed to shallow (<10 km) crustal levels, as inferred from the Early-Middle Devonian (380-400 Ma) muscovite ^{40}Ar-^{39}Ar cooling ages from the area (Kendrick et al., 2004; Walsh et al., 2013).

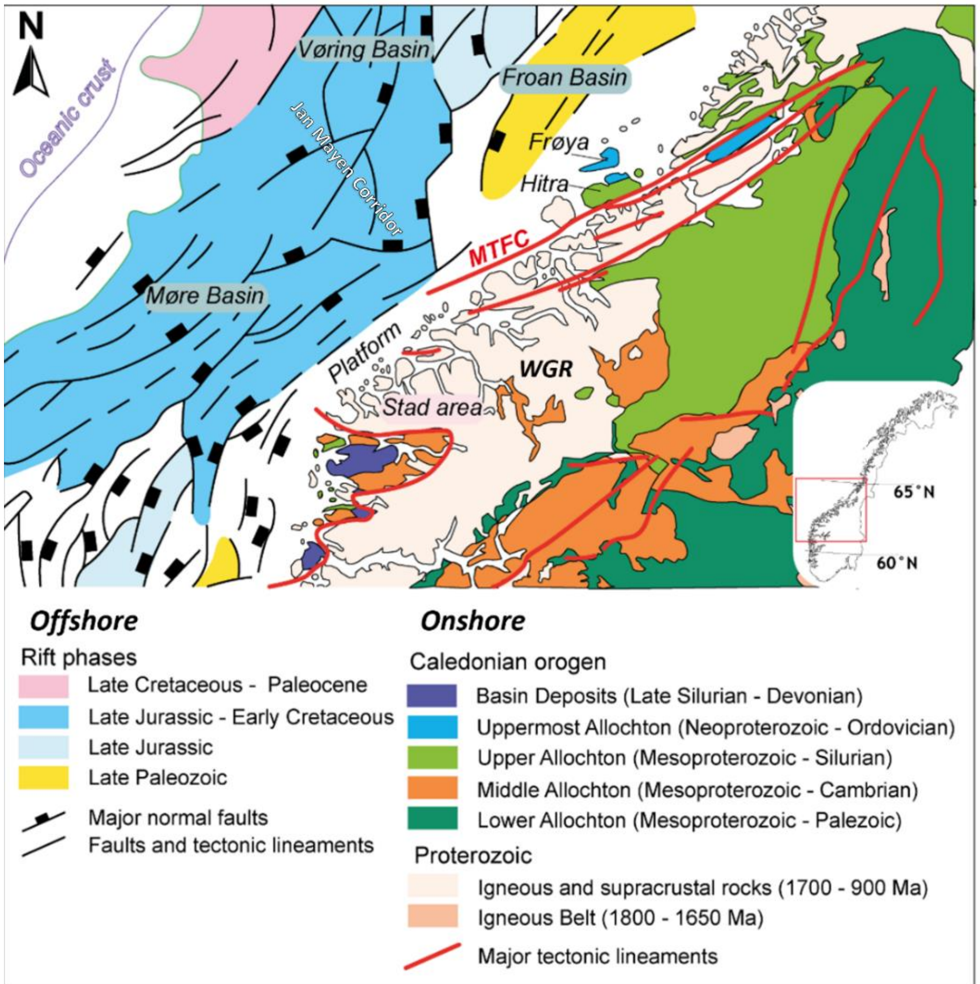

Figure 5.1 - Simplified geological map of the on- and offshore mid-Norwegian Passive Margin. Drawn after Faleide et al. (2008) and Slagstad et al. (2011). (MTFC: Møre-Trøndelag Fault Complex; WGR: Western Gneiss Region).

The MNPM accommodated two main phases of rifting, in the Permo-Triassic and Late Jurassic-Cretaceous, respectively (Gernigon et al., 2020), with its early rifting history strongly controlled by the structural grain inherited from the Caledonian orogen (Doré et al., 1997; Schiffer et al., 2019). During the ENE-WSW-oriented Permo-Triassic rifting phase, the inherited brittle Caledonian fault network was repeatedly reactivated (Faleide et al., 2008). This rifting stage controlled the evolution of the North Sea and the proximal parts of the Vøring margin. (Fig. 5.1). A quiescent post-rift phase ensued and lasted from the Middle Triassic to the Early Jurassic, when the depositional environment in the area changed from marine to coastal (Gernigon et al., 2020). In the Early and Middle Jurassic, intermittent and moderate episodes of E-W crustal stretching occurred (Scheiber and Viola, 2018; Gernigon et al., 2020), leading to the initial development of the Møre and Vøring margins (Fig. 5.1). The Late Jurassic–earliest Cretaceous rifting event is related to the northward propagation of the Atlantic rifting (Lundin and Doré, 2011), when bulk extension shifted to a NW-SE direction and the final opening direction was roughly perpendicular to the present-day coastline (Doré et al., 1999). During this phase, crustal stretching and pervasive faulting created space to accumulate significant Cretaceous syn-rift deposits (Osmundsen and Péron-Pinvidic, 2018; Zastrozhnov et al., 2020; Osmundsen et al., 2021).

During the Cretaceous, the large and deep Møre and Vøring basins formed in the distal part of the MNPM (Fig. 5.1, Blystad, 1995; Zastrozhnov et al., 2020). Both tectonic and thermal subsidence led to the accumulation of up to 8 km thick sedimentary successions in local depocenters. From the Late Cretaceous, the Møre Basin was subjected to thermal subsidence and passive sedimentation without any significant tectonism (Osmundsen and Péron-Pinvidic, 2018; Osmundsen et al., 2021). The Vøring Basin, instead, experienced renewed extension in the Late Cretaceous (Zastrozhnov et al., 2018; 2020; Osmundsen et al., 2021). The final breakup of the NE Atlantic Ocean initiated at 58-57 Ma in the Møre segment of the margin and later propagated northward to the outer Vøring Margin at 56-55 Ma (Ren et al., 2003; Gernigon et al., 2020; Zastrozhnov et al., 2020). Finally, compressional events affected the Vøring Basin from the Eocene to the Pleistocene as indicated by local basin inversion structures and partial reactivation of the faults bordering the many structural highs of the area (Lundin and Doré, 2002; Doré et al., 2008; Zastrozhnov et al., 2020).

The investigated areas include the islands of Hitra, Frøya, and Smøla and the Stad area onshore Norway, located at the transition between the NE-SW oriented MNPM and the N-S oriented North Sea margin (Fig. 5.1). In the northern MNPM, the islands of Hitra and Smøla consist of the 450-428 Ma granitic to granodioritic Smøla-Hitra batholith (Gautneb and Roberts, 1989), attributed to the Upper Allochthon of the Norwegian Caledonides (Fig. 5.1). The batholith is overlain by Late Silurian-Devonian sandstone and conglomerate exposed along the southeastern coast of Hitra. On the northern part of Hitra and on Frøya, micaschist and foliated migmatite of the Uppermost Allochthon are exposed. In the Stad area, the tip of Kråkenes peninsula is composed of a gabbroic enclave within the WGR (*cf*. Krabbendam et al., 2000).

5.2.1 The Møre-Trøndelag Fault Complex (MTFC)

The regional-scale, ENE-WSW Møre-Trøndelag Fault Complex (MTFC) extends onshore for more than 300 km in central-mid Norway before it runs into the Norwegian Sea (Fig. 5.1; Gabrielsen et al., 1999; Redfield et al., 2005; Nasuti et al., 2012). This structure has been related to similarly oriented faults in the Scottish Highlands, such as the Highland Boundary Fault (e.g., Fossen, 2010). In the offshore domain, it separates the Jurassic-Cretaceous North Sea basin system to the south from the wider and deeper Cretaceous basins of the MNPM to the north (Fig. 5.1; Redfield et al., 2005). Onshore, the MTFC crosscuts the Precambrian autochthonous basement and the overlying Caledonian nappes (Corfu et al., 2014). The MTFC consists of different fault strands (e.g., Hitra-Snåsa Fault, Verran Fault), and an enveloping volume of rock deformed by second-order fault zones (Bering, 1992; Séranne, 1992; Redfield et al., 2004, 2005; Osmundsen et al., 2006; Redfield and Osmundsen, 2009). Each fault strand is defined by a several meter thick mylonitic core, superimposed and reworked by brittle fault rocks (Kendrick et al., 2004). The MTFC has been repeatedly reactivated in response to stress regimes varying through time, resulting in a complex finite deformation pattern (e.g., Bering, 1992; Séranne, 1992; Gabrielsen et al., 1999; Redfield et al., 2005; Osmundsen et al., 2006; Nasuti et al., 2011). A possible initial dextral transpression has likely been accommodated by the MTFC in pre-Devonian times (Séranne, 1992). However, overall sinistral ductile Early to Middle Devonian shear is recorded by up to 2 km thick, mylonitic shear zones, as documented by $^{40}Ar/^{39}Ar$ dating of synkinematic white micas (Kendrick et al., 2004). From the Devonian onward, progressive regional exhumation led to the transition into a shallower, brittle deformation regime. Previous studies propose multiple oblique reactivations of the MTFC during the Late Devonian, Permo-Triassic, and Jurassic (e.g., Grønlie and Roberts, 1989; Grønlie et al., 1991; Séranne, 1992; Redfield et al., 2004, 2005). Pseudotachylytes from the Hitra-Snåsa Fault have been dated to the Late Carboniferous-Early Permian by Sherlock et al. (2004). Additionally, the MTFC experienced normal faulting in the Late Jurassic-Early Cretaceous, as well as possible Quaternary post-glacial reactivation (Redfield et al., 2005). The area is still seismically active in an oblique-normal mode (Gabrielsen and Færseth, 1988; Bungum et al., 1991).

5.3. Materials and Methods

We carried out a multidisciplinary and multiscalar study to better constrain the brittle evolution of the MNPM in space and through time. Our approach includes the remote sensing of bedrock lineaments, field structural and microstructural analysis, paleostress inversion, and radiometric K-Ar dating coupled with the detailed mineralogical characterisation of selected fault rocks. In the following we provide details of the used methodologies.

5.3.1 Remote sensing lineament detection

Lineament mapping was performed manually on a grayscale hillshaded Digital Elevation Model (DEM) of the onshore MNPM obtained from high-resolution (1m/pixel) airborne-LiDAR (Light Detection And Ranging) surveys. Grayscale hillshade DEMs with an illumination direction from the NW were used to map the lineaments. Lineaments were mapped at the 1:10.000 and 1:100.000 scales to test the regional significance of local (smaller scale) fracture patterns. The mapped lineaments are regarded as representing the surface expression of fault and fracture zones (*cf.* Gabrielsen and Braathen, 2014; Scheiber et al., 2015). To this purpose, mapping was assisted by and compared with available geological and topographic maps of the region to prevent tracing ductile foliations and shear zones and artificial lineaments (e.g., roads, fences). The strike of the mapped lineaments is displayed in rose diagrams computed with the MARD (Moving Average Rose Diagram) application by Munro and Blenkinsop (2012).

5.3.2 Structural analysis

Field structural analysis focused on the easily accessible coastline of the MNPM, from Hitra in the north to the Stad area in the south (Fig. 5.1). Fieldwork was used to ground truth the remotely detected lineaments. 86 different structural sites from selected key areas of the MNPM were studied by systematically collecting fault-slip data, including information on fracture or fault orientation, slip direction and sense of movement, lithotype, fault rock type, and fracture mineralogy. In some cases, throw and spatial persistence/extension could also be were measured. This fault-slip dataset represents the input data for our paleostress inversion.

In addition, oriented thin sections of selected fault rock samples, cut parallel to the transport direction (fault slip lineation) and perpendicular to the fault plane, were prepared for optical microscopy and petrographic analysis.

5.3.3 Paleostress inversion

Paleostress inversion analysis is useful to reconstruct the orientation of the stress field that caused slip along a given homogeneous set of cogenetic faults. When studying a multiply reactivated and complexly deformed area, paleostress inversion analysis can ideally help to distinguish and reconstruct how the stress field orientation varied through time, during different deformation events. In our study, the collection of fault-slip data included the fault plane orientation, the slip direction and the sense of slip (normal, reverse, dextral or sinistral). Kinematic analysis relied on the growth direction of slickenfibers behind slickensides, Riedel shears and small-scale pull-apart structures (e.g., Hancock, 1985; Petit, 1987).

Starting from the fault-slip data, paleostress inversion calculates the reduced stress tensor that best accounts for an internally homogeneous set of faults. This approach is based on the following assumptions (e.g., Wallace, 1951; Bott, 1959; Twiss and Unruh, 1998; Pollard, 2000; Lacombe, 2012; Lacombe et al., 2013): 1) the observed slip direction is parallel to the maximum shear stress resolved on the fault plane; 2) the faulted volume of rock is physically homogeneous and isotropic; 3) the faulted rock volume has to be large compared to the dimension of the studied faults and a homogenous stress distribution therein is necessary; 4) the studied medium responds to the applied stresses as a rheologically linear material; 5) faults do not mutually interact, and 6) no block rotation occurred at the time of faulting. These assumptions still represent oversimplifications of the complexity of faulting in natural systems and by accepting them we necessarily introduce uncertainties in any paleostress analysis. Moreover, they are only seldomly met when studying complexly fractured basements, where the finite fault and fracture pattern derives from multiple and thus superimposed faulting events. This may result in reduced stress tensors whose definition and interpretation are dubious.

On the other hand, all these uncertainties notwithstanding, several studies have shown that it is possible to obtain consistent paleostress reconstructions even in multiply deformed metamorphic terrains by acquiring a large dataset, carefully sorting statistically fault populations and by validating the results against independent constraints (e.g., Viola et al., 2009; Saintot et al., 2011; Mattila and Viola, 2014).

When dealing with multiple faulting events, the identification of internally consistent subsets of faults separated from the total and heterogeneous available dataset is a fundamental step. A homogeneous set of faults is defined as a group of faults and fractures in any given area that can be genetically bundled together because they formed in response to the same stress field and, as such, they are compatible from a geometric, kinematic and dynamic perspective and have similar fault rock assemblages and mineral coatings. In this study, observations from remote sensing, field constraints and microstructural analysis were considered to sort the total fault-slip dataset into internally consistent subsets of faults from along the studied margin.

The individual fault sets were analysed using the WinTensor software (Delvaux and Sperner, 2003) to obtain their reduced stress tensors. This software iteratively applies an inversion algorithm to search for the state of stress that best accounts for the input fault-slip dataset (e.g., Angelier, 1984; Delvaux and Sperner, 2003). The robustness of the optimization process is measured by the fit between the theoretical slip vectors and those measured in the field (Delvaux and Sperner, 2003). This is achieved by analysing for all faults in a set the misfit angle α, which is defined as the acute angle between the theoretical maximum shear traction vector and the measured slip vector for an individual fault plane. A set of faults can be considered as homogeneous if the slip deviation (the α value) is lower or equal to 30°, a condition that implies that all processed faults are compatible with the calculated stress tensor. If the α value for a given fault is greater than 30°, then that fault is incompatible with the computed reduced tensor, suggesting that it belongs to a different set and that it formed in a different stress field and, thus, during a different deformation episode (Delvaux and Sperner, 2003).

The calculated reduced stress tensor is defined by the orientation of the three main compressional stress axes (σ_1, σ_2, and σ_3, with $\sigma_1 \geq \sigma_2 \geq \sigma_3$) and by the stress ratio R ($R = (\sigma_2 - \sigma_3)/(\sigma_1 - \sigma_3)$) (Angelier, 1984; Lacombe, 2012). To express in a clearer way the stress ratio and the resulting stress regime, we rely on the R' index, which is calculated by R' = R, when σ_1 is vertical (extensional stress regime), R' = 2 – R, when σ_2 is vertical (strike-slip stress regime) and R' = 2 + R, when σ_3 is vertical (compressional stress regime; Delvaux and Sperner, 2003). R' ranges from 0 to 3. R' = 0.5 describes a pure extensional regime, R' = 1.5 describes a pure strike slip regime and R' = 2.5 indicates a pure compressional regime. All the intermediate values indicate a mixed regime, e.g., R' = 1.0 translates to a transtensional regime.

In summary, the reduced stress tensors presented in this study describe paleostress regimes inverted from different, manually sorted sets of faults from along the margin. The obtained paleostress regimes are correlated with specific tectonic events in the regional framework experienced by the MNPM.

5.3.4 K-Ar radiometric dating of fault rocks coupled with mineralogical analysis

K-Ar radiometric dating and X-ray diffraction (XRD) were performed on twelve fault gouges and one non-cohesive altered rock at the laboratories of the Geological Survey of Norway (Trondheim, Norway) following the procedure described by Viola et al. (2018). Collected fault rock samples are representative of the main trends of structural lineaments defined by remote sensing analysis. Each sample was disintegrated by repeated freezing and thawing cycles to avoid mechanical grain size reduction of coarse-grained minerals and their contamination in the finer fractions. Samples were, then, separated into five grain size fractions (<0.1, 0.1-0.4, 0.4-2, 2-6 and 6-10 µm). The <2, 2-6 and 6-10 µm grain size fractions were separated in distilled water using Stokes' law, whereas the finer fractions (<0.1, 0.1-0.4 and 0.4-2 µm) were concentrated by high-speed centrifugation of the <2 µm fraction. The mineralogical composition of each grain size fraction was determined by XRD analysis (with a Bruker D8 Advance diffractometer). Mineral quantification was carried out on randomly prepared specimens using Rietveld modelling with the TOPAS 5 software. The lower limit of quantification and accuracy are mineral-dependent but are generally 1 wt% and 2-3 wt%, respectively. For further details, the reader is referred to Viola et al. (2018) and Tartaglia et al. (2020).

5.4 Results

5.4.1 Bedrock lineament pattern

The results of the manual extraction of bedrock lineaments from the coastal area of the MNPM at the 1:100.000 (Fig. 5.2a) and 1:10.000 scales (Fig. 5.2b, c) show that lineaments can be grouped into four main sets:

i) (E)NE-(W)SW lineaments, largely parallel to the coastline and to the MTFC;
ii) NNW-SSE lineaments;
iii) WNW-ESE lineaments;
iv) E-W lineaments.

The (E)NE-(W)SW oriented trend is dominant and particularly evident on Hitra and Smøla (Fig. 5.2b), where one of the strands of the MTFC, the Hitra-Snåsa Fault, is well exposed.

When comparing the rose diagrams obtained from the two different scales at which the remote sensing was carried out, some differences can be recognized. This reflects the number of picked lineaments, which is generally one or two orders of magnitude greater at the 1:10.000 scale than at the smaller scale (Fig. 5.2). Despite the different number of mapped lineaments, however, the same main trends emerge from both mapping scales, with some exceptions for the Runde and Kråkenes areas. The 1:100.000 scale lineament trends in the Runde area are oriented NNW-SSE, NNE-SSW and ENE-WSW (Fig. 5.2a). The ENE-WSW lineaments define the main trend in the 1:10.000 scale stereoplot of the Runde area (Fig. 5.2c), but the NNW-SSE oriented lineaments are less abundant than at the 1:100.000 scale (Fig. 5.2a). A similar situation is evident in the Kråkenes area, where the distinct WNW-ESE lineament trend derived from the 1:100.000 scale is less abundant at the 1:10.000 scale (Fig. 5.2a, c). This observation could indicate that NNW-SSE and WNW-ESE lineaments tend to be better expressed at smaller scale because they represent older, regional structural trends. Their abundance at the 1:10.000 scale could also be relatively smaller in comparison to the great number of variably oriented faults and fractures recorded and mapped at this scale.

The mapped lineaments exhibit crosscutting relationships that can be summarized as follows (Fig. 5.3): WNW-ESE trending lineaments show mutual crosscutting relationships with all the detected trends. In the area of Hitra, the ENE-WSW lineaments are persistent and seem to cut all other lineaments, even if they are locally crosscut by NNW-SSE and NE-SW trends. NNW-SSE and NE-SW trending lineaments are generally crosscut by all the detected trends, and locally, NE-SW trending lineaments crosscut the NNW-SSE lineaments. According to these results, ENE-WSW striking lineaments thus appear to be the youngest, or the ones that have been reactivated more recently, and the NNW-SSE and NE-SW the oldest.

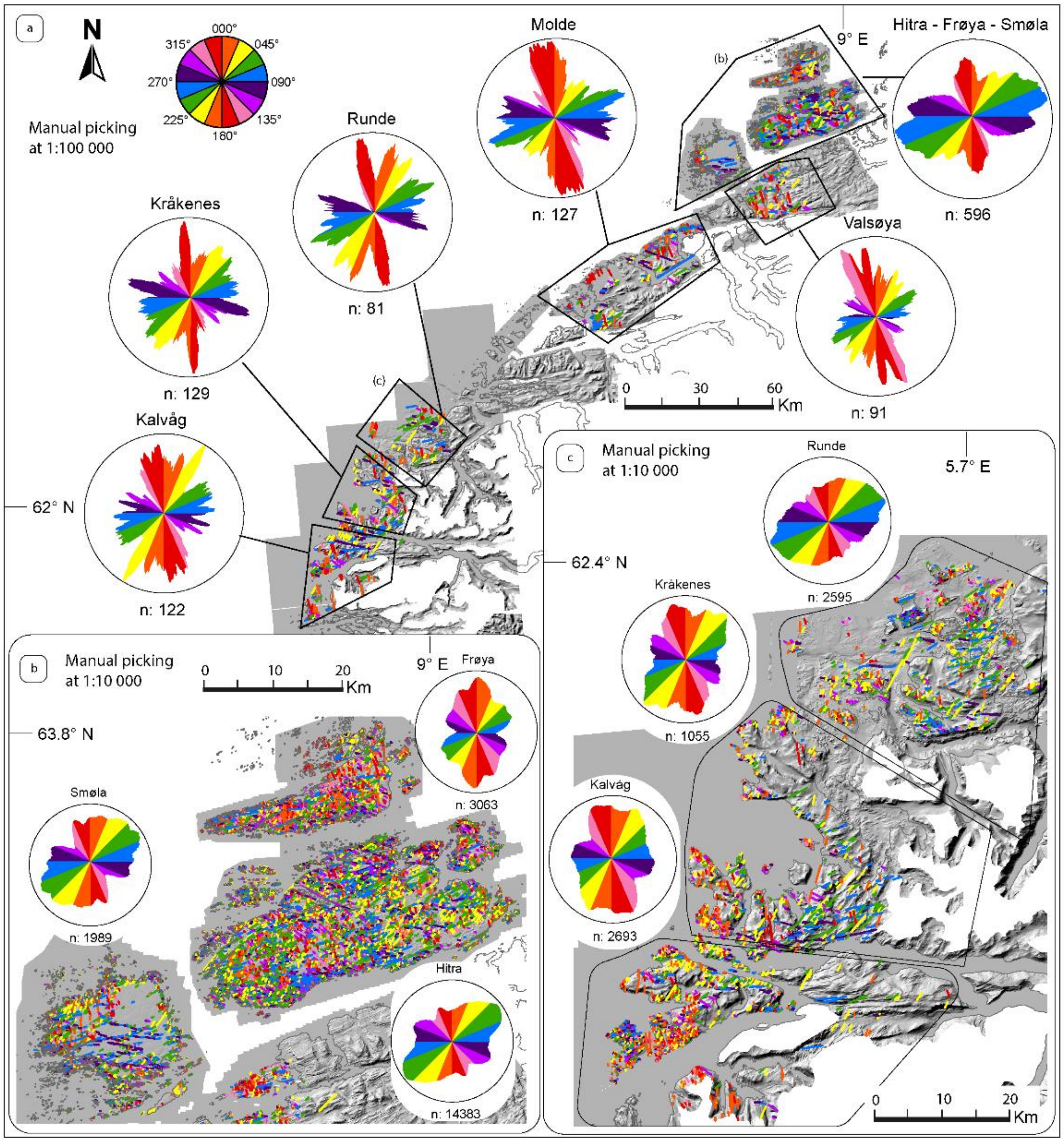

Figure 5.2 - Map showing hillshaded LiDAR DEMs and bedrock lineaments from the coastal MNPM color-coded according to their strike (as shown in the associated rose diagrams). (a) Lineaments from the entire MNPN, mapped at the 1:100.000 scale. (b) Lineaments from the northern MNPM (Hitra, Frøya and Smøla), mapped at the 1:10.000 scale, (c) Lineaments from the southern segment of the MNPM, mapped at the 1:10.000 scale.

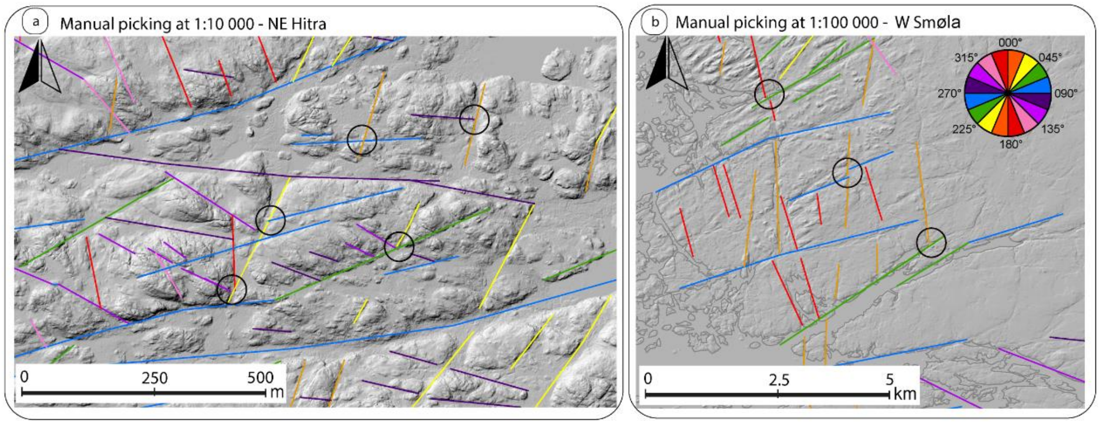

Figure 5.3 - Maps showing examples of manually mapped lineaments at two different scales on (a) north-eastern Hitra and (b) western Smøla. The black circles highlight mapped crosscutting relationships between variably oriented lineaments.

5.4.2 Mesostructural brittle fault characterisation

The structural stations studied along the MNPN are shown in Figure 5.4a. Faults and fractures at the studied sites cut across different types of rock. The host rocks along the MNPM are mainly represented by granitic and granodioritic gneiss of the WGR, Devonian sandstone and conglomerates, micaschist, foliated migmatite and locally eclogitic lenses.

The collected fault-slip data have variable strike and dip. The associated striae are also variably oriented, indicating both dip-slip, predominantly with normal kinematics, and, to a lesser extent, strike-slip faulting. Faults locally rework and exploit inherited ductile planar fabrics, mainly the mylonitic foliation (Fig. 5.5a). On the island of Jøsnøya, south of Hitra, high-angle conjugate sinistral ENE-WSW and dextral NE-SW oriented fault planes are exposed. The sinistral ENE-WSW high-angle faults rework the mylonitic fabric (Fig. 5.5a). The strikes of these faults are parallel to the main remotely detected lineament set in the area. These faults reactivate the mylonitic planar fabric and are systematically cut by high angle NNW-SSE trending normal faults (Fig. 5.5b). These normal faults are locally decorated by fine-grained epidote mineral coatings. Also, the strike slip faults on Jøsnøya are, in turn, cut by younger calcite veins.

Brittle fault zones along the margin are associated with a broad range of fault rock assemblages. In highly fractured fault cores, fine-grained cataclasite is associated with or crosscut by distinct layers of clay-rich fault gouges (Fig. 5.5c, d). Due to the lack of marker horizons in the study area, the amount of displacement along individual faults remains largely unknown. Locally, along some brittle structures, the host rock is dismembered, and appears as unconsolidated coarse-grained material. In these fault and fracture zones, the mostly granitic or gabbroic host rock is altered.

Brittle structures along the MNPM exhibit different mineralogical coatings, including epidote, chlorite, calcite, and quartz, sometimes decorating the same plane but also crosscutting and overprinting each other, forming a complex multi-layered arrangement of fault rocks. Epidote coatings on faults and fractures are generally reworked and/or cut by younger, few mm-thick, milky white prehnite veins (Fig. 5.5e). Calcite occurs as mm-thick striated synkinematic coating on the fault planes (Fig. 5.5f), as variably thick veins, or secondary, coarse-grained, post-kinematic fracture infill.

The studied fault and fracture planes have been classified according to their mineralizations and plotted in rose diagrams (Fig. 5.4b). Green, ultrafine-grained, epidote coatings are mainly associated with c. N-S trending faults but are also locally present on differently oriented faults (Fig. 5.4b). Fine-grained quartz mineralizations and quartz veins show a similar pattern but are particularly abundant on E-W striking faults. Red iron oxide coating mainly occurs on WNW-ESE striking faults (Fig. 5.4b). Milky white, extremely fine-grained, mm to cm thick prehnite coating is mainly associated with roughly N-S and NNW-SSE striking faults. Dark blue/green, mm-thick, chlorite coating does not display any preferential orientation. Calcite is present on all sets of fractures and faults, irrespective of their orientation, but shows a predominance along N-S striking brittle structures (Fig. 5.4b).

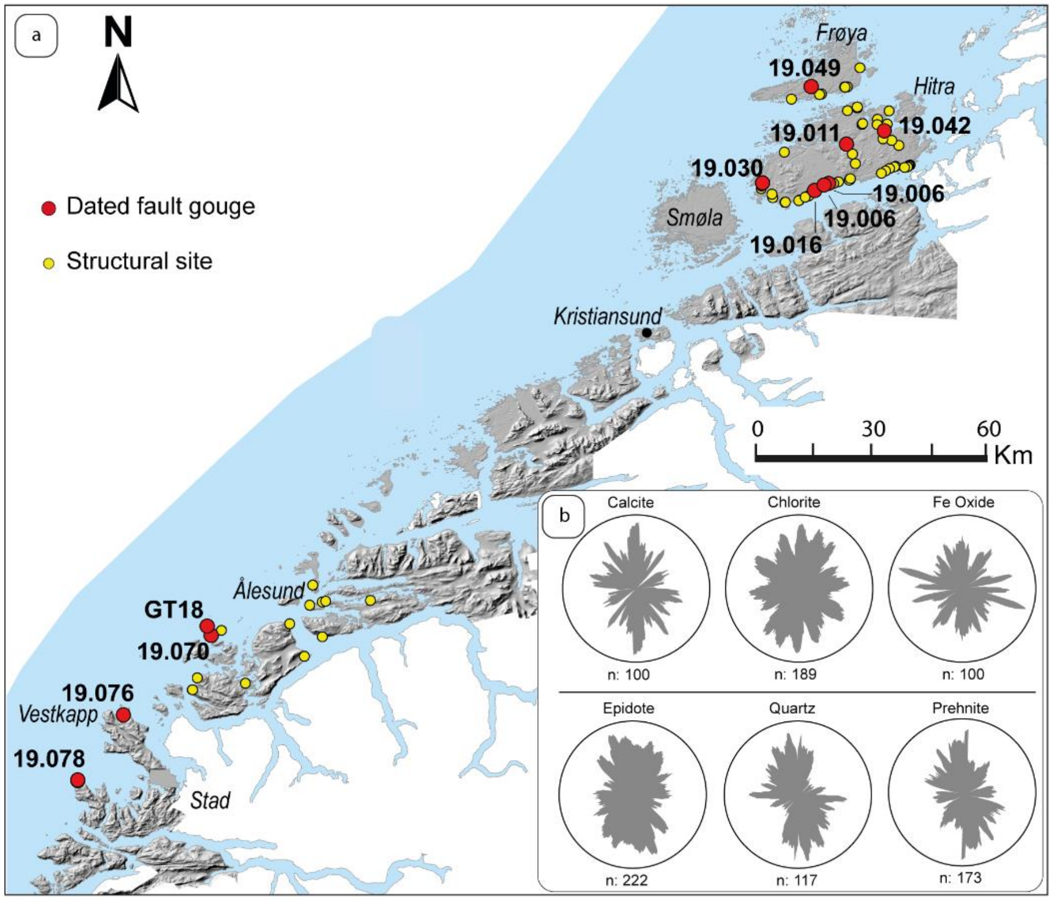

Figure 5.4 - (a) Map of the investigated structural sites. Dark grey dots indicate the location of the dated fault gouge samples (Table 5.1); (b) Rose diagrams showing the strike orientation of fault and fracture zones, sorted according to the main decorating mineral phase.

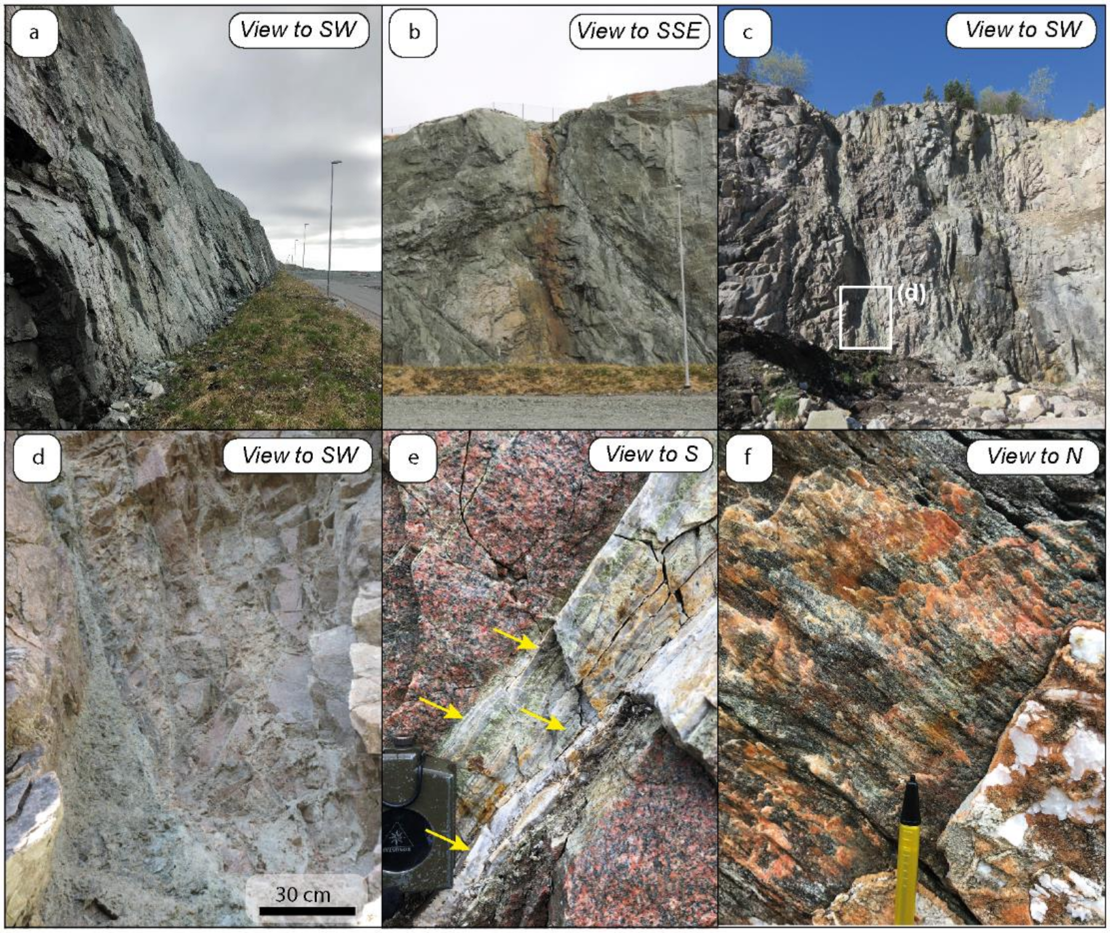

Figure 5.5 - Photographs of representative fault zones. (a) ENE-WSW outcrop of a strand of the MTFC (Jøsnøya, Hitra island); (b) same outcrop as in (a), this strand of the MTFC is cut by high-angle normal faults, oriented NNW-SSE; (c) c. 10 m thick fault zone, with the principal slip surface oriented 322/76 and a (d) fault core containing cataclasite and gouge (Hitra island); (e) E-dipping fault plane with a 10 cm-thick core containing fine grained quartz and epidote cut by milky white prehnite veins (pointed out by yellow arrows, Hitra island); (f) NE-SW transtensional fault plane with calcite and zeolite coating (Runde island).

5.4.2.1 Fault zone K-Ar dating

Twelve fault gouges and one altered rock were sampled for radiometric K-Ar dating. The details of the sampled fault zones are reported in Table 5.1 and Figure 5.6. The sampled fault gouges belong to three main sets of faults: i) low-angle (W)NW-(E)SE striking fault planes (samples 19.006B, 19.078, and 19.016; Fig. 5.6.1); ii) variably dipping, ENE-WSW oriented faults (samples 19.007A, 19.011, 19.042A, GT18_01/2; Fig. 5.6.2); iii) medium to high-angle, oblique and dip-slip, NNE-SSW oriented faults (samples 19.030A, 19.049, 19.070, 19.076; Fig. 5.6.3). Samples are from different rock types (Table 5.1), mainly granitic and gabbroic rocks (19.006B, 19.007A, 19.016, 19.030A, 19.042A/E, 19.078), migmatite (19.049) and amphibolite or gneiss (19.011, 19.070, 19.076, GT18_01, GT18_02).

Some of the sampled fault zones contain a complex assemblage of different fault rocks within the core with different generations of fault gouges, cataclasites and veins. The low-angle N-dipping fault of sample location 19.006B (Fig. 5.6.1a), for example, contains a 7 cm thick fault gouge layer associated with a subparallel blocky calcite vein. The NNE-dipping fault at location 19.016 contains a layer of gouge associated with subparallel veins of calcite and zeolite (Fig. 5.6.1c). Fault zones 19.078 and 19.011 are composed of a few cm thick fault gouge layer (Fig. 5.6b, e).

Samples 19.042A and E are from an ENE-WSW striking strike-slip fault and are from two different structural levels (Fig. 5.6f, g). In the lower part of the outcrop, a grey, very plastic fault gouge is exposed (sample 19.042A), whereas the upper part of the same brittle structure is filled with altered/weathered sandy granite (sample 19.042E).

Samples 19.030A and 19.049 are from SE-dipping fault zones; both their fault cores are composed of a c. 3 cm thick layer of cohesive fine-grained cataclasite, chunks of blocky calcite veins and the sampled fault gouge (Fig. 5.6j, k). The reddish fault gouge of the ENE-WSW striking fault at locality 19.007A also embeds calcite veins (Fig. 5.6d).

Samples GT18_01 and GT18_02 were collected from the same c. 7 m thick fault zone on the island of Runde (Fig. 5.6h). They are from two distinct generations of gouge, with GT18_01 cutting across GT18_02. The two gouge layers have different angle of dip, where the younger gouge layer (GT18_01) has a steeper dip (Fig. 5.6i).

Finally, some brittle fault zones exploit inherited ductile planar fabrics. For example, NNE-SSW striking mylonitic shear zones were reworked by brittle faulting (e.g., samples 19.070 and 19.076; Fig. 5.6l, m).

Table 5.1 - Table of collected data of sampled and dated fault zones divided according to their strike in three sets (WNW-ESE, ENE-WNW, and NE-SW). (N: Normal fault, R: Reverse fault; S: Sinistral fault; X: Unknown sense of slip).

Set	Sample ID	Locality	Coordinates (WGS84)		Host Rock	Strike	Fracture Plane		Slip Line		Slip	Description of fault core	Mineralisation
			N	E			Dip Dir	Dip	Trend	Plunge			
WNW-ESE and E-W	19.006B	Hitra	63°28.339'	08°40.505'	Granite	103	13	21	344	27	N	reddish and grey gouges	Subparallel calcite vein
	19.016	Hitra	63°28.116'	08°39.247'	Granodiorite	108	18	37	4	30	I/N	4-cm-thick gouge	calcite vein and zeolite
	19.078	Kråkenes	62°02.087'	04°59.667'	Gabbro	129	219	29				grey light blue gouge and reddish gouge layer	none
ENE-WSW	19.007A	Hitra	63°27.347'	08°36.213'	Granite	235	325	27				cm-thick reddish gouge	Reworked network of thin calcite veins
	19.011	Hitra	63°33.823'	08°46.071'	Amphibolite	250	340	42				foliated gouge	none
	19.042A	Hitra	63° 35.661'	08° 57.858'	Granodiorite	252	162	79	86	10	X	1.5-2 m thick fault zone with clay-rich gouge and cataclasite clasts in the lower part; altered granite in the upper part of the fault	none
	19.042E	Hitra	63° 35.661'	08° 57.858'	Granodiorite								none
	GT18_01	Runde	62° 24.318'	5° 35.563'	Amphibolitic gneiss	260	170	62				foliated gouge	none
	GT18_02	Runde	62° 24.318'	5° 35.563'	Amphibolitic gneiss	270	180	12				foliated gouge cut by a high angle second generation of gouge (GT18_01)	none
NE-SW	19.049	Frøya	63°41.762'	08°34.944'	Migmatite	196	106	66	59	52	N	cataclasite layer and gouge	quartz vein and calcite vein
	19.07	Runde	62°23.168'	05°36.732'	Amphibolitic gneiss	203	113	72	152	63	N	Reworked shear zone; grey gouge layer embedding deformed lenses of the protolith	calcite vein cuts across the fault
	19.076	Vestkapp	62°11.487'	05°11.918'	Amphibolitic gneiss	206	296	84	12	36	S	Reworked shear zone; 10-cm-thick core with gouge, cataclasite and clasts of host rock	hematite

	19.030A	Hitra	63°28.251'	08°20.128'	Granite	212	122	46				pinkish gouge reworking cataclastic layers, embedding chunks of calcite veins	Coarse-grained calcite vein

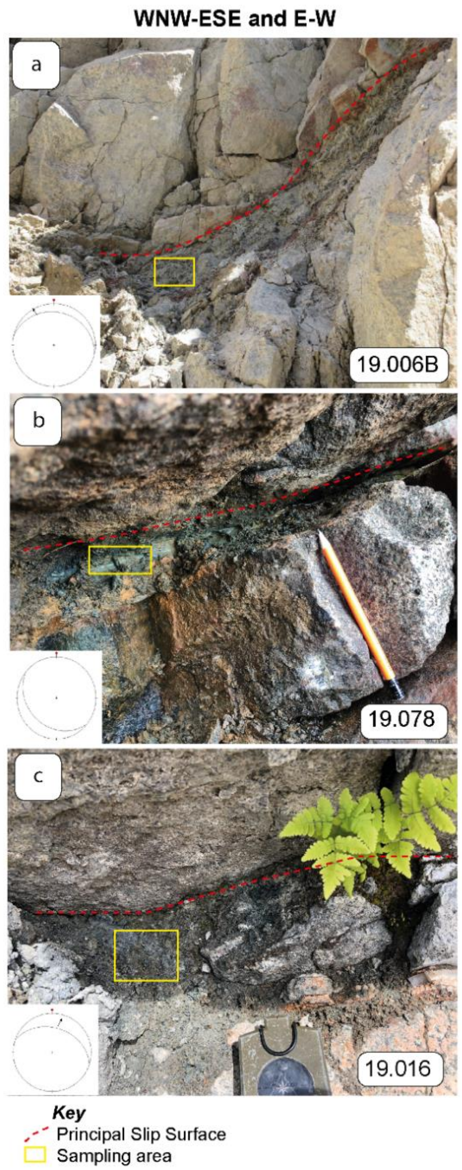

Figure 5.6.1 - Sampled and dated fault zones divided into three sets according to their strike: WNW-ESE and E-W (Fig. 5.6.1); ENE - WSW (Fig. 5.6.2); NNE-SSW (Fig. 5.6.3). Red lines highlight principal slip surfaces, and the yellow squares indicate the sampled area. Schmidt stereonets show the orientation of the fault planes. More details in the text and Table 5.1.

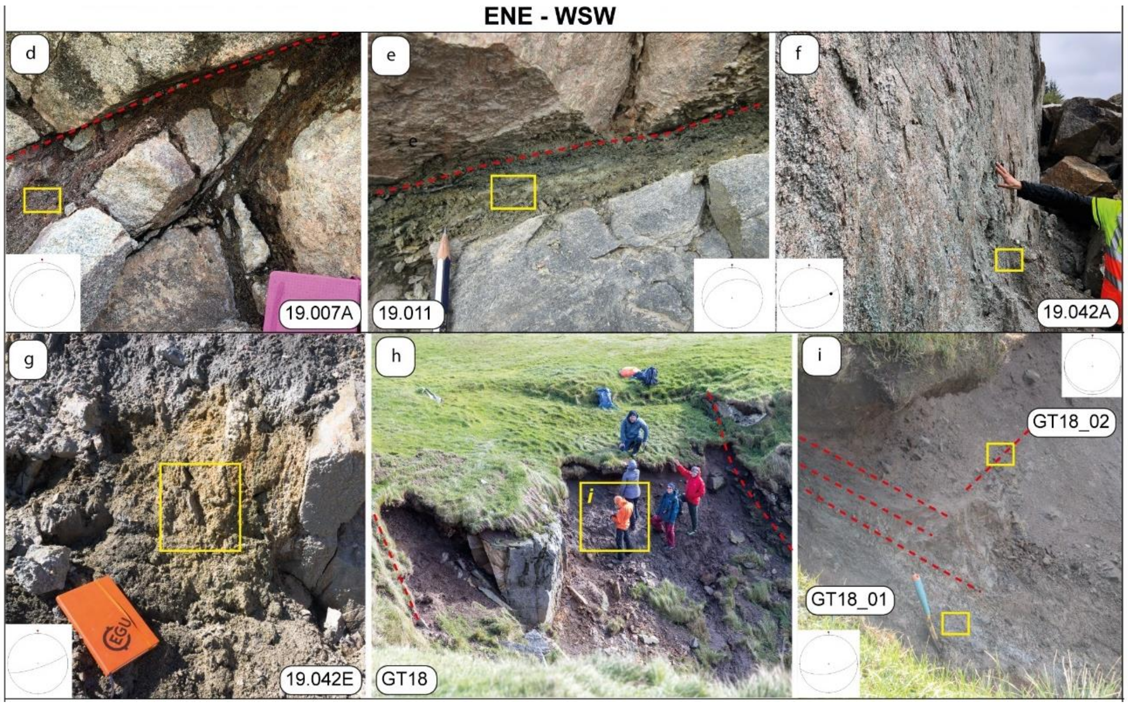

Figure 5.6.2 - Sampled and dated fault zones divided into three sets according to their strike: WNW-ESE and E-W (Fig. 5.6.1); ENE - WSW (Fig. 5.6.2); NNE-SSW (Fig. 5.6.3). Red lines highlight principal slip surfaces, and the yellow squares indicate the sampled area. Schmidt stereonets show the orientation of the fault planes. More details in the text and Table 5.1.

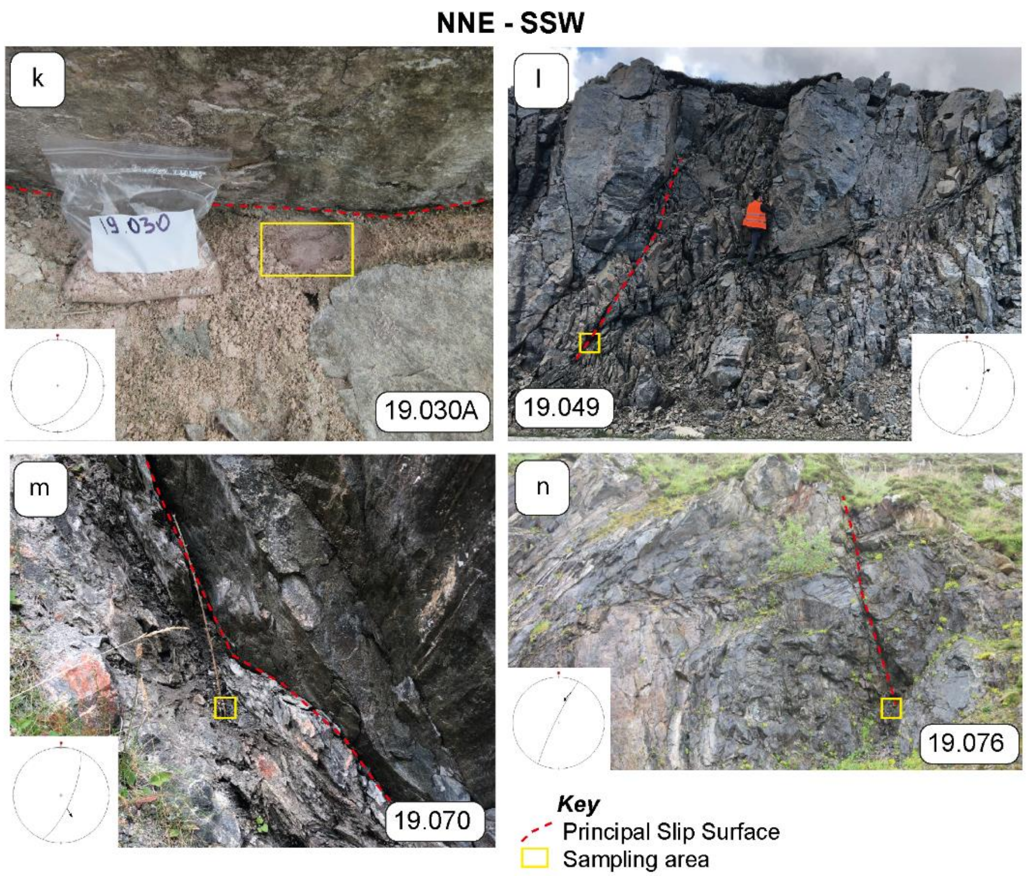

Figure 5.6.3 - Sampled and dated fault zones divided into three sets according to their strike: WNW-ESE and E-W (Fig. 5.6.1); ENE - WSW (Fig. 5.6.2); NNE-SSW (Fig. 5.6.3). Red lines highlight principal slip surfaces, and the yellow squares indicate the sampled area. Schmidt stereonets show the orientation of the fault planes. More details in the text and Table 5.1.

5.4.3 Microstructural data

Eight samples of cataclasite were collected from outcrops of representative fault zones at the investigated structural sites (Fig. 5.4a) for microstructural characterisation. Although the collected samples cannot be considered representative of the entire population of faults along the margin, their analysis allows us to derive structural and mineralogical inferences as to the conditions of deformation and to define systematic and mineralogically-constrained crosscutting relationships. Microstructural analyses focused on: (i) the identification of the mineralogy and microstructure of different mineral coatings observed in the field; (ii) the identification of overprinting relationships between different coatings and thereby (iii) deducing a temporal sequence of deformation events.

Our study revealed a systematic sequence of overprinting relationships between veins and cataclastic layers characterized by specific mineral phases. From the oldest to the youngest, this sequence is defined by the following evidence:

(i) Protocataclasites are generally pervasively fractured and characterized by the occurrence of (coarse-grained) epidote mineralizations (Fig. 5.7a). Multiple events of fracturing and precipitation of epidote-bearing mineralizations are inferred from the occurrence of epidote-bearing cataclasites with remarkably different grain size and crosscutting relationships (e.g., Ep1, Ep2 and Ep3 in Fig. 5.7a).

(ii) Quartz veins and quartz-rich cataclasites of variable grain size dissect the epidote-bearing cataclasites (Fig. 5.7b). Several generations of quartz veins and quartz-rich cataclasites can be identified (e.g., Qtz1, Qtz2 in Fig. 5.7b).

(iii) Prehnite-bearing veins and cataclastic layers cut across and disrupt the quartz- and epidote-bearing cataclasites described above (Fig. 5.7c-d). Quartz- and epidote-layers are observed as mm-size clasts embedded within prehnite veins and cataclastic layers.

(iv) Fine-grained cataclasites of mixed mineralogical composition containing large clasts of epidote-, quartz-, and prehnite-bearing cataclastic layers and veins (Fig. 5.7e).

Fault gouges are commonly associated with calcite mineralization and subordinated red iron oxides and quartz (Table 5.1). Calcite-bearing mineralizations can be coarse-grained (mm-size) and are locally associated with euhedral zeolite (Fig. 5.7f).

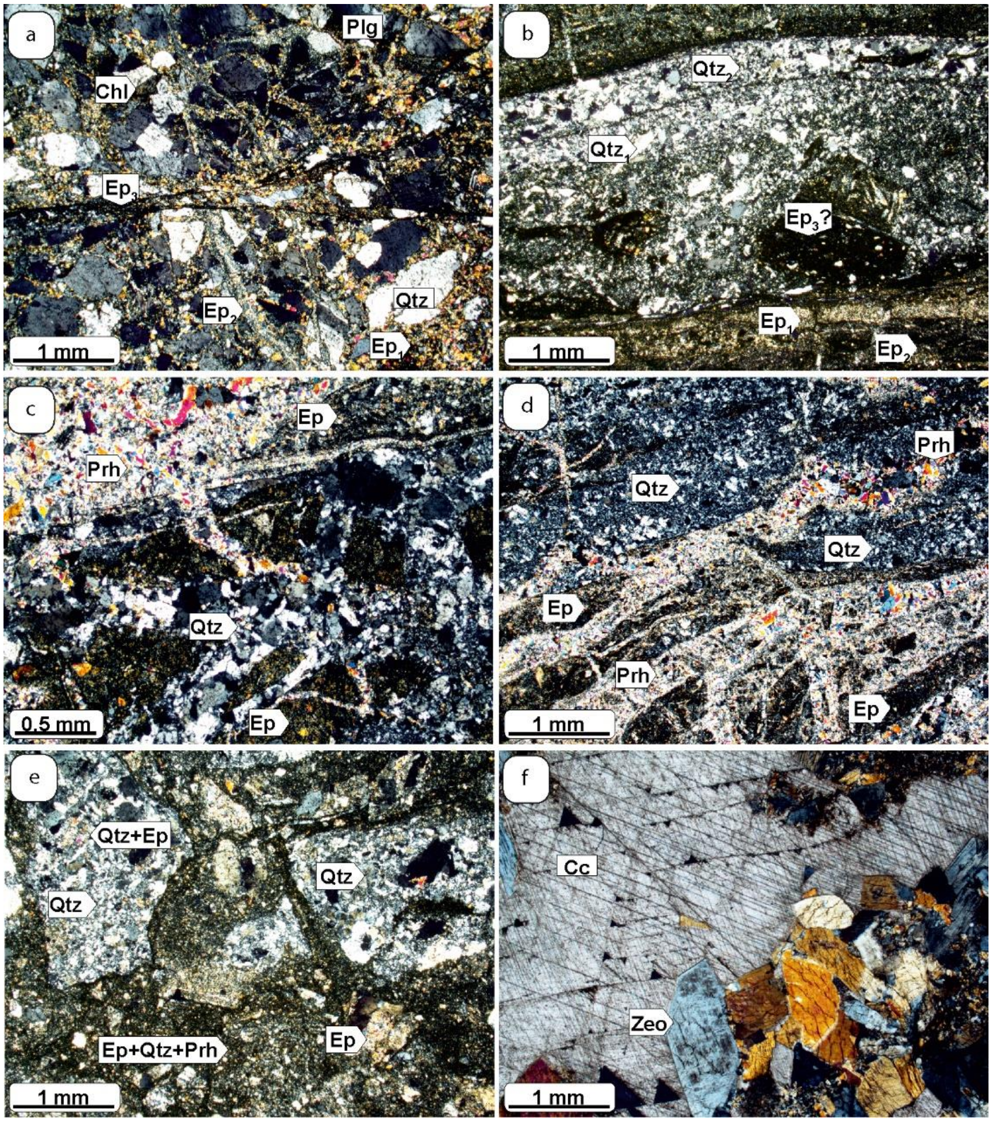

Figure 5.7 - Microphotographs of representative fault rocks from Hitra island. (a) Granitic protocataclasite characterized by pervasive fracturing and epidote mineralisation. The host rock is partially altered, as indicated by the occurrence of chlorite (Chl) and saussurritic plagioclase (Plg). Several generations of progressively finer-grained epidote mineralisations can be identified (Ep1, Ep2, Ep3). (b) Quartz (Qtz)-rich cataclasite containing a clast of fine-grained epidote-bearing cataclasite (Ep3). The quartz-rich layer contains a younger quartz vein (Qtz2) localised at the contact between an epidote-bearing cataclastic layer (top) and the quartz-rich cataclasite (bottom, Qtz1). Note the occurrence of multiple layers of variably sized epidote cataclasites (Ep2, Ep1). (c) Prehnite (Prh) vein and cataclastic layer (top) cutting across an older quartz-epidote-bearing cataclasite. This cataclasite contains clasts of epidote-bearing layers embedded in a coarse-grained, quartz-rich vein/cataclastic layer. (d) Prehnite vein disrupting the layered structure of older epidote- and quartz-bearing cataclasites. (e) Fine grained, cataclasite containing coarse grained clasts of epidote-, quartz and prehnite-bearing cataclasites embedded in a fine-grained matrix. (f) Calcite (Cc) vein associated with euhedral zeolite crystals. (a, c-e) Sample 19.009°, N 63°31.079' E 08°48.838'; (b) Sample 19.002B, N 63°28.868' E 08°47.255'; (f) Sample 19.006, N 63°28.339' E 08°40.505'.

5.4.4. Paleostress inversion

The total analysed fault-slip dataset was subdivided into heterogeneous subsets according to a geographic position criterion in order to obtain subsets not exceeding 350 fault-slip data each, which are more easily handled. Inversion was then applied to fault-slip data subsets that were defined based on the criteria explained above, aiming at the identification of internally consistent data according to field constraints, fault orientation, kinematics, and fault characteristics, such as specific mineralization (quartz, epidote, calcite, chlorite), or a specific area with a given geological feature (occurrence of foliation, type of protolith, etc.).

Each obtained dataset was inverted, and initial results were progressively refined by discarding faults with misfit angles >30°. The inversion procedure was reiterated until stable results were obtained (see also Scheiber and Viola, 2018). As this approach was applied iteratively, fault-slip data of potentially cogenetic faults were tested against their geometric and kinematic compatibility and, in case the misfit angle did not exceed 30°, included into the final dataset to be inverted. Faults without any recorded mineralization were also tested for their compatibility with the calculated stress field. By such an approach, we identified similar stress fields for the different subareas, which stresses the regional significance of the obtained stress regimes. Among them, the most recurrent are shown in Figure 5.8 from older to younger.

A pure compressional stress regime with the maximum horizontal compressional stress axis (σ_1) oriented NW-SE was obtained by the inversion of low angle N-dipping faults (R': 2.54), that invariably containing brittle fault rocks in their cores (Fig. 5.8a). Some of these faults are reverse, while other faults recorded a later extensional reactivation.

Pure compression was followed by a transpressional stress regime (R':1.98) with σ_1 oriented NW-SE, which formed conjugate strike-slip faults, oriented NW-SE (sinistral) and E-W (dextral), invariably decorated by epidote and chlorite (Fig. 5.8b).

A well recorded stress regime along the entire MNPM is an extensional stress field with σ_3 oriented E-W (R':0.37; Fig. 5.8c). It generated NNE-SSW and NNW-SSE normal faults and reactivated some NW-SE oblique fault planes. This stress field is recorded by fault zones mainly decorated by epidote and quartz coatings, and subordinately exposing brittle fault rocks in their cores.

The last two inverted stress regimes reactivated variably oriented faults and fractures inherited from the previous deformation episodes. An extensional field with σ_3 oriented NW-SE reactivated faults and fractures decorated by prehnite, quartz, zeolite and calcite coatings (R': 0.52; Fig. 5.8d). Finally, prehnite decorated faults and/or associated with brittle fault rocks, oriented NE-SW and NW-SE formed or were reactivated by an extensional stress regime with σ_3 oriented WNW-ESE (R': 0.24, Fig. 5.8e).

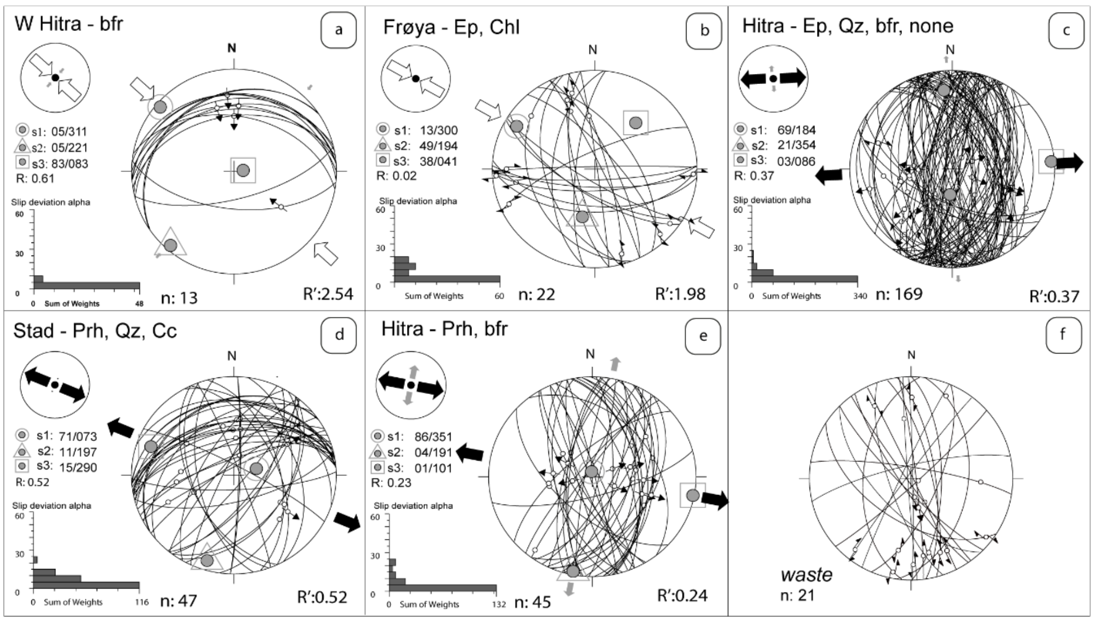

Figure 5.8 - Paleostress tensors computed from the inversion of fault-slip data from the onshore MNPM: stereonets (a) to (e) are tentatively sorted from oldest to youngest (see text for explanation). Stereoplots are Schmidt, lower hemisphere projections. (bfr: brittle fault rocks; Ep: epidote; Chl: chlorite; Qz: quartz: Prh: Prehnite; Cc: Calcite). (f) Fault slip data not used for paleostress analysis.

5.4.5 K-Ar data

The twelve sampled fault rocks and the altered rock were characterized mineralogically by XRD analysis and dated by the K-Ar method. The XRD data are not always quantitative, because of the little amount of material recovered from some of the samples (Table 5.2). The (semi)quantitative XRD data show that in the different samples the percentage of clay minerals (smectite, illite/muscovite, vermiculite, and palygorskite) increases with decreasing grain size (Table 5.2, Fig. 5.9), such that the analysed < 0.1 µm grain size fraction of all the samples only comprise clay minerals (Fig. 5.9). The amount of quartz, K-feldspar, plagioclase, epidote, amphibole, calcite, zeolite (when present) generally decreases with decreasing grain size. Generally, the chlorite content also decreases with decreasing grain size and is accompanied by an increase of the smectite content. Focusing on the K-bearing phases, the finer grain size fractions are invariably enriched in K-bearing clay minerals, such as illite, illite-smectite mixed layers and illite-vermiculite (Fig. 5.9). K-feldspar is not present in all the samples, but when present, its amount decreases progressively and is absent in the finest grain size fraction (Fig. 5.9, Table 5.2).

The sixty-two new K-Ar data obtained from twelve fault gouges and one altered granitic rock sample range from 848 ± 11 to 71 ± 1 Ma (Table 5.3). The ages are plotted on an “Age vs. grain size fraction” diagram (Fig. 5.10). However, sample 19.049 did not contain sufficient material for dating of grain sizes <0.4 µm, and samples 19.016 and 19.042E did not contain sufficient material for dating of the finest (<0.1 µm) grain size fractions. The graph shows inclined curves with a common trend: coarser grain size fractions have older ages while the younger ages are associated with the finest fractions. The K-Ar ages of the finest grain size fractions (< 0.1 µm) are 197 ± 3, 176 ± 2, 138 ± 3, 130 ± 3, 126 ± 3 (twice), 91 ± 3, 86 ± 1, 80 ± 1 and 71 ± 1 Ma (Table 5.3).

Table 5.2 - XRD results of the dated samples separated in five different grain size fractions (<0.1, 0.1-0.4, 0.4-2, 2-6 and 6-10 µm). (Qtz: quartz, Kfs: K-feldspar, Plg: plagioclase; Cc: calcite, Ep: epidote; Amp: amphibole; Px: pyroxene; Ill: illite; Ms: muscovite; Palyg: palygorskite; Kln: kaolinite;

Chl: chlorite; Sm: smectite; Verm: vermiculite; Lepid: lepidocrocite; Zeo: zeolite; Stb: stilbite; Ap: apatite; Anl: analcime; GOF: Goodness of Fit). The table continues in the next page.

Sample	Grain size fraction	Qtz	Kfs	Plg	Cc	Ep	Amp	Px	Ill/Ms	mica	Palyg	Kln	Chl	Sm	Chl-Sm	Sm and Chl-Sm	Ill-Sm and Sm	Ill-Verm	Lepid	Zeo	Stb	Ap	Anl	*GOF*
19.006B	<0.1			4		6			38				35	17										*1.63*
	0.1-0.4		2	5		15			27				30	21										*1.81*
	0.4-2	12	3	7		28			14				22	14										*1.68*
	2-6	27	3	9		28			8				15	10										*1.68*
	6-10	31	3	9		26			6				14	11										*1.7*
19.007A	<0.1	*too little material*																						
	0.1-0.4													>95									<5	
	0.4-2	<5		5-10					trace				<5	>60									<5	
	2-6	<5		10-15					5-10				5-10	>50									<5	
	6-10	<5		10-15					5-10				10-15	>50									<5	
19,011	<0.1	*too little material*																						
	0.1-0.4								trace				<5	>95										
	0.4-2	<5		<5					<5				5-10	>80										
	2-6	<5		5-10					5-10				5-10	>70										
	6-10	<5		5-10					5-10				5-10	>70										
19,016	<0.1	*too little material*																						
	0.1-0.4			<5									trace	>90									<5	
	0.4-2	trace		<5			trace						trace	>85									<5	
	2-6	<5		5-10			trace		trace				trace	>80									<5	
	6-10	<5		5-10			trace		trace				trace	>80									<5	
19.030A	<0.1	*too little material*																						
	0.1-0.4					<10						<10		>80										
	0.4-2			9		24						10		57										*2.94*
	2-6			25		22						10	6	37										*2.48*
	6-10	2		35		19						10	6	28										*2.43*
19.042A	<0.1																100							
	0.1-0.4																100							
	0.4-2	5	7	15					37				23				13							*2.37*
	2-6	10	18	13	1				31				16				11							*2.34*
	6-10	14	16	12	2				26				14				16							*2.23*
19,049	<0.1	*too little material*																						
	0.1-0.4	*too little material*																						
	0.4-2	3		trace?	trace				30					67										*1.38*
	2-6	5		7					35				trace	53										*2.45*
	6-10	5		7					35				trace	53										*2.46*

Sample	Grain size fraction	Qtz	Kfs	Plg	Cc	Ep	Amp	Px	Ill/Ms	mica	Palyg	Kln	Chl	Sm	Chl-Sm	Sm and Chl-Sm	Ill-Sm and Sm	Ill-Verm	Lepid	Zeo	Stb	Ap	Anl	*GOF*
19.070	<0.1												4	96										*4.00*
	0.1-0.4												7	93										*3.21*
	0.4-2	3											17	78						2				*2.48*
	2-6	7											17	70						4		2		*2.63*
	6-10	8											17	69						4		2		*2.52*
19,077	<0.1	*too little material*																						
	0.1-0.4	7											23			70								*2.32*
	0.4-2	9		4			6	6					22			53								*1.99*
	2-6	12		5			11	7	trace				20			45								*2.07*
	6-10	12		5			12	6	trace				20			45								*2.06*
19,078	<0.1									x			x	x	x				x					
	0.1-0.4									x			x	x	x				x					
	0.4-2	trace		trace									xxxx	xxxx	xxx				xx					
	2-6	x		x									xxxx	xxxx	xxx				x					
	6-10	x		x									xxxx	xxxx	xxx				x					
GT18_01	<0.1										xxxx			xxxx										
	0.1-0.4										xxxx			xxxx										
	0.4-2	trace									xxxx	trace?		xxxx										
	2-6	x	xx								xxxx	x		xxxx										
	6-10	xx	xxx								xxx	xx		xxxx										
GT18_02	<0.1																							
	0.1-0.4			trace?										xxxx				x?			x?			
	0.4-2	x		xx										xxxx				x			xxx			
	2-6	xx		xx										xxxx				x			xxxx			
	6-10	xx		xx										xxxx				x			xxx			
Altered rock sample																								
19.0042E	<0.1	*too little material*																						
	0.1-0.4	*too little material*																						
	0.4-2	x		xx					xxx				xxx	xxxx										*2.36*
	2-6	x		xx					xxx				xxx	xxxx										*2.58*
	6-10	x		xx					xxx				xxx	xxxx										*2.62*

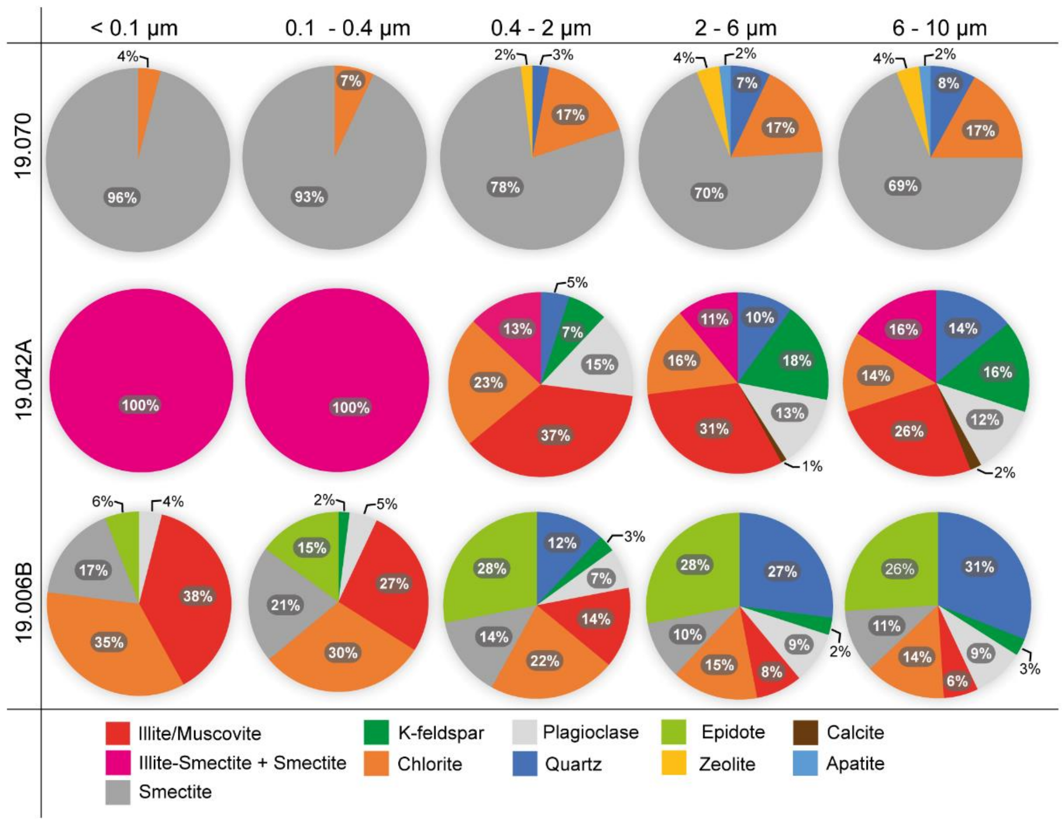

Figure 5.9 - Pie charts of the XRD compositional data of each of the dated fractions of three representative fault gouges of different ages: 19.070 (80 ± 1 Ma), 19.042A (86 ± 1 Ma), 19.006B (197 ± 3 Ma).

5.5 Discussion

The complex network of lineaments with different orientations along the MNPM, the abundance of brittle structures and the high variability of mineralogical assemblages within the studied faults and fractures document the polyphase, brittle evolution experienced by the MNPM. Despite its long and, at times, convoluted history, our systematic approach contributes to unravelling its deformation and adds new temporal constraints to its multiphase history.

5.5.1 Fault Rock Mineral Assemblages

The sequence of mineral coatings established for the analysed fault cataclasites constrains a progressive evolution of retrograde cooling of the MNPM, presumably from the Carboniferous onward. Indeed, the epidote + chlorite (+ quartz) assemblage observed in the oldest cataclasite generations suggest deformation conditions close to the frictional-viscous transition in the continental crust under sub-greenschist facies conditions (T ≤275 °C; e.g., Wehrens et al., 2016).

This mineral assemblage occurs in several generations of coherent (ultra-)cataclasite (Fig. 5.7a), suggesting recurrent events of brittle fracturing, fluid infiltration and mineralization precipitation and cataclasis. The mixed mineralogical composition and prehnite-bearing cataclasites indicate the continuation of brittle cataclasis and fluid infiltration processes at lower temperatures at which prehnite becomes stable (T ≈ 200-250 °C; e.g., Malatesta et al., 2021). More than the other described mineralization types, quartz- and prehnite-bearing cataclasites exhibit evidence of fluid-overpressure and vein formation, preserving several generations of both comminuted and euhedral quartz and prehnite crystals (Fig. 5.7c). Furthermore, gouge-bearing faults are commonly associated with calcite and zeolite mineralizations. Unpublished clumped isotope thermochronological data on calcite veins from the studied faults constrain calcite growth temperatures between c. 190 and 30 °C (see Chapter 6). These temperature estimates are in line with zeolite formation temperatures, commonly well below 200 °C (Weisenberger and Bucher, 2010). The preservation of coarse euhedral crystals of both calcite and zeolite (Fig. 5.7f) may indicate that these veins overprint and post-date the latest stages of brittle faulting and gouge formation.

All in all, this sequence of mineralogical assemblages within the studied fault rocks supports a general cooling trend throughout the brittle evolution of the MNPM. However, the lack of a clear systematic relationship correlating fault strike and fault mineralogy (or sequence of mineral assemblages; see Section 5.2 below, Fig. 5.8) does not allow us to retrieve general conclusions at the scale of the MNPM. Nevertheless, the mineral paragenesis coupled with K-Ar data from fault zones may provide local, but valuable constraints on the thermal and temporal evolution of the brittle deformation history.

5.5.2 Absolute dating of MNPM faults

The obtained inclined “age vs. grain size” curves (Fig. 5.10) are interpreted as recording variable degrees of physical mixing between authigenic and synkinematic mineral phases and inherited protolithic minerals, and/or mixing of different generations of authigenic minerals (van der Pluijm et al., 2001; Verdel et al., 2012; Torgersen et al., 2015; Viola et al., 2016; Vrolijk et al., 2018). This interpretation is in accordance with the “Age Attractor Model” by Torgersen et al. (2015), wherein the amount of authigenic and synkinematic K-bearing phases progressively increases with decreasing grain size. The finer grain size fractions are, therefore, enriched in synkinematic, authigenic minerals (van der Pluijm et al., 2001; Zwingmann and Mancktelow, 2004). However, they may still include inherited protolithic minerals or different generations of K-bearing authigenic phases reworked during multiple stages of deformation, such that the ages obtained from the finest grain size fractions are still to be considered as maximum ages. At the same time, the ages yielded by the <0.1 µm grain size fractions represent the best available constraint on the absolute timing of the most recent faulting event recorded by the studied fault rock (van der Pluijm et al., 2001; Zwingmann and Mancktelow, 2004; Torgersen et al., 2015; Viola et al., 2016, Tartaglia et al., 2020). Within fault rocks, authigenic mineral formation occurs because faulting is a dilatational process that enhances fluid ingress and promotes the (re)-crystallization of synkinematic mineral phases. However, also post-tectonic fluid infiltration within a permeable fault core may lead to authigenesis and, therefore, to dates that do not reflect the age of faulting. Careful fault rock characterisation is, thus, necessary to ascertain the details of faulting as preserved and constrained by the microstructure of the fault rocks and to be able to produce a meaningful interpretation of the obtained K-Ar ages. The fact that the fault gouges sampled in this study can be generally associated with the last faulting event experienced by the sampled fault zones (as indicated by our multiscalar structural analysis) and that the obtained ages are comparable to the timing of already known regional tectonic events (e.g., Fossen et al., 2021; Osmundsen et al., 2021) suggests that the obtained K-Ar fault gouge dates are truly due to synkinematic crystallization and not to post-tectonic authigenesis and or alteration due to later fluid ingress.

The coarser grain size fractions can include protolithic, inherited minerals such as, for example, K-feldspar from the host rock lithology. If several of the coarser grain size fractions from one sample yield a statistically identical or similar age, it is reasonable to conclude that this age has a geological significance (e.g., Viola et al., 2016; Vrolijk et al., 2018; Scheiber et al., 2019; Tartaglia et al., 2020). The “Age Attractor Model” considers the intermediate grain size fractions (0.1-0.4, 0.4-2 and 2-6 µm) as representing a mix of different (synkinematic and protolithic) grains with varying isotopic signatures and they are, therefore, commonly devoid of a geological meaning.

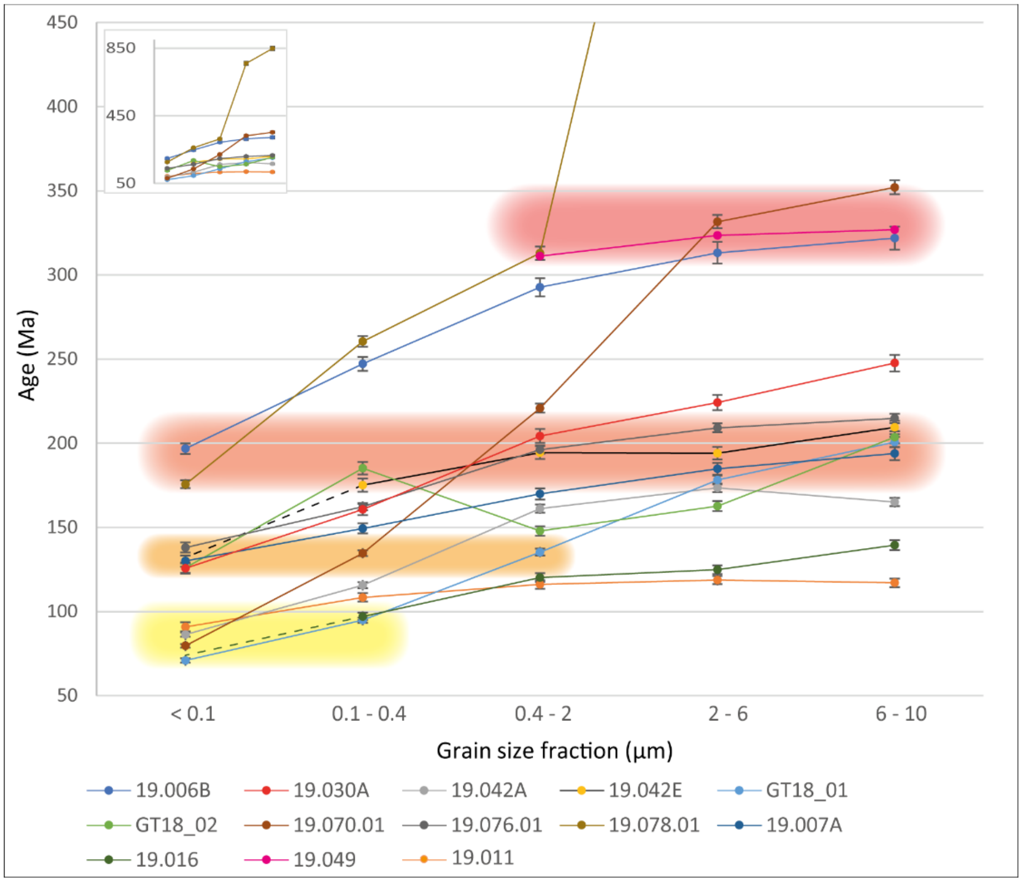

Figure 5.10 - K-Ar age vs. grain size fraction diagram. Each point in the diagram represents the age of a specific grain size fraction. The coloured bars are reported also in Fig. 5.10 and 5.11, and they indicate different tectonic events.

In the obtained K-Ar age vs. grain size plots, some age clusters are clearly recognizable (Fig. 5.10). The ages of the >2 µm grain size fractions of samples 19.006B, 19.049, 19.070 and of the 0.4-2 µm grain size fraction of sample 19.078 form a Carboniferous cluster with a mean age of 321 ± 8 Ma (MSWD=2.74). A Triassic/Jurassic mean age of 202 ± 6 Ma (MSWD=5.9) is calculated from the age cluster constituted by the <0.1 µm finest grain size fraction of sample 19.006B, the coarsest 6-10 µm fraction of samples 19.007A, GT18_01 and GT18_02 and the >2 µm fractions of the samples 19.042E and 19.076. The ages of the intermediate fractions of 19.042E and GT18_01 and of the finest fractions of 19.042E and 19.078 yield a Jurassic cluster with a mean age of 177 ± 12 (MSWD=0.1). The ages of the finest <0.1 µm grain size fractions of samples 19.007A, 19.011, GT18_02, 19.076, and of the >0.4 µm fractions of sample 19.030A define an Early Cretaceous cluster with a mean age of 122 ± 5 Ma (MSWD=3.5). Finally, three <0.1 µm fraction ages are younger than 100 Ma (c. 71, 80, 86, 91 Ma), indicating an episode of illite and smectite crystallization in the Late Cretaceous.

The finest grain size fractions, in addition to also some coarser fractions that define the age clusters in the Late Triassic-Early Jurassic and Early and Late Cretaceous, are all composed of authigenic K-bearing minerals, mainly k-bearing smectite, smectite-illite and illite-muscovite. Therefore, they allow to constrain discrete faulting events through the synkinematic (re)crystallization of K-bearing clay minerals. Two exceptions are the 6-10 µm grain size fraction ages of samples 19.042A and GT18_01. In the case of sample 19.042A, the coarser fraction ages show an oscillating trend, suggesting a mixing of protolithic and authigenic grains. The age of its coarser grain size fraction thus remains devoid of an apparent geological meaning. Sample GT18_01 was collected from the same fault zone as sample GT18_02. These two gouges represent two different generations of fault rock, with GT18_01 cutting across GT18_02. Their finest fraction ages (<0.1 µm), 71 Ma and 126 Ma for GT18_01 and GT18_02, respectively, confirm the crosscutting relationship identified at the outcrop (Fig. 5.6i). Their coarser grain size fractions yield the same age range (201 ± 3, 204 ± 4 Ma), suggesting that the two gouges derive from a common Triassic "protolith", developed during a faulting or alteration event, and then reactivated at different times during the subsequent brittle deformation history.

To summarize, the obtained K-Ar ages can be grouped into four significant clusters, which, from older to younger, date to:

1) Carboniferous, with a mean age of 321 ± 8 Ma (MSWD=2.74);

2) Late Triassic-Jurassic with two distinct mean ages at 202 ± 6 Ma (MSWD=5.9) and at 177 ± 12 Ma (MSWD=0.1);

3) Early Cretaceous with a mean age of 122 ± 5 Ma (MSWD=3.5);

4) Late Cretaceous with ages between c. 91 and 71 Ma.

The Carboniferous cluster is constrained by only the coarser grain size fractions of the dated samples. Among the fractions yielding Carboniferous ages, only the coarser grain size fraction of sample 19.006B contains K-feldspar (3%) in addition to 14% illite/muscovite (Table 5.2, Fig. 5.9).

The K-feldspar is presumably inherited from the granitic protolith and likely records the Upper Devonian-Carboniferous age of cooling during exhumation of the WGR (cf. Walsh et al., 2013). The other Carboniferous ages derive from illite-smectite mixed layers or illite/muscovite, which most probably formed during faulting. This Carboniferous age cluster possibly represents brittle activity along the MNPM during the initial stages of the Norwegian-Greenland Sea rifting (Rotevatn et al., 2018; Gernigon et al., 2020). More specifically, similar Carboniferous ages (c. 320 Ma) have been constrained by K-feldspar $^{39}Ar/^{40}Ar$ dating from a cataclastic granite in the hanging wall of the Høybakken Detachment, NE of Hitra (Kendrick et al., 2004). This result has been interpreted as recording the early stages of brittle transtension along the MTFC (Kendrick et al., 2004). A very similar K-Ar illite age (312 Ma) has also been documented from the onshore East Greenland rift system and interpreted as evidence of a Palaeozoic rifting phase associated with Carboniferous faulting (Rotevatn et al., 2018). Additionally, similar Carboniferous ages have been reported in a study reporting a microstructurally controlled K-Ar dating approach by Scheiber et al. (2019) and, also, by Viola et al. (2016) farther south in coastal western Norway. In summary, the new results highlight early Carboniferous tectonic activity (likely transtensional, e.g., Kendrick et al., 2004; Osmundsen et al., 2021) onshore the MNPM. Also, Osmundsen et al. (2021) describe a "core-complex and basin" architecture for the proximal MNPM, arguing it to be the result of Late Palaeozoic-Early Mesozoic tectonic activity (Osmundsen et al., 2021). It is plausible that these structures formed during the Carboniferous. Finally, the Late Carboniferous ages are coeval also with the Late Carboniferous to Early Triassic Oslo rifting (Larsen et al., 2008; Fossen et al., 2021).

Although during the Triassic the offshore MNPM is known to have experienced a relatively quiescent period characterized by only moderate extension (Gernigon et al., 2020), our results indicate some Late Triassic activity. Thus, the c. 202 Late Triassic/Early Jurassic and the 177 Ma Jurassic mean ages possibly represent a distinct tectonic phase associated with crustal stretching during and/or slightly after the first rifting phase reported for the NE Atlantic (Gernigon et al., 2020).

Our 122 ± 5 Ma Early Cretaceous age may reflect onshore faulting related to the second rifting phase. In fact, in the Early Cretaceous extension is known to have occurred as recorded by movement along major boundary faults causing block rotation in the offshore MNPM, as well as the reactivation of the MTFC (e.g., Fjellanger et al., 2005; Osmundsen and Péron-Pinvidic, 2018). Finally, in the Late Cretaceous, a rifting episode is recorded in the outer Møre and Vøring basins. That rifting defined the pre-breakup setting with the structuring of the complex outer ridges and sub-basin system (Ren et al., 2003; Péron-Pinvidic et al., 2013). However, in the Late Cretaceous the proximal offshore domain is generally described as quiescent (Péron-Pinvidic et al., 2013; Gernigon et al., 2020) Thus, the obtained < 100 Ma Late Cretaceous ages could reflect later reactivation of onshore suitably-oriented faults, due to the later stages of rifting prior to the final breakup of the NE Atlantic Ocean (Gernigon et al., 2020). Similar ages have been reported by other authors onshore along the North Sea Margin (Tartaglia et al., 2020; Fossen et al., 2021 and references therein).

Table 5.3 - K-Ar dating results of 12 fault gouge and 1 altered rock (19.042E) samples.

		^{40}Ar*				K			Age Data	
Sample Name	**Fraction**	**Mass mg**	**mol/g**	**σ (%)**	**^{40}Ar* %**	**Mass mg**	**wt %**	**σ (%)**	**Age (Ma)**	**σ (Ma)**
19.006B	<0.1	2.272	9.34E-10	0.29	75.2	50.7	2.592	1.7	196.8	±3.1
	0.1-0.4	4.796	9.06E-10	0.24	82.5	50.9	1.972	1.8	247.2	±4.1
	0.4-2	2.884	6.02E-10	0.28	86.6	50.9	1.092	2.0	292.7	±5.4
	2-6	2.678	3.78E-10	0.32	88.5	51.0	0.637	2.2	313.2	±6.4
	6-10	6.752	3.23E-10	0.24	88.9	50.7	0.528	2.3	321.9	±6.8
19.007A	<0.1	2.508	4.00E-10	0.31	26.6	6.5	1.710	2.7	130.0	±3.4
	0.1-0.4	1.754	3.70E-10	0.39	26.7	51.6	1.370	2.0	149.4	±3.0
	0.4-2	4.040	5.10E-10	0.25	39.6	50.8	1.650	2.0	169.9	±3.3
	2-6	2.020	5.84E-10	0.32	52.1	50.4	1.730	2.0	184.9	±3.6
	6-10	1.580	5.96E-10	0.37	55.4	50.5	1.680	2.0	193.9	±3.8
19.011	<0.1	1.854	1.52E-10	0.61	12.6	10.1	0.671	2.4	125.7	±3.0
	0.1-0.4	1.898	1.85E-10	0.53	15.4	50.7	0.635	2.1	160.7	±3.4
	0.4-2	3.556	2.80E-10	0.30	19.2	52.3	0.746	2.1	204.3	±4.1
	2-6	2.560	3.43E-10	0.32	26.0	51.5	0.827	2.1	224.3	±4.5
	6-10	1.778	4.05E-10	0.38	33.6	53.5	0.880	2.1	247.7	±4.9
19.016	0.1-0.4	1.662	9.50E-11	0.97	13.4	50.6	0.549	2.1	97.1	±2.2
	0.4-2	1.858	1.43E-10	0.64	19.4	52.7	0.664	2.1	120.2	±2.6
	2-6	3.300	1.58E-10	0.39	23.5	50.1	0.705	2.1	125.0	±2.6
	6-10	2.270	1.91E-10	0.44	27.2	50.7	0.759	2.1	139.5	±2.9
19.030A	<0.1	2.310	1.20E-10	0.72	40.2	10.5	0.739	2.9	90.9	±2.7
	0.1-0.4	3.198	1.02E-10	0.61	57.0	51.8	0.528	2.3	108.4	±2.5
	0.4-2	2.428	1.50E-10	0.56	66.3	51.8	0.722	2.2	116.1	±2.5
	2-6	4.718	1.72E-10	0.31	79.2	50.5	0.809	2.1	118.8	±2.5
	6-10	1.760	1.81E-10	0.66	79.5	51.2	0.865	2.1	117.1	±2.5
19.042A	<0.1	3.394	4.60E-10	0.29	12.4	51.6	3.001	1.6	86.3	±1.4
	0.1-0.4	2.472	6.26E-10	0.30	18.9	51.9	3.020	1.6	115.7	±1.8
	0.4-2	2.902	9.40E-10	0.27	37.4	50.1	3.216	1.6	161.2	±2.5
	2-6	3.028	1.10E-09	0.26	49.1	50.2	3.473	1.5	173.6	±2.6
	6-10	2.644	1.01E-09	0.27	54.5	50.8	3.373	1.5	165.1	±2.5
19.049	0.4-2	1.104	1.27E-09	0.43	86.5	25.2	2.150	2.1	311.3	±6.2
	2-6	1.646	1.36E-09	0.33	87.4	50.6	2.210	1.9	323.6	±5.9

	6-10	1.744	1.47E-09	0.32	89.8	53.9	2.370	1.9	326.9	±5.8
19.07	<0.1	3.444	1.88E-10	0.37	28.4	50.1	1.330	1.3	79.6	±1.1
	0.1-0.4	2.202	3.42E-10	0.36	43.6	52.6	1.410	1.3	134.7	±1.7
	0.4-2	2.206	7.70E-10	0.30	69.9	54.3	1.890	1.2	220.9	±2.7
	2-6	1.554	1.06E-09	0.35	83.3	51.2	1.680	1.3	331.7	±4.0
	6-10	2.058	1.15E-09	0.30	85.0	54.0	1.700	1.3	352.1	±4.1
19.076	<0.1	1.036	3.26E-10	0.68	41.5	7.1	1.310	2.2	138.1	±3.0
	0.1-0.4	2.390	3.89E-10	0.33	55.9	50.3	1.320	1.3	162.4	±2.1
	0.4-2	1.936	4.75E-10	0.36	66.2	52.4	1.320	1.3	196.2	±2.5
	2-6	2.268	4.66E-10	0.32	68.3	52.7	1.210	1.3	209.2	±2.7
	6-10	2.750	4.71E-10	0.29	71.0	51.7	1.190	1.3	214.8	±2.8
19.078	<0.1	0.736	6.21E-10	0.70	32.5	51.5	1.940	1.2	175.7	±2.4
	0.1-0.4	1.596	9.14E-10	0.35	37.3	50.8	1.880	1.3	260.6	±3.2
	0.4-2	1.130	7.65E-10	0.46	37.6	54.8	1.290	1.3	312.9	±4.0
	2-6	1.766	7.07E-10	0.34	38.4	51.7	0.432	1.5	759.4	±9.6
	6-10	1.456	8.56E-10	0.38	47.6	51.1	0.456	1.5	847.8	±10.5
GT18_01	<0.1	1.868	1.93E-10	0.58	20.5	50.9	1.533	1.8	71.0	±1.3
	0.1-0.4	3.094	3.69E-10	0.30	32.5	49.9	2.183	1.6	94.9	±1.5
	0.4-2	4.078	6.08E-10	0.26	48.3	50.3	2.493	1.6	135.3	±2.1
	2-6	2.100	9.03E-10	0.31	65.3	50.6	2.780	1.5	178.2	±2.6
	6-10	1.694	1.06E-09	0.34	74.2	49.9	2.879	1.5	200.8	±3.0
GT18_02	<0.1	2.028	1.74E-10	0.60	40.3	23.2	0.768	2.5	126.0	±3.1
	0.1-0.4	1.792	3.10E-10	0.45	55.2	50.0	0.917	2.0	185.2	±3.7
	0.4-2	1.910	2.99E-10	0.44	54.8	50.5	1.120	1.9	147.8	±2.8
	2-6	1.604	3.91E-10	0.44	65.7	49.7	1.324	1.9	162.7	±3.0
	6-10	1.592	5.07E-10	0.40	69.1	50.8	1.356	1.9	203.6	±3.6
Altered rock sample										
19.042E	0.1-0.4	1.822	2.94E-10	0.45	37.4	30.7	0.921	2.3	175.2	±3.9
	0.4-2	2.440	3.49E-10	0.34	42.7	50.2	0.980	2.0	194.4	±3.8
	2-6	3.112	3.96E-10	0.29	47.9	51.0	1.115	2.0	194.0	±3.7
	6-10	1.988	4.42E-10	0.36	53.4	50.2	1.147	2.0	209.5	±4.0

5.5.3 Brittle evolution in time

Our study has allowed us to define and characterize the main trends of the brittle structural grain along the MNPM by remote sensing at the 1:10.000 and 1:100.000 scales and field work ground truthing. In order to obtain a comprehensive evolutionary model of the brittle deformation history recorded by the MNPM, the obtained structural and mineralogical data coupled with the K-Ar ages interpreted as geologically meaningful, are discussed for each set of brittle structures, subdivided according to their orientation. Moreover, a radial plot of structural data vs. obtained K-Ar ages is shown in Figure 5.11 and described in the following paragraphs.

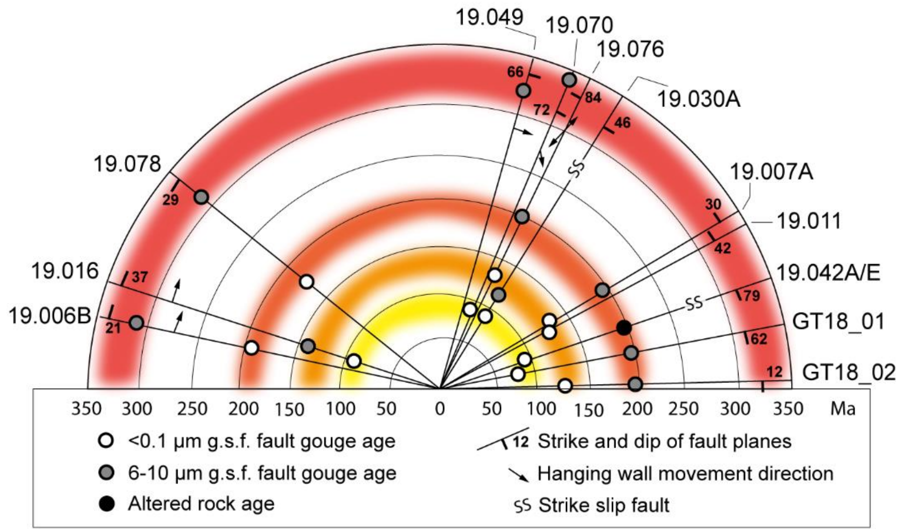

Figure 5.11 - Radial diagram of fault gouge and altered rock K-Ar ages plotted as a function of the fault plane orientation. (G.s.f.: grain size fraction).

5.5.3.1 NE-SW and NNW-SSE striking faults

The NE-SW and NNW-SSE striking lineaments are very common along the MNPM. By remote sensing, these lineaments appear to be the oldest structural features, as they are generally cut the other lineament trends (Fig. 5.3). Most of the NE-SW and NNW-SSE faults and fractures accommodate normal and transtensional kinematics. They are decorated by quartz, epidote, chlorite, calcite, prehnite, and commonly contain fault rocks such as fine-grained cataclasite and distinct layers of fault gouge.

The complex arrangement of cataclastic layers and mineral coatings (see Fig. 5.5e) derives mainly from this set of faults. They mainly contain epidote cataclasites dissected by quartz veins and by later thin prehnite cataclastic layers (Fig. 5.7).

Four dated samples belong to this set of lineaments (Fig. 5.11). Their K-Ar ages of the <0.1 µm grain size fractions are Early and Late Cretaceous. The coarser grain size fractions consisting of illite-smectite mixed layers and illite yield Carboniferous, Triassic, and Early Cretaceous ages (Fig. 5.11). These radiometric data, the widespread occurrence in the field of the NE-SW and NNW-

SSE striking faults and their variability in mineralogical coatings suggest that this set of faults recorded several brittle deformation events affecting the margin from the Carboniferous down to the last documented reactivation in the Late Cretaceous.

The NE-SW and NNW-SSE striking faults are geometrically and kinematically compatible with a transpressional stress regime with σ1 oriented NW-SE, which formed epidote and chlorite mineralizations. Additionally, they could be reactivated during the NW-SE extensional stress regime characterized by prehnite, quartz and calcite mineralizations. Some of these faults may thus have exploited a pre-existing Caledonian fabric, prior to their own repeated reactivation and reworking during rifting due to their geometrical compatibility with the extensional stress fields.

5.5.3.2 ENE-WSW striking faults

The ENE-WSW striking lineaments are parallel to the northern part of the MNPM coastline, specifically the trend of the MTFC. They are particularly abundant on the island of Hitra, where the main strand of the MTFC, the Hitra-Snåsa Fault, is exposed (Redfield et al., 2005, 2009). Remote sensing analysis indicates that this trend generally cut all the other detected trends, in particular in the area of Hitra. The radiometric dating of our selected ENE-WSW striking fault zones (Fig. 5.11) indicates that these faults have recorded brittle events along the MNPM ranging from the Late Triassic to the Late Cretaceous. The oldest radiometric age of this set of faults is Late Triassic (201 ± 3 Ma, GT18_01, Table 5.3).

The ENE-WSW striking faults have a variable dip and accommodate strike-slip (mainly sinistral) or normal kinematics. They are mainly associated with chlorite and iron oxide mineralizations and locally with epidote and prehnite. These faults are geometrically compatible with the E-W and NE-SW extensional regimes experienced by the MNPM (Fig. 5.8). The high angle ENE-WSW striking faults are generally localized along the MTFC mylonitic foliation. According to their radiometric ages, these studied faults record only the evidence of the brittle deformation due to the multiphase rifting of the NE Atlantic. However, pre-Triassic activity along the ENE-WSW faults, parallel to the MTFC, cannot be excluded. Potential evidence is to be found in the presented crosscutting relationships at the macroscale, the absolute dating of strands of the MTFC as Devonian and Late Carboniferous-Early Permian (e.g., Kendrick et al., 2004; Sherlock et al. 2004), as well as in the offshore ENE-WSW-trending lineaments bounding pre-middle Triassic strata in the Froan basin (Osmundsen et al. 2021). Indeed, ENE-WSW striking fault patterns in the area have been previously interpreted as Riedel-shears related the main branches of the MTFC (Hitra- Snåsa and Verran Faults), resulting from sinistral strike-slip tectonics during the late Devonian (e.g., Grønlie and Roberts, 1989). Thus, the inception of activity along the ENE-WSW trending faults is likely older than the obtained K-Ar ages of the studied gouges, and may have started already in the Devonian (Doré et al., 1999; Kendrick et al., 2004; Faleide et al., 2008; Gernigon et al., 2020).

5.5.2.3 WNW-ESE and E-W striking faults

As shown by the remote sensing analysis, WNW-ESE and E-W striking lineaments show mutual crosscutting relationship with the other trends (Fig. 5.3). In the field, WNW-ESE trending faults record dip-slip or strike-slip kinematics. The WNW-ESE and E-W striking faults are mainly associated with iron oxide mineralizations, incohesive brittle fault rocks, quartz, and calcite mineral coatings.

Three faults belonging to this lineament set have been dated (Fig. 5.11). Samples 19.006B and 19.078 were taken from two low angle dip-slip faults. These faults are situated in the northern- and southernmost studied segments of the MNPM where they cut across a granite (19.006B) and a gabbro (19.078). From a structural point of view, these faults are compatible with a compressional stress regime (NW-SE oriented σ_1, Fig. 5.1a). This compressional stress field may represent the stress field during the Caledonian orogeny. However, E-W and NW-SE thrusts and folds reported by previous authors in the Sunnfjord region and on Hitra and Frøya have been associated with a N-S shortening related to a contractional/transpressional event in the Late Devonian-Early Carboniferous, referred to as the “Solundian phase” (Braathen, 1999; Osmundsen and Andersen, 2001; Sturt and Braathen, 2001). It cannot be excluded that this set of faults originated during the Solundian phase.

K-Ar data of the samples 19.006B and 19.078 indicate that these two faults record a Carboniferous thermal/faulting event, c. 320 Ma ago, and later reactivation during Triassic-Jurassic rifting in an overall E-W extensional regime (Fig. 5.11). Therefore, they probably experienced a compressional event (the Caledonian or the Solundian phase) and were later reactivated in an extensional manner during Carboniferous and Triassic-Jurassic rifting.

Fault gouge 19.016 was collected from a moderately dipping normal fault. It records a different, younger brittle history which documents an Early Cretaceous origin and bears testimony of a Late Cretaceous reactivation (<97 Ma, Fig. 5.11) during a NW-SE extensional phase.

5.5.3 Regional implications

The mapping, characterisation and dating of the brittle structural framework along the MNPM allows us to place new temporal constraints onto the evolution of the margin, as summarized in Figure 5.12. This figure shows the obtained inverted paleostress fields through time and the strike of the brittle structures that accommodated faulting during the constrained deformation phases.

Out of the many structures preserved along the MNPM, some sets of faults in the Smøla-Hitra batholith may represent the brittle expression of Caledonian deformation. These sets of faults (Fig. 5.8a-b) show similar orientations and kinematics as along the North Sea Margin, where $^{39}Ar/^{40}Ar$ ages of ca. 450 and 435 Ma were obtained from synkinematic micas (Scheiber et al., 2016). In fact, paleostress inversion of our fault sets resulted in a pure compressional stress regime with σ_1 oriented NW-SE and a transpressional stress regime (R':1.98) with σ_1 oriented NW-SE, both of which are compatible with the Caledonian tectonic stresses reconstructed by other studies (e.g., Séranne, 1992; Scheiber and Viola, 2018; Fig. 5.12). Another possible interpretation (not illustrated in Fig. 5.12) is that the compressional stress regime could be related to the Late Devonian-Early Carboniferous N-S-oriented contractional/transpressional Solundian phase, which generated the E-W-trending folds and thrusts in the Solund Basin (North Sea) and on Hitra and Frøya (Braathen, 1999; Osmundsen and Andersen, 2001; Sturt and Braathen, 2001). The same compressional structures on Hitra and Frøya have been also previously interpreted as due to Early Devonian transtensional activity of the MTFC, which would have caused local NW-SE compression, coeval to slightly younger than the emplacement of the Smøla-Hitra batholith (e.g., Bering, 1992; Krabbendam and Dewey, 1998).

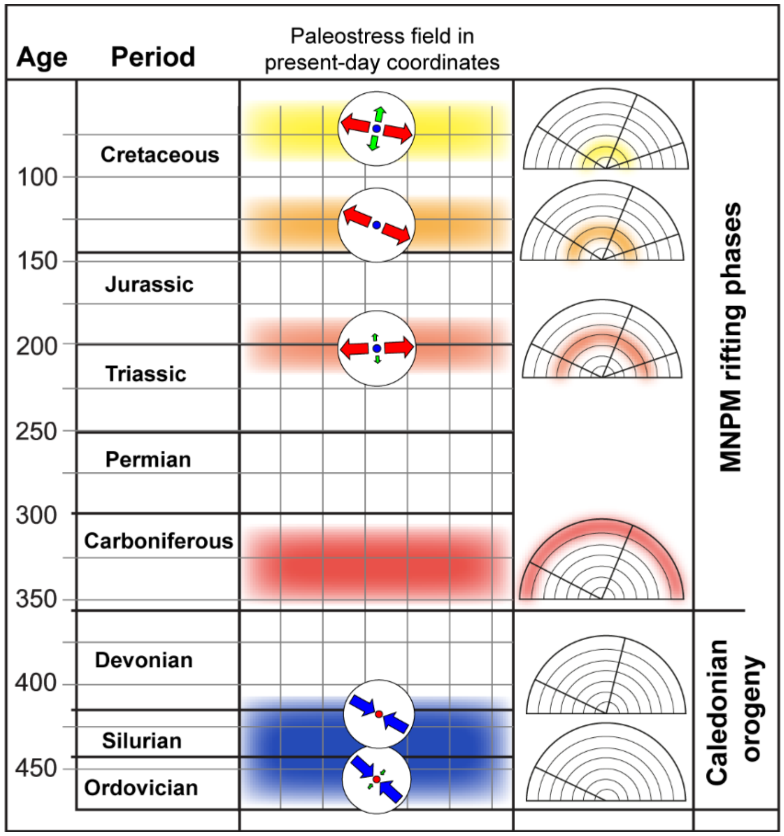

Figure 5.10 - Schematic summary of the obtained paleostress fields through time and strike of active brittle structures. The stereoplots represent the inverted paleostress regimes in present-day coordinates. The blue, green, and red arrows in the stereoplots represent the orientation of σ_1, σ_2 and σ_3, respectively.

In the area, the MTFC was possibly active in pre-Devonian times accommodating dextral transpression (Séranne, 1992) with the formation of pervasive ductile fabrics that were reactivated during the formation of the MNPM. The MNPM accommodated an extensional history that started in the Early Devonian with the collapse of the Scandinavian Caledonides (Doré et al., 1999; Faleide et al., 2008; Gernigon et al., 2020). A few structural observations onshore East Greenland support the idea that the first rifting phase affecting the NE Atlantic was in the mid-Carboniferous, but this model remains poorly constrained in the MNPM (e.g., Stemmerik et al., 2000; Rotevatn et al., 2018). However, our K-Ar ages from NE-SW and NW-SE striking faults support rift initiation along the MNPM in the Carboniferous. This is also in agreement with the dating of Late Carboniferous-Early Permian pseudotachylytes from the Hitra-Snåsa Fault (Sherlock et al., 2004) and of Late Carboniferous cataclasites along the Høybakken Detachment (Kendrick et al., 2004). It can be argued that this Carboniferous event is responsible for the formation of sedimentary basins in the proximal offshore domain of the MNPM, now possibly ascribed to the Late Palaeozoic-Early Mesozoic (Osmundsen et al., 2021). More evidence of the Late Carboniferous faulting along the MNPM may have been partly or fully obliterated by later slip deformation and the reworking of originally Carboniferous faults (Fossen et al., 2021). The main rifting phases experienced by the MNPM recorded in the offshore domain are reported in the Permo-Triassic and in the Late Jurassic-Cretaceous (Gernigon et al., 2020). Our data, however, clearly indicate that faulting took place already in the Late Triassic-Early Jurassic and in two pulses during the Cretaceous (Figs. 5.10, 5.11, 5.12). These rifting phases are well documented in the North Sea margin by a rapidly growing database of absolute K-Ar deformation ages (Ksienzyk et al. 2016; Viola et al. 2016; Scheiber and Viola, 2018; Scheiber et al. 2019; Fossen et al., 2021). According to our new dataset, the onshore MNPM recorded the effects of two slightly younger rifting phases in comparison to the rifting phases established in the North Sea margin which may be a result of the northward propagation of rifting (Ren et al., 2003; Gernigon et al., 2020; Zastrozhnov et al., 2020).

During the Triassic-Jurassic faulting event recorded by the onshore MNPM, E-W crustal stretching occurred, as well documented by previous studies from the North Sea and the MNPM (Gómez et al., 2004; Scheiber and Viola, 2018; Gernigon et al., 2020). This rifting phase reactivated older structures and formed epidote-rich cataclasites and quartz veins associated with NE-SW, NW-SE, and ENE-WSW-striking faults (Figs. 5.11, 5.12). Coeval alteration/deep weathering occurred, likely due to fluid circulation along brittle structures dissecting tilted blocks during rifting (e.g., Fredin et al., 2017).

The Cretaceous events along the MNPM have played a key role in the reactivation of older fault zones, forming extensive low temperature mineralizations along the exploited fault planes, such as calcite, prehnite and zeolite. The Early Cretaceous event recorded onshore correlates well with the formation of the offshore Møre and Vøring sedimentary basins and the activity of offshore major boundary faults (Osmundsen and Péron-Pinvidic, 2018; Zastrozhnov et al., 2018, 2020). The Late Cretaceous faulting event could also reflect the reactivation of suitably oriented faults during later stages of rifting prior to the final breakup of the NE Atlantic Ocean (Gernigon et al., 2020). Although similar ages have been reported from onshore faults along the North Sea Margin (Tartaglia et al., 2020; Fossen et al., 2021 and references therein), the Late Cretaceous faulting activity in the MNPM is only documented in the distal offshore domain (e.g., Péron-Pinvidic et al., 2013; Gernigon et al., 2020).

In the offshore domain, the MTFC separates the Jurassic–Cretaceous North Sea basins from the Cretaceous basins of the MNPM (Redfield et al., 2005), suggesting important offshore Cretaceous activity (Péron-Pinvidic et al., 2013). The faults parallel to the onshore MTFC recorded the rifting events from the Early Jurassic to the Late Cretaceous, supporting the active tectonic role of the multiply reactivated MTFC during rifting and the development of the margin.

5.6 Conclusions

The MNPM derives from a complex polyphase faulting history. Its evolution was influenced by the effects of the spatial orientation of old, inherited structures, such as the Caledonian orogen-parallel structural grain and the MTFC (cf. Osmundsen et al., 2006; Phillips et al., 2019; Schiffer et al., 2019). By means of remote sensing lineament analysis, field work, microstructural analysis, paleostress inversion, mineralogical characterisation and K-Ar dating of illite separated from selected fault zones, six tectonic events have been identified. From older to younger these are (Fig. 5.12):

i) Palaeozoic NE-SW compression forming WNW-ESE-trending and N(NE)-dipping low-angle thrust faults;

ii) Palaeozoic transpression with σ_1 oriented NW-SE forming conjugate NW-SE sinistral and E-W dextral strike slip faults;

iii) A Carboniferous faulting event associated with rift initiation forming NW-SE and NE-SW, variably dipping, faults.

iv) Late Triassic-Early Jurassic E-W extension at c. 202 and 177 Ma forming epidote and quartz-coated, N-S striking, generally normal faults, and coeval alteration of the host rock due to faulting-enhanced fluid circulation;

v) Early Cretaceous NW-SE extension representing the second rifting stage documented from the offshore domain of the MNPM, leading to the formation of normal, transtensional NE-SW and N-S striking faults;

vi) Late Cretaceous (K-Ar ages of c. 71, 80, 86, 91 Ma) extension reactivating suitably oriented pre-existing faults, with extensive synkinematic precipitation of low temperature coatings (prehnite, zeolite).

The lack of a preserved sedimentary cover and the long brittle evolution of the MNPM make the reconstruction of the tectonic evolution of the margin challenging. However, our new radiometric ages fill in the gap of absolute dating of fault activity along the MNPM.

Fault dating coupled with multiscalar structural analysis has been shown to be key to the study of the polyphase history of the margin. Finally, the applied workflow may assist the interpretation of the structural framework of the offshore domain, leading to high-resolution structural models and better exploration predictive tools.

Chapter 6

Clumped isotope thermometry of calcite veins within rifted basement

Giulia Tartaglia, Giulio Viola, Stefano M. Bernasconi, Thomas Scheiber, Alberto Ceccato

In preparation for Geology

Abstract

This paper presents the first application of clumped thermometry to calcite mineralisations within crystalline basements devoid of sedimentary cover. The Norwegian margin exposes a dense network of faults, formed since the Devonian, with calcite commonly decorating discrete slip planes and/or forming multiple generations of veins. 41 samples of calcite veins within faults from the Mid-Norwegian Passive Margin (MNPM) and 43 from the North Sea Margin have been analysed by carbonate clumped thermometry. This technique measures stable isotopic ratios and calculates the temperature and the $\delta^{18}O$ of the fluid from which calcite has crystallised.

The wide range of documented fluid temperature (21 – 186 °C) proves that calcite precipitated at varying thermal conditions during a multiphase evolution. Structural data integrated with geochemical results suggest a trend of decreasing fluid temperature in time. Results also constrain a varying source of fluids and carbon through time, from marine fluids circulating within marine carbonatic sediments (associated with higher temperature) to mixed fluids with increasing meteoric component (associated with lower temperature). The comparison of results from the MNPM and North Sea margins indicates that MNPM calcites mainly derive from highly mixed meteoric and marine fluids, locally circulating within paleosols in surficial environments, while North Sea calcites derive from seawater and mixed seawater fluids, probably at greater depth and with higher fluid temperature.

In conclusion, the presented dataset assists the reconstruction of synkinematic fluid circulation during rifting, adding new thermal and isotopic constraints to the tectonic brittle evolution of a complexly rifted basement.

6.1 Introduction

Carbonate clumped thermometry is an innovative geochemical methodology that measures the stable isotopic ratios of oxygen and carbon and calculates the temperature and the $\delta^{18}O$ of the fluid from which calcite has precipitated (Ghosh et al., 2006; Schauble et al., 2006; Eiler, 2007; Bernasconi et al., 2018, 2021). Carbonate clumped thermometry has been recently applied to address several research issues in the Earth Sciences (cf. Bernasconi et al., 2021 and references therein). The application of clumped isotope thermometry in structural geology, although still limited, has greatly improved the understanding of fluid flow within fault zones and the possibility to derive conceptual as well as numerical constraints upon the origin and temperature of mineralising synkinematic fluids (e.g., Bergman et al., 2013; Huntington and Lechler, 2015; Curzi et al., 2020; Salomon et al., 2020; Smeraglia et al., 2020). So far, however, this technique has been almost exclusively applied on carbonate samples (carbonatic rocks, travertines, calcite veins) from carbonatic successions, such that the obtained isotopic values can be directly compared to those of the host rock. This comparison is useful to deal with fluid circulation and possible system buffering processes (e.g., Smeraglia et al., 2020). On the other hand, the potential and limitations of carbonate clumped thermometry on calcite veins or tectonic carbonates emplaced within crystalline rocks have not yet been explored.

The Mid-Norwegian Passive Margin (MNPM) and the adjacent North Sea margin are examples of multiphase rifted margins (e.g., Gernigon et al., 2020, 2021; Fossen et al., 2021; Osmundsen et al., 2021). They experienced a long brittle evolution from the Devonian to the Cretaceous (Scheiber and Viola, 2018, Gernigon et al., 2020, 2021; Osmundsen et al., 2021). During their complex structural evolution, several fault, fault systems and fractures formed, many of which are extensively decorated by various mineral phases. Calcite veins and slickenfibers are quite commonly associated with these structures along the MNMP and the North Sea margin, at all scales (Scheiber and Viola, 2018; Scheiber et al., 2019).

Studying fluid circulation and characterizing different veining episodes in crystalline basement rocks can provide key elements towards a multidisciplinary reconstruction of the tectonic evolution of passive margins, particularly where the absence of sedimentary successions prevents detailed local and regional correlations. In order to better constrain the calcite veining episodes along the margin, to study fluid origin and migration modes and to quantitatively constrain different generations of calcite veins, clumped isotope thermometry has thus been applied to a large set of 84 calcite mineralisations collected from within fault zones along both the MNPM and the North Sea margin. It has to be pointed out that whereas the fractured and faulted basement along the studied tracts of the onshore Norwegian margin is devoid of any sedimentary cover, the corresponding offshore faulted basement is covered by thick sedimentary successions (Fredin et al., 2017a; Fazlikhani et al., 2020; Zastrozhnov et al., 2020; Osmundsen et al., 2021).

Adding geochemical constraints to existing tectonic models of the margin represents a significant step forward in the study of important geodynamic processes, can shed new light onto the evolution of both onshore and offshore domains and, thus, strengthen geological and structural correlations along and across strike the Norwegian coastline.

6.2 Geological setting

The North Sea Margin is a c. N-S-trending passive margin in Norway between latitude 57° 58’ and 61° 54’ N. Its northern continuation is the ENE-WSW-oriented MNPM (between 61° 54’ and 63° 55’ N). They both represent major morphotectonic features resulting from a multiphase rifting history that culminated with crustal breakup in the Eocene. The North Sea margin experienced two main rifting phases, the first in the Permian-Early Triassic and the second in the Jurassic, locally extending into the Early Cretaceous (Scheiber and Viola, 2018; Fossen et al., 2021; Gernigon et al., 2021; Osmundsen et al., 2021). The MNPM also recorded two rifting phases, albeit slightly younger than the North Sea. Recent reconstructions of the structural-geochronological evolution of the brittle deformation recorded along the MNPM constrain a Triassic-Jurassic extensional phase, and a second rifting phase in the Cretaceous (cf. Gernigon et al., 2020; Fossen et al., 2021). During this long brittle history, calcite repeatedly crystallised along faults and fractures. Field evidence and microstructural analysis indeed indicate several episodes of calcite crystallisation, whereby calcite precipitated during the entire documented brittle evolution, sometimes being dismembered and embedded within younger fault gouge, and cut by subsequent fault reactivations (Scheiber and Viola, 2018; Scheiber et al., 2019).

In order to add much needed constraints upon this complex evolution, calcite mineralisations from selected fault zones have been collected from two areas along the MNPM, on the islands of Hitra and Frøya to the north (Fig. 6.1A) and around the city of Ålesund in the southern sector of the MNPM (Fig. 6.1B). Samples from the North Sea Margin have been collected on the island of Bømlo (Fig. 6.1C). The chosen sampling areas expose crystalline basement rocks of the Scandinavian Caledonides. While Bømlo is composed of metamorphosed magmatic and sedimentary sequences, intruded by Ordovician granodiorite and gabbro (Scheiber et al., 2016), the area around Ålesund exposes rocks belonging to the Western Gneiss Region Complex, composed of Baltican Proterozoic gneiss (Walsh et al., 2013). Hitra consists of a Late Ordovician granodioritic batholith (Gautneb and Roberts, 1989), with micaschist and foliated migmatite of the Uppermost Allochthon cropping out in the northern part of Hitra and Frøya (Walsh et al., 2013).

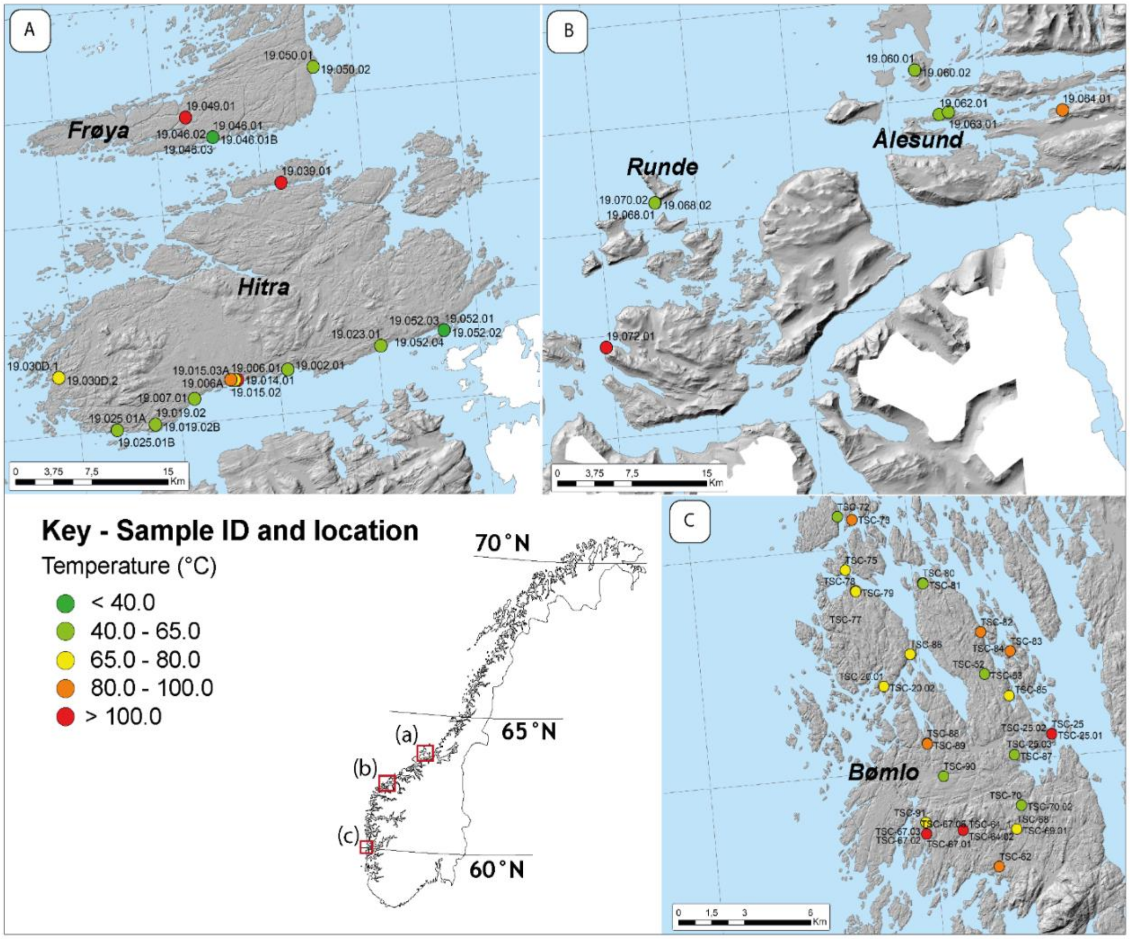

Figure 6.1: Maps of calcite sample locations, along the MNPM (A, B) and the North Sea margin (C). Labels indicate the sample ID.

6.3 Methods

During fieldwork we collected fault slip data for many faults and shear fractures, including fault orientation, slip direction, sense of movement, characteristics of the faulted lithotype, fault rock type and fracture mineralogy. The orientation of calcite-coated fault planes has been systematically measured. Calcites have been collected mainly from normal, N-S, NE-SW and NW-SE striking faults, and to a lesser extent from E-W striking faults.

Sampled calcites were subsequently grouped according to their geometrical properties in five types: matrix, blocky, fibrous, parallel and randomly oriented. *Matrix* samples are brecciated calcite veins or layers, where calcite represents the matrix embedding clasts of the host rock (Fig. 6.2a). *Blocky* samples are euhedral, cm-thick calcite crystals formed during the post-deformation infill of dilatant brittle structures (Fig. 6.2b). *Fibrous* samples are calcite slickenfibers, which therefore refer to a synkinematic crystallisation along striated fault surfaces (Fig. 6.2c). *Parallel* samples are from veins that crystallised parallel to the principal slip surface of the fault (Fig. 6.2d). Finally, *randomly oriented* samples are from calcite veins in fault zones whose orientation is discordant to the main slip surface.

As some of the samples exhibit an internally heterogeneous structure with different domains and/or generations of veins (Fig. 6.2), multiple domains have locally been drilled from the same hand specimen. In total, the remarkable number of 41 samples from the MNPM and 43 from Bømlo have been collected and analysed.

Clumped thermometry was carried out at the ETH Zurich, following the method described in Schmid and Bernasconi (2010), Meckler et al. (2014), and Müller et al. (2017). The methodology determines the temperature-dependent excess abundance of ^{13}C-^{18}O bonds in the carbonate lattice above a theoretical random distribution (Ghosh et al., 2006; Schauble et al., 2006; Eiler, 2007). This method retrieves the formation temperature of carbonate minerals independently from the $\delta^{18}O$ of the fluid in which the mineral grew (Bernasconi et al., 2018). Hence, it measures the stable isotopic ratios of oxygen and carbon and calculates the temperature and the $\delta^{18}O$ of the fluid (Ghosh et al., 2006; Bernasconi et al., 2021). Carbon and oxygen isotope compositions are reported in the conventional delta-notation with respect to VPDB and VSMOW, respectively. All structural and isotope data are listed in Table I.1 in the Appendix I at the end of this thesis.

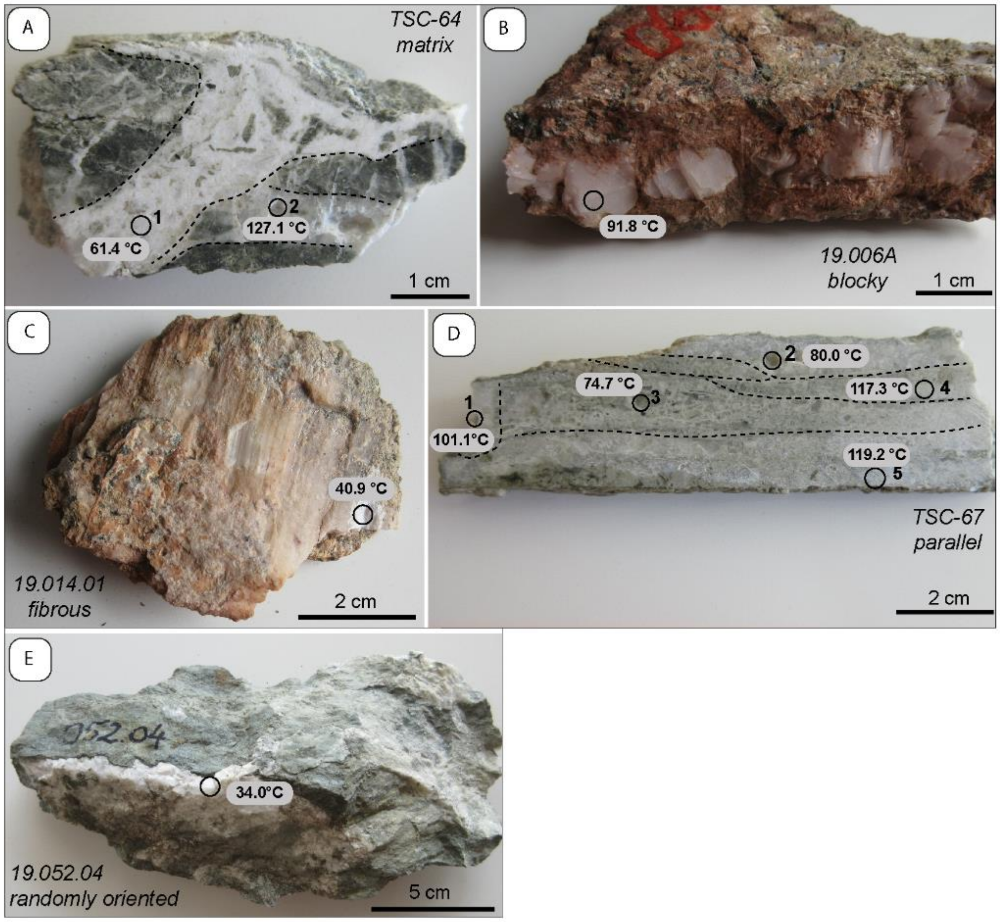

Figure 6.2: Types of calcite samples: A) *Matrix* sample type, in which calcite is the matrix of a brecciated material with clasts of the host rock; B) *Blocky* calcite is a post-deformation infill, crystallised as coarse grains; C) *Fibrous* synkinematic slickenfibers; D) *Parallel* calcite vein, the vein is parallel to the fault plane; E) *Randomly oriented* calcite vein with respect to the main slip surface of the fault (not visible in the photo).

6.4 Results

Stable isotope ratios of carbon and oxygen of MNPM vary in a broad range: $\delta^{13}C$ varies from -22.8 to 0.5‰, and $\delta^{18}O$ from +6.0 to 23.6‰ (Fig. 6.3A). Bømlo samples, however, show smaller range, with $\delta^{13}C$ between -9.9 and 10.2 ‰, and $\delta^{18}O$ between +13.9 and 33.1‰ (Fig. 6.3D). Both regions show a broad range of calcite formation temperatures ranging between 26 ± 5 and 186 ± 7 °C and between 21 ± 4 to 127 ± 7 °C for the MNPM and Bømlo, respectively (Fig. 6.3B, E, F).

The two groups of samples exhibit a correlation between increasing $\delta^{18}O$ and decreasing $\delta^{13}C$ (Fig. 6.3A, D). MNPM calcite veins with higher formation temperature are associated with higher, slightly negative $\delta^{13}C$ values (Fig. 6.3B). The higher temperatures from Bømlo are shown also by samples with slightly negative $\delta^{13}C$ values (> -4.0 ‰; Fig. 6.3E).

The mean temperature values from the two margin segments are similar (Fig. 6.3E). MNPM samples locally recorded a higher fluid temperature, even if the median value for that margin tract is lower than that from Bømlo samples by c. 15 °C. In total, 11 samples (6 from MNPM and 5 from Bømlo) recorded a growth temperature higher than 100 °C. They all derive from high angle, normal and locally dextral fault zones, oriented N-S and NW-SE.

Values of fluid $\delta^{18}O$ positively correlate with calculated temperature (Fig. 6.3C, F). This correlation is better expressed in the Bømlo dataset (Fig. 6.3F). However, the mean, median and the value ranges of fluid $\delta^{18}O$ are lower, albeit within error, between the two margins, with values of Bømlo samples ranging from -9.3 to +3.2‰, and those from the MNPM ranging from -15.8 to +0.4‰, (Fig. 6.3H).

The correlation between the isotopic data and the five different sample types documents that *blocky* calcite in both margins yield $\delta^{13}C$ values < -5.0‰, $\delta^{18}O$ >15‰, fluid $\delta^{18}O$ ranging between -4 and -2‰, and a temperature between 45 and 100° C (Fig. 6.3). All the *fibrous* samples yield $\delta^{18}O$ > 13‰ and a temperature < 100 °C. Matrix samples in the two margins have different isotopic values, but they crystallised from fluid at T≥60 °C. *Randomly oriented* samples have only been collected along the MNPM and generally yield quite scattered values with fluid $\delta^{18}O$ <-4‰. Also, calcite veins parallel to the principal slip surfaces of faults of the MNPM yield scattered values. *Parallel* samples from Bømlo record a fluid temperature >50 °C (Fig. 6.3).

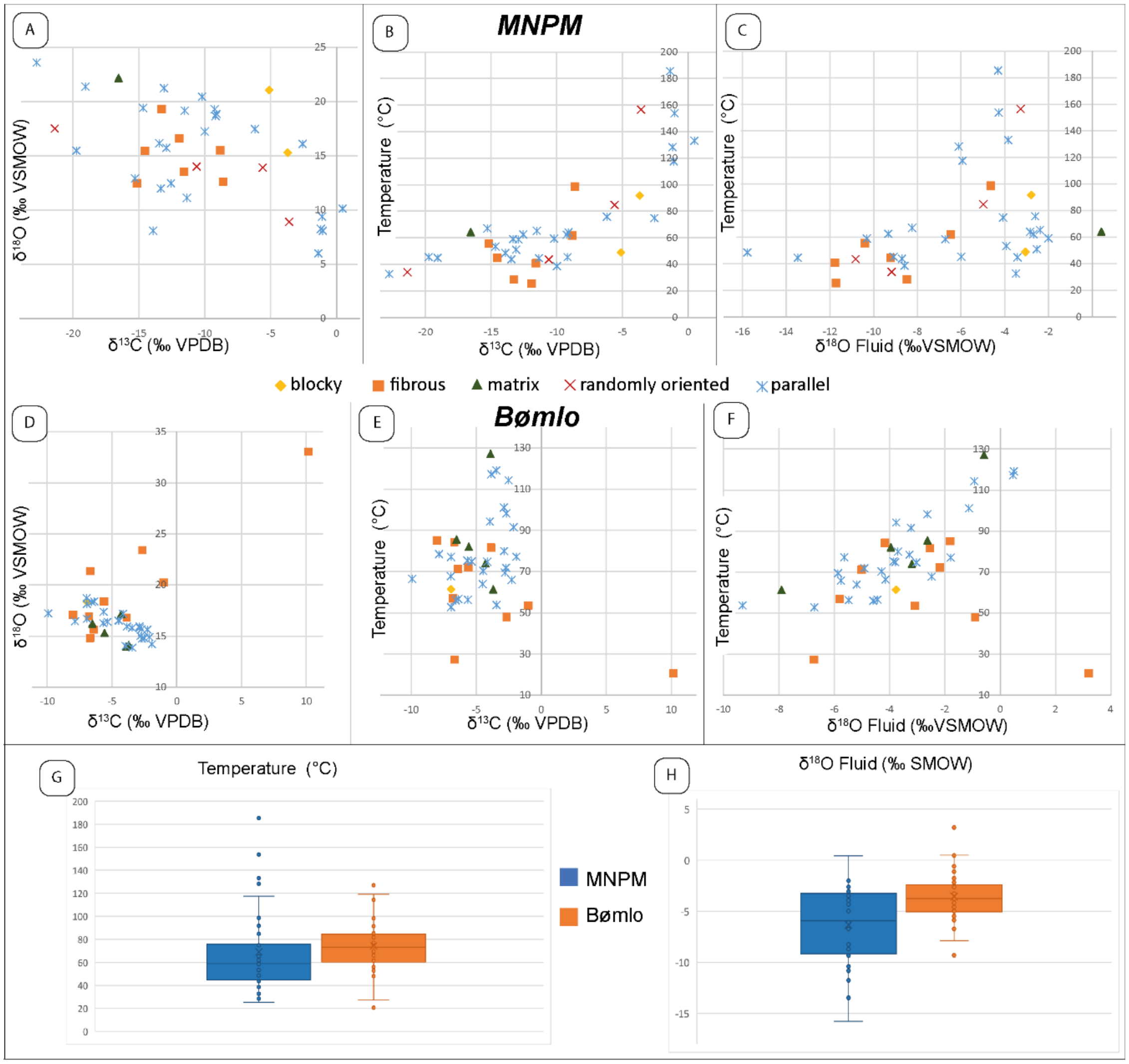

Figure 6.3: Clumped isotope palaeothermometry results. δ^{13}C (VPDB)-δ^{18}O (VSMOW) diagrams for MNPM (A) and Bømlo samples (D); δ^{13}C (VPDB)-Temperature diagrams for MNPM (B) and Bømlo samples (E); Fluid δ^{18}O (VSMOW)-Temperature (°C) diagrams for MNPM (C) and Bømlo samples (F); box plots of measured temperature (G) and fluid δ^{18}O (VSMOW) (H) of the two study areas. Fluid δ^{18}O (VSMOW) is calculated according to O'Neil et al. (1969). The x in the plots indicates the mean value and the horizontal line in the box indicates the median value.

6.4 Discussion

Fluid δ^{18}O allows us to assess the fluid source from which calcite of the studied tectonic carbonates crystallised. In general, the δ^{18}O VSMOW of seawater ranges from −1.5‰ to +1.5‰ (LeGrande and Schmidt, 2006; Salomon et al., 2020). The calculated fluid δ^{18}O, therefore, likely reflects a marine fluid source with a variable contribution of meteoric waters. Generally lower, highly negative values of $\delta^{18}O$ fluids are associated with lower temperatures, suggesting that low temperature fluids are more significantly affected by meteoric influx.

The slightly negative $\delta^{13}C$ VPDB values, associated with positive, $\delta^{18}O$ values (Fig. 3A, D) are in a range typical of marine carbonates (Trumbore and Druffel, 1995). The lowest $\delta^{13}C$ VPDB values of the Bømlo calcite veins (-9.9 ‰) suggest an origin from atmospheric fluids and CO_2 from soil respiration (Trumbore and Druffel, 1995). The same can be inferred for the MNPM samples. An exception is represented by the lowest obtained $\delta^{13}C$ values that range between c. -10 to -23‰. A carbon isotope ratio <-15‰ requires a significant source of soil CO_2, dominated by organic matter respiration (Trumbore and Druffel, 1995; Drake et al., 2017). Therefore, the highly negative $\delta^{13}C$ VPDB and positive $\delta^{18}O$ of MNPM samples suggest mixing of meteoric fluids with organic matter during their migration in paleosols.

The formation temperature of the sampled calcites can be assessed from the clumped isotope temperatures, but their interpretation needs to be taken with caution, specifically in case the samples have been heated after initial precipitation. Calcite is subject to solid-state reordering of C-O bonds at ambient temperatures >90-120 °C, affecting the abundance of heavy clumped bonds and thus deviating the clumped isotope-derived temperature from the real initial formation temperature (Passey and Henkes, 2012; Stolper and Eiler, 2015; Hemingway and Henkes, 2021; Salomon et al., 2020). Thermochronological reconstructions of the North Sea and MNPM indicate a general uplift of faulted blocks during the two main rifting phases (Johannessen et al., 2013; Ksienzyk et al., 2016). Although thermochronological data and the occurrence of highly weathered horizons indicate a possible basement exposure in the Late Triassic and reburial in the Jurassic, thermochronological studies indicate that ambient temperatures remained <150 °C during rifting (Ksienzyk et al., 2016; Fredin et al., 2017a). Thus, calcite lattice reordering was probably minor and can be ignored.

Obtained temperatures define a wide range, from 186 to 21 °C (Fig. 6.3G). The higher temperatures are generally associated with carbon and oxygen isotopes corresponding to a fluid of marine origin, whereas lower temperatures indicate a larger influence of meteoric fluids. Our data allow us to conclude that the *matrix* samples from the brecciated veins all derive from medium to high temperature fluids with T≥60 °C. *Fibrous* calcite yield growth temperature <100 °C, deriving from a mixed seawater/meteoric fluid. *Blocky* calcite crystals in both margins show a smaller influence of meteoric fluids than the other fibrous synkinematic. *Parallel* and *randomly oriented* samples do not show any evident trend related to the temperature or origin of the involved fluid. This confirms the high variability of type and temperature of fluid circulation experienced during the polyphase tectonic history of the margin. Moreover, the lack of an isotopic cluster among the *parallel* samples suggest that this group likely includes synkinematic and post-deformational infills, formed from various fluids.

6.4.1 Tectonic implications

The broad range of temperature and stable isotope ratios suggest that the formation of the sampled calcite mineralisations occurred at variable conditions, under the effects of evolving multiple fluid batches during a polyphase tectonic evolution (cf. Grønlie et al., 1990; Scheiber and Viola, 2018; Scheiber et al., 2019; Osmundsen et al., 2021).

It has been documented that during the tectonic evolution of these segments of the Norwegian margin, the ambient temperature generally decreased with the decreasing depth of the system *en route* to surface during exhumation (Ksienzyk et al., 2016; Scheiber and Viola, 2018). Mesoscopic crosscutting relationships integrated with the new geochemical results indicate that lower temperature veins cut across higher temperature veins, compatible with a progressively decreasing fluid temperature through time, and, in turn, compatible with a retrograde deformation history (Fig. 6.2A, D). In addition, calcite veins that precipitated from fluids at T>100 °C are structurally associated with high angle, N-S and NW-SE striking fault zones with normal and locally dextral strike-slip kinematics. These faults mainly nucleated during the Permian and Late Triassic-Jurassic rifting stages, for the North Sea and MNPM, respectively, and are the oldest recorded during the rifting history (Scheiber and Viola, 2018; Gernigon et al., 2020). Thus, calcite growth temperatures likely decreased in time, such that high temperature veins are generally the oldest. The associated isotopic ratios indicate that these high temperature veins likely derive from fluids dominated by seawater, where seawater infiltrated through thin, still unconsolidated carbonatic successions.

On the other hand, veins with T<100 °C derive from seawater mixed with a significant meteoric fluid component. In the analysed regional framework, this change of fluid origin implies a change of burial depth, likely related to the retrograde uplift of the margin. The probable tectonic environment may be described by the presence of uplifted faulted blocks, in which meteoric fluids infiltrated and exploited faults and fractures as high-permeability corridors.

The MNPM samples that yielded negative (<-10‰) $\delta^{13}C$ values and associated to T<67 °C likely formed from meteoric fluids that previously infiltrated soils enriched in organic matter (Trumbore and Druffel, 1995; Drake et al., 2017). This context is conceivable in a rifting framework where tectonic blocks can be tilted and locally become exposed subaerially. In fact, highly weathered horizons affecting basement rocks onshore and offshore the Norwegian margin have been dated to the Late Triassic-Jurassic (Fredin et al., 2017a; Scheiber and Viola, 2018), and the coeval subaerial uplift is also supported by thermochronological studies (Ksienzyk et al., 2016).

Comparing the two margins, Bømlo calcite veins constrain a c. 15 °C higher mean temperature than those from the MNPM. This difference is not related to the number of analysed samples, because it is comparable among the margins. The mean temperature variation could be due to the sampling area (Fig. 6.1), which is much wider for MNPM samples than for Bømlo, or to an actual generally higher fluid infiltration during rifting along the North Sea margin. This hypothesis could be supported by the variation of fluid $\delta^{18}O$ values (Fig. 6.2H): MNPM samples derive mainly from highly mixed meteoric and marine fluid, while Bømlo samples derive from seawater and mixed seawater fluids, probably at deeper conditions with higher temperature fluids.

6.5 Conclusions

Clumped thermometry helped constrain the precipitation temperature and fluid origin of calcite veins collected from a multiphase rifted basement, devoid of any sedimentary cover. Results permit a plausible reconstruction of fluid pathways during rifting phases. The >100 °C calcite veins are likely the oldest recorded (Permian and/or Late Triassic-Jurassic; Scheiber and Viola, 2018; Gernigon et al., 2020), precipitated from syntectonic fluids of marine derivation at higher depth. The majority of calcite veins and slickenfibers crystallised from mixed fluids, at temperature ranging between c. 40 and 80 °C.

The isotopic values of the MNPM permit to constrain the presence of exposed tectonic blocks where meteoric fluids circulated within paleosols and infiltrated the faulted basement, crystallising calcite veins (cf. Riber et al., 2017; Fredin et al., 2017a). Analysis of the offshore analogue sedimentary sequences above the faulted basement structural highs may assist in the interpretation of the data and add information on the fluid circulation pathways through time.

Chapter 7

This chapter summarises the results of the study presented in the papers "*Constraints upon fault zone properties by combined structural analysis of virtual outcrop models and discrete fracture network modelling"* by Alberto Ceccato, Giulio Viola, Marco Antonellini, myself and Eric J. Ryan (Ceccato et al., 2021a) and "*In-situ quantification of mechanical and permeability properties on outcrop analogues of offshore fractured and weathered crystalline basement: Examples from the Rolvsnes granodiorite, Bømlo, Norway"* written by Alberto Ceccato, Giulio Viola, myself and Marco Antonellini (Ceccato et al., 2021b).

In order to link the structural analysis of onshore fractured outcrops to the offshore basement fracture pattern, the modelling of geometrical, mechanical and permeability properties of fractured and weathered outcrops was performed by relying on the assumption that they are effective analogues of highly inaccessible offshore crystalline basement highs. Specifically, we combined field structural analysis with Virtual Outcrop Models (VOM) to quantify the geometrical parameters of several fracture sets associated with a regional fault zone, the Goddo Fault Zone (Bømlo, southwestern Norway). Results were used as input to Discrete Fracture Network (DFN) modelling to quantify the structural permeability related to the presence of mesoscale fracture networks across the fault. In addition, we measured *in-situ* structural, geomechanical (uniaxial compressive strength, UCS), and petrophysical (permeability, k) properties to characterise the Goddo Fault Zone and other selected and representative outcrops of fractured and weathered crystalline basement rocks on the island of Bømlo (Fig. 7.1a and b).

7.1 Rationale of the study

Pristine, unaltered crystalline basement rocks are characterised by a very low intrinsic porosity, and, consequently, by low matrix permeability (<10^{-4} mD), i.e., the permeability directly related to the textural, compositional and alteration characteristics of host crystalline basement rocks (Braathen et al., 2018). A "structural" permeability may instead exist within fractured crystalline volumes in relation to the presence of structural discontinuities at all scales, from microfractures to crustal-scale fracture and fault zones (Sibson and Rowland, 2003; Holdsworth et al., 2020). Brittle deformation may affect the geometrical arrangement of brittle structural facies within a fault zone, and, in turn, the fault's overall mechanical strength and permeability through the development of secondary porosity. This reflects directly upon the fluid flow and storage capabilities of basement rocks and the definition of potential unconventional plays (Caine et al., 1996; Stober and Bucher, 2007; Place et al., 2016; Braathen et al., 2018; Bonter and Trice, 2019; Trice et al., 2019; Holdsworth et al., 2020).

The geometrical and spatial features of a fractured rock volume in the offshore domain are commonly defined by means of seismic geophysical investigations. Textural variations, fracture, and fault zones displaying sufficient seismic impedance contrast as well as fault dimensions and/or throws > 4-10 m are usually detected by reservoir-scale seismic investigations and are thus classified as seismic-resolution-scale (SRS) features (Tanner et al., 2019). However, the site-scale fluid transport and storage capabilities are mostly controlled by sub-seismic-resolution scale (SSRS) features (thickness/throw <4-10 m; Damsleth et al., 1998; Walsh et al., 1998). Therefore, to build a comprehensive and quantitative model of a fractured weathered basement volume, it is necessary to deal with the three-dimensional spatial arrangement of fault networks at all scales, and also to characterise the details of the petrophysical and mechanical properties of SRS and SSRS fault zones.

Our structural, geometrical modelling and *in situ* petrophysical results are thus useful to help bridge the gap between field observations and large-scale geological contexts, where the lack of direct access to the geological objects of interest and the processes determining their spatial and temporal evolution commonly preclude straightforward correlations and quantifications. Moreover, quantitative, high-resolution geomechanical and petrophysical datasets are quite rare, yet fundamental for interpreting increasingly higher-resolution geophysical datasets, for reducing the uncertainty in reservoir modelling, for better constraining fault zone mechanics and for assessing borehole stability during exploration and drilling (Rutqvist and Stephansson, 2003; Wibberley et al., 2008).

An unconventional reservoir is composed by the following constituents (Riber et al., 2015, 2017; Fredin et al., 2017a; Braathen et al., 2018; Lothe et al., 2018):

(1) host crystalline rock, characterised by primary low porosity/permeability;

(2) fractures, fault zones, mineral veins and open fissures characterised by enhanced micro- and mesoscopic fracture porosity;

(3) fluid-rock interaction zones related to either alteration along structural discontinuities or to top-basement paleo-weathering profiles;

(4) fault zones buffering/sealing and bounding the structural highs;

(5) sedimentary cover overlying the weathered crystalline basement acting as either reservoir rock, top-seal and/or source rock.

7.2 Geological background

The island of Bømlo is located in southwestern Norway. It exposes igneous basement (granodiorite, granite and gabbro) and volcano-sedimentary units of Ordovician-Silurian age belonging to the Upper Allochthon (Slagstad et al., 2011). The Bømlo crystalline basement is considered as the potential onshore analogue of fractured and weathered basement reservoirs of the Utsira High, an unconventional reservoir located offshore western Norway in the northern North Sea (Fig. 7.1a-7.2a; Trice et al., 2019). The study area is made of the Rolvsnes granodiorite (RGD, 466 ± 3 Ma, U/Pb on zircon) (Scheiber et al., 2016; Fig. 7.1b). After its emplacement in the Ordovician, the RGD remained at shallow crustal levels (<10-15 km depth), thus escaping pervasive ductile deformation and metamorphic re-equilibration during the Scandian tectonometamorphic event (Scheiber et al., 2016; Scheiber and Viola, 2018).

During the post-Caledonian orogenic collapse and extension, the Upper Allochthon units in the Bømlo region were part of the hanging wall of the Hardangerfjord Shear Zone, (Fig. 7.1a) (Fossen and Hurich, 2005), and recorded the prolonged brittle deformation history described in Chapter 2 (Scheiber et al., 2016; Scheiber and Viola, 2018; Fossen et al., 2021). This area mainly recorded the North Sea rifting phases in the Permo-Triassic and in the Late Triassic-Jurassic, with some discrete Cretaceous extensional episodes (Scheiber and Viola, 2018; Gernigon et al., 2020; Fossen et al., 2021).

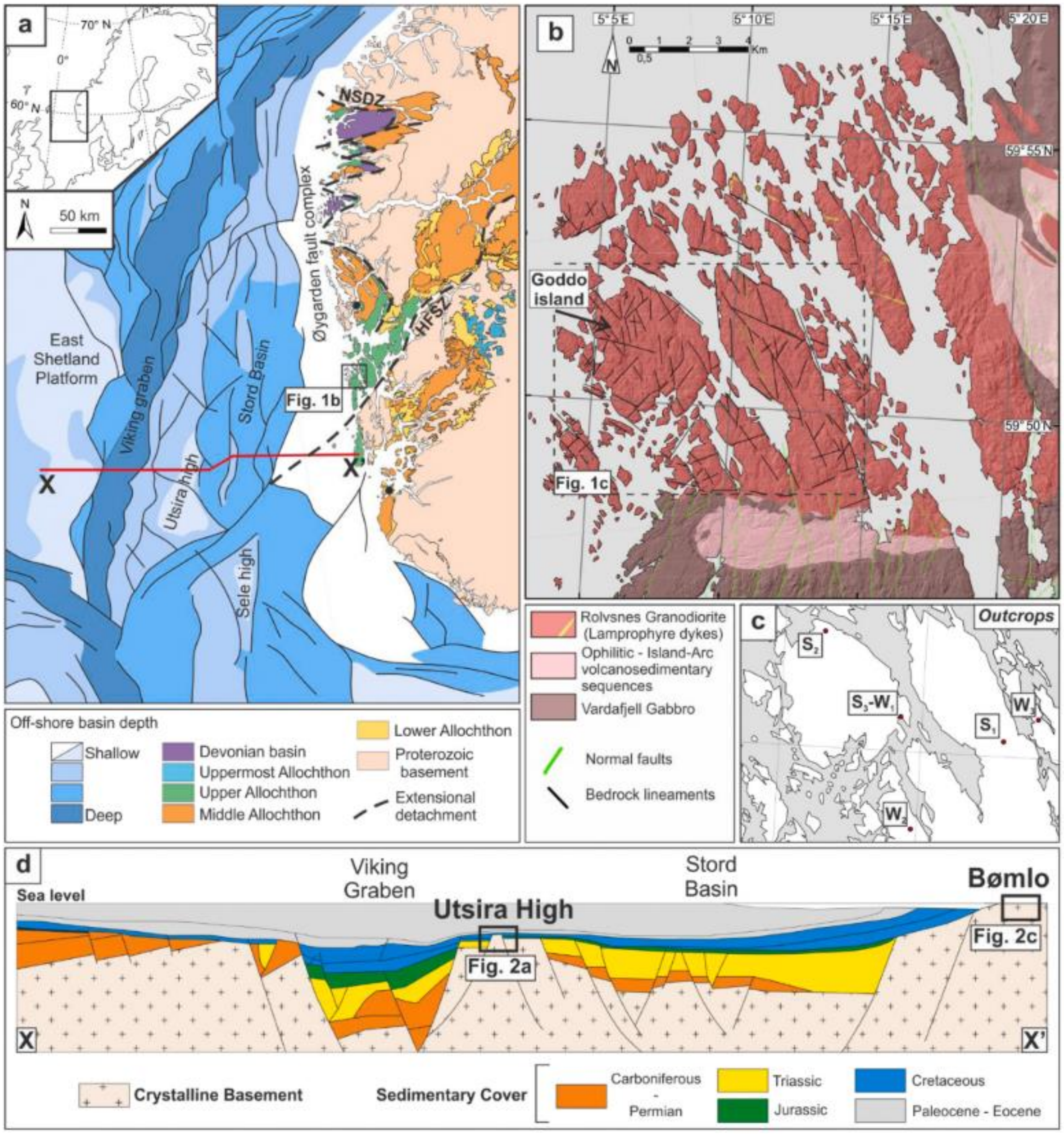

Figure 7.1 - a) Geological map of southwestern Norway and the northern North Sea (modified after Slagstad et al., 2011; Scheiber and Viola, 2018). HFSZ: Hardangerfjord Shear Zone; NSDZ: Nordfjord - Sogn Detachment Zone. The red line X-X′ represents the trace of the geological cross section presented in (d); b) Geological map of the northern Bømlo area, including the island of Goddo (redrawn from the NGU geological map of Norway 1:50000). (c) Simplified topographic map of Bømlo showing the locations of the studied outcrops, S3 represents the Goddo Fault Zone. (d) Schematic geological cross section through the central North Sea (X-X′ in (a)) (Ceccato et al., 2021b).

The basement on Bømlo also experienced pervasive alteration/weathering in response to subaerial exposure in tropical humid climate conditions during the Triassic, forming a thick weathering profile (Fredin et al., 2017a). Similarly, the offshore Utsira High reservoir is characterised by a pervasively fractured crystalline basement, mainly composed of intrusive and gabbroic rocks of Ordovician-Silurian age (Slagstad et al., 2011; Riber et al., 2015), on top of which rests a paleo-weathering profile formed during the late Triassic (Fredin et al., 2017a; Riber et al., 2017; Lothe et al., 2018) (Fig. 7.2b).

On Bømlo, we have worked on five selected outcrops (Fig. 7.1c) that are thought to be representative of the structural discontinuities that affect the crystalline basement "matrix" properties at different scales, from SSRS fracture corridors to SRS fault zones (Fig. 7.2c) and textural heterogeneities related to the progressive development of alteration/weathering products (Fig. 7.2b).

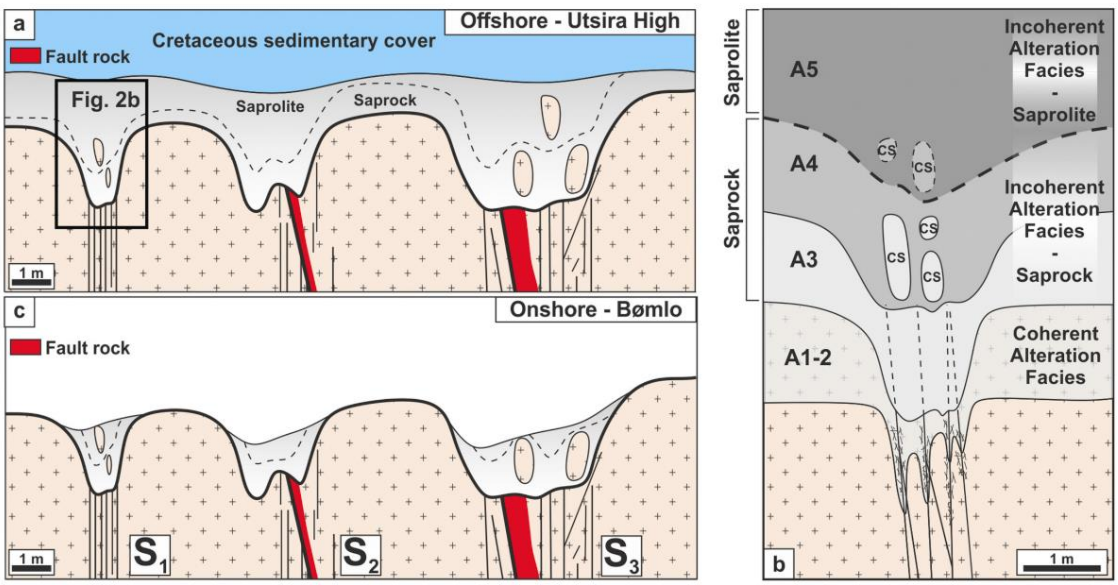

Figure 7.2 - a) Schematic representation of the fractured and weathered basement top section preserved offshore in the Utsira High beneath the Mesozoic sedimentary cover. This representation focuses on the fractured crystalline basement, the weathering profile (in grey) and the overlying sedimentary cover (light blue). b) Simplified sketch of the top-basement weathering profile showing the gradual transition from unaltered and fractured host rock at the base of the profile, toward saprock and saprolite at the top. The weathering profile reaches greater depths where in correspondence with structural discontinuities (in this case, a SSRS fracture corridor, S1 of Fig. 7.2a, c). The progression of weathering is illustrated by the continuous darkening of the grey shades and the increasing number in the alteration/weathering grade on the left (A1-A5). (CS: core stones). c) Schematic representation of the fractured and weathered basement top section now exposed onshore on Goddo island. The erosion of the weathering profile led to the exposure of an "etched" basement top surface (Fredin et al., 2017a, b). S1, S2 and S3 represent the three typologies of deformation structures studied. S1: SSRS fracture corridors; S2: SSRS fault zone; S3: SRS fault zone (Ceccato et al., 2021b).

7.3 Methods

Our structural analysis focussed on the identification and characterisation of meso-scale fracture patterns and the definition of the main structural domains related to faulting. Field structural analysis was integrated with analyses of Virtual Outcrop Models (VOM) of the Goddo Fault Zone (GFZ) to quantify the geometrical parameters of the fracture sets associated with the fault zone. Results were subsequently used as input to Discrete Fracture Network (DFN) modelling (computed in FracMan) to quantify the structural permeability related to the meso-scale fracture network developed across the large-scale GFZ.

The proposed workflow includes four main steps: (1) creation of VOMs from UAV imagery; (2) detection and interpretation of fractures from VOMs; (3) analysis of fracture intensity and spatial organisation by means of virtual cross-sections and scanlines; (4) stochastic DFN modelling in FracMan.

For the five selected outcrops, direct petrophysical and geomechanically measurements have been done. *In-situ* permeability measurements have been carried out with an air-minipermeameter on both fault and altered/weathered rocks. The instrument allows a reliable field investigation of rock permeability within small volumes (1-1.5 cm3) in the 10^{-5}-10 D range (Filomena et al., 2014). The geomechanical characterisation has been carried out with a Schmidt hammer according to international standards. UCS values were retrieved from the analysis of Schmidt hammer rebound values (Aydin and Basu, 2005). The reliability range of the instrument extends between 10 MPa and 300 MPa of UCS (Aydin and Basu, 2005). Further details about the methodology are described in Sections §3.7 and §3.8.

7.4 Selected outcrops

Studied outcrops are grouped into Group S (representative of Structural features, S1 to S3) and Group W (Weathering features, W1 to W3) (Fig. 7.1c, 7.2c-d). Group S includes outcrops where the geomechanical and petrophysical characteristics of discrete mesoscopic deformation zones have been measured (Fig. 7.2c).

The field criteria adopted for the classification of different structures include: (i) the width of the deformation zone, as indicated by the across-strike thickness of the fractured domain; (ii) the occurrence/lack of fault rocks within the deformation zone; (iii) the width of the fault rock-bearing deformation zone (fault core). The width of the fault core may help us to quantify the minimum fault throw, and thus discriminate between SSRS and SRS deformation zones. The structural features included in Group S are: SSRS fracture corridors (S1), a SSRS fault zone (S2), and a SRS fault zone (S3). Group S is numbered according to the increasing size of the studied structural features (fracture/fault zone width) as constrained by outcrop observations.

Group W includes K-Ar dated outcrops used to characterise the weathering features affecting the crystalline basement (Viola et al., 2016; Fredin et al., 2017a; Scheiber and Viola, 2018). Group W includes the following outcrops: (i) outcrop W1 formed by partially altered RGD with incipient weathering and discolouring mainly localised along fractures; (ii) outcrop W2 formed by cohesionless, altered RGD, still preserving the magmatic structure but completely transformed into a sandy aggregate (saprock); (iii) outcrop W3 formed by cohesionless, altered RGD with increasing clay content (saprolite). The W outcrops are numbered from W1 to W3 according to the increasing degree of weathering (from incipient to evolved weathering). In all the analysed outcrops, alteration/weathering products invariably postdate the formation of brittle deformation zones.

7.2.1 Group S - fractures and fault zones within the crystalline basement

Outcrop S1 contains a deformation zone defined by a 10-15 m thick fracture corridor. The central portion of the fracture corridor is characterised by a 2-5 m thick zone of high fracture-intensity (average fracture spacing = 0.05-0.1 m), composed of NNE-SSW-trending subvertical open fractures (Fig. 7.3a). Their typical aperture (*sensu* Ortega et al., 2006) is in the order of <1 mm. This deformation zone likely accommodated minor (<1m) lateral displacement, as inferred by the only local and rare development of fault striae (mainly strike-slip) on fracture surfaces and the limited offset (c. 6 cm) of crosscut magmatic markers (Scheiber and Viola, 2018). The presence of eroded saprolite horizons has been inferred above the outcrop (Fig. 6g, h in Scheiber and Viola, 2018). The finest grain-size fractions of the alteration rock observed within the fractures are enriched in smectite-like clays of Jurassic age (187.5 ± 16.7 Ma; sample TSC-1 of Scheiber and Viola, 2018). Alteration of the rock postdates the formation of the fracture corridor, which is thus older than Jurassic in age. The only limited throw (<1 m) and width of the fracture corridor core (<10 m) suggest that outcrop S1 represents a SSRS fracture corridor.

Outcrop S2 contains two subparallel SSRS fault zones embedding a 10 cm thick cataclastic fault core (Fig. 7.3b). Each fault zone is characterised by a polished principal slip surface (PSS) oriented 140°/70° (dip direction/dip) (Fig. 7.3b). The PSS is decorated by transtensive-kinematics slickenlines. The thickness of the fault core (10 cm) would be consistent with a fault throw in the order of 1-10 m (Torabi and Berg, 2011). The host RGD and the cataclastic core are locally altered, as documented by the occurrence of an irregular volume of sandy material (Fig. 7.3b). The alteration product is characterised by an increasing kaolinite content over smectite (sample TSC-36 of Scheiber and Viola, 2018). K-Ar dating on authigenic clays constrains alteration to the Cretaceous (127.4 ± 16.5 Ma; Scheiber and Viola, 2018). Therefore, the age of faulting must be older than Cretaceous in age.

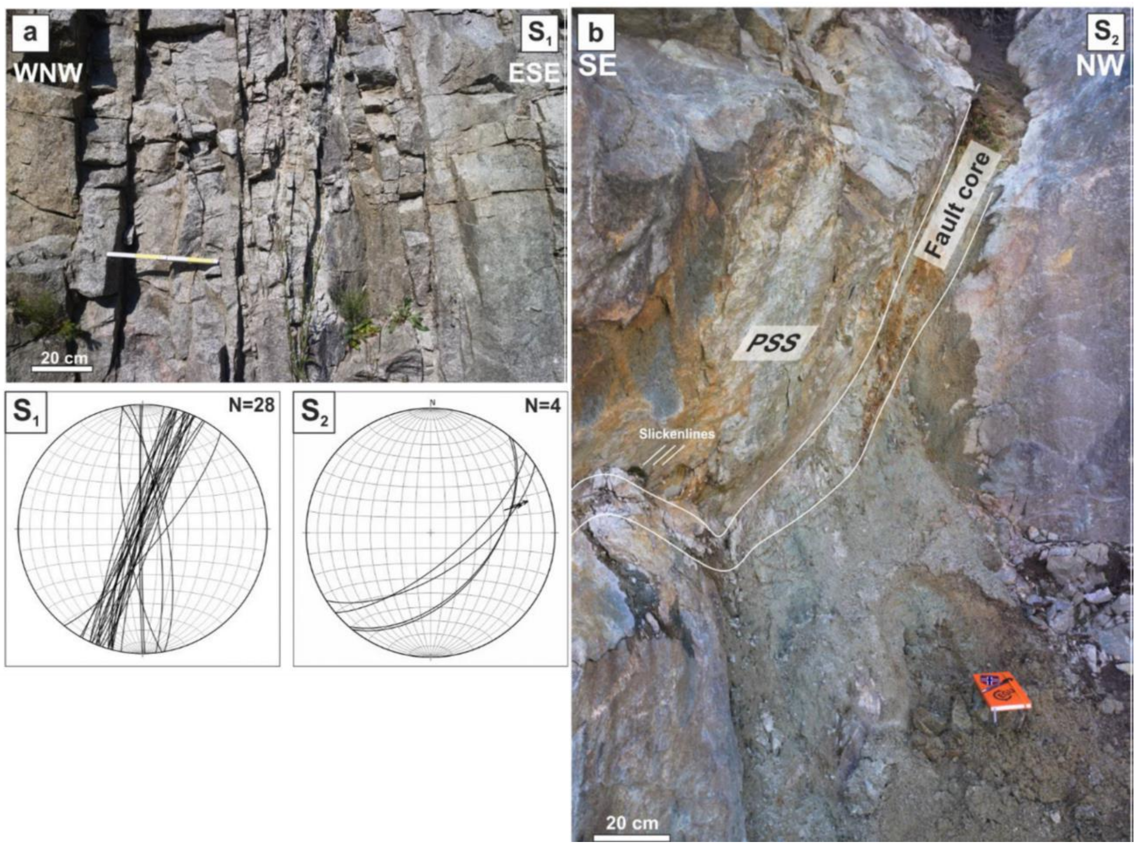

Figure 7.3 - a) Fracture corridor at outcrop S1. b) The fault zone of outcrop S2 is characterised by a thin, gouge- and cataclasite-rich fault core enveloped by a 1 m thick, poorly developed damage zone. Fluids percolating through the fault core led to the alteration of cataclasite and the damage zone observed in the central portion of the image. PSS: Principal Slip Surface. Stereonets: Lower hemisphere, equal area projection of fractures and fault planes. The black arrows represent the direction of movement of the hanging wall along the fault plane (modified after Ceccato et al., 2021b)

Outcrop S3 is the Goddo Fault Zone (GFZ) on the island of Goddo (North-western Bømlo, Fig. 7.1b, 7.4). The GFZ represents an E-dipping normal fault zone formed and reactivated during Permian-to-Cretaceous extensional tectonics (Viola et al., 2016; Fredin et al., 2017a; Scheiber and Viola, 2018). It is characterised by two separate and distinct fault cores (marked as S3A and

S3B in Fig. 7.4) separated and surrounded by highly fractured damage zones (Fig. 7.4, 7.5a-b). The two fault cores consist of several Brittle Structural Facies including: (a) a polished PSS overlain by (b) a massive, well-sorted clay-rich gouge, (c) a phyllonitic gouge, and (d) a cataclasite (Fig. 7.5a-d). The PSS of the GFZ consists of a 1-2 cm-thick fine-grained quartz-coated polished surface, dipping N160° and bearing dip-slip slickenlines associated with top-to-the-east normal fault steps (Fig. 7.5c, d). The overlying gouge core is 20-30 cm thick, and it is composed of two main gouge layers showing different textures and age of formation (Viola et al., 2016). The clay-rich gouge consists of a 5-10 cm thick homogeneous and isotropic plastic gouge (Fig. 7.5c, d). The phyllonitic-gouge consists of a scaly, phyllosilicate-rich gouge containing a pervasive S-C' composite fabric (Fig. 7.5d). K-Ar illite dating showed that the phyllonitic gouge of the fault core S3B developed during Permian extension (264.1 ± 5.4 Ma; Scheiber and Viola, 2018); Triassic-Early Jurassic fault reactivation led to the formation of the clay-rich gouge and reworking of the phyllonitic gouge in the S3B fault core (200.2 ± 4.1 Ma, Viola et al., 2016). The gouges are overlain by a 20-40 cm thick layer of cataclasite, containing internal discrete shear planes with Fe-oxides coatings (Fig. 7.5d).

The thickness of each fault core is in the order of 0.6-1 m (Fig. 7.5c, d), suggesting that each fault core may have accommodated a cumulative normal throw of 10-100 m (Torabi and Berg, 2011), thus defining a valuable example of a SRS fault zone (Viola et al., 2016). Accordingly, the damage zone width would be in the order of 10-100 m (Faulkner et al., 2010). The GFZ damage zone is well exposed in the footwall, and between fault cores, whereas the geometry and exposure of the outcrop did not allow us to quantify the exact thickness of the hanging wall damage zone and the entire fault zone in the field (Fig. 7.4).

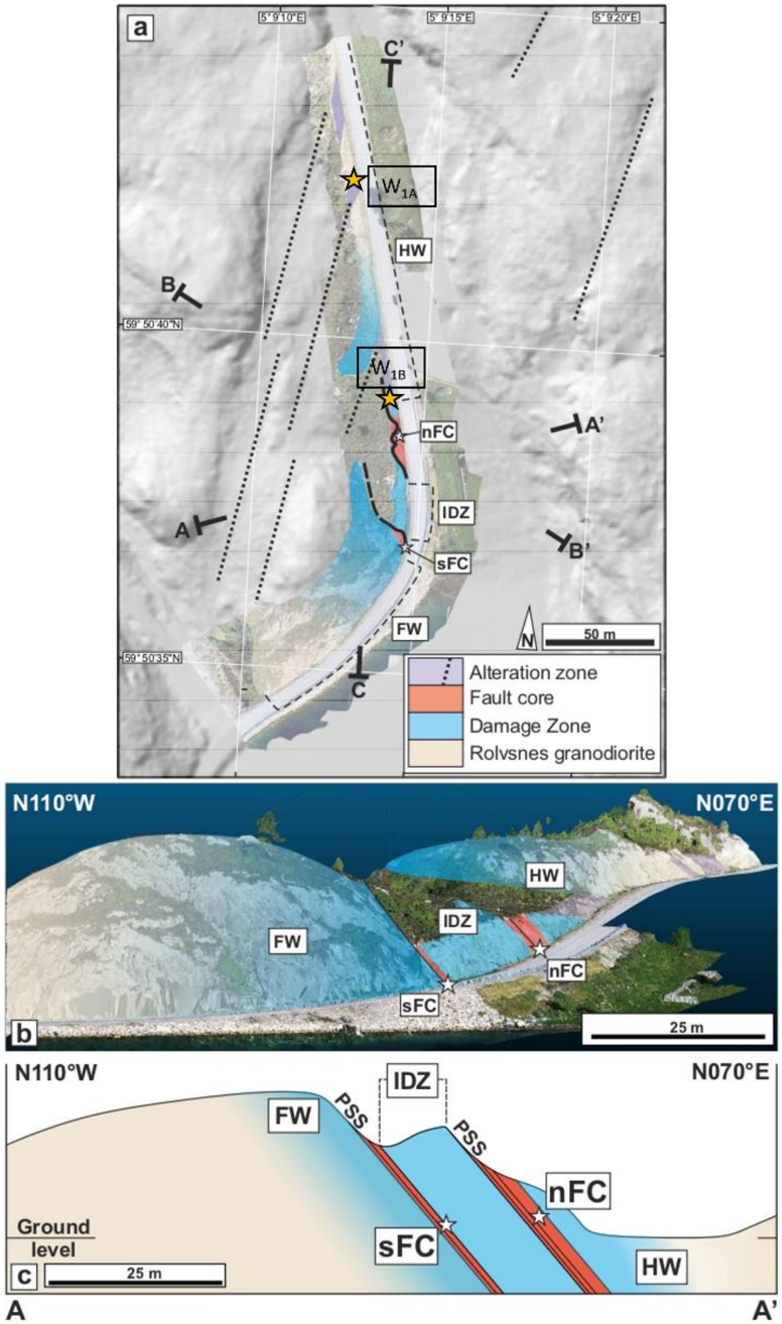

Figure 7.4 - a) Schematic map of the Goddo Fault Zone (outcrop S3) overlain on a composite UAV orthophoto and LiDAR digital elevation model image. The location of the studied outcrops (W1A, W1B) is reported, and the outcrops S3A, S3B correspond to the two fault cores. Black thick lines represent fracture lineaments spatially related to discrete alteration zones. The black dashed lines bracket the supposed maximum width of the damage zone; b) Perspective view and interpreted domains of the GFZ outcrop perpendicular to the cross-section A-A′ (from CloudCompare); c) Geological cross-section along the A-A′ profile of the GFZ outcrop. FW: Footwall; HW: Hanging wall; IDZ: Internal Damage Zone; nFC: norther Fault Core; PSS: Principal Slip Surface; sFC: southern Fault Core FC: Fault core; DZ: Damage zone. (Modified after Ceccato et al., 2021a).

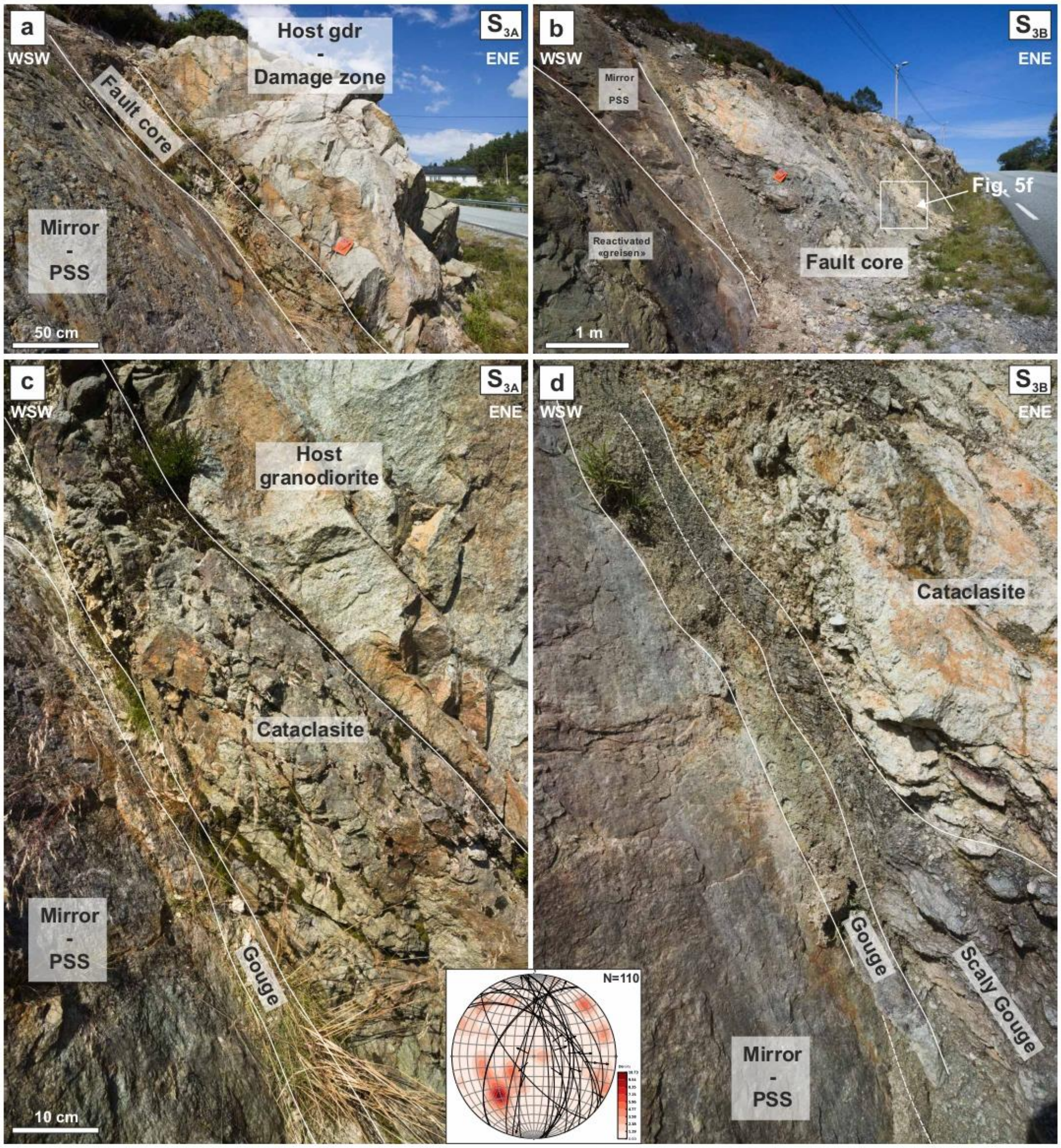

Figure 7.5 - Representative outcrops of the Goddo Fault Zone. a) Fault core at outcrop S3A, showing the composite fault core. b) Composite fault core and a reactivated slip surface exposed at S3B. c) Composite fault core at S3A, showing the juxtaposition of cataclasite, gouges, and PSS. d) Composite fault core at S3B, showing the juxtaposition of cataclasite, gouge, and PSS. Note the alteration of the cataclasite layers. Stereonets: Lower hemisphere, equal area projection of fractures and fault planes at S3. The whole dataset of fracture and fault planes collected on the field is reported as contoured distribution of poles to fracture and fault planes (in red). Black great circle represents only those fracture and fault planes characterised by slickenlines. The black arrows represent the direction of movement of the hanging wall along the fault plane (Ceccato et al., 2021b).

7.2.2 Group W - weathered outcrops

Outcrop W1 is found in the same locality of outcrop the GFZ (Fig. 7.4). The whole GFZ is crosscut by a series of poorly exposed alteration/weathering zones (marked with W1A-W1B in Fig. 7.4a; Fig. 7.6a, b). These weathering zones are spatially related to NNE-SSW, 1-2 m thick fracture corridors cutting across both the undeformed RGD host (Fig. 7.6a) and fault rocks (Fig. 7.6b; Viola et al., 2016; Scheiber and Viola, 2018). The granodiorite within the fracture corridor mostly preserves its primary structure and cohesion at the hand specimen scale. Partially altered host rock lithons within the fracture corridor are embedded in a granular matrix of quartz and clay minerals (Fig. 7.6a, b). The weathering material included therein has been dated to the Early Cretaceous (125.2 ± 4.2 Ma, sample BO-OFR-1 in Viola et al., 2016; Fredin et al. 2017a). The mineralogical composition and textural characteristics of the weathering products suggest that this outcrop is equivalent to the alteration facies A1 described by Riber et al. (2016).

Outcrop W2 is characterised by the occurrence of a pervasive NNW-SSE-trending fracture set (Fig. 7.6c). Fractures are preferentially organised in 1-m-thick clusters, separated by 2-5 m of non-fractured RGD host. Commonly, rock volumes within fracture clusters are heavily altered and transformed in a variably cohesive granular material preserving the magmatic fabric. This outcrop exposes three main domains: (i) partially altered host granodiorite with some localised mesoscopic fractures (domain d1, Fig. 7.6c), (ii) granular cohesionless aggregate preserving the granodiorite fabric but no mesoscopic fractures (domain d2, Fig. 7.6c), (iii) granular aggregate with increasing clay content (domain d3, 7.6c). Unpublished K-Ar illite dating data suggest that this alteration is older than Triassic (A. Margreth personal communication).

Outcrop W3 is characterised by a 2m-thick altered rock volume within granodiorite, bounded by N-S trending fractures. The altered volume consists of a cohesionless granular aggregate, grading from saprock to mature, fine-grained clay-rich saprolite, enveloping variably altered core stones, i.e., remnant blocks of granodiorite less weathered than the embedding material and resulting from spheroidal weathering processes (cf. Ryan et al., 2005, Fig. 7.6d, Fredin et al., 2017a, b). Weathering products likely formed during sub-aerial exposure of the crystalline basement in the Triassic (220-200 Ma; Fredin et al., 2017b).

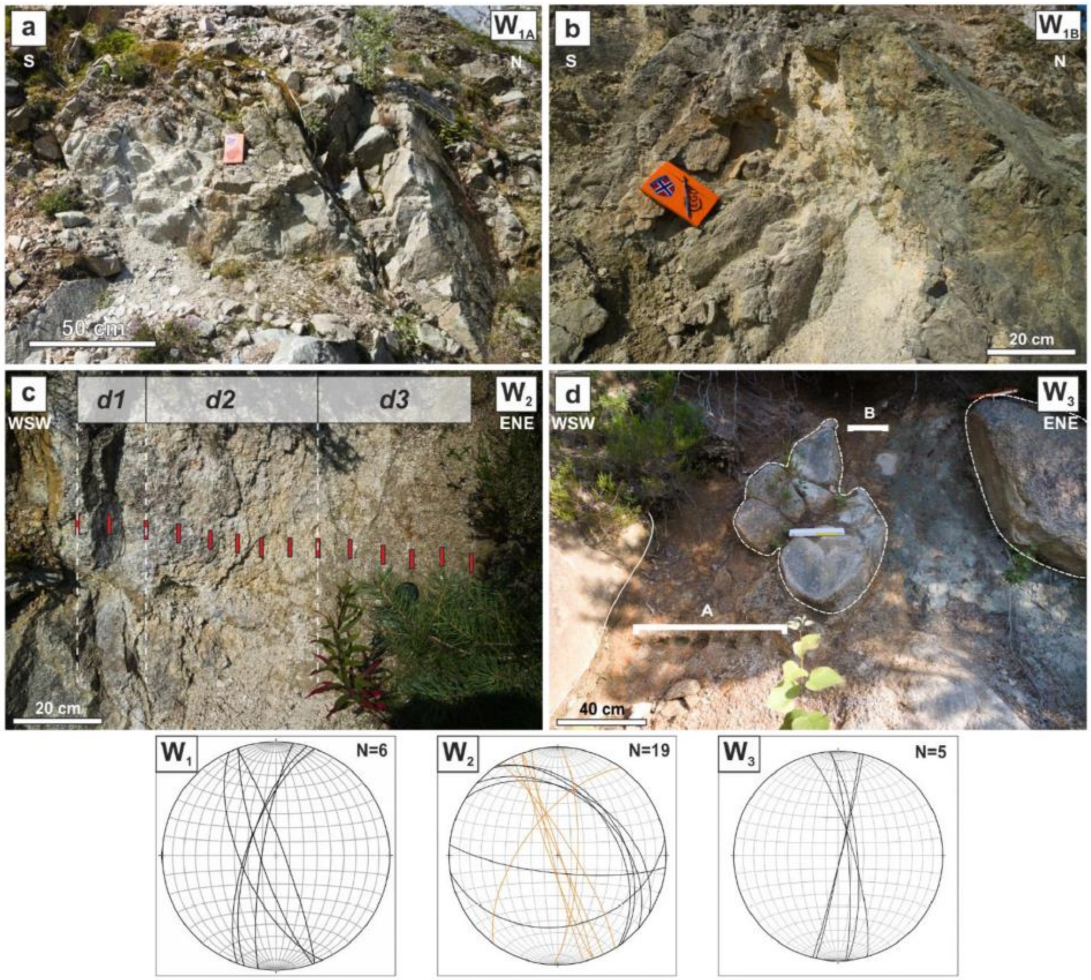

Figure 7.6 - Representative outcrops of weathered granodiorite. a) Alteration zone W1A related to a NNE-SSW-trending fracture lineament. b) Alteration of the host granodiorite within the damage zone of the GFZ at W1B (detail of Fig. 7.5b). c) Outcrop W2 showing an increasing alteration profile along which Schmidt hammer analysis and permeability measurements have been done. d) Outcrop W3 (saprolite) showing relatively unaltered core stones (enclosed by dashed white lines). The thick white lines (A, B) represent the profile along which permeability and UCS measurements have been performed. Stereonets: Lower hemisphere, equal area projection of fracture planes at outcrops W1, W2 and W3. Orientation of fractures within fracture clusters related to weathering zones at outcrop W2 are highlighted in orange in the stereoplot.

7.5 Structural characterisation of VOM point clouds

Georeferenced Virtual Outcrop Models (VOM) of the Goddo Fault Zone (outcrop S3) were generated using UAV-drone imagery. The obtained VOMs were plotted in CloudCompare as point clouds. The comparison of the 3D point cloud with structural field data led to identification of three different domains composing the GFZ (Fig. 7.4, 7.7): the footwall (FW) damage zone, the central GFZ, and the northern hanging wall (HW) damage zone. The southern portion of the outcrop exposes the damage zone in the footwall of the main fault plane (main PSS, Fig. 7.7a, b), which is characterised by rather spaced, up to 20 m long fractures organised in clusters and oriented in two main sets, trending NNE-SSW and ENE-WSW, respectively (Fig. 7.7c, d). A third set of NW-SE-trending fractures becomes increasingly prominent moving toward the southern fault core (sFC, Fig. 7.7a, b). These sets of fractures dip toward either NE or SW (Fig. 7.7d). The central GFZ includes the Internal Damage Zone (IDZ), the southern (sFC) and northern (nFC) fault cores (Fig. 7.7e, f). The sFC is defined by a large areal exposure of the main PSS above which a 50-60 cm thick fault core is exposed (Fig. 7.7f). The nFC is characterised by a limited exposure of the main PSS, which crops out at the bottom of a c. 2-m-thick zone of cataclasites. The sFC and nFC bound an Internal Damage Zone (IDZ) characterised by high fracture intensity to the southern and northern side, respectively (Fig. 7.7g). The northern portion of the outcrop exposes the hanging wall (HW) damage zone (Fig. 7.7i, j). This portion of the outcrop is characterised by a decreasing fracture intensity moving northward from the nFC and by large (up to 10-15 m wide) volumes of weathered granodiorite ("Alteration zone" in Fig. 7.7j). These alteration zones are related to NNE-SSW-trending fracture clusters (Viola et al., 2016; Scheiber and Viola, 2018).

7.5.1 Fracture trace length, intensity and spatial distribution

Fracture surfaces and traces were interpreted in CloudCompare and plotted on stereographic projections in MOVE (Fig. 7.8). The total dataset of interpreted planes includes more than 2300 fractures (Fig. 7.8a). Clusters of fracture orientations were manually selected and classified into 5 main fracture sets (A-E; Fig. 7.8b) in MOVE. The identified fracture sets represent a good first approximation of the entire dataset (1806 fractures included in the interpreted clusters out of 2347 fractures identified from VOMs - 77% of 2347 fractures).

The trace length of fractures has been retrieved from the projection of either the fracture trace or the horizontal dimension of a fracture plane on the horizontal plane. Trace length distributions for each set is reported in the Supplementary Data Table T1 of Ceccato et al., 2021a. All retrieved fracture trace length distributions range between 0.1 and 5 m in length and are best fitted by negative exponential functions.

In the VOM displayed in MOVE, several cross-sections were traced through the outcrop, oriented perpendicularly to the average strike of the selected fracture set and cutting across the areas of the VOM populated by the largest density of fractures. The virtual cross-sections are reported in the Supplementary Data S1, and the related scanline results are reported in the Supplementary Data Table T2 of Ceccato et al., 2021a.

The identified sets are:

- **Set A** corresponds to the NNE-SSE trending clustered fractures, mainly observed in the southern footwall damage zone and within the alteration zones in the northern HW damage zone (Fig. 7.7i-l). Set A fractures mainly occur in clusters with a high fracture intensity (up to P_{10} = 6 m^{-1}; Fig. 7.9a). In the southern portion of the GFZ outcrop (FW) Set A fractures are on average 10-15 m apart from one another (Fig. 7.9a). Set A fracture clusters occur also in the northern GFZ outcrop (HW), where they are associated with alteration zones (Fig. 7.7j) (Viola et al., 2016; Scheiber and Viola, 2018; Ceccato et al., 2021a).
- **Set B** corresponds to WSW-ENE-trending fractures. They are scattered, and they do not exhibit any obvious preferential spatial distribution. The measured P_{10} ranges between 0.5 and 2.5 m^{-1} (1.4 m-1 on average, Fig. 7.9a).
- **Sets C** and **D** correspond to the NW-SE-trending fractures found throughout the GFZ, dipping toward NE and SW, respectively. Set D fractures occur mainly in the central and southern portion of the GFZ outcrop, as small clusters with variable fracture intensity moving from south to north across the outcrop.
- **Set E** fractures have the same orientation of the main PSS of the GFZ. Sets C and E display a similar orientation but different spatial distributions (Fig. 7.7d, h, l). Fracture intensity of Set E varies spatially, displaying larger P_{10} values close to the main fault cores and progressively decreasing values moving away from the central fault zone both northward and southward.

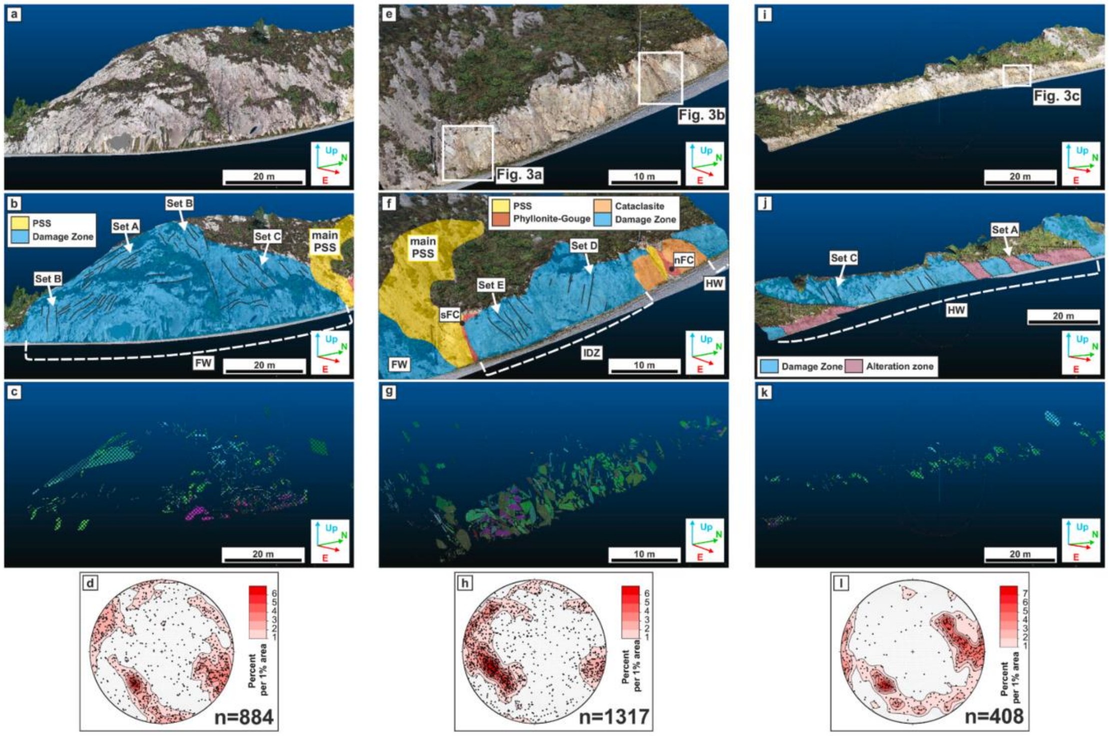

Figure 7.7 - Virtual Outcrop Model of the Goddo Fault Zone as obtained from elaboration of the UAV-drone imagery and related structural interpretation and analyses performed in CloudCompare. a-e-i) Point cloud representing the VOM of the GFZ as visualised in CloudCompare. b-f-j) Structural interpretation of the GFZ virtual outcrop showing the fault domains, including: the footwall (FW), hanging wall (HW), and Internal Damage Zone (IDZ), and the southern (sFC) and northern (nFC) fault cores. Fracture sets are also highlighted (Set A-E). c-g-k) Virtual fracture planes resulting from the structural analyses and manual interpretation of fracture traces and fracture planes in CloudCompare. d-h-l) Equal area, lower hemisphere stereonets presenting the contoured poles of virtual fracture planes interpreted in CloudCompare (Ceccato et al., 2021a).

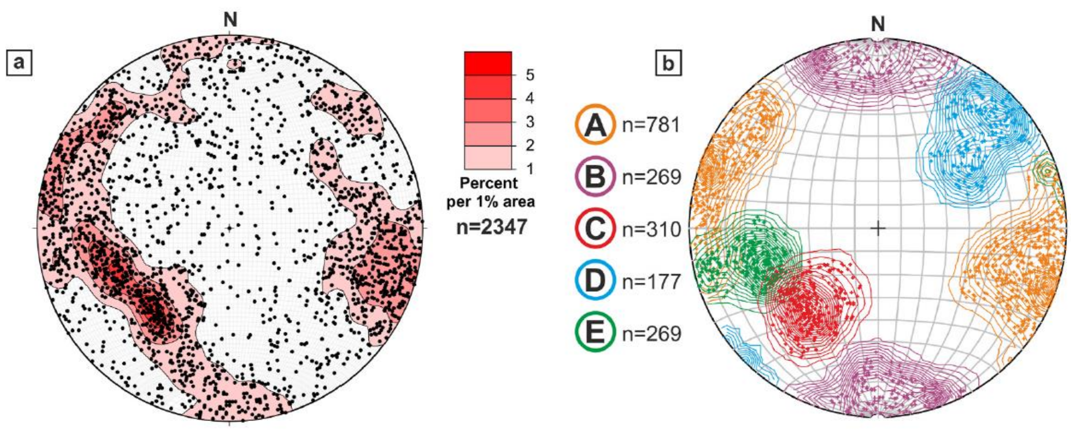

Figure 7.8 - Equal area, lower hemisphere stereonets presenting the total dataset of poles to virtual fracture planes as interpreted from VOM (a), the poles to fracture planes classified in Sets A-E and the number of planes for each set (b) (from MOVE - Petex) (Ceccato et al., 2021a).

Finally, to compare results from different scanlines and cross-sections, we projected the virtual scanlines of set C, D and E on a single cross-section to track the variation of fracture intensity for each set across the profile (Fig. 7.9b). On this cross-section, we assessed the spatial distribution of P_{10} intensity on a profile perpendicular to the fault dip (black line in Fig. 7.9b). This investigates the relationship between P_{10} intensity of each fracture set and the distance perpendicular to the main fault planes (Fig. 7.9c). The intensity of Set C fractures does not display any obvious spatial trend (constant P_{10} = 1.1 m^{-1} on average; Fig. 7.9c). The diagram in Fig. 7.9c highlights two different spatial trends for fracture Sets D and E intensity. P_{10} for Set D varies from 0.5 m^{-1} in the southern GFZ outcrop up to a maximum of 5.5 m^{-1} just north of the nFC outcrop (Fig. 7.9c). A second peak in intensity (P_{10} = 2.9 m^{-1}) is observed next to the sFC. Set D fractures show an increasing intensity moving from SW to NE across the fault zone. The spatial trend of Set E fracture intensity increases next to the two main fault cores (Fig. 7.9c), showing 5.7 m^{-1} and 4.5 m^{-1} close to the sFC and nFC, respectively. The IDZ is characterised by variable intensity ranging between 1.2 and 1.9 m^{-1}. In the footwall, fracture intensity increases quite abruptly from <1 m^{-1} to >5 m^{-1} over less than 5 m from the southern PSS. Conversely, in the hanging wall, Set E fracture intensity decreases slowly, and P_{10} values larger than 2 m^{-1} are still observed ~15 m away from the northern PSS (Fig. 7.9c).

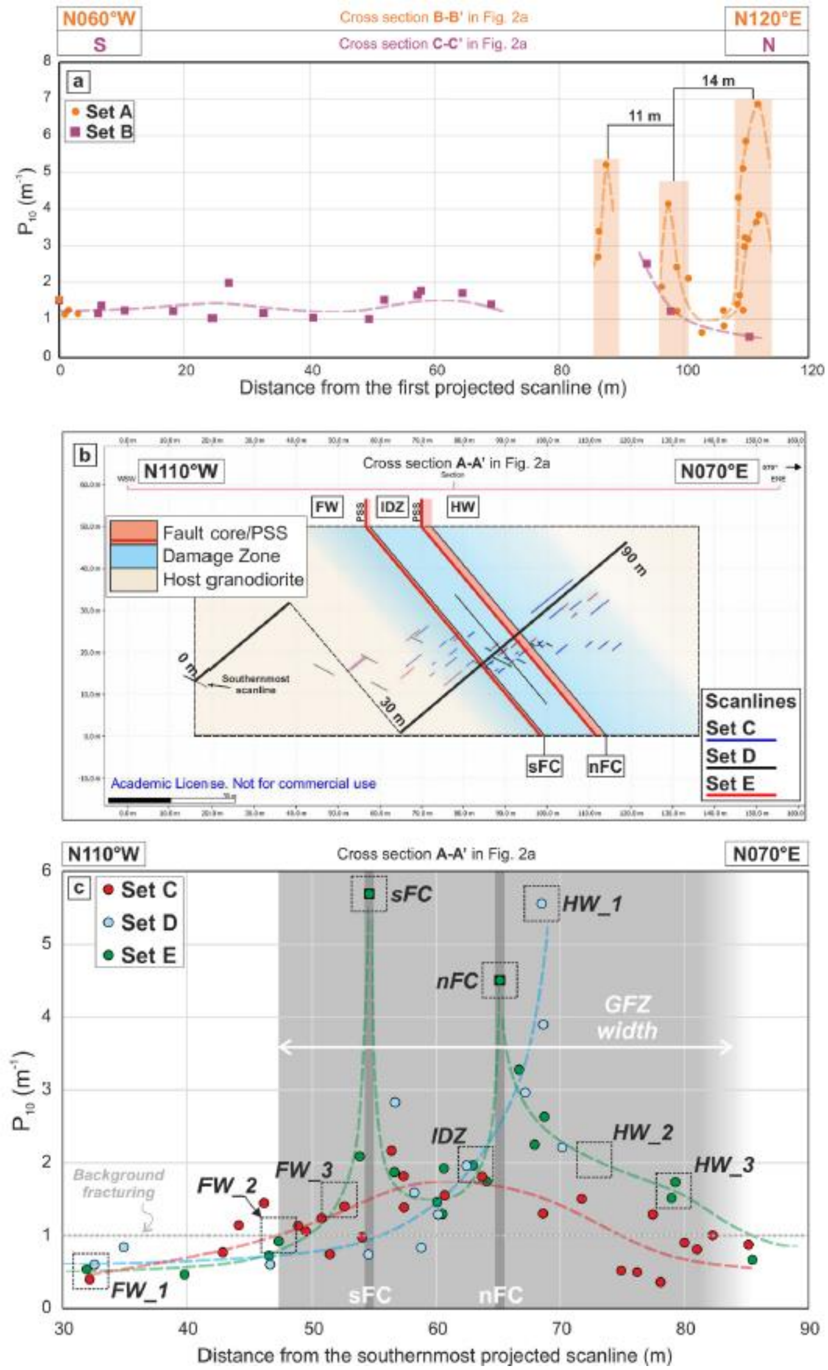

Figure 7.9 - a) P_{10} intensity profiles for Sets A and B, along the cross-section B-B′ and C-C′ of Fig. 7.4a, respectively. The "first projected scanline" to which the X axis refers to is indicated in the Supplementary material of Ceccato et al. (2021a). Fracture clusters are highlighted in the P_{10} profile for Set A (light orange rectangles). Set B shows a rather constant P_{10} intensity. b) Schematic cross-section of the GFZ along the A-A′ profile of Fig. 7.4a showing the identified domains composing the GFZ on which the virtual scanlines adopted to quantify the local fracture intensity P_{10} of Sets C, D, and E are projected. c) Diagram showing the variation of the fracture intensity P_{10} of Sets C, D, and E along the fault-perpendicular profile as reported in the schematic cross-section in (b). The locations of the modelled fault zone domains (FW_1, FW_2, FW_3, sFC, IDZ, nFC, HW_1, HW_2, HW_3) are also reported.

7.6 Discrete Fracture Network models

To track the variation of the magnitude and orientation of the permeability (K) tensor principal components across the fault zone, several DFN models for different combinations of fracture sets and related P_{10} have been computed to simulate the observed fracture networks of selected portions of the GFZ and recreate a synthetic fault zone (Fig. 7.10a).

The DFN models include: (i) model FW_1, representing the crystalline basement affected by background fracturing alone in the footwall of the GFZ; (ii) model FW_2, representing the transition from background fracturing toward the footwall damage zone (Set E P_{10} = 1 m^{-1}); (iii) model FW_3, representing the footwall damage zone; (iv) model sFC, representing the damage zone close to the southern fault core (max Set E intensity); (v) model IDZ, representing the Internal Damage Zone; (vi) model nFC, representing damage zone close to the northern fault core; (vii) model HW_1, representing the hanging wall damage zone affected by the maximum observed Set D intensity; (viii) model HW_2, representing the intermediate portion of hanging wall damage zone; (ix) model HW_3, representing the external portion of the hanging wall damage zone without the contribution of Set D. Additionally, we created a model targeting the permeability properties of the crystalline basement affected by Set A fracture clusters (model Clus, Fig. 7.10a). An example of the graphical output of a DFN model computation is reported in Fig. 7.11.

The input parameters required for stochastic DFN modelling include: (i) the average orientation and orientation variability; (ii) the target P_{32} local intensity; (iii) a function describing the shape of the cumulative distribution of some fracture size (length, height, radius); (iv) the fracture shape. The input P_{32} for each fracture set in each model was calculated from the measured P_{10} intensity retrieved from the virtual scanlines following the approach suggested by Antonellini et al. (2014). A constant mechanical fracture aperture of 100 μm for all the fracture sets in the DFN models is assumed.

The magnitude and orientation of the permeability tensor principal components retrieved from the DFN models are reported in Fig. 7.10. The magnitudes of the principal components of the permeability tensor show a significant variation across the GFZ (Fig. 7.10b). The K_1 component ranges between 0.03 mD and 0.13 mD on average, showing maximum values as high as 0.4 mD and displaying a relative increase of about one order of magnitude between the least and the most fractured zone. The K_2 component shows a variation trend similar to K_1.

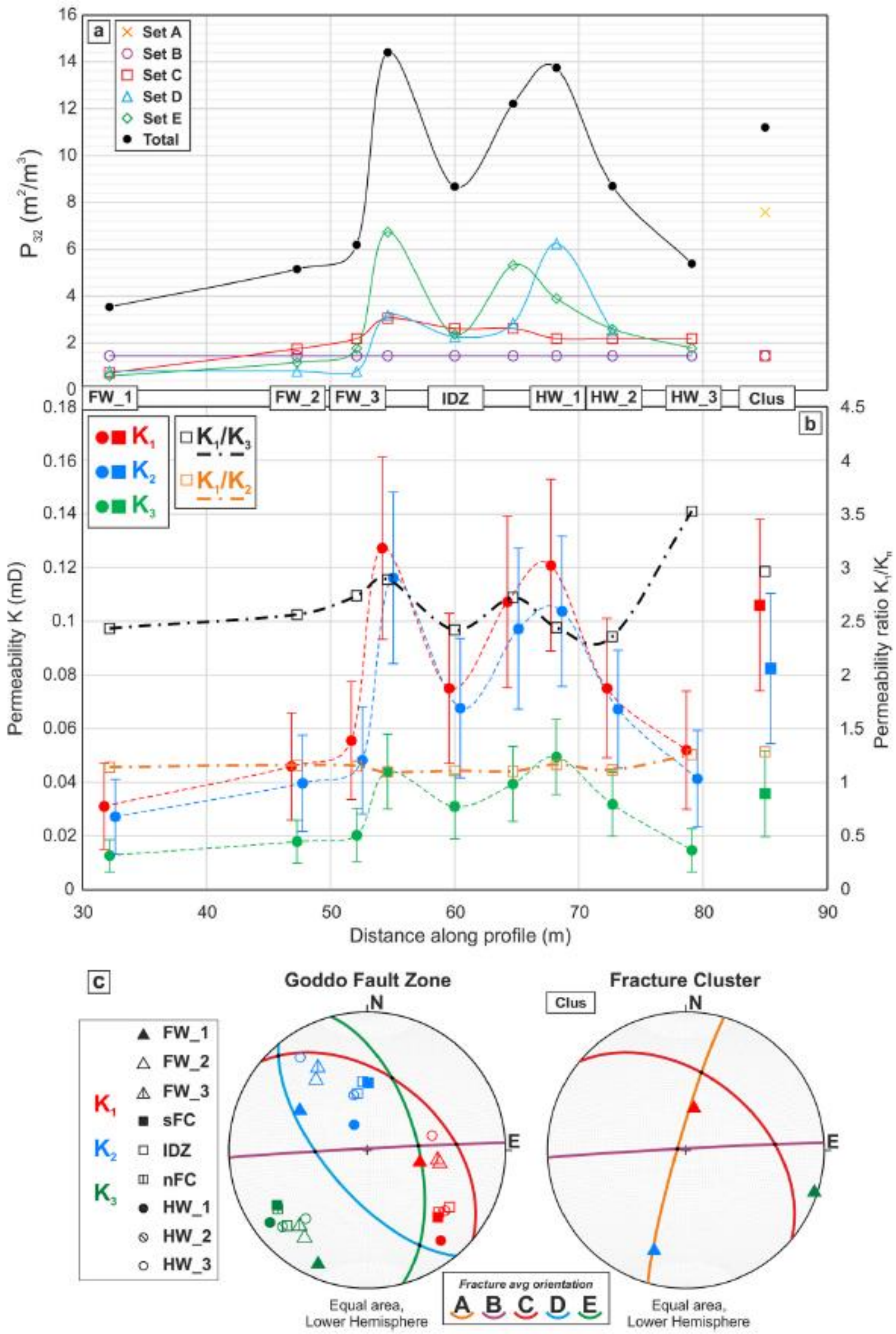

Figure 7.10 - a) Diagram showing the P_{32} intensities for each fracture set, adopted for each DFN model and the total P_{32} resulting from DFN modelling; b) diagram showing the magnitude (vertical axis on the left) and the relative ratio (K_1/K_n with n=2.3, vertical axis on the right) of the principal components of the permeability tensor ($K_1>K_2>K_3$) resulting from the DFN model computations. The average permeability values (dots and squares) are reported along with their statistical variation (±2σ); c) equal area, lower hemisphere stereonets of the orientation of the principal components of K and the main orientation of the fracture planes for each set (Ceccato et al., 2021a).

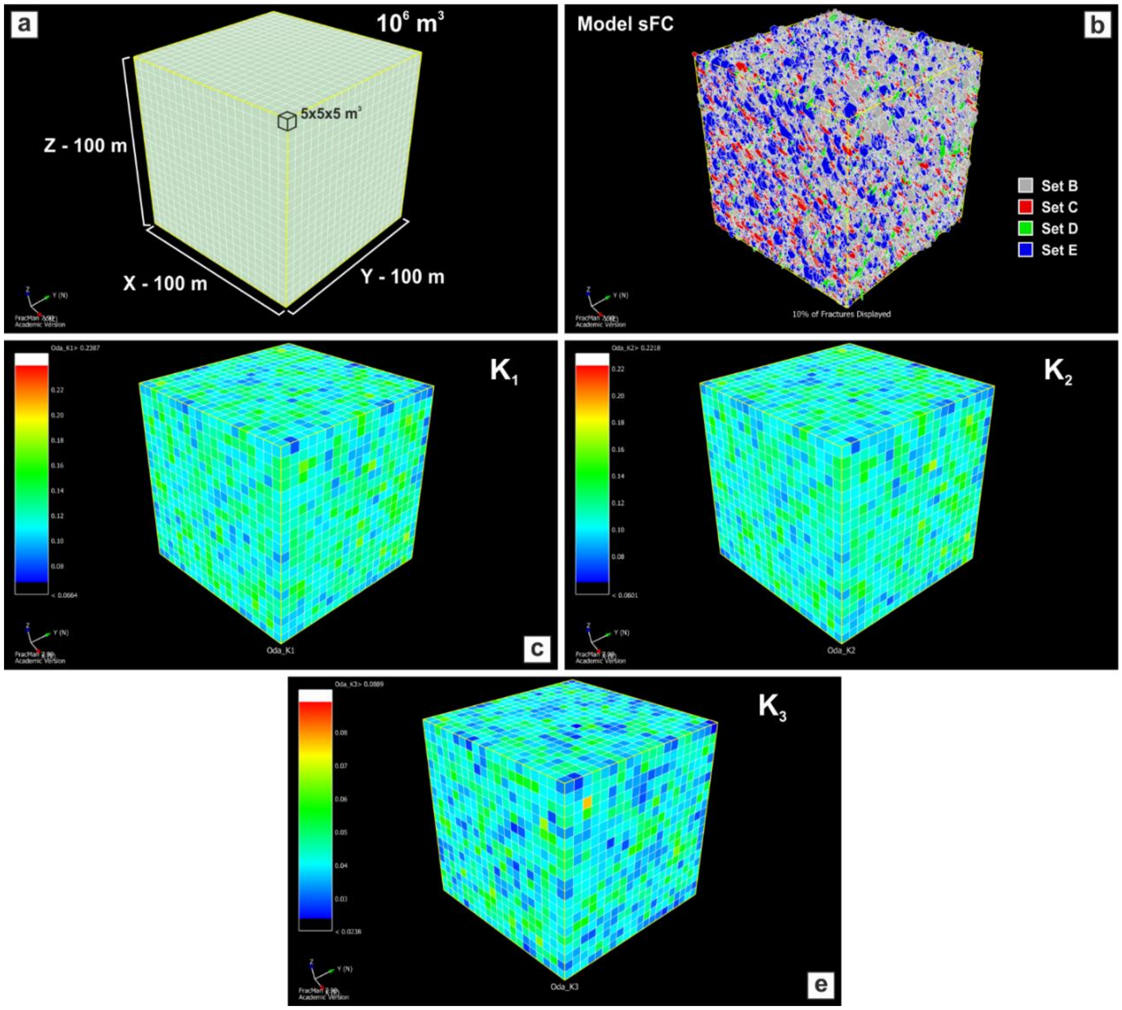

Figure 7.11 - Example of the DFN model setup and graphical representations of the results of permeability computation. a) 106 m^3 volumetric grid composed of 8000 Representative Elementary Volumes of 125 m^3 each. b) Volumetric grid showing the fracture sets generated for the computation of the DFN model. (c-d-e) Graphical output of the magnitude of the principal component of the permeability tensor (K_1, K_2, K_3 respectively) computed for the DFN model.

The K_3 component is the least variable component, ranging between 0.01 mD and 0.05 mD. The relative magnitude of the tensor components suggests that in all cases the shape of the K tensor is oblate, having very similar K_1 and K_2 permeability values that are much larger than K_3 (Fig. 7.10b). As to the orientation of the K principal components (Fig. 7.10c), the orientation of the K_3 component is constant for all models, being almost sub-horizontal and NE-striking. The orientation of K_1 varies across the GFZ: in the footwall and in the most distal portions of the GFZ hanging wall (FW_1, FW_2, FW_3, HW_3), K_1 plunges N45°, laying subparallel to the intersection direction between Sets B and E or Sets B and C. In these domains, the K_2 direction is close to the intersection direction between Sets C and D (Fig. 7.10c). In the central and most fractured portions of the GFZ (sFC, IDZ, nFC, HW_1, HW_2), on the other hand, K_1 is almost sub-horizontal and NW-trending, laying subparallel to the intersection direction between Sets D and E (Fig. 7.10c).

The maximum permeability K_1 of fracture clusters (Clus) is equal to 0.11 mD (Fig. 7.10b) and the K_1-K_2 principal component vectors rest on a plane parallel to Set A average orientation (Fig. 7.10c). Accordingly, the K_3 principal component is equal to 0.04 mD, is sub-horizontal, and plunges toward WNW. Overall, the computed principal components of K increase linearly with the computed total P_{32} fracture intensity both within the GFZ and Set A clusters.

7.7 Concluding Remarks on the Goddo Fault Zone

A high-resolution study of the GFZ has been performed by means of VOM structural analysis. The intensity profile of the ENE-dipping Set E fractures allowed us to describe the GFZ as an asymmetric fault zone. In fact, the intensity of Set E fractures varies from <1 m^{-1} m from the main fault zone to ~6 m^{-1} adjacent to the main fault cores. If fracture intensity in the most external portions of the GFZ represents the "background" fracture intensity of Set E, c. 1 m^{-1} is likely the limit between the background fracture intensity and the GFZ damage zone (Choi et al., 2016; Torabi et al., 2020). The transition from background intensity values to values > 1 m^{-1} occurs in the footwall ~5 m from the southern fault core, and in the hanging wall at >20 m from the nFC (Fig. 7.9c). Therefore, the intensity profile displayed by Set E fractures depicts the fault zone as asymmetric, with the damage zone preferentially developed in the hanging wall of the fault zone.

Set A fracture clusters overprinted the fractured and faulted Rolvsnes granodiorite during Jurassic-Cretaceous deformation (Viola et al., 2016; Scheiber and Viola, 2018). These clusters occur in the footwall of the GFZ and in the hanging wall as "alteration zones" (Fig. 7.2a, Viola et al., 2016). Set A fractures seem to be rather homogeneously distributed over the GFZ outcrop, forming high-fracture intensity corridors clustered with a spacing of 10-15 m and separated by low-fracture intensity (c. 1 m^{-1}) domains. Fracture clusters are quite common in the crystalline basement of southwestern Norway (Gabrielsen and Braathen, 2014; Torabi et al., 2018). Observations from the published literature and from the studied outcrop suggest that the fracture clusters are a ubiquitous feature of the fractured crystalline basement, yet impossible to detect by commonly adopted seismic investigation methods (Torabi et al., 2018). Their occurrence, however, controls the hydrology and fluid-flow within fractured rock masses at different crustal levels and scales (Place et al., 2016; Souque et al., 2019).

The results of our DFN models also highlight the effects of fracture intensity variations on the magnitude and orientation of the **K** principal components across the GFZ. The magnitude of the **K** principal components increases linearly with the computed total P_{32}, despite the different assemblage of fracture sets and related intensity characterising each DFN model. The computed increase of c. one order of magnitude in total intensity P_{32} of fractures longer than 10^{-1} m leads to a relative increase of one order of magnitude of the principal maximum (K_1) permeability. In all cases, the shape of **K** tensor is strongly oblate ($K_1 \approx K_2 \gg K_3$; Fig. 7.10c). The shape of the oblate permeability tensor, whose major principal axes are oriented parallel to the fault planes, is due to the occurrence of PSSs and microstructurally anisotropic fault gouges within the fault cores (Faulkner and Rutter, 1998). Our DFN models consistently indicate that the minimum principal component K_3 of the structural permeability related to meso-scale fractures within the damage zone is also oriented normal to the main fault planes. The values of K_1 and K_3 within the damage zone usually do not differ more than one order of magnitude (Fig. 7.10b).

In the specific case of the GFZ, the asymmetric architecture of the damage zone suggests that, even though the magnitude of the **K** components may be comparable throughout the fault zone, the hanging wall damage zone could be the principal conduit for fault-parallel fluid-flow given the larger volumetric extension compared to the footwall damage zone (Fig. 7.9c).

The average orientation of the K_1 principal component is generally subparallel to the intersection directions of the dominant fracture sets (Fig. 7.10c). The variability of K_1 orientation depends on three main factors: (1) the variability in orientation of each fracture set; (2) the similarity of the average orientation of intersecting fracture sets, and (3) the relative frequency of fracture sets in each model. A well-defined cluster distribution of K_1 orientation occurs when the model is characterised by either two predominant fracture sets (e. g. Set D and E in model HW_1) or fracture sets exhibiting similar orientations and relative frequencies (e.g., Set B, C and E in model HW_3).

In summary, the bulk (matrix + structural) permeability of an SRS fault zone is expected to be characterised by a strongly oblate permeability tensor, with the minimum permeability component (K_3) perpendicular to the main fault plane. Instead, the direction of the maximum permeability component (K_1) is controlled by the intersection direction of the dominant meso-scale fracture sets.

7.4 UCS and permeability results

The direct permeability and UCS measurements on the five selected outcrops presented above are pivotal to better understand the structural and weathering features controlling the matrix permeability and mechanical properties of the fractured and altered crystalline basement.

Petrophysical and geomechanical analyses were performed perpendicular and parallel to the dominant planar rock fabric, aiming at evaluating the anisotropy of petrophysical and geomechanical properties. The average obtained values of UCS, and related standard deviations are reported in Fig. 7.12a. Permeability ranges and data distributions are reported as boxplots in Fig. 7.12b.

The obtained data represent the present-day mechanical strength and permeability at surficial, ambient conditions. The extrapolation of these values to depth (at deeper structural levels or buried below a sedimentary cover) needs to take into consideration the effect of increasing confining pressure and temperature and the compaction processes (Lothe et al., 2018). A further complication arises from the fact that the analysed onshore outcrops may have been affected by renewed alteration related to Cenozoic geomorphic and glaciogenic processes, which the fractured and weathered crystalline basement buried in the North Sea by the Mesozoic cover has, instead, probably escaped. The petrophysical and mechanical data presented, however, are comparable (on average) with other results in the literature from standardised laboratory tests on fresh samples from onshore outcrops and offshore core samples of the same rock types analysed here (Walter et al., 2018; Lothe et al., 2018; Høien et al., 2019). This suggests that possible Cenozoic geomorphic and glaciogenic processes have only slightly affected the textural, mechanical and petrophysical characteristics of the studied onshore outcrops.

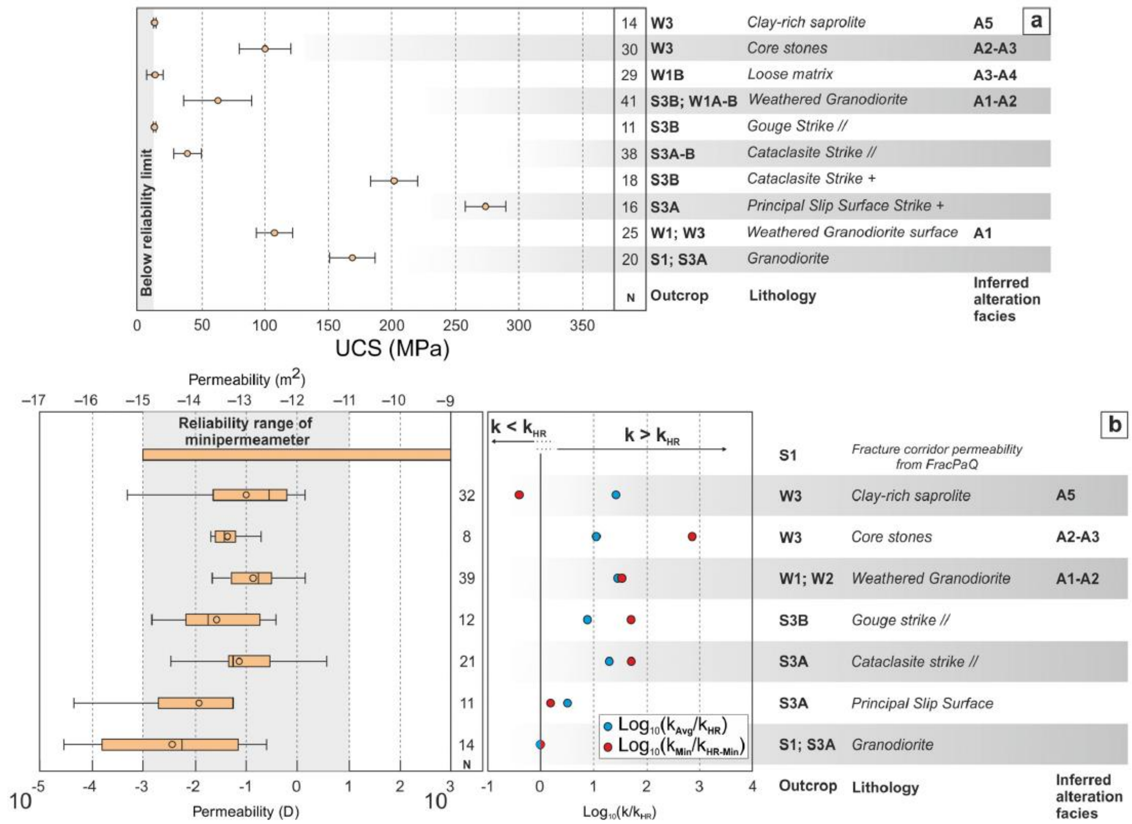

Figure 7.12 - Mechanical strength and permeability box-plot diagrams. "Strike//" stands for data measured parallel to the fault plane. "Strike +" stands for data measured perpendicular to the fault plane. a) Uniaxial Compressive Strength (UCS, MPa). For each analysed lithology, the mean (orange dot), the standard deviation (1σ, black bars), the number of measurements (N), the outcrop(s) name on which the measurements were performed, and the corresponding alteration facies are reported. b) Permeability (m2, D). The outcrop name and the corresponding alteration facies are reported. N: number of measurements for each lithology. Each box of the box-and-whiskers plot represents the range between the 1st and 3rd quartile of the distribution. The whole data range is represented by the extension of the whiskers. In (b) we also plot the logarithm of the permeability ratio (Log10(k/kHR)) between the host rock and the selected lithology (Scibek, 2020). The ratio between mean values of permeability (blue dots) and the ratio between the minimum reported values (red dots) for each lithology are also reported. It is worth noting that air-minipermeametry retrieved permeability values for saprolites are comparable to those obtained from laboratory measurements on saprolite samples from Bømlo and the Utsira High exploration wells (Lothe et al., 2018).

7.3.1 Host rock properties

Field observations confirm that the RGD preserves its magmatic texture, without any superimposed pervasive ductile. Fresh, non-altered and non-mineralised granodiorite surfaces yield an average UCS value of 169 ± 36 MPa (measured from outcrops S1-S2-W3). Granodiorite surfaces bounding alteration/weathering zones (measured at outcrops W2-W3) exhibit a lower range of UCS variability, with an average value of 107 ± 29 MPa ("Weathered Granodiorite surface" in Fig. 7.12a). The observed host granodiorite UCS is comparable to the reference values reported in the database by SINTEF for Norwegian rock types (Høien et al., 2019). Results from permeability measurements on the pristine, non-fractured host granodiorite at different outcrops range between <10^{-4} D (below the actual reliability limit of the air-minipermeameter) and 0.1 D (Fig. 7.12b).

Permeability data from the RGD are quite different from available laboratory permeability measurements on intact rocks (Sibson and Rowland, 2003). Most of the host rock permeability values are comparable with permeability values obtained from fractured crystalline rock in fault damage zones (Evans et al., 1997; Mitchell and Faulkner, 2012; Gomila et al., 2016). This discrepancy might be related to either: (i) an analytical error during measurement (i.e., air slippage from the non-perfectly sealed contact between the probe tip and the rough surface); (ii) enhanced permeability related to the increased microfracture density in the proximity of fracture and fault zones (Torabi et al., 2018); (iii) enhanced permeability related to recent, very local surficial weathering processes.

7.3.2 SSRS fracture corridor properties

Fracture corridors are characterised by high-fracture-intensity deformation zones, accommodating <1m throw, mostly barren of fault rock. UCS measurements for SSRS fracture corridors (S1) are from along a transect perpendicular to fracture strike.

To evaluate the influence of fracture intensity on the UCS, fracture intensity has been quantified with circular scan windows (10 cm in diameter) centred on each measurement spot along the transect (Fig. 7.13a) (Watkins et al., 2015). Mechanical strength drastically decreases to 15-20 MPa toward the centre of the fracture corridor, where fracture intensity is higher (P_{21} = 74 m^{-1}; Fig. 7.13b-c, e). 2D structural permeability at the scale of the outcrop has been evaluated to have a relative comparison with the other permeability data, by means of the digitised fracture network obtained from line drawing on a field photo of the core zone with the software FracPaQ (Healy et al., 2017). The 2D permeability of the fracture pattern in the direction of flow was calculated considering a range of different values of fracture aperture, ranging from 0.01 to 1 mm and perfect connectivity among fractures. The outcrop-scale maximum permeability is always oriented parallel to the dominant subvertical fractures, and maximum values range between 10^3 D to 10^{-3} D, for a fracture aperture of 1 mm and 0.01 mm, respectively (Fig. 7.13e).

The outcrop mechanical strength and bulk permeability of SSRS fracture corridors are mainly controlled by the spatial distribution of meso-scale fractures (Fig. 7.13c, e). Thus, the increase in local fracture intensity leads to a drastic decrease of the host rock mechanical strength and to a significant increase of fracture permeability up to 1-10^3 D (Fig. 7.12). The largest 2D permeability in the direction of flow is observed parallel to the longer, subvertical and well interconnected fractures (Fig. 7.13e). Such a fracture network represents a preferential pathway for fluid flow (Souque et al., 2019). Thus, the permeability of limited-throw SSRS fracture corridors is controlled by the mesoscopic fracture porosity. On the other hand, microscopic fracture porosity may contribute to the matrix mechanical strength and permeability to only a very limited extent (Mitchell and Faulkner, 2012). A local increase in permeability related to microscopic fracture porosity is reported by Torabi et al. (2018) for fracture corridors developed within the Øygarden Gneiss Complex in the Bergen area. Therefore, such SSRS, limited-throw fractures remarkably affect both the overall mechanical and permeability properties of the crystalline basement.

7.3.3 SSRS and SRS fault cores

SSRS fault cores are likely to be characterised by thin (<1m thick), single fault cores surrounded by poorly developed damage zones (e.g., outcrop S2). SRS fault zones, instead, may be characterised by the occurrence of thicker (≥1 m), multi-strand fault cores surrounded by complex, thick and high-fracture-intensity damage zones (Gabrielsen and Braathen, 2014). In both SSRS and SRS fault zones, the fault core is characterised by a composite fault plane-parallel sequence of fault rocks including a PSS, cataclasite, and potentially (several) gouge layers.

UCS bulk rock data on fault rocks have been measured at the S2 and S3 outcrops. The PSS is characterised by high UCS values when analysed normal to the surface (274 ± 32 MPa, Fig. 7.12a). Permeability measured normal to the slip surface is in the 0.05-0.06 D range (Fig. 7.12b). Extreme strain localisation and rock comminution resulted in the formation of a thin, yet mechanically strong, PSS with a low permeability (Fig. 7.12a, b).

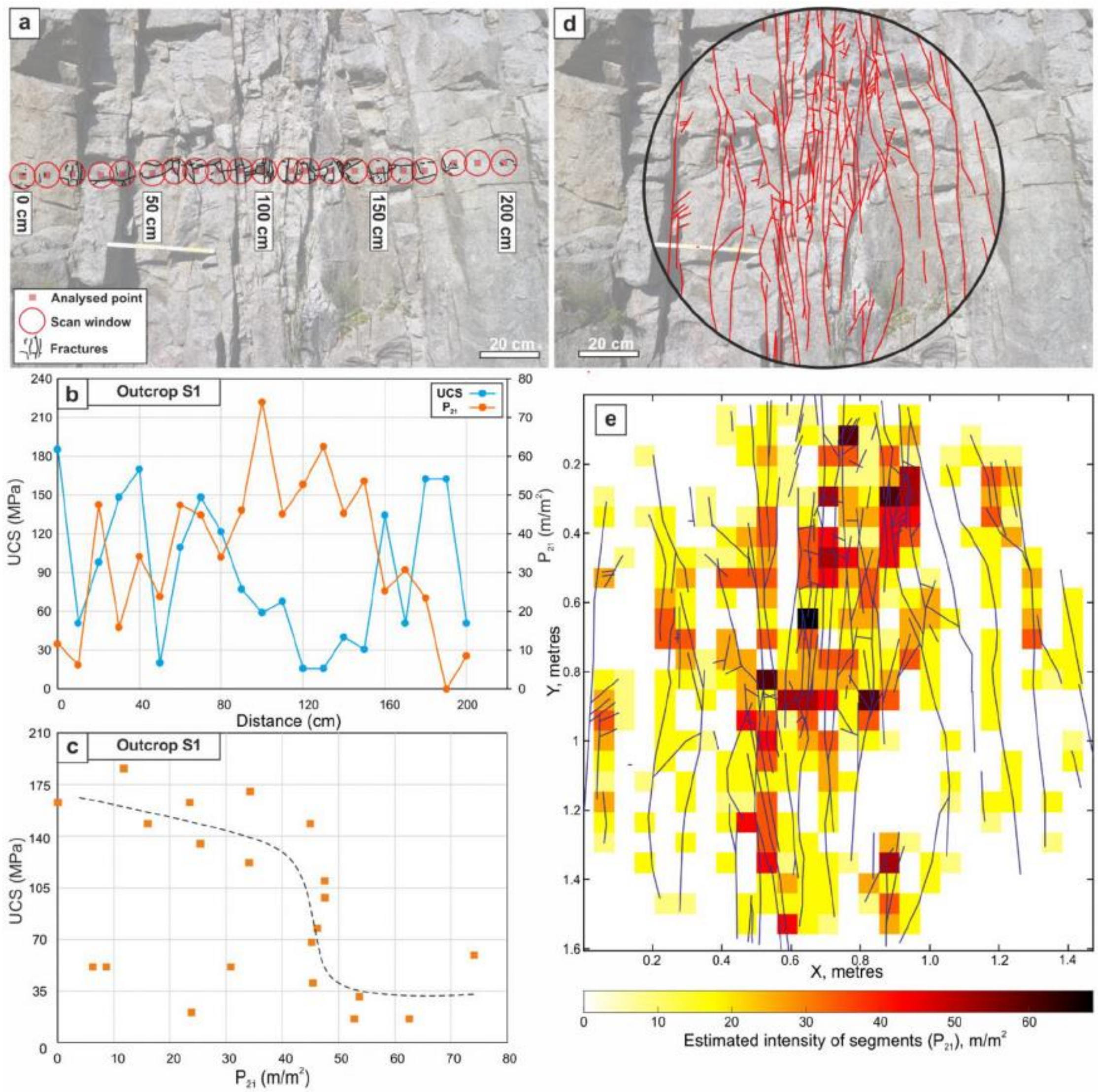

Figure 7.13 - Results of the geomechanical and permeability measurements at outcrop S1. a) Location of the measurements for the Schmidt hammer analysis, and circular scan windows for fracture intensity P_{21} quantification; b) Variation of mechanical strength (UCS) and fracture intensity (P_{21}) along the analysed transect; c) UCS vs. fracture intensity P_{21}. Note the drastic decrease of mechanical strength after a threshold value of P_{21} at about 45 m^{-1}. d) Line drawing of the subvertical fracture network analysed with FracPaQ (Healy et al., 2017); e) Results of 2D permeability and fracture intensity quantification from FracPaQ (Ceccato et al., 2021b).

The cataclasite shows strongly anisotropic UCS, as inferred comparing the results obtained from measurements performed parallel (36 ± 22 MPa) and perpendicular (195 ± 37 MPa) to fault strike (Fig. 7.12a). So, cataclasites are stronger where measured normal to the fault plane and weaker where measured parallel to the fault plane. Cataclasite permeability is up to two orders of magnitude larger than the average permeability of the host rock (Fig. 7.12b).

Gouge layers yield a very-low mechanical strength (UCS < 20 MPa), and low permeability parallel to the fault plane (k < 10^{-1} D, Fig.7.12). A strong anisotropy in permeability is expected for both cataclasite and gouge layers (up to three orders of magnitude) (Faulkner and Rutter, 1998). The lower strength and increased permeability parallel to the fault plane is probably also related to a higher density of fault-parallel microfractures and micro-shear planes within cataclasite and gouge layers (Zhang and Tullis, 1998). A pervasive phyllosilicate-bearing foliation characterises the phyllonitic gouge of the GFZ. Thus, even though we lack direct measurements, a strong permeability and strength anisotropy should be expected for the phyllonitic gouge (Niemeijer and Spiers, 2005).

Cataclasites and gouge layers are in any case two orders of magnitude more permeable that the host RGD (Fig. 7.12b). Grain-size reduction, cataclasis and microfracturing processes likely led to the increased micro-fracture-related porosity of fault rocks with respect to that of the host granodiorite (Staněk and Géraud, 2019).

The discrete and multi-strand fault cores are surrounded by variably developed fracture-dominated damage zones, whose width is one order of magnitude larger than fault core thickness (Faulkner et al., 2010). The mechanical strength and bulk permeability of the damage zone is strictly dependent on the intensity, mechanical properties and geometry of multi-scale fractures related to both the fault zone and the basement background fracturing (Mitchell and Faulkner, 2012). Local permeability within the damage zone might be as large as the permeability of similarly high-fracture-intensity fracture corridors (Gabrielsen and Braathen, 2014).

Low-strain, low-displacement SSRS fracture corridors characterised by open, non-mineralised fractures greatly enhance the permeability of the crystalline basement at the SSRS. They form very localised, narrow (1-10 m in width) highly efficient conduits for fluid flow. The largest permeability is observed parallel to the average fracture plane orientation. SSRS and SRS fault zones are characterised by two domains with characteristic permeability (Caine et al., 1996; Evans et al., 1997): (i) the fault core, including low-permeability fault rocks; (ii) the damage zone, defined by a high-permeability multiscale fracture network. The permeability of fault rocks and damage zones is in any case several orders of magnitude larger than the host rock. Therefore, despite their effective (SSRS or SRS) or relative (fault core/damage zone width ratio) size characteristics, fault zones developed within the granodioritic crystalline basement of Bømlo are likely to act invariably as preferential conduits for fluid flow. Fluid flow from footwall to hanging wall of SRS fault zones, or vice versa, might be buffered/limited by the occurrence of relatively low-permeability fault cores.

7.3.4 Altered host rock and weathering profile

UCS for altered granodiorite ranges between 30 and 90 MPa (outcrop W1 in Fig. 7.12a). In the fracture corridor, lithons of altered granodiorite are surrounded by a fine-grained sandy, non-cohesive matrix that exhibits low UCS values (<15 MPa) ("loose matrix" W1B in Fig. 7.12a). The host granodiorite altered lithons exhibit a variable permeability, ranging between 10^{-3} D and 0.84 D (Fig. 7.12b).

Outcrop W2 displays a clear variation of mechanical strength and permeability with increasing weathering grade (Fig. 7.6c, 7.14a). Incipient alteration of domain d1 yields UCS of 20-50 MPa and permeability ranging between 10^{-3} D and 1 D. Cohesionless alteration products yield UCS values < 20 MPa. Permeability increases (from 0.1 D up to several Darcy's) and then decreases (from >1 D down to 0.01-0.1 D) moving from the left-hand side boundary to domain d1 toward the right-hand side boundary to domain d3 (Fig. 7.6c and 7.14a). Alteration domain d3 is characterised by variable UCS <20 MPa, and low permeability (from 0.01 to 0.1 D down to few mD).

Partially weathered core stones exhibit a broad range of UCS values, ranging between 75 MPa and 125 MPa (Fig. 7.12a). They have a permeability included between 0.01 D and 0.1 D (Fig. 7.7b). The clay-rich saprolite volume has been analysed along two transects (Fig. 6d). Both transects yield almost constant UCS and permeability values within the clay-rich saprolite (UCS=10-15 MPa, k= 10^{-2}-10^{-3} D) (Fig. 7.14b).

Previous authors described the mineralogical and textural changes of the granitoid crystalline basement of the Utsira High related to the development of a saprolitic weathering profile identified in the core samples of offshore exploratory wells (Riber et al., 2015, 2016, 2017, 2019; Lothe et al., 2018). They describe five different alteration facies accounting for the gradual disaggregation of the igneous host rock, the alteration of feldspar, and clay mineral formation. In their model, progressive downward penetration of meteoric fluids from the top-basement surface led to the development of a thick weathering profile containing both saprock and more mature saprolite formed at the expense of the host granitoid (Fig. 7.2a, b; Riber et al., 2015; Walter et al., 2018). Weathering extends from the top-basement surface (that was exposed to a subaerial tropical and humid climate) into depth in the rock column: the progressive degradation of the host rock primary structure and the presence of a pervasive network of fractures and fault zones promoted the penetration at depth of fluids enhancing alteration (Braathen et al., 2018; Walter et al., 2018; Zauyah et al., 2018). Incipient weathering along fractures leads to discolouring and limited mineral alteration while still preserving the igneous/metamorphic rock texture ("altered coherent facies A1-A2" in Riber et al., 2016, Fig. 7.2b). The alteration of biotite and plagioclase leads to progressive grain disaggregation and grain fracturing, clay mineral and Al-Fe oxide formation ("altered incoherent facies A3-A5" in Riber et al., 2016; Hayes et al., 2019). Progressive weathering is also reflected in a varying mineralogy of authigenic clay minerals, with smectite being progressively substituted by kaolinite as the degree of weathering increases (Coggan et al., 2013; Riber et al., 2016).

A similar transition in mineralogical and textural characteristics of the RGD with increasing alteration can be deduced by the comparison of the analysed Group W outcrops. Each outcrop effectively shows different textural, mineralogical, and mechanical characteristics, which indicate progressive weathering and alteration. Outcrops W1-S1 only display partial alteration of the wall rock along fractures while preserving the textural and mechanical properties of the host rock. The finest-fractions of these samples are enriched in smectite-like phases, suggesting only incipient alteration (Coggan et al., 2013; Riber et al., 2016). The alteration products observed at outcrop W2 document, instead, a transition from a coherent host rock (domain d1 in Fig. 7.6c) toward a sandy aggregate preserving the magmatic texture but not the mechanical cohesion of the host rock and increasing clay content (domain d3 in Fig. 7.6c). The clay content and the textural characteristics of domain d2 at outcrop W2 and outcrop S2 are similar to those described for "alteration facies A3-A4" by Riber et al. (2016). The clay-rich alteration product in outcrop W3, analysed by Fredin et al. (2017b), is enriched in kaolinite over smectite-like phases, suggesting an advanced stage of alteration (Coggan et al., 2013; Riber et al., 2016). Outcrop W3 mineralogical and textural characteristics are similar to the alteration facies A5 described by Riber et al. (2016).

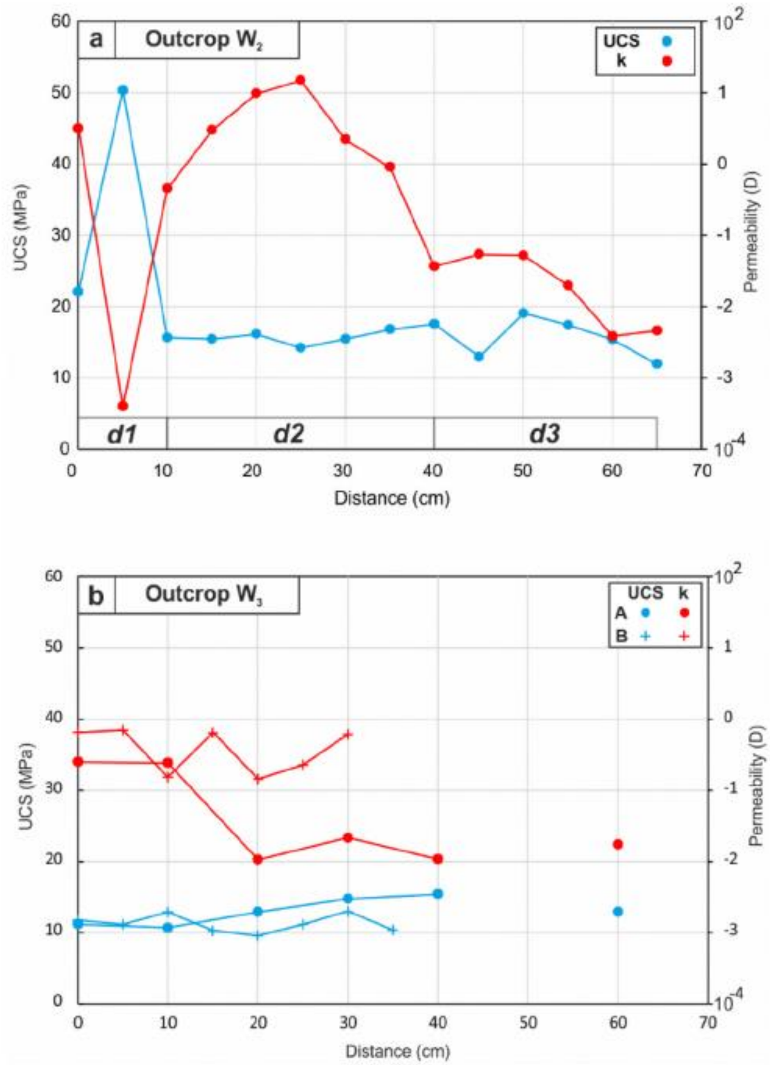

Figure 7.14 - Results of mechanical strength and permeability quantification along the transect at outcrops (a) W2 and (b) W3. Letters A and B in (b) refer to the two transects shown in Fig. 7.6d (Ceccato et al., 2021b).

The alteration products analysed in the Group W outcrops all present textural and mineralogical characteristics which are ascribable to kaolinitisation and/or saprolitisation of the RGD host (Coggan et al., 2013; Riber et al., 2016; Fredin et al., 2017a). Indeed, alteration processes took place at either shallow crustal levels (<6 km? depth, Scheiber and Viola, 2018) or surficial conditions (weathering - saprolitisation) (Fredin et al., 2017a). It is worth noting that, in each of the analysed outcrops, the weathering products postdate the formation of brittle structures and are not overprinted by any subsequent brittle deformation. This may suggest that weathering likely developed during periods of quiescent tectonic activity, as it is postulated for the development of thick saprolitic horizons (Fredin et al., 2017a). Therefore, we speculate that the studied Group W outcrops may be adopted as representative of the different stages of progressive weathering. The partially altered outcrop W1 represents the deepest portions of the weathering profile; the outcrop W2 represents the intermediate alteration stage and the transition toward more evolved alteration products, which are well represented by outcrop W3 (Fig. 7.15) (Lothe et al., 2018).

Such a defined weathering profile displays a progressive degradation of mechanical strength and an overall permeability enhancement with the increasing weathering grade (from A1 to A5, Fig. 7.15b). Incipient alteration leads to a progressive decrease in mechanical strength of about 50% of the intact RGD. The permeability at this stage of weathering is increased up to 0.01-1 D. The transition from coherent (A2) to incoherent alteration facies (A3-A5) is characterised by a drastic decrease in mechanical strength (UCS down to < 20 MPa, Fig. 7.15b). Conversely, the permeability increases up to 10 D within alteration facies A3-A4, and then progressively decreases toward 10^{-4} D when approaching alteration facies A5 (Fig. 7.15b; cf. Coggan et al., 2013; Lothe et al., 2018; Walter et al., 2018). Microstructural investigations suggest that the petrophysical properties of incipient alteration stages (coherent alteration facies A1-A2) are controlled by microfracture-related porosity and biotite and plagioclase alteration into clay-minerals (Goodfellow et al., 2016; Walter et al., 2018). The increasing alteration of biotite and plagioclase promotes the development of vacuole-shaped porosity and triggers micro-fracturing as a consequence of positive volume changes caused by the oxidation reactions in the altering rock (Goodfellow et al., 2016; Walter et al., 2018).

Highly interconnected pores and micro-fractures enhance the effective permeability and storage capacity of the weathered rock (Walter et al., 2018) and the drastic decrease in mechanical strength between cohesive and cohesionless alteration facies (Coggan et al., 2013).

The most advanced stages of weathering (alteration facies A5) are characterised by the complete alteration of biotite and plagioclase into clay-minerals and Fe-oxides. At this stage, mineral alteration and neoblastesis lead to obstruction of the previously developed micro-porosity and to the observed reduction of permeability (Walter et al., 2018). As a result, weathering leads to immediate and drastic decrease of mechanical strength, whereas permeability firstly increases and then decreases during weathering process progression (Fig. 7.15).

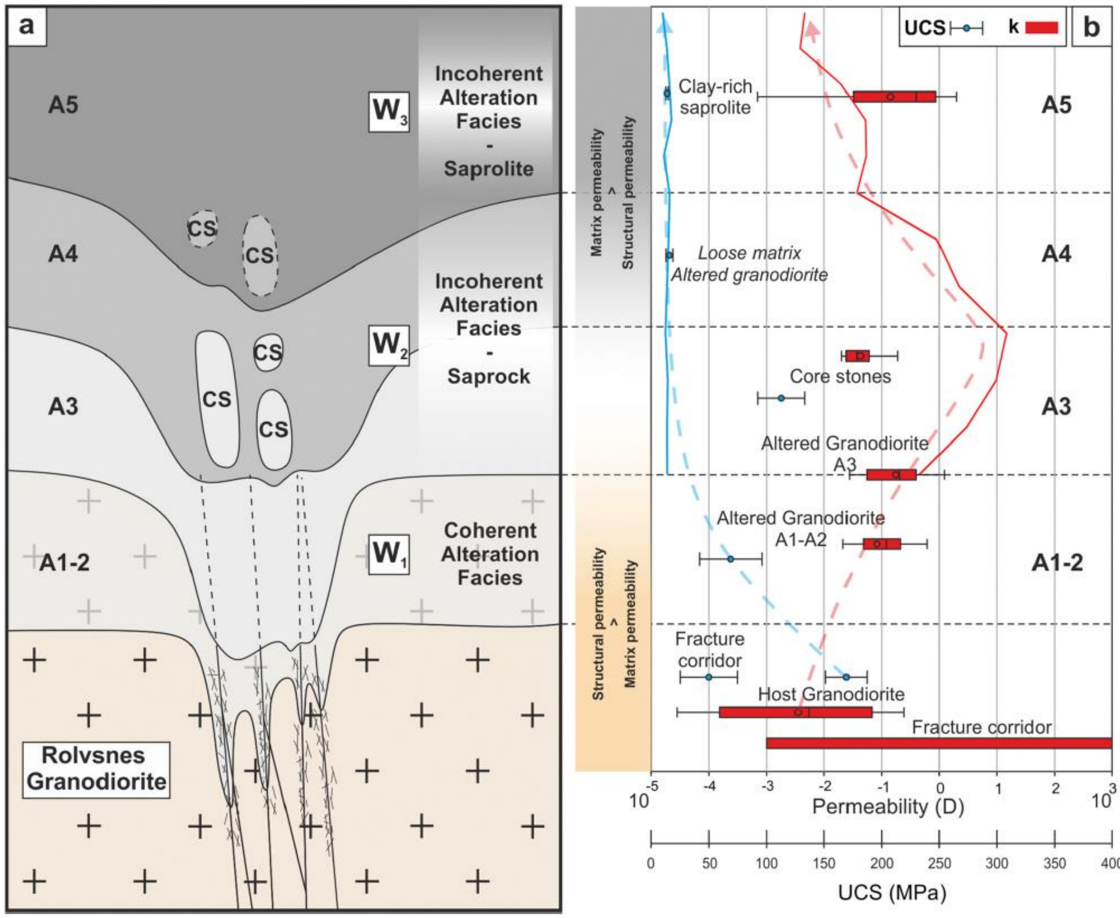

Figure 7.15 - a) Schematic representation of the top-basement weathering profile. The penetration of weathering processes into the crystalline basement is promoted by the structural discontinuities, such as SSRS fractures and fault zones. Alteration intensity decreases with depth. With increasing alteration, structural permeability is progressively replaced by matrix permeability related to the alteration products. (b) Mechanical strength and permeability variations through the alteration profile. The continuous red and light blue curves represent the mechanical strength and permeability observed at W2. The dashed red and blue curves represent the overall general trend of variation of k and UCS, respectively, through the weathering profile. An initial permeability increment in the deepest portion of the alteration profile is superseded by a drastic permeability decrement toward the more evolved weathering stages (Ceccato et al., 2021b).

The characteristics of the weathering profile studied here have three main important implications for the characterisation of reservoir rocks buried offshore beneath the sedimentary cover in the North Sea structural highs.

i. Weathering around fracture zones drives the transition from structurally controlled permeability of the intact host rock toward the matrix-controlled permeability of intermediate alteration facies (Fig. 7.15). Fracture zones are characterised by high permeability, which is, however, spatially confined to the mesoscopic fracture porosity and fracture aperture. The highly permeable alteration facies A3 is two orders of magnitude less permeable than the maximum permeability inferred for fracture corridors (with a fracture aperture of 1 mm). However, it involves larger volumes of the host rock, and thus dramatically increases the storage capacity of the reservoir rocks.

ii. The low permeability of alteration facies A5 (saprolite) suggests that the top layers of the weathering profile, when preserved, may act as a partial seal to fluid flow at the base of the sedimentary cover atop the basement structural highs (Walter et al., 2018).

iii. The studied paleo-weathering profile developed during the Mesozoic and was then buried below the Jurassic-Cretaceous sedimentary succession of the central North Sea. The observed differential mechanical strength may have led to different compaction patterns and behaviours, and thus a differential modification of the permeability of weathering products during the burial history of the paleo-weathering profile (Lothe et al., 2018). The weaker clay-rich saprolites may have undergone to a significant change of the original secondary porosity and permeability when compared to the more stiff, granular saprock and incipient alteration facies (Lothe et al., 2018; Walter et al., 2018).

7.5 Reservoir rocks in fractured and weathered basement

The fractured and weathered unconventional reservoir under consideration is thus heterogenous and composed of several structural and textural elements with different mechanical strength and permeability. It is the result of prolonged and complex interplay between tectonics and lithosphere-atmosphere interactions (Fredin et al., 2017a, b).

The reservoir rocks in fractured and weathered crystalline basement are made up of (Braathen et al., 2018): (1) the fractures and fault (damage) zones within the non-weathered crystalline basement, in which permeability is structurally controlled (Fig. 7.16), and (2) the products of weathering and alteration, such as the overlying top-basement paleo-weathering profile where the permeability is dominated by the matrix properties of the weathered products (Fig. 7.15, 7.16).

The crystalline basement is characterised by the occurrence of a complex network of SSRS and SRS, variably oriented brittle deformation zones that represent high-permeability conduits for fluid flow (Gabrielsen and Braathen, 2014; Scheiber and Viola, 2018). The volume of the fractured reservoir suited for fluid storage is therefore limited to the overall deformation zone volume. However, the occurrence of fault rocks within fault cores may limit the migration of fluids between highly permeable footwall and hanging wall damage zones. In addition, the intersection of variably oriented fault zones may limit the overall lateral fluid flow through the large-scale network of fracture lineaments. This would lead to the formation of fault bounded polyhedral domains (i.e., "reservoir compartments") of the fractured crystalline basement. Within each domain, fluid flow is limited to the high permeability fracture corridors and footwall/hanging wall damage zone connected to the domain bounding faults.

The reservoir storage volume is likely increased within the top-basement weathering profile and fracture-related alteration zones. Weathering may lead to the formation of very thick (up to 100 m thick) profiles characterised by high porosity and permeability (Braathen et al., 2018; Walter et al., 2018; Fig. 7.16). In addition, fluid percolation through fracture zones may lead to the deep penetration of weathering processes, down to even 300 m below the top-basement paleo-surface (Place et al., 2016; Walter et al., 2018). On the other hand, the most altered A5 facies may represent a top-seal layer to the underlying weathered and fractured basement high, buffering the upward migration of fluids toward the overlying sedimentary succession (Fig. 7.15, 7.16; Walter et al., 2018).

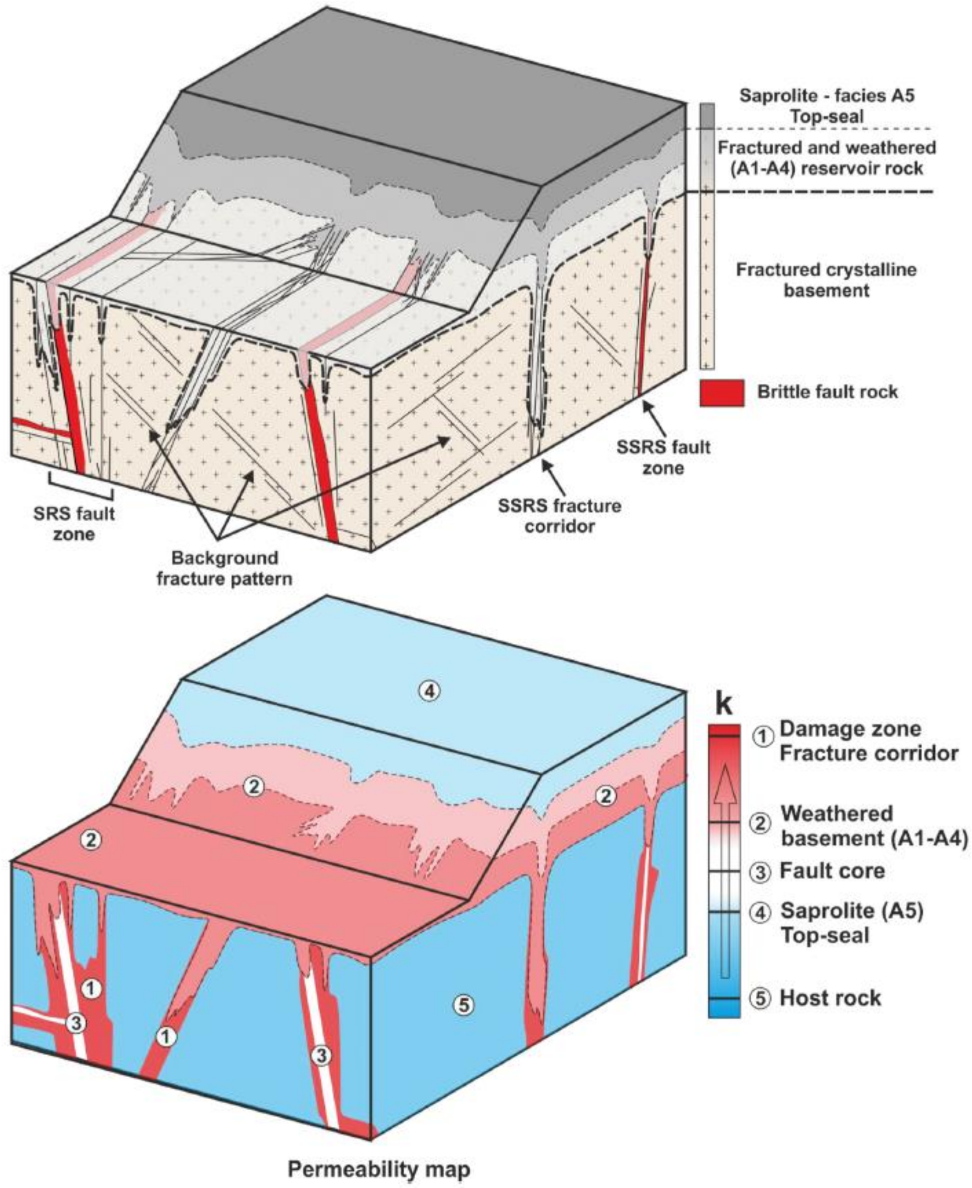

Figure 7.16 - Block diagram summarising a conceptualised model of reservoir within fractured and weathered crystalline basement (not to scale). a) The top-basement weathering profile overprints the fractured crystalline basement, exploiting the network of fractures and fault zones to penetrate to even great depth (down to 300 m, Walter et al., 2018). b) Schematic permeability map of the conceptualised model described in (a). The reservoir is deformed by highly permeable fractures and fault zones (1) and contains the deepest portion of the weathering profile (2). Fault cores (3) are inherently more permeable than the unaltered host rock, thus acting as a conduit for fluid flow parallel to fault strike. The potential reservoir rocks (1-2) and potential fluid conduits (1 and 3) are overlain by the low permeability saprolitic horizon (4), which may act as top-seal layer. Weathering processes greatly increase the fluid storage and transport potential of the reservoir close to the top-basement surface, which is otherwise limited to the network of fractures and fault zones (Ceccato et al., 2021b).

Chapter 8 - Conclusions

This thesis presents the results of an integrated study of the Mid-Norwegian Passive Margin. Difficulties in unravelling the MNPM evolution lie in the summation of and interference between several first-order, fundamental tectonic processes, such as crustal stretching, rifting and magma emplacement in a thinning lithosphere (Berndt et al., 2019; Zastrozhnov et al., 2020; Biari et al., 2021), and second-order features related to local stress fields and faulting regimes, evolving temperature and pressure conditions and/or fluid presence, composition and circulation modes (e.g., Wintsch et al., 1995; Faulkner and Rutter, 2003; Marchesini et al., 2019). Additionally, also third-order, peculiar and site-specific factors may affect the response of the deforming rock mass along passive margins, as, for example, lithology, the presence of pre-existing discontinuities, and the intrinsic geomechanical and petrophysical properties of the rock (e.g., Holdsworth, 2004; Bistacchi et al., 2012; Traforti et al., 2018). All these issues may be further complicated because of the effects of another crucial geological variable: time! It is indeed the summation and interaction of all these factors that created the intricate, complex, and multiphase brittle network now exposed along the MNPM.

In order to unravel the evolution in time of this brittle network, a multidisciplinary and multiscalar approach has demonstrated to be necessary. Defining and applying one such workflow has allowed us to collect data at several scales of observations and to effectively deal with the many different structural, mineralogical, geochemical and isotopic features that characterize the complex local brittle deformation.

As first step of this workflow, a conceptual tool for the characterisation of complex fault zones has been developed and tested, the so-called “Brittle Structural Facies”. This conceptual tool is extremely useful when dealing with the geometrical and temporal heterogeneity recorded and preserved within fault architectures (e.g., Caine et al., 1996). The identification and structural and mineralogical characterisation and dating of BSF’s permit to identify and resolve multiple reactivation events recorded even within a single fault zone, as demonstrated for the Lærdal-Gjende Fault zone case study, where the obtained results constrain up to four distinct and geochronologically resolvable periods of faulting and a coseismic rupture.

The BSF concept has been applied to faults and fractures along the Mid Norwegian Passive Margin within a much wider region. There, the reconstruction of the brittle tectonic evolution of the margin has required remote sensing lineament analysis, systematic field work, microstructural analysis, paleostress inversion, mineralogical characterisation and K-Ar dating of illite separated from selected and representative fault zones. The integration of different methodologies has made it possible to produce a comprehensive evolutionary model and to deal with the complexity of the exposed, polyphase fracture network. The obtained results, in particular the new sixty-two obtained K-Ar ages, help to fill the knowledge gap due to the lack of absolute time constraints on the margin's phases of brittle deformation and alteration. More specifically, six tectonic events have been identified: i) Caledonian NE-SW compression forming WNW-ESE striking thrust faults; ii) Caledonian transpression with a NW-SE oriented maximum compressional stress axis forming conjugate strike slip faults; iii) Carboniferous event associated with the early stage of the Atlantic rifting forming NW-SE and NE-SW striking faults; iv) Late Triassic-Jurassic E-W extension at c. 202 and 177 Ma causing faulting along ca. N-S striking, epidote and quartz-coated normal faults and coeval alteration of the host rock; v) second rifting stage in the Early Cretaceous (c. 122 Ma) with a NW-SE extension direction; vi) finally, Late Cretaceous extensional pulses (c. 71, 80, 86, 91 Ma) reactivating pre-existing faults, crystallising prehnite and zeolite.

One of the second order factors playing a significant role during the margin's evolution was fluid circulation and fluid-rock interaction. This thesis has tested an innovative approach by providing the first clumped isotopic constraints on calcite veins and mineralisations associated with fault zones deforming the MNPM basement rocks. This technique measures stable isotopic ratios and calculates the temperature and the $\delta^{18}O$ of the fluid from which calcite crystallised (Ghosh et al., 2006). Results from the MNPM and North Sea Margin samples add new important constraints on the definition of the fluid sources that were tapped during faulting and the progressive evolution of the margin. The obtained wide ranges of fluid temperature and stable isotopic ratios allowed us to discriminate a sequence of discrete calcite veining episodes at different temperatures, and to propose a correlation with the broader and independently constrained MNPM and North Sea rift evolution.

Another interest of studying the MNPM lies in the possibility to better understand the occurrence of large hydrocarbon unconventional plays within fractured and weathered basement blocks (Trice, 2014; Riber et al., 2015, 2017; Fredin et al., 2017; Trice et al., 2019). One of the most important factors affecting hydrocarbon production from unconventional fractured and weathered basement reservoirs is permeability, mainly dependant on secondary structural porosity (Braathen et al., 2018). Constraining the petrophysical properties of fractured and weathered basement outcrops was pivotal to better understand how brittle deformation and alteration processes steer the development of unconventional hydrocarbon plays. Thus, our *in situ* petrophysical measurements provide a novel contribution to the quantification of basement rocks geomechanical properties, which, in turn, are fundamental for better constraining fault zone localisation, nucleation, and mechanics, and significantly reduce the uncertainty in reservoir modelling. Additionally, in order to deal with the relative variation of permeability in fractured crystalline basements (Mitchell and Faulkner, 2012), structural and geometrical data were integrated with Discrete Fracture Network modelling to constrain the relationship between mesoscopic and sub-seismic resolution fracture patterns and the bulk permeability of a regional-scale fault zone, the Goddo Fault Zone.

There remain, however, unresolved aspects regarding the specific evolution in time and space of the MNPM. Hence, further fieldwork, structural analysis and fault rock dating need to be performed in specific key areas, for example around Kristiansand and on Smøla island, which were not studied during this research project as originally planned due to sever COVID restrictions. Future studies can thus specifically focus on the microstructural characterisation of calcite veins, studied by clumped thermometry, in order to link new data on the activated deformation mechanisms with the obtained isotopic values and temperature constraints. Finally, oxygen and carbon isotopic ratios are currently missing from the offshore sedimentary domain draping the basement structural highs. The correlation between on- and offshore isotopic data from onshore calcite veins and offshore sedimentary sequences may add valuable constraints on the origin of fluids and on the relative age of calcite veins decorating faults and fractures.

In conclusion, studying at different scales the brittle fracture pattern along the MNPM has permitted to obtain a new and detailed tectonic evolutionary model for the margin. The generated model finds its application for both up- and down-scaling purposes: thus, a mesoscopic fault characterised at the outcrop in terms of its geometry, kinematics, fault rock association and mineral coating is included in a regional framework by also adding an absolute age (or several ages) for its deformation phase(s), which makes it possible to correlate it to a specific tectonic stress regime. At the same time, a kilometric regional lineament can be correlated to coeval brittle structures at the outcrop scale, and their associated mineralisations. The proposed and tested multidisciplinary and multiscalar workflow has therefore demonstrated to be pivotal for unravelling complex, multiply fractured crystalline basement blocks and passive margin segments, as well as for further innovative, 3D modelling of fractured (and weathered) rock volumes to be studied and understood for their potential as reservoirs for extracting georesources or for Carbon and/or Hydrogen Storage.

References

Aldega, L., Viola, G., Casas-Sainz, A., Marcén, M., Román-Berdiel, T., and Lelij, R., 2019, Unravelling multiple thermo-tectonic events accommodated by crustal-scale faults in northern Iberia, Spain: Insights from K-Ar dating of clay gouges: Tectonics./10.1029/2019tc005585

Andersen, T. B., Corfu, F., Labrousse, L., and Osmundsen, P.-T., 2012, Evidence for hyperextension along the pre-Caledonian margin of Baltica: Journal of the Geological Society, v. 169, no. 5, p. 601-612./10.1144/0016-76492012-011

Andersen, T. B., Torsvik, T. H., Eide, A. E., Osmundsen, P. T., and Faleide, J. I., 1999, Mesozoic extensional faulting within the Caledonides of central south Norway: J. Geol. Soc., v. 156, p. 1073-1080

Angelier, J., 1984, Tectonic analysis of fault slip data sets: Journal of Geophysical Research: Solid Earth, v. 89, no. B7, p. 5835-5848

Aydin, A., 2000, Fractures, faults, and hydrocarbon entrapment, migration and flow: Marine and Petroleum Geology, v. 17, p. 797-814

Aydin, A., and Basu, A., 2005, The Schmidt hammer in rock material characterisation: Engineering Geology, v. 81, no. 1, p. 1-14./10.1016/j.enggeo.2005.06.006

Beltrando, M., Manatschal, G., Mohn, G., Dal Piaz, G. V., Brovarone, A. V., and Masini, E., 2014, Recognizing remnants of magma-poor rifted margins in high-pressure orogenic belts: The Alpine case study: Earth-Science Reviews, v. 131, p. 88-115. /10.1016/j.earscirev.2014.01.001

Bense, F. A., Wemmer, K., Loebens, S., and Siegesmund, S., 2013, Fault gouge analyses: K-Ar illite dating, clay mineralogy and tectonic significance - A study from the Sierras Pampeanas, Argentina: Int. J. Earth Sci./10.1007/s00531-013-0956-7

Bering, 1992. The orientation of minor fault plane striae and the associated deviatoric stress tensor as a key to the fault geometry in part of the Møre-Trøndelag Fault Zone, on-shore central Norway. In Structural and Tectonic Modelling and its Application to Petroleum Geology (pp. 83–90). /10.1016/B978-0-444-88607-1.50010-3

Bergman, S. C., Huntington, K. W., and Crider, J. G., 2013, Tracing paleofluid sources using clumped isotope thermometry of diagenetic cements along the Moab Fault, Utah: American Journal of Science, v. 313, no. 5, p. 490-515./10.2475/05.2013.03

Bernasconi, S. M., Daeron, M., Bergmann, K. D., Bonifacie, M., Meckler, A. N., Affek, H. P., Anderson, N., Bajnai, D., Barkan, E., Beverly, E., Blamart, D., Burgener, L., Calmels, D., Chaduteau, C., Clog, M., Davidheiser-Kroll, B., Davies, A., Dux, F., Eiler, J., Elliott, B., Fetrow, A. C., Fiebig, J., Goldberg, S., Hermoso, M., Huntington, K. W., Hyland, E., Ingalls, M., Jaggi, M., John, C. M., Jost, A. B., Katz, S., Kelson, J., Kluge, T., Kocken, I. J., Laskar, A., Leutert, T. J., Liang, D., Lucarelli, J., Mackey, T. J., Mangenot, X., Meinicke, N., Modestou, S. E., Muller, I. A., Murray, S., Neary, A., Packard, N., Passey, B. H., Pelletier, E., Petersen, S., Piasecki, A., Schauer, A., Snell, K. E., Swart, P. K., Tripati, A., Upadhyay, D., Vennemann, T., Winkelstern, I., Yarian, D., Yoshida, N., Zhang, N., and Ziegler, M., 2021, InterCarb: A Community Effort to Improve Interlaboratory Standardization of the Carbonate Clumped Isotope Thermometer Using Carbonate Standards: Geochem Geophys Geosyst, v. 22, no. 5, p. e2020GC009588./10.1029/2020GC009588

Bernasconi, S. M., Muller, I. A., Bergmann, K. D., Breitenbach, S. F. M., Fernandez, A., Hodell, D. A., Jaggi, M., Meckler, A. N., Millan, I., and Ziegler, M., 2018, Reducing Uncertainties in Carbonate Clumped Isotope Analysis Through Consistent Carbonate-Based Standardization: Geochem Geophys Geosyst, v. 19, no. 9, p. 2895-2914./10.1029/2017GC007385

Berndt, C., Planke, S., Teagle, D., Huismans, R., Torsvik, T., Frieling, J., Jones, M. T., Jerram, D. A., Tegner, C., Faleide, J. I., Coxall, H., and Hong, W.-L., 2019, Northeast Atlantic breakup volcanism and consequences for Paleogene climate change – MagellanPlus Workshop report: Scientific Drilling, v. 26, p. 69-85./10.5194/sd-26-69-2019

Biari, Y., Klingelhoefer, F., Franke, D., Funck, T., Loncke, L., Sibuet, J.-C., Basile, C., Austin, J. A., Rigoti, C. A., Sahabi, M., Benabdellouahed, M., and Roest, W. R., 2021, Structure and evolution of the Atlantic passive margins: A review of existing rifting models from wide-angle seismic data and kinematic reconstruction: Marine and Petroleum Geology, v. 126./10.1016/j.marpetgeo.2021.104898

Bistacchi, A., Massironi, M., Menegon, L., Bolognesi, F., and Donghi, V., 2012 On the nucleation of non-Andersonian faults along phyllosilicate-rich mylonite belts. Geological Society, London, Special Publications, 367, 185-199. / 10.1144/SP367.13

Blystad, P., 1995, Structural elements of the Norwegian continental shelf. Part 2: The Norwegian Sea region: NPD Bull., v. 8

Bonter, D. A., and Trice, R., 2019, An integrated approach for fractured basement characterisation: the Lancaster Field, a case study in the UK: Petroleum Geoscience, v. 25, no. 4, p. 400-414./10.1144/petgeo2018-152

Bott, M. H. P., 1959, The mechanics of oblique slip faulting: Geological magazine, v. 96, no. 2, p. 109-117

Braathen, A., 1999, Kinematics of post-Caledonian polyphase brittle faulting in the Sunnfjord region, western Norway, Tectonophysics, v. 302(1–2), p. 99-121, doi:10.1016/S0040-1951(98)00281-9.

Braathen, A., Abdel Fattah, M. M., Olaussen, S., Abdel-Gawad, G., and Ogata, K., 2018, Basement–cover reservoir analogue in rift-margin fault blocks; Gulf of Suez Rift, Sinai, Egypt: Petroleum Geoscience, v. 24, no. 4, p. 449-468./10.1144/petgeo2016-163

Braathen, A., Osmundsen, P. T., and Gabrielsen, R. H., 2004, Dynamic development of fault rocks in a crustal-scale detachment: An example from western Norway: Tectonics, v. 23, no. 4, p. 21./10.1029/2003tc001558

Braathen, A., Osmundsen, P. T., Nordgulen, Ø., Roberts, D., and Meyer, G. B., 2002, Orogen-parallel extension of the Caledonides in northern Central Norway: an overview: Norwegian Journal of Geology, v. 82, p. 225-241

Braathen, A., Tveranger, J., Fossen, H., Skar, T., Cardozo, N., Sernshaug, S. E., Bastesen, E., and Sverdrup, E., 2009, Fault facies and its application to sandstone reservoirs: Aapg Bull., v. 93, no. 7, p. 891-917./10.1306/03230908116

Breivik, A. J., Mjelde, R., Raum, T., Faleide, J. I., Murai, Y., and Flueh, E. R., 2011, Crustal structure beneath the Trøndelag Platform and adjacent areas of the mid--Norwegian margin, as derived from wide-angle seismic and potential field data: Norwegian Journal of Geology, v. 90, p. 141-161

Brekke, H., 2000, The tectonic evolution of the Norwegian Sea continental margin, with emphasis on the Voring and More basins: Special Publication-Geological Society of London, v. 167, p. 327-378

Brockamp, O., and Clauer, N., 2013, Hydrothermal and unexpected diagenetic alteration in Permian shales of the Lodève epigenetic U-deposit of southern France, traced by K–Ar illite and K-feldspar dating: Chem. Geol., v. 357, p. 18-28./10.1016/j.chemgeo.2013.08.009

Brune, S., Heine, C., Perez-Gussinye, M., and Sobolev, S. V., 2014, Rift migration explains continental margin asymmetry and crustal hyper-extension: Nat Commun, v. 5, p. 4014./10.1038/ncomms5014

Bugge, T., Elvebakk, G., Fanavoll, S., Mangerud, G., Smelror, M., Weiss, H. M., Gjelberg, J., Kristensen, S. E., and Nilsen, K., 2002, Shallow stratigraphic drilling applied in hydrocarbon exploration of the Nordkapp Basin, Barents Sea: Marine and Petroleum Geology, v. 19, no. 1, p. 13-37./10.1016/s0264-8172(01)00051-4

Bungum, H., Alsaker, A., Kvamme, L., and Hansen, R., 1991, Seismicity and seismotectonics of Norway and nearby continental shelf areas: Journal of Geophysical Research: Solid Earth, v. 96, no. B2, p. 2249-2265

Bungum, H., Alsaker, A., Kvamme, L., and Hansen, R., 1991, Seismicity and seismotectonics of Norway and nearby continental shelf areas: Journal of Geophysical Research: Solid Earth, v. 96, no. B2, p. 2249-2265, doi:10.1029/90JB02010

Caine, J. S., Evans, J. P., and Forster, C. B., 1996, Fault zone architecture and permeability structure: Geology, v. 24, no. 11, p. 1025-1028

Ceccato, A., Viola, G., Antonellini, M., Tartaglia, G., and Ryan, E. J., 2021a, Constraints upon fault zone properties by combined structural analysis of virtual outcrop models and discrete fracture network modelling: Journal of Structural Geology, v. 152./10.1016/j.jsg.2021.104444

Ceccato, A., Viola, G., Tartaglia, G., and Antonellini, M., 2021b, In–situ quantification of mechanical and permeability properties on outcrop analogues of offshore fractured and weathered crystalline basement: Examples from the Rolvsnes granodiorite, Bømlo, Norway: Marine and Petroleum Geology, v. 124./10.1016/j.marpetgeo.2020.104859

Charbit, S., Guillou, H., Turpin, L., 1998. Cross calibration of K–Ar standard minerals using an unspiked Ar measurement technique. Chem. Geol.150 (1–2), 147–159.

Chester, F. M., and Logan, J. M., 1986, Implications for Mechanical Properties of Brittle Faults from Observations of the Punchbowl Fault Zone, California: Pure Appl. Geophys., v. 124, p. 79–106

Choi, J. H., Edwards, P., Ko, K., and Kim, Y. S., 2016, Definition and classification of fault damage zones: A review and a new methodological approach: Earth Sci. Rev., v. 152, p. 70-87./10.1016/j.earscirev.2015.11.006

Clauer, N., 2013, The K-Ar and 40Ar/39Ar methods revisited for dating fine-grained K-bearing clay minerals: Chem. Geol., v. 354, p. 163-185./10.1016/j.chemgeo.2013.05.030

Clerc, C., Ringenbach, J.-C., Jolivet, L., and Ballard, J.-F., 2018, Rifted margins: Ductile deformation, boudinage, continentward-dipping normal faults and the role of the weak lower crust: Gondwana Research, v. 53, p. 20-40./10.1016/j.gr.2017.04.030

Coggan, J. S., Stead, D., Howe, J. H., and Faulks, C. I., 2013, Mineralogical controls on the engineering behavior of hydrothermally altered granites under uniaxial compression: Engineering Geology, v. 160, p. 89-102./10.1016/j.enggeo.2013.04.001

Corfu, F., Andersen, T. B., and Gasser, D., 2014, The Scandinavian Caledonides: main features, conceptual advances and critical questions: Geol. Soc. London, Spec. Publ., v. 390, no. 1, p. 9-43./10.1144/sp390.25

Curzi, M., Aldega, L., Bernasconi, S. M., Berra, F., Billi, A., Boschi, C., Franchini, S., Van der Lelij, R., Viola, G., and Carminati, E., 2020, Architecture and evolution of an extensionally-inverted thrust (Mt. Tancia Thrust, Central Apennines): Geological, structural, geochemical, and K–Ar geochronological constraints: Journal of Structural Geology, v. 136./10.1016/j.jsg.2020.104059

Daëron, M., 2021, Full Propagation of Analytical Uncertainties in Δ47 Measurements: Geochemistry, Geophysics, Geosystems, v. 22, no. 5./10.1029/2020gc009592

Dalrymple, G. B., and Lanphere, M. A., 1969, Potassium-argon dating: Principles, techniques and applications to geochronology, (Freeman) San Francisco, California, p. 258-258

Damsleth, E., Sangolt, V., and Aamodt, G., 1988, Sub-seismic faults can seriously affect fluid flow in the njord field off western norway-a stochastic fault modeling case study, *in* Proceedings SPE Annual Technical Conference and Exhibition, OnePetro

Davids, K., Wemmer, K., Zwingmann, H., Kohlmann, F., Jacobs, J., and Bergh, S. G., 2013, K–Ar illite and apatite fission track constraints on brittle faulting and the evolution of the northern Norwegian passive margin: Tectonophysics, v. 608, p. 196-211./10.1016/j.tecto.2013.09.035

Deer, W., Howie, R., and Zussman, J., 2013, An introduction to the rock-forming minerals. Mineralogical Society of Great Britain and Ireland, Book

Delvaux, D., and Sperner, B., 2003, Stress tensor inversion from fault kinematic indicators and focal mechanism data: the TENSOR program.: Geol. Soc. London, Spec. Publ., v. 212, p. 75-100

Dewez, T., Girardeau-Montaut, D., Allanic, C., and Rohmer, J., 2016, Facets: A Cloudcompare Plugin to Extract Geological Planes from Unstructured 3d Point Clouds: International Archives of the Photogrammetry, Remote Sensing & Spatial Information Sciences, v. 41. /10.5194/isprsarchives-XLI-B5-799-2016

Di Toro, G., and Pennacchioni, G., 2004, Superheated friction-induced melts in zoned pseudotachylytes within the Adamello tonalites (Italian Southern Alps): J. Struct. Geol., v. 26, no. 10, p. 1783-1801./10.1016/j.jsg.2004.03.001

Doré, A., Lundin, E., Fichler, C., and Olesen, O., 1997, Patterns of basement structure and reactivation along the NE Atlantic margin: Journal of the Geological Society, v. 154, no. 1, p. 85-92, doi:10.1144/gsjgs.154.1.0085

Doré, A., Lundin, E., Jensen, L., Birkeland, Ø., Eliassen, P., and Fichler, C., 1999, Principal tectonic events in the evolution of the northwest European Atlantic margin, *in* Proceedings Geological society, London, petroleum geology conference series, Volume 5, Geological Society of London, p. 41-61

Doré, A. G., Lundin, E. R., Kusznir, N. J., and Pascal, C., 2008, Potential mechanisms for the genesis of Cenozoic domal structures on the NE Atlantic margin: pros, cons and some new ideas: Geological Society, London, Special Publications, v. 306, no. 1, p. 1-26./10.1144/sp306.1

Doré, T., and Lundin, E., 2015, Research focus: Hyperextended continental margins—knowns and unknowns: Geology, v. 43, no. 1, p. 95-96, /10.1130/focus012015.1

Drake, H., Heim, C., Roberts, N. M. W., Zack, T., Tillberg, M., Broman, C., Ivarsson, M., Whitehouse, M. J., and Åström, M. E., 2017, Isotopic evidence for microbial production and consumption of methane in the upper continental crust throughout the Phanerozoic eon: Earth and Planetary Science Letters, v. 470, p. 108-118./10.1016/j.epsl.2017.04.034

Duffy, O. B., Bell, R. E., Jackson, C. A. L., Gawthorpe, R. L., and Whipp, P. S., 2015, Fault growth and interactions in a multiphase rift fault network: Horda Platform, Norwegian North Sea: Journal of Structural Geology, v. 80, p. 99-119./10.1016/j.jsg.2015.08.015

Eiler, J. M., 2007, “Clumped-isotope” geochemistry—The study of naturally-occurring, multiply-substituted isotopologues: Earth and Planetary Science Letters, v. 262, no. 3-4, p. 309-327./10.1016/j.epsl.2007.08.020

Eiler, 2011, Paleoclimate reconstruction using carbonate clumped isotope thermometry: Quaternary Science Reviews, v. 30, no. 25-26, p. 3575-3588./10.1016/j.quascirev.2011.09.001

Eiler, J. M., and Schauble, E., 2004, 18O13C16O in Earth’s atmosphere: Geochimica et Cosmochimica Acta, v. 68, no. 23, p. 4767-4777./10.1016/j.gca.2004.05.035

Evans, J. P., Forster, C. B., and Goddard, J. V., 1997, Permeability of fault-related rocks, and implications for hydraulic structure of fault zones: Journal of Structural Geology,, v. 19, no. 11, p. 1393-1404

Færseth, R. B., 1996, Interaction of Permo-Triassic and Jurassic extensional fault-blocks during the development of the northern North Sea: J. Geol. Soc. London, v. 153, p. 931-944

Faleide, J. I., Bjørlykke, K., and Gabrielsen, R. H., 2010, Geology of the Norwegian Continental Shelf, *in* Heidelberg, S.-V. B., ed., Petroleum Geoscience: From Sedimentary Environments to Rock Physics./10.1007/978-3-642-02332-3_22

Faleide, J. I., Tsikalas, F., Breivik, A. J., Mjelde, R., Ritzmann, O., Engen, Ø., Wilson, J., and Eldholm, O., 2008, Structure and evolution of the continental margin off Norway and the Barents Sea: Episodes, v. 31, no. 1, p. 82-91./10.18814/epiiugs/2008/v31i1/012

Faulkner, D., and Rutter, E., 1998, The gas permeability of clay-bearing fault gouge at 20 C: Geological Society, London, Special Publications, v. 147, no. 1, p. 147-156

Faulkner, D. R., Jackson, C. A. L., Lunn, R. J., Schlische, R. W., Shipton, Z. K., Wibberley, C. A. J., and Withjack, M. O., 2010, A review of recent developments concerning the structure, mechanics and fluid flow properties of fault zones: Journal of Structural Geology, v. 32, no. 11, p. 1557-1575./10.1016/j.jsg.2010.06.009

Faulkner, D. R., and Rutter, E. H., 2003, The effect of temperature, the nature of the pore fluid, and subyield differential stress on the permeability of phyllosilicate-rich fault gouge: Journal of Geophysical Research: Solid Earth, v. 108, no. B5./10.1029/2001jb001581

Fazlikhani, H., Aagotnes, S. S., Refvem, M. A., Hamilton-wright, J., Bell, R., Fossen, H., Gawthorpe, R., Jackson, C. A.-L., and Rotevatn, A., 2020, Strain migration during multiphase extension, Stord Basin, northern North Sea rift./10.31223/osf.io/b8acf

Fernandez, A., Müller, I. A., Rodríguez-Sanz, L., van Dijk, J., Looser, N., and Bernasconi, S. M., 2017, A Reassessment of the Precision of Carbonate Clumped Isotope Measurements: Implications for Calibrations and Paleoclimate Reconstructions: Geochemistry, Geophysics, Geosystems, v. 18, no. 12, p. 4375-4386./10.1002/2017gc007106

Ferrill, D. A., Morris, A. P., Evans, M. A., Burkhard, M., Groshong, R. H., and Onasch, C. M., 2004, Calcite twin morphology: a low-temperature deformation geothermometer: J. Struct. Geol., v. 26, no. 8, p. 1521-1529./10.1016/j.jsg.2003.11.028

Filomena, C., Hornung, J., and Stollhofen, H., 2014, Assessing accuracy of gas-driven permeability measurements: a comparative study of diverse Hassler-cell and probe permeameter devices: Solid Earth, v. 5, no. 1, p. 1-11. /10.5194/se-5-1-2014

Fjellanger, E., Surlyk, F., Wamsteeker, L. C., & Midtun, T., 2005, Upper Cretaceous basin-floor fans in the Vøring Basin, Mid Norway shelf. In B. Wandaas, et al. (Eds.), Onshore-Offshore Relationships on the North Atlantic Margin, Special Publications, v. 12, pp. 135–164. Trondheim, Norway: Norwegian Petroleum Society, doi:10.1016/S0928-8937(05)80047-5

Fossen, H., 2010, Extensional tectonics in the North Atlantic Caledonides: a regional view: Geol. Soc. London, Spec. Publ./10.1144/SP335.31 0305-8719

Fossen, H., and Dunlap, W. J., 1998, Timing and kinematics of Caledonian thrusting and extensional collapse, southern Norway: Evidence from $^{40}Ar/^{39}Ar$ thermochronology: J. Struct. Geol., v. 20, no. 6, p. 765-781

Fossen, H., and Hurich, C. A., 2005, The Hardangerfjord Shear Zone in SW Norway and the North Sea: a large-scale low-angle shear zone in the Caledonian crust: J. Geol. Soc. London, v. 162, no. 4, p. 675-687./10.1144/0016-764904-136

Fossen, H., Khani, H. F., Faleide, J. I., Ksienzyk, A. K., and Dunlap, W. J., 2016, Post-Caledonian extension in the West Norway–northern North Sea region: the role of structural inheritance: Geol. Soc. London, Spec. Publ., v. 439, no. 1, p. 465-486./10.1144/sp439.6

Fossen, H., Ksienzyk, A. K., and Jacobs, J., 2017, Correspondence: Challenges with dating weathering products to unravel ancient landscapes: Nat. Commun., v. 8, no. 1, p. 1502./10.1038/s41467-017-01457-9

Fossen, H., Ksienzyk, A. K., Rotevatn, A., Bauck, M. S., and Wemmer, K., 2021, From widespread faulting to localised rifting: Evidence from K-Ar fault gouge dates from the Norwegian North Sea rift shoulder: Basin Research./10.1111/bre.12541

Fredin, O., Viola, G., Zwingmann, H., Sorlie, R., Bronner, M., Lie, J. E., Grandal, E. M., Muller, A., Margreth, A., Vogt, C., and Knies, J., 2017a, The inheritance of a Mesozoic landscape in western Scandinavia: Nat. Commun., v. 8, p. 14879./10.1038/ncomms14879

Fredin, O., Viola, G., Zwingmann, H., Sorlie, R., Bronner, M., Lie, J. E., Grandal, E. M., Muller, A., Margreth, A., Vogt, C., and Knies, J., 2017b, Correspondence: Reply to 'Challenges with dating weathering products to unravel ancient landscapes': Nat Commun, v. 8, no. 1, p. 1503./10.1038/s41467-017-01468-6

Fuhrmann, U., Lippolt, H., Hess, J.C., 1987. HD-B1 biotite reference material for K-Ar chronometry. Chem. Geol.66, 41–51.

Gabrielsen, R., and Færseth, R., 1988 Cretaceous and Tertiary reactivation of master fault zones of the Barents Sea, *in* Proceedings Tertiary Tectonics of Svalbard. Extended Abstracts from Symposium Held in Oslo. Norwegian Polar Institute Report Series, Volume 46, p. 93-97

Gabrielsen, R. H., and Braathen, A., 2014, Models of fracture lineaments — Joint swarms, fracture corridors and faults in crystalline rocks, and their genetic relations: Tectonophysics, v. 628, p. 26-44./10.1016/j.tecto.2014.04.022

Gabrielsen, R. H., Braathen, A., Dehls, J., and Roberts, D., 2002, Tectonic lineaments of Norway: Norw. J. Geol., v. 82, p. 153-174

Gabrielsen, R. H., Odinsen, T., and Grunnaleite, I., 1999, Structuring of the Northern Viking Graben and the More Basin; the influence of basement structural grain and the particular role of the More Trondelag Fault Complex: Marine and Petroleum Geology, v. 16, p. 443-465

Gautneb, H., and Roberts, D., 1989, Geology and petrochemistry of the Smela-Hitra Batholith, Central Norway: Nor. geol. unders. Bull., v. 416, p. 1-24

Geoffroy, L., Burov, E. B., and Werner, P., 2015, Volcanic passive margins: another way to break up continents: Sci Rep, v. 5, p. 14828./10.1038/srep14828

Gernigon, L., Franke, D., Geoffroy, L., Schiffer, C., Foulger, G. R., and Stoker, M., 2020, Crustal fragmentation, magmatism, and the diachronous opening of the Norwegian-Greenland Sea: Earth-Science Reviews, v. 206./10.1016/j.earscirev.2019.04.011

Gernigon, L., Zastrozhnov, D., Planke, S., Manton, B., Abdelmalak, M. M., Olesen, O., Maharjan, D., Faleide, J. I., and Myklebust, R., 2021, A digital compilation of structural and magmatic elements of the Mid-Norwegian continental margin (version 1.0): Norwegian Journal of Geology./10.17850/njg101-3-2

Ghosh, P., Adkins, J., Affek, H., Balta, B., Guo, W., Schauble, E. A., Schrag, D., and Eiler, J. M., 2006, ^{13}C–^{18}O bonds in carbonate minerals: A new kind of paleothermometer: Geochimica et Cosmochimica Acta, v. 70, no. 6, p. 1439-1456./10.1016/j.gca.2005.11.014

Gómez, M., Vergés, J., Fernàndez, M., Torne, M., Ayala, C., Wheeler, W., and Karpuz, R., 2004, Extensional geometry of the Mid Norwegian Margin before Early Tertiary continental breakup: Marine and Petroleum Geology, v. 21, no. 2, p. 177-194./10.1016/j.marpetgeo.2003.11.017

Gomila, R., Arancibia, G., Mitchell, T. M., Cembrano, J. M., and Faulkner, D. R., 2016, Palaeopermeability structure within fault-damage zones: A snap-shot from microfracture analyses in a strike-slip system: Journal of Structural Geology, v. 83, p. 103-120./10.1016/j.jsg.2015.12.002

Gordon, S. M., Whitney, D. L., Teyssier, C., Fossen, H., and Kylander-Clark, A., 2016, Geochronology and geochemistry of zircon from the northern Western Gneiss Region: Insights into the Caledonian tectonic history of western Norway: Lithos, v. 246-247, p. 134-148./10.1016/j.lithos.2015.11.036

Grant, N. T., 2019, Stochastic modelling of fault gouge zones: implications for fault seal analysis: Geological Society, London, Special Publications./10.1144/sp496-2018-135

Grathoff, G. H., Moore, D. M., Hay, R. L., and Wemmer, K., 2001, Origin of illite in the lower Paleozoic of the Illinois basin: Evidence for brine migrations: GSA Bulletin, v. 113, no. 8, p. 1092-1104./10.1130/0016-7606(2001)113<1092:Ooiitl>2.0.Co;2

Grønlie, A., and Roberts, D., 1989, Resurgent strike-slip duplex development along the Hitra-Snåsa and Verran faults, Møre-Trøndelag fault zone, central Norway: Journal of structural geology, v. 11, no. 3, p. 295-305

Grønlie, A., Roberts, D., and Nilsen, B., 1991, Brittle deformation history of fault rocks on the Fosen Peninsula, Trøndelag, Central Norway

Grønlie, G., and Ramberg, I. B., 1970, Gravity indications of deep sedimentary basins below the Norwegian continental shelf and the Vøring Plateau: Norsk Geologisk Tidsskrift, v. 50, p. 374-391

Haines, S. H., and van der Pluijm, B. A., 2008, Clay quantification and Ar-Ar dating of synthetic and natural gouge: Application to the Miocene Sierra Mazatan detachment fault, Sonora, Mexico.: J. Struct. Geol., v. 30, no. 525-538./10.1016/j.jsg.2007.11.012

Hałas, S., and Wójtowicz, A., 2014, Propagation of error formulas for K/Ar dating method: Geochronometria, v. 41, no. 3, p. 202-206./10.2478/s13386-013-0162-1

Hancock, P. L., 1985, Brittle microtectonics: principles and practice. Journal of structural geology, 7(3-4), 437-457

Hayes, J. L., Riebe, C. S., Holbrook, W. S., Flinchum, B. A., and Hartsough, P. C., 2019, Porosity production in weathered rock: Where volumetric strain dominates over chemical mass loss: Sci Adv, v. 5, no. 9, p. eaao0834./10.1126/sciadv.aao0834

Healy, D., Rizzo, R. E., Cornwell, D. G., Farrell, N. J. C., Watkins, H., Timms, N. E., Gomez-Rivas, E., and Smith, M., 2017, FracPaQ: A MATLAB™ toolbox for the quantification of fracture patterns: J. Struct. Geol., v. 96, p. 1-16./10.1016/j.jsg.2016.12.003

Hemingway, J. D., and Henkes, G. A., 2021, A disordered kinetic model for clumped isotope bond reordering in carbonates: Earth and Planetary Science Letters, v. 566, p. 116962. /10.1016/j.epsl.2021.116962

Høien, A. H., Nilsen, B., and Olsson, R., 2019, Main aspects of deformation and rock support in Norwegian road tunnels: Tunnelling and Underground Space Technology, v. 86, p. 262-278./10.1016/j.tust.2019.01.026

Holdsworth, R. E., 2004, Weak faults - Rotten cores: Science, v. 303, p. 181-182

Holdsworth, R. E., Trice, R., Hardman, K., McCaffrey, K. J. W., Morton, A., Frei, D., Dempsey, E., Bird, A., and Rogers, S., 2020, The nature and age of basement host rocks and fissure fills in the Lancaster field fractured reservoir, West of Shetland: Journal of the Geological Society, v. 177, no. 5, p. 1057-1073./10.1144/jgs2019-142

Hower, J., Hurley, P., Pinson, W., and Fairbairn, H., 1963, The dependence of K-Ar age on the mineralogy of various particle size ranges in a shale: Geochimica et cosmochimica acta, v. 27, no. 5, p. 405-410

Huismans, R., and Beaumont, C., 2011, Depth-dependent extension, two-stage breakup and cratonic underplating at rifted margins: Nature, v. 473, no. 7345, p. 74-78. /10.1038/nature09988

Huntington, K. W., and Lechler, A. R., 2015, Carbonate clumped isotope thermometry in continental tectonics: Tectonophysics, v. 647-648, p. 1-20./10.1016/j.tecto.2015.02.019

Hunziker, J. C., Frey, M., Clauer, N., Dallmeyer, R. D., Friedriehsen, H., Flehmig, W., Hoehstrasser, K., Roggwiler, P., and Schwander, H., 1986, The evolution of illite to muscovite: mineralogical and isotopic data from the Glarus Alps, Switzerland: Contrib Mineral Petrol, v. 92, p. 157-180

Johannessen, K. C., Kohlmann, F., Ksienzyk, A. K., Dunkl, I., and Jacobs, J., 2013, Tectonic evolution of the SW Norwegian passive margin based on low-temperature thermochronology from the innermost Hardangerfjord area: Norw. J. Geol., v. 93, p. 243-260

Keen, C., and Beaumont, C., 1990, Geodynamics of rifted continental margins: Geology of the continental margin of eastern Canada, v. 2, p. 391-472

Kelley, S. P., 2002, Excess argon in K–Ar and Ar–Ar geochronology: Chem. Geol., v. 188, p. 1-22

Kendrick, M. A., Eide, E. A., Roberts, D., and Osmundsen, P. T., 2004, The Middle to Late Devonian Høybakken detachment, central Norway: 40Ar–39Ar evidence for prolonged late/post-Scandian extension and uplift: Geological Magazine, v. 141, no. 3, p. 329-344./10.1017/s0016756803008811

Krabbendam, M., and Dewey, J. F., 1998, Exhumation of UHP rocks by transtension in the Western Gneiss Region, Scandinavian Caledonides: Geol. Soc. London, Spec. Publ., v. 135, p. 159-181

Krabbendam, M., Wain, A., and Andersen, T. B., 2000, Pre-Caledonian granulite and gabbro enclaves in the Western Gneiss Region, Norway: indications of incomplete transition at high pressure: Geological Magazine, v. 137, p. 235–255

Ksienzyk, A. K., Dunkl, I., Jacobs, J., Fossen, H., and Kohlmann, F., 2014, From orogen to passive margin: constraints from fission track and (U-Th)/He analyses on Mesozoic uplift and fault reactivation in SW Norway., Geol. Soc. London Spec. Publ. /10.1144/SP390.27

Ksienzyk, A. K., Wemmer, K., Jacobs, J., Fossen, H., Schomberg, A. C., Süssenberger, A., Lünsdorf, N. K., and Bastesen, E., 2016, Post-Caledonian brittle deformation in the Bergen area: Norw. J. Geol., v. 96, no. 3./10.17850/njg96-3-06

Kylander-Clark, A. R. C., Hacker, B. R., Johnson, C. M., Beard, B. L., and Mahlen, N. J., 2009, Slow subduction of a thick ultrahigh-pressure terrane: Tectonics, v. 28, no. 2, p. n/a-n/a./10.1029/2007tc002251

Labrousse, L., Hetényi, G., Raimbourg, H., Jolivet, L., and Andersen, T. B., 2010, Initiation of crustal-scale thrusts triggered by metamorphic reactions at depth: Insights from a comparison between the Himalayas and Scandinavian Caledonides: Tectonics, v. 29, no. 5, p. n/a-n/a./10.1029/2009tc002602

Lacombe, O., 2012, Do fault slip data inversions actually yield "paleostress" that can be compared with contemporary stresses? A critical discussion: Comptes Rendus Geoscience, v. 344, p. 159-173. /10.1016/j.crte.2012.01.006

Lacombe, O., 2012, Do fault slip data inversions actually yield "paleostress" that can be compared with contemporary stresses? A critical discussion: Comptes Rendus Geoscience, v. 344, p. 159-173, doi: 10.1016/j.crte.2012.01.006

Lacombe, O., Jolivet, L., Le Pourhiet, L., Lecomte, E., and Mehl, C., 2013, Initiation, geometry and mechanics of brittle faulting in exhuming metamorphic rocks: insights from the northern Cycladic islands (Aegean, Greece): Bull. Soc. géol. France, v. 184, no. 4-5, p. 383-403. /10.2113/gssgfbull.184.4-5.383

Larsen, B. T., Oulassen S., Sundvoll B., Heeremans M. 2008, The Permo-Carboniferous Oslo Rift through six stages and 65 million years. Episodes, 31.1: 52-58.

Lavier, L. L., and Manatschal, G., 2006, A mechanism to thin the continental lithosphere at magma-poor margins: Nature, v. 440, no. 7082, p. 324-328. /10.1038/nature04608

Lee, J.-Y., Marti, K., Severinghaus, J. P., Kawamura, K., Yoo, H.-S., Lee, J. B., and Kim, J. S., 2006, A redetermination of the isotopic abundances of atmospheric Ar: Geochimica et Cosmochimica Acta, v. 70, no. 17, p. 4507-4512. /10.1016/j.gca.2006.06.1563

LeGrande, A. N., and Schmidt, G. A., 2006, Global gridded data set of the oxygen isotopic composition in seawater: Geophysical Research Letters, v. 33, no. 12./10.1029/2006gl026011

Levell, B., Argent, J., Doré, A. G., and Fraser, S., 2010, Passive margins: overview: Geological Society, London, Petroleum Geology Conference series, v. 7, no. 1, p. 823-830./10.1144/0070823

Lin, A., 1994, Microlite Morphology and Chemistry in Pseudotachylite, from the Fuyun Fault Zone, China: The Journal of Geology, v. 102, p. 317-329

Lothe, A. E., Emmel, B., Bergmo, P. E., Akervoll, I., Todorovic, J., Bhuiyan, M. H., and Knies, J., 2018, Porosity, permeability and compaction trends for Scandinavian regoliths: Marine and Petroleum Geology, v. 92, p. 319-331./10.1016/j.marpetgeo.2017.10.027

Luetkemeyer, P. B., Kirschner, D. L., Huntington, K. W., Chester, J. S., Chester, F. M., and Evans, J. P., 2016, Constraints on paleofluid sources using the clumped-isotope thermometry of carbonate veins from the SAFOD (San Andreas Fault Observatory at Depth) borehole: Tectonophysics, v. 690, p. 174-189./10.1016/j.tecto.2016.05.024

Lundberg, E., Juhlin, C., and Nasuti, A., 2012, High resolution reflection seismic profiling over the Tjellefonna fault in the Møre-Trøndelag Fault Complex, Norway: Solid Earth, v. 3, no. 1, p. 175-188./10.5194/se-3-175-2012

Lundin, E., and Doré, A., 2002, Mid-Cenozoic post-breakup deformation in the ‘passive’margins bordering the Norwegian–Greenland Sea: Marine and Petroleum Geology, v. 19, no. 1, p. 79-93. /10.1016/S0264-8172(01)00046-0

Lundin, E. R., and Doré, A. G., 2011, Hyperextension, serpentinization, and weakening: A new paradigm for rifted margin compressional deformation: Geology, v. 39, no. 4, p. 347-350. /10.1130/G31499.1

Lundin, E. R., and Doré, A. G., 2019, Non-Wilsonian break-up predisposed by transforms: examples from the North Atlantic and Arctic: Geological Society, London, Special Publications, v. 470, no. 1, p. 375-392./10.1144/sp470.6

Malatesta, C., Crispini, L., Ildefonse, B., Federico, L., Lisker, F., and Läufer, A., 2021, Microstructures of epidote-prehnite bearing damaged granitoids (northern Victoria Land, Antarctica): clues for the interaction between faulting and hydrothermal fluids. Journal of Structural Geology,147, 104350, doi:10.1016/j.jsg.2021.104350

Manatschal, G., 2004, New models for evolution of magma-poor rifted margins based on a review of data and concepts from West Iberia and the Alps: International Journal of Earth Sciences, v. 93, no. 3, p. 432-466. 10.1007/s00531-004-0394-7

Marchesini, B., Garofalo, P. S., Menegon, L., Mattila, J., and Viola, G., 2019, Fluid-mediated, brittle–ductile deformation at seismogenic depth – Part 1: Fluid record and deformation history of fault veins in a nuclear waste repository (Olkiluoto Island, Finland): Solid Earth, v. 10, no. 3, p. 809-838./10.5194/se-10-809-2019

Mark, D. F., Kelley, S. P., Lee, M. R., Parnell, J., Sherlock, S. C., and Brown, D. J., 2008, Ar-Ar dating of authigenic K-feldspar: Quantitative modelling of radiogenic argon-loss through subgrain boundary networks: Geochim. Cosmochim. Ac., v. 72, p. 2695-2710./10.1016/j.gca.2008.03.018

Mattila, J., and Viola, G., 2014, New constraints on 1.7 Gyr of brittle tectonic evolution in southwestern Finland derived from a structural study at the site of a potential nuclear waste repository (Olkiluoto Island): J. Struct. Geol., v. 67, p. 50-74./10.1016/j.jsg.2014.07.003

McKenzie, D., 1978, Active tectonics of the Alpine—Himalayan belt: the Aegean Sea and surrounding regions: Geophysical Journal International, v. 55, no. 1, p. 217-254

Meckler, A. N., Affolter, S., Dublyansky, Y. V., Krüger, Y., Vogel, N., Bernasconi, S. M., Frenz, M., Kipfer, R., Leuenberger, M., Spötl, C., Carolin, S., Cobb, K. M., Moerman, J., Adkins, J. F., and Fleitmann, D., 2015, Glacial–interglacial temperature change in the tropical West Pacific: A comparison of stalagmite-based paleo-thermometers: Quaternary Science Reviews, v. 127, p. 90-116./10.1016/j.quascirev.2015.06.015

Meckler, A. N., Ziegler, M., Millan, M. I., Breitenbach, S. F., and Bernasconi, S. M., 2014, Long-term performance of the Kiel carbonate device with a new correction scheme for clumped isotope measurements: Rapid Commun Mass Spectrom, v. 28, no. 15, p. 1705-1715./10.1002/rcm.6949

Medvedev, S., Hartz, E. H., Schmid, D. W., Zakariassen, E., and Varhaug, P., 2019, Influence of glaciations on North Sea petroleum systems: Geological Society, London, Special Publications./10.1144/sp494-2018-183

Meunier, A., Velde, B., and Zalba, P., 2004, Illite K–Ar dating and crystal growth processes in diagenetic environments: a critical review: Terra Nova, v. 16, p. 296-304./10.1111/j.1365-3121.2004.00563.x

Millán, M. I., Machel, H., and Bernasconi, S. M., 2016, Constraining temperatures of formation and composition of dolomitizing fluids in the Upper Devonian Nisku Formation (Alberta, Canada) with clumped isotopes: Journal of Sedimentary Research, v. 86, no. 1, p. 107-112. /10.2110/jsr.2016.6

Milnes, A. G., and Corfu, F., 2011, Structural Geology and Tectonic Evolution of the Sognefjord Transect, Caledonian Orogen, Southern Norway—A Field Trip Guide: Geol. Soc. Am. Field Guide, v. 19./10.1130/2011.0019

Mitchell, T. M., and Faulkner, D. R., 2012, Towards quantifying the matrix permeability of fault damage zones in low porosity rocks: Earth and Planetary Science Letters, v. 339-340, p. 24-31./10.1016/j.epsl.2012.05.014

Mosar, J., ,, Eide, E. A., Osmundsen, P. T., Sommaruga, A., and Torsvik, T. H., 2002, Greenland – Norway separation: A geodynamic model for the North Atlantic: Norwegian Journal of Geology v. 82, p. 282-299

Mottram, C. M., Kellett, D. A., Barresi, T., Zwingmann, H., Friend, M., Todd, A., and Percival, J. B., 2020, Syncing fault rock clocks: Direct comparison of U-Pb carbonate and K-Ar illite fault dating methods: Geology, v. 48, no. 12, p. 1179-1183./10.1130/g47778.1

Muller, I. A., Fernandez, A., Radke, J., van Dijk, J., Bowen, D., Schwieters, J., and Bernasconi, S. M., 2017, Carbonate clumped isotope analyses with the long-integration dual-inlet (LIDI) workflow: scratching at the lower sample weight boundaries: Rapid Commun Mass Spectrom, v. 31, no. 12, p. 1057-1066./10.1002/rcm.7878

Müller, R., Ngstuen, J. P., Eide, F., and H., L., 2005, Late Permian to Triassic basin infill history and palaeogeography of the Mid-Norwegian shelf—East Greenland region: Norwegian Petroleum Society Special Publications,, v. 12, p. 165-189./10.1016/S0928-8937(05)80048-7

Munro, M. A., and Blenkinsop, T. G., 2012, MARD—A moving average rose diagram application for the geosciences: Computers & Geosciences, v. 49, p. 112-120./10.1016/j.cageo.2012.07.012

Nasuti, A., Pascal, C., and Ebbing, J., 2012, Onshore–offshore potential field analysis of the Møre–Trøndelag Fault Complex and adjacent structures of Mid Norway: Tectonophysics, v. 518-521, p. 17-28./10.1016/j.tecto.2011.11.003

Nasuti, A., Pascal, C., Ebbing, J., and Tønnesen, J. F., 2011, Geophysical characterisation of two segments of the Møre-Trøndelag Fault Complex, Mid Norway: Solid Earth, v. 2, no. 2, p. 125-134./10.5194/se-2-125-2011

Niemeijer, A. R., and Spiers, C. J., 2005, Influence of phyllosilicates on fault strength in the brittle-ductile transition: insights from rock analogue experiments: Geological Society, London, Special Publications, v. 245, no. 1, p. 303-327./10.1144/gsl.Sp.2005.245.01.15

Nordbäck, N., Mattila, J., Zwingmann, H., and Viola, G., 2022, Precambrian fault reactivation revealed by structural and K-Ar geochronological data from the spent nuclear fuel repository in Olkiluoto, southwestern Finland: Tectonophysics, 824, pp. 1 – 22, doi:10.1016/j.tecto.2022.229208

Oda, M., 1985, Permeability tensor for discontinuous rock masses: Geotechnique, v. 35, no. 4, p. 483-495

Olsen, M. P., Scholz, C. H., and Léger, A., 1998, Healing and sealing of a simulated fault gouge under hydrothermal conditions: Implications for fault healing: J. Geoph. Res., v. 103, p. 7421-7430

Ortega, O. J., Marrett, R. A., and Laubach, S. E., 2006, A scale-independent approach to fracture intensity and average spacing measurement: AAPG bulletin, v. 90, no. 2, p. 193-208

Osmundsen, P. T., and Andersen, T. B. 2001, The middle Devonian basins of western Norway: sedimentary response to large-scale transtensional tectonics?. Tectonophysics, 332(1-2), 51-68. doi:10.1016/S0040-1951(00)00249-3

Osmundsen, P. T., Braathen, A., Sommaruga, A., Skilbrei, J. R., Nordgulen, O., Roberts, D., Andersen, T. B., Olesen, O., and Mosar, J., 2005, Metamorphic core complexes and gneiss-cored culminations along the Mid-Norwegian margin: an overview and some current ideas: Onshore-Offshore Relationships on the North Atlantic Margin, v. 12, p. 29-41. /10.1016/S0928-8937(05)80042-6

Osmundsen, P. T., and Ebbing, J., 2008, Styles of extension offshore mid-Norway and implications for mechanisms of crustal thinning at passive margins: Tectonics, v. 27, no. 6, p. n/a-n/a./10.1029/2007tc002242

Osmundsen, P. T., Eide, A. E., Haabesland, N. E., Roberts, D., Andersen, T. B., Kendrick, M., Bingen, B., Braathen, A., and Redfield, T. F., 2006, Kinematics of the Høybakken detachment zone and the Møre–Trøndelag Fault Complex, central Norway: J. Geol. Soc. London, v. 163, p. 303-318. /10.1144/0016-764904-129

Osmundsen, P. T., and Péron-Pinvidic, G., 2018, Crustal-scale fault interaction at rifted margins and the formation of domain-bounding breakaway complexes: Insights from offshore Norway. Tectonics, 37, p. 935–964, doi:10.1002/2017TC004792

Osmundsen, P. T., Péron-Pinvidic, G., and Bunkholt, H., 2021, Rifting of Collapsed Orogens: Successive Incision of Continental Crust in the Proximal Margin Offshore Norway: Tectonics, v. 40, no. 2./10.1029/2020tc006283

Osmundsen, P. T., Redfield, T. F., Hendriks, B. H. W., Bergh, S., Hansen, J. A., Henderson, I. H. C., Dehls, J., Lauknes, T. R., Larsen, Y., Anda, E., and Davidsen, B., 2010, Fault-controlled alpine topography in Norway: J. Geol. Soc. London, v. 167, no. 1, p. 83-98./10.1144/0016-76492009-019

Passey, B. H., and Henkes, G. A., 2012, Carbonate clumped isotope bond reordering and geospeedometry: Earth and Planetary Science Letters, v. 351, p. 223-236. /10.1016/j.epsl.2012.07.021

Péron-Pinvidic, G., and Manatschal, G., 2019, Rifted margins: state of the art and future challenges: Frontiers in Earth Science, v. 7, p. 218. /10.3389/feart.2019.00218

Péron-Pinvidic, G., Manatschal, G., and Osmundsen, P. T., 2013, Structural comparison of archetypal Atlantic rifted margins: A review of observations and concepts: Marine and Petroleum Geology, v. 43, p. 21-47./10.1016/j.marpetgeo.2013.02.002

Péron-Pinvidic, G., and Osmundsen, P. T., 2016, Architecture of the distal and outer domains of the Mid-Norwegian rifted margin: Insights from the Rån-Gjallar ridges system: Marine and Petroleum Geology, v. 77, p. 280-299./10.1016/j.marpetgeo.2016.06.014

Péron-Pinvidic, G., and Osmundsen, P. T., 2020, From orogeny to rifting: insights from the Norwegian 'reactivation phase': Sci Rep, v. 10, no. 1, p. 14860./10.1038/s41598-020-71893-z

Péron-Pinvidic, G., Osmundsen, P. T., and Bunkholt, H., 2020, The proximal domain of the Mid-Norwegian rifted margin: The Trøndelag Platform revisited: Tectonophysics./10.1016/j.tecto.2020.228551

Petford, N., and McCaffrey, K., 2003, Hydrocarbons in crystalline rocks: an introduction: Geological Society, London, Special Publications, v. 214, no. 1, p. 1-5./10.1144/gsl.Sp.2003.214.01.01

Petit, J. P., 1987, Criteria for the sense of movement on fault surfaces in brittle rocks. Journal of structural Geology, 9(5-6), 597-608.

Pevear, D. R., 1999, Illite and hydrocarbon exploration: P. Nat. Acad. Sci. USA, v. 96, no. 7, p. 3440-3446

Phillips, T. B., Fazlikhani, H., Gawthorpe, R. L., Fossen, H., Jackson, C. A. L., Bell, R. E., Faleide, J. I., and Rotevatn, A., 2019, The influence of structural inheritance and multiphase extension on rift development, the northern North Sea: Tectonics./10.1029/2019tc005756

Place, J., Géraud, Y., Diraison, M., Herquel, G., Edel, J. B., Bano, M., Le Garzic, E., and Walter, B., 2016, Structural control of weathering processes within exhumed granitoids: Compartmentalisation of geophysical properties by faults and fractures: Journal of Structural Geology, v. 84, p. 102-119./10.1016/j.jsg.2015.11.011

Pleuger, J., Mancktelow, N., Zwingmann, H., and Manser, M., 2012, K–Ar dating of synkinematic clay gouges from Neoalpine faults of the Central, Western and Eastern Alps: Tectonophysics, v. 550-553, p. 1-16./10.1016/j.tecto.2012.05.001

Pollard, D. D., 2000, Strain and stress: Discussion: Journal of Structural Geology, v. 22, p. 1359-1367

Ranero, C. R., and Perez-Gussinye, M., 2010, Sequential faulting explains the asymmetry and extension discrepancy of conjugate margins: Nature, v. 468, no. 7321, p. 294-299./10.1038/nature09520

Redfield, T. F., Braathen, A., Gabrielsen, R. H., Osmundsen, P. T., Torsvik, T. H., and Andriessen, P. A. M., 2005, Late Mesozoic to Early Cenozoic components of vertical separation across the Møre–Trøndelag Fault complex, Norway: Tectonophysics, v. 395, no. 3-4, p. 233-249./10.1016/j.tecto.2004.09.012

Redfield, T. F., and Osmundsen, P. T., 2009, The Tjellefonna fault system of Western Norway: Linking late-Caledonian extension, post-Caledonian normal faulting, and Tertiary rock column uplift with the landslide-generated tsunami event of 1756: Tectonophysics, v. 474, no. 1-2, p. 106-123./10.1016/j.tecto.2009.02.006

Redfield, T. F., Torsvik, T. H., Andriessen, P. A. M., and Gabrielsen, R. H., 2004, Mesozoic and Cenozoic tectonics of the Møre Trøndelag Fault Complex, central Norway: constraints from new apatite fission track data: Physics and Chemistry of the Earth, Parts A/B/C, v. 29, no. 10, p. 673-682./10.1016/j.pce.2004.03.005

Ren, S., Faleide, J. I., Eldholm, O., Skogseid, J., and Gradstein, F., 2003, Late Cretaceous–Paleocene tectonic development of the NW Vøring Basin: Marine and Petroleum Geology, v. 20, no. 2, p. 177-206./10.1016/s0264-8172(03)00005-9

Renne, P. R., Balco, G., Ludwig, K. R., Mundil, R., and Min, K., 2011, Response to the comment by W.H. Schwarz et al. on "Joint determination of 40K decay constants and 40Ar∗/40K for the Fish Canyon sanidine standard, and improved accuracy for $^{40}Ar/^{39}Ar$ geochronology" by P.R. Renne et al. (2010): Geochim. Cosmochim. Ac., v. 75, no. 17, p. 5097-5100./10.1016/j.gca.2011.06.021

Reston, T., 2007, Extension discrepancy at North Atlantic nonvolcanic rifted margins: Depth-dependent stretching or unrecognized faulting?: Geology, v. 35, no. 4, p. 367-370. /10.1130/G23213A.1

Reston, T. J., 2005, Polyphase faulting during the development of the west Galicia rifted margin: Earth and Planetary Science Letters, v. 237, no. 3-4, p. 561-576./10.1016/j.epsl.2005.06.019

Riber, L., Driese, S. G., Stinchcomb, G. E., Dypvik, H., and Sørlie, R., 2019, Reconstructing a high paleolatitude Mesozoic paleoenvironment from a truncated and deeply buried regolith, Norwegian North Sea: Palaeogeography, Palaeoclimatology, Palaeoecology, v. 528, p. 60-77./10.1016/j.palaeo.2019.04.031

Riber, L., Dypvik, H., and Sørlie, R., 2015, Altered basement rocks on the Utsira High and its surroundings, Norwegian North Sea: Norw. J. Geol./10.17850/njg95-1-04

Riber, L., Dypvik, H., Sorlie, R., Aal-E-Muhammad Naqvi, S. A., Stangvik, K., Oberhardt, N., and Schroeder, P. A., 2017, Comparison of deeply buried paleoregolith profiles, Norwegian North Sea, with outcrops from southern Sweden and Georgia, USA —Implications for petroleum exploration: Palaeogeogr. Palaeocl., v. 471, p. 82-95./10.1016/j.palaeo.2017.01.043

Riber, L., Dypvik, H., Sorlie, R., and Ferrell, R. E., 2016, Clay minerals in deeply buried paleoregolith profiles, Norwegian North Sea: Clay Clay Miner., v. 64, no. 5, p. 588-607./10.1346/CCMN.2016.064036

Rocchini, D., Petras, V., Petrasova, A., Chemin, Y., Ricotta, C., Frigeri, A., Landa, M., Marcantonio, M., Bastin, L., Metz, M., Delucchi, L., and Neteler, M., 2017, Spatio-ecological complexity measures in GRASS GIS: Comput. Geosci., v. 104, p. 166-176./10.1016/j.cageo.2016.05.006

Rodríguez-Sanz, L., Bernasconi, S. M., Marino, G., Heslop, D., Mueller, I. A., Fernandez, A., Grant, K. M., and Rohling, E. J., 2017, Penultimate deglacial warming across the Mediterranean Sea revealed by clumped isotopes in foraminifera: Scientific Reports, v. 7, no. 1, p. 1-11. / 10.1038/s41598-017-16528-6

Rønnevik, H., Eggen, S., and Vollset, J., 1983, Exploration of the Norwegian shelf: Geological Society, London, Special Publications, v. 12, no. 1, p. 71-93

Rotevatn, A., Kristensen, T. B., Ksienzyk, A. K., Wemmer, K., Henstra, G. A., Midtkandal, I., Grundvåg, S. A., and Andresen, A., 2018, Structural Inheritance and Rapid Rift-Length Establishment in a Multiphase Rift: The

East Greenland Rift System and its Caledonian Orogenic Ancestry: Tectonics, v. 37, no. 6, p. 1858-1875./10.1029/2018tc005018

Rutqvist, J., and Stephansson, O., 2003, The role of hydromechanical coupling in fractured rock engineering: Hydrogeology Journal, v. 11, no. 1, p. 7-40. /10.1007/s10040-002-0241-5

Rutter, E. H., Holdsworth, R. E., and Knipe, R. J., 2001, The nature and tectonic significance of fault-zone weakening: an introduction: Geol. Soc. London, Spec. Publ., v. 186, no. 1, p. 1-11. /10.1144/GSL.SP.2001.186.01.01

Ryan, R., O'Beirne-Ryan, A. M., and Zentilli, M., 2005, Rounded cobbles that have not travelled far: incorporation of corestones from saprolites in the South Mountain area of southern Nova Scotia, Canada: Sedimentology, v. 52, no. 5, p. 1109-1121. /10.1111/j.1365-3091.2005.00730.x

Saintot, A., Stephens, M. B., Viola, G., and Nordgulen, Ø., 2011, Brittle tectonic evolution and paleostress field reconstruction in the southwestern part of the Fennoscandian Shield, Forsmark, Sweden: Tectonics, v. 30, no. 4, p. n/a-n/a./10.1029/2010tc002781

Salomon, E., Rotevatn, A., Kristensen, T. B., Grundvåg, S.-A., Henstra, G. A., Meckler, A. N., Albert, R., and Gerdes, A., 2020, Fault-controlled fluid circulation and diagenesis along basin-bounding fault systems in rifts – insights from the East Greenland rift system: Solid Earth, v. 11, no. 6, p. 1987-2013./10.5194/se-11-1987-2020

Samakinde, C. A., Van Bever Donker, J. M., Durrheim, R., and Manzi, M., 2020, Application of seismic stratigraphy in reservoir characterisation: a case study of the passive margin deposits of the northern Orange Basin, South Africa: Journal of Petroleum Exploration and Production Technology./10.1007/s13202-020-01050-9

Sasseville, C., Tremblay, A., Clauer, N., and Liewig, N., 2008, K–Ar age constraints on the evolution of polydeformed fold–thrust belts: The case of the Northern Appalachians (southern Quebec): J. Geodyn., v. 45, no. 2-3, p. 99-119./10.1016/j.jog.2007.07.004

Schauble, E. A., Ghosh, P., and Eiler, J. M., 2006, Preferential formation of 13C–18O bonds in carbonate minerals, estimated using first-principles lattice dynamics: Geochimica et Cosmochimica Acta, v. 70, no. 10, p. 2510-2529./10.1016/j.gca.2006.02.011

Scheiber, T., Fredin, O., Viola, G., Jarna, A., Gasser, D., and Łapińska-Viola, R., 2015, Manual extraction of bedrock lineaments from high-resolution LiDAR data: methodological bias and human perception: Gff, v. 137, no. 4, p. 362-372./10.1080/11035897.2015.1085434

Scheiber, T., Viola, G., Wilkinson, C.M., Ganerød, M., Skår, O. and Gasser D., 2016, Direct $^{40}Ar/^{39}Ar$ dating of Late-Ordovician and Silurian brittle faulting in the southwestern Norwegian Caledonides. Terra Nova 28, 374-382, doi:10.1111/ter.12230

Scheiber, T., and Viola, G., 2018, Complex Bedrock Fracture Patterns: A Multipronged Approach to Resolve Their Evolution in Space and Time: Tectonics, v. 37, no. 4, p. 1030-1062./10.1002/2017tc004763

Scheiber, T., Viola, G., van der Lelij, R., Margreth, A., and Schönenberger, J., 2019, Microstructurally-constrained versus bulk fault gouge K-Ar dating: J. Struct. Geol., v. 127./10.1016/j.jsg.2019.103868

Schiffer, C., Doré, A. G., Foulger, G. R., Franke, D., Geoffroy, L., Gernigon, L., Holdsworth, B., Kusznir, N., Lundin, E., McCaffrey, K., Peace, A., Petersen, K. D., Phillips, T., Stephenson, R., Stoker, M. S., and Welford, K., 2019, Structural inheritance in the North Atlantic: Earth-Science Reviews./10.1016/j.earscirev.2019.102975

Schmid, T. W., and Bernasconi, S. M., 2010, An automated method for 'clumped-isotope' measurements on small carbonate samples: Rapid Commun Mass Spectrom, v. 24, no. 14, p. 1955-1963./10.1002/rcm.4598

Scibek, J., 2020, Multidisciplinary database of permeability of fault zones and surrounding protolith rocks at world-wide sites: Sci Data, v. 7, no. 1, p. 95./10.1038/s41597-020-0435-5

Séranne, M., 1992, Late Palaeozoic kinematics of the Møre-Trøndelag Fault Zone and adjacent areas, central Norway·: Norsk Geologisk Tidsskrift, v. 72, p. 141-158

Sherlock, S. C., Watts, L. M., Holdsworth, R. E., and Roberts, D., 2004, Dating fault reactivation by Ar/Ar laserprobe: an alternative view of apparently cogenetic mylonite–pseudotachylite assemblages: J. Geol. Soc. London, v. 161, no. 3, p. 335-338./10.1144/0016-764903-160

Sibson, R. H., and Rowland, J. V., 2003, Stress, fluid pressure and structural permeability in seismogenic crust, North Island, New Zealand: Geophysical Journal International, v. 154, no. 2, p. 584-594. /10.1046/j.1365-246X.2003.01965.x

Slagstad, T., Davidsen, B., and Daly, J. S., 2011, Age and composition of crystalline basement rocks on the Norwegian continental margin: offshore extension and continuity of the Caledonian–Appalachian orogenic belt: J. Geol. Soc. London, v. 168, no. 5, p. 1167-1185./10.1144/0016-76492010-136

Smeraglia, L., Fabbri, O., Choulet, F., Buatier, M., Boulvais, P., Bernasconi, S. M., and Castorina, F., 2020, Syntectonic fluid flow and deformation mechanisms within the frontal thrust of a foreland fold-and-thrust belt: Example from the Internal Jura, Eastern France: Tectonophysics, v. 778./10.1016/j.tecto.2019.228178

Solum, J. G., van der Pluijm, B. A., and Peacor, D. R., 2005, Neocrystallization, fabrics and age of clay minerals from an exposure of the Moab Fault, Utah: J. Struct. Geol., v. 27, no. 9, p. 1563-1576./10.1016/j.jsg.2005.05.002

Sommaruga, A., Bøe, R., 2002. Geometry and subcrop maps of shallow Jurassic basins along the Mid-Norway coast. Marine and Petroleum Geology 19, 1029–1042

Souque, C., Knipe, R. J., Davies, R. K., Jones, P., Welch, M. J., and Lorenz, J., 2019, Fracture corridors and fault reactivation: Example from the Chalk, Isle of Thanet, Kent, England: Journal of Structural Geology, v. 122, p. 11-26./10.1016/j.jsg.2018.12.004

Staněk, M., and Géraud, Y., 2019, Granite microporosity changes due to fracturing and alteration: secondary mineral phases as proxies for porosity and permeability estimation: Solid Earth, v. 10, no. 1, p. 251-274./10.5194/se-10-251-2019

Steiger, R. H., and Jäger, E., 1977, Subcommission on geochronology: convention on the use of decay constants in geo-and cosmochronology: Earth and planetary science letters, v. 36, no. 3, p. 359-362

Stemmerik, L., 2000, Late Palaeozoic evolution of the North Atlantic margin of Pangea: Palaeogeography, Palaeoclimatology, Palaeoecology, v. 161, no. 1-2, p. 95-126

Stemmerik, L., Christiansen, F., Piasecki, S., Jordt, B., Marcussen, C., and Nøhr-Hansen, H., 1993, Depositional history and petroleum geology of the Carboniferous to Cretaceous sediments in the northern part of East Greenland, Norwegian Petroleum Society Special Publications, Volume 2, Elsevier, p. 67-87

Stemmerik, L., Ineson, J. R., and Mitchell, J. G., 2000, Stratigraphy of the Rotliegend Group in the Danish part of the Northern Permian Basin, North Sea: Journal of the Geological Society, London, v. 157, p. 1127–1136

Stober, I., and Bucher, K., 2007, Hydraulic properties of the crystalline basement: Hydrogeology Journal, v. 15, no. 2, p. 213-224. / 10.1007/s10040-006-0094-4

Stoker, M. S., Stewart, M. A., Shannon, P. M., Bjerager, M., Nielsen, T., Blischke, A., Hjelstuen, B. O., Gaina, C., McDermott, K., and Ólavsdóttir, J., 2017, An overview of the Upper Palaeozoic–Mesozoic stratigraphy of the NE Atlantic region: Geological Society, London, Special Publications, v. 447, no. 1, p. 11-68./10.1144/sp447.2

Stolper, D. A., and Eiler, J. M., 2015, The kinetics of solid-state isotope-exchange reactions for clumped isotopes: A study of inorganic calcites and apatites from natural and experimental samples: American Journal of Science, v. 315, no. 5, p. 363-411. /10.2475/05.2015.01

Sturt, B. A., and Braathen, A., 2001, Deformation and metamorphism of Devonian rocks in the outer Solund area, western Norway: implications for models of Devonian deformation. International Journal of Earth Sciences: Geologische Rundschau, 90(2), 270, doi:10.1007/s005310000131

Surace, I. R., Clauer, N., Thélin, P., and Pfeifer, H. R., 2011, Structural analysis, clay mineralogy and K–Ar dating of fault gouges from Centovalli Line (Central Alps) for reconstruction of their recent activity: Tectonophysics, v. 510, no. 1-2, p. 80-93./10.1016/j.tecto.2011.06.019

Tagami, T., 2012, Thermochronological investigation of fault zones: Tectonophysics, v. 538, p. 67-85./10.1016/j.tecto.2012.01.032

Talwani, M., and Eldholm, O., 1972, Continental margin off Norway: a geophysical study: Geological Society of America Bulletin, v. 83, no. 12, p. 3575-3606

Tanner D.C., Buness H., Igel J., Gunther T., Gabriel G., Skiba P., Planefisch T., Gasterann N., Walter T.R., 2019 Fault detection, Understanding Faults: Detecting, Dating, and Modeling. /10.1016/B978-0-815985-9.00003-5.

Tartaglia, G., Viola, G., van der Lelij, R., Scheiber, T., Ceccato, A., and Schönenberger, J., 2020, "Brittle structural facies" analysis: A diagnostic method to unravel and date multiple slip events of long-lived faults: Earth and Planetary Science Letters, v. 545./10.1016/j.epsl.2020.116420

Theissen-Krah, S., Zastrozhnov, D., Abdelmalak, M. M., Schmid, D. W., Faleide, J. I., and Gernigon, L., 2017, Tectonic evolution and extension at the Møre Margin – Offshore mid-Norway: Tectonophysics, v. 721, p. 227-238./10.1016/j.tecto.2017.09.009

Thiele, S. T., Grose, L., Samsu, A., Micklethwaite, S., Vollgger, S. A., and Cruden, A. R., 2017, Rapid, semi-automatic fracture and contact mapping for point clouds, images and geophysical data: Solid Earth, v. 8, no. 6, p. 1241-1253. /10.5194/se-8-1241-2017

Tikoff, B., and Fossen, H., 1999, Three-dimensional reference deformations and strain facies: Journal of Structural Geology, v. 21, no. 11, p. 1497-1512

Torabi, A., Alaei, B., and Ellingsen, T., 2018, Faults and fractures in basement rocks, their architecture, petrophysical and mechanical properties: Journal of Structural Geology, v. 117, p. 256-263. /10.1016/j.jsg.2018.07.001

Torabi, A., and Berg, S. S., 2011, Scaling of fault attributes: A review: Marine and Petroleum Geology, v. 28, no. 8, p. 1444-1460./10.1016/j.marpetgeo.2011.04.003

Torabi, A., Ellingsen, T. S. S., Johannessen, M. U., Alaei, B., Rotevatn, A., and Chiarella, D., 2020, Fault zone architecture and its scaling laws: where does the damage zone start and stop?: Geological Society, London, Special Publications, v. 496, no. 1, p. 99-124./10.1144/sp496-2018-151

Torgersen, E., Viola, G., Zwingmann, H., and Harris, C., 2015a, Structural and temporal evolution of a reactivated brittle-ductile fault - Part II: Timing of fault initiation and reactivation by K-Ar dating of synkinematic illite/muscovite: Earth Planet. Sc. Lett., v. 410, p. 212-224./10.1016/j.epsl.2014.11.013

Torgersen, E., Viola, G., Zwingmann, H., and Henderson, I. H. C., 2015b, Inclined K-Ar illite age spectra in brittle fault gouges: effects of fault reactivation and wall-rock contamination: Terra Nova, v. 27, no. 2, p. 106-113./10.1111/ter.12136

Traforti, A., Massironi, M., Bistacchi, A., Zampieri, D., and Viola, G., 2018, Slip-tendency analysis as a tool to constrain the mechanical properties of anisotropic rocks: Journal of Structural Geology, v. 117, p. 136-147./10.1016/j.jsg.2018.09.001

Trice, R., 2014, Basement exploration, West of Shetlands: progress in opening a new play on the UKCS: Geol. Soc. London, Spec. Publ., v. 397, no. 1, p. 81-105./10.1144/sp397.3

Trice, R., Hiorth, C., and Holdsworth, R., 2019, Fractured basement play development on the UK and Norwegian rifted margins: Geological Society, London, Special Publications./10.1144/sp495-2018-174

Trumbore, S. E., and Druffel, E. R. M., 1995, Carbon isotopes for characterizing sources and turnover of nonliving organic matter

Tveranger, J., Braathen, A., Skar, T., and Skaugen, A., 2005, Centre for Integrated Petroleum Research: Research activities with emphasis on fluid flow in fault zones: Norw. J. Geol.

Twiss, R. J., and Unruh, J. R., 1998, Analysis of fault slip inversions: Do they constrain stress or strain rate?: Journal of Geophysical Research: Solid Earth, v. 103, no. B6, p. 12205-12222

van der Pluijm, B. A., Hall, C. M., Vrolijk, P. J., Pevear, D. R., and Covey, M. C., 2001, The dating of shallow faults in the Earth's crust: Nature, v. 412, p. 172-174

van Noort, R., and Yarushina, V., 2018, Water, CO2 and Argon Permeabilities of Intact and Fractured Shale Cores Under Stress: Rock Mechanics and Rock Engineering, v. 52, no. 2, p. 299-319./10.1007/s00603-018-1609-8

Verdel, C., van der Pluijm, B. A., and Niemi, N., 2012, Variation of illite/muscovite 40 Ar/39 Ar age spectra during progressive low-grade metamorphism: an example from the US Cordillera: Contrib. Mineral. Petr., v. 164, no. 3, p. 521-536./10.1007/s00410-012-0751-7

Viola, G., Ganerod, G. V., and Wahlgren, C. H., 2009, Unraveling 1.5 Ga of brittle deformation history in the Laxemar-Simpevarp area, southeast Sweden: A contribution to the Swedish site investigation study for the disposal of highly radioactive nuclear waste: Tectonics, v. 28./10.1029/2009tc002619

Viola, G., Scheiber, T., Fredin, O., Zwingmann, H., Margreth, A., and Knies, J., 2016, Deconvoluting complex structural histories archived in brittle fault zones: Nat. Commun., v. 7, p. 13448./10.1038/ncomms13448

Viola, G., Torgersen, E., Mazzarini, F., Musumeci, G., van der Lelij, R., Schönenberger, J., and Garofalo, P. S., 2018, New Constraints on the Evolution of the Inner Northern Apennines by K-Ar Dating of Late Miocene-Early Pliocene Compression on the Island of Elba, Italy: Tectonics./10.1029/2018tc005182

Viola, G., Zwingmann, H., Mattila, J., and Kapyaho, A., 2013, K-Ar illite age constraints on the Proterozoic formation and reactivation history of a brittle fault in Fennoscandia: Terra Nova, v. 25, no. 3, p. 236-244./10.1111/ter.12031

Vrolijk, P., Pevear, D., Covey, M., and LaRiviere, A., 2018, Fault gouge dating: history and evolution: Clay Minerals, v. 53, no. 3, p. 305-324./10.1180/clm.2018.22

Wallace, R. E., 1951, Geometry of shearing stress and relation to faulting: The Journal of geology, v. 59, no. 2, p. 118-130

Walsh, E. O., Hacker, B. R., Gans, P. B., Wong, M. S., and Andersen, T. B., 2013, Crustal exhumation of the Western Gneiss Region UHP terrane, Norway: 40Ar/39Ar thermochronology and fault-slip analysis: Tectonophysics, v. 608, p. 1159-1179./10.1016/j.tecto.2013.06.030

Walsh, J., Watterson, J., Heath, A., and Childs, C., 1998, Representation and scaling of faults in fluid flow models: Petroleum Geoscience, v. 4, no. 3, p. 241-251

Walter, B., Géraud, Y., Bartier, D., Kluska, J. M., Diraison, M., Morlot, C., and Raisson, F., 2018, Petrophysical and mineralogical evolution of weathered crystalline basement in western Uganda: Implications for fluid transfer and storage: AAPG Bulletin, v. 102, no. 06, p. 1035-1065./10.1306/0810171610917171

Wasserburg, G., Hayden, R. J., and Jensen, K. J., 1956, A40-K40 dating of igneous rocks and sediments: Geochimica et Cosmochimica Acta, v. 10, no. 3, p. 153-165

Wehrens, P., Berger, A., Peters, M., Spillmann, T., and Herwegh, M., 2016, Deformation at the frictional-viscous transition: Evidence for cycles of fluid-assisted embrittlement and ductile deformation in the granitoid crust.Tectonophysics,693, 66-84, doi:10.1016/j.tecto.2016.10.022

Weisenberger, T., and Bucher, K., 2010, Zeolites in fissures of granites and gneisses of the Central Alps: J. Metamorph. Geol., v. 28, no. 8, p. 825-847./10.1111/j.1525-1314.2010.00895.x

Wernicke, B., Walker, J. D., and Beaufait, M. S., 1985, Structural discordance between Neogene detachments and frontal Sevier thrusts, central Mormon Mountains, southern Nevada: Tectonics, v. 4, no. 2, p. 213-246

Wibberley, C. A., Yielding, G., and Di Toro, G., 2008, Recent advances in the understanding of fault zone internal structure: a review: Geological Society, London, Special Publications, v. 299, no. 1, p. 5-33. /10.1144/SP299.2

Will, T. M., and Frimmel, H. E., 2018, Where does a continent prefer to break up? Some lessons from the South Atlantic margins: Gondwana Research, v. 53, p. 9-19./10.1016/j.gr.2017.04.014

Wilson, R. W., McCaffrey, K. J. W., Holdsworth, R. E., Imber, J., Jones, R. R., Welbon, A. I. F., and Roberts, D., 2006, Complex fault patterns, transtension and structural segmentation of the Lofoten Ridge, Norwegian margin: Using digital mapping to link onshore and offshore geology: Tectonics, v. 25, no. 4, p. n/a-n/a./10.1029/2005tc001895

Winkler, H. G., 1976, Classification Principles: Metamorphic Facies versus Metamorphic Grade, Petrogenesis of Metamorphic Rocks, Springer, p. 55-63

Wintsch, R. P., Christoffersen, R., and Kronenberg, A. K., 1995, Fluid-rock reaction weakening of fault zones: Journal of Geophysical Research: Solid Earth, v. 100, no. B7, p. 13021-13032./10.1029/94jb02622

Yamasaki, S., Zwingmann, H., Yamada, K., Tagami, T., and Umeda, K., 2013, Constraining the timing of brittle deformation and faulting in the Toki granite, central Japan: Chem. Geol., v. 351, p. 168-174./10.1016/j.chemgeo.2013.05.005

Zastrozhnov, D., 2020, Regional Structure and Basin Development of the mid-Norwegian Volcanic Passive Margin: Anatomy of a Polyphased Rifted System: PhD Thesis, University of Oslo, 264 p.

Zastrozhnov, D., Gernigon, L., Gogin, I., Abdelmalak, M. M., Planke, S., Faleide, J. I., Eide, S., and Myklebust, R., 2018, Cretaceous-Paleocene Evolution and Crustal Structure of the Northern Vøring Margin (Offshore Mid-Norway): Results from Integrated Geological and Geophysical Study: Tectonics, v. 37, no. 2, p. 497-528./10.1002/2017tc004655

Zastrozhnov, D., Gernigon, L., Gogin, I., Planke, S., Abdelmalak, M. M., Polteau, S., Faleide, J. I., Manton, B., and Myklebust, R., 2020, Regional structure and polyphased Cretaceous-Paleocene rift and basin development of the mid-Norwegian volcanic passive margin: Marine and Petroleum Geology./10.1016/j.marpetgeo.2020.104269

Zhang, S., and Tullis, T. E., 1998, The effect of fault slip on permeability and permeability anisotropy in quartz gouge: Tectonophysics, v. 295, no. 1-2, p. 41-52./10.1016/s0040-1951(98)00114-0

Zwingmann, H., and Mancktelow, N., 2004, Timing of Alpine fault gouges: Earth Planet. Sc. Lett., v. 223, no. 3-4, p. 415-425./10.1016/j.epsl.2004.04.041

Zwingmann, H., Mancktelow, N., Antognini, M., and Lucchini, R., 2010, Dating of shallow faults: New constraints from the AlpTransit tunnel site (Switzerland): Geology, v. 38, no. 6, p. 487-490./10.1130/g30785.1

Appendix I

Table I.1 – Dataset of the analysed calcite veins and mineralisations from the MNPM and the North Sea margin. The clumped isotope thermometry results are listed. The different type of calcite samples are described in the text (Sense: N = normal, D = dextral, S = sinistral, X= unknown; Temperature: CL = Confidence Level).

Sample				Fault Plane			Line					d13C (VPDB)		d18O (VPDB)			D47 ‰			Temperature					Delta 18O Fluid (SMOW)			
Number	ID	Margin	Host rock	Strike	Dip Azimuth	Dip	Trend	Plunge	Sense	Type	Replicates	value (‰)	Standard Deviation	value (‰)	Standard Deviation	d18O (VSMOW)	(I-CDES)	Standard Deviation	Standard Error	Average value (°C)	Standard Deviation	Standard Error	68% CL	95% CL	Kim and O'Neil (5 - 45°C)	Daeron et al.2019 (5- 45°C)	Kele et al. 2015 (5- 95°C)	O'Neil et al. (1969) 0-500°C
S1	19 002 01	MNPM	Arkose	182	92	73				parallel	7	-19.1	0.3	-9.2	0.1	21.4	0.5	0.0	0.0	44.9	9.7	3.7	4.0	9.0	-3.1	-4.9	-6.3	-3.4
S2	19 006 01	MNPM	Granite	147	57	22			X	fibrous	7	-8.8	0.0	-15.0	0.1	15.5	0.5	0.0	0.0	61.9	12.9	4.9	5.3	11.9	-6.0	-7.9	-9.3	-6.5
S3	19 007 01	MNPM	Granite	83	353	53				randomly oriented	17	-10.6	0.1	-16.4	0.4	14.0	0.5	0.0	0.0	43.6	7.1	1.7	1.8	3.7	-10.5	-12.3	-13.6	-10.8
S4	19 014 01	MNPM	Granodiorite	53	323	65	46	32		fibrous	11	-11.6	0.0	-16.8	0.1	13.6	0.6	0.0	0.0	40.9	7.7	2.3	2.4	5.2	-11.5	-13.3	-14.6	-11.8
S5	19 014 02	MNPM	Granodiorite	358	268	74				parallel	13	-1.0	0.1	-22.1	0.2	8.1	0.4	0.0	0.0	153.8	23.2	6.4	6.7	14.0	-1.7	-4.0	-5.7	-4.3
S6	19 015 02	MNPM	Granodiorite	88	358	89				parallel	13	-10.2	0.0	-10.1	0.1	20.5	0.5	0.0	0.0	59.3	17.7	4.9	5.1	10.7	-1.6	-3.5	-4.9	-2.0
S7	19 015 03A	MNPM	Granodiorite	130	40	58				parallel	6	0.5	0.0	-20.2	0.1	10.1	0.4	0.0	0.0	133.1	11.3	4.6	5.1	11.9	-1.9	-4.0	-5.7	-3.9
S8	19 015 03D	MNPM	Granodiorite	130	40	58				blocky	7	-5.1	0.1	-9.6	0.1	21.1	0.5	0.0	0.0	48.9	10.8	4.1	4.4	10.0	-2.7	-4.6	-5.9	-3.1
S9	19 015 3B	MNPM	Granodiorite	130	40	58				parallel	7	-6.2	0.1	-13.0	0.1	17.5	0.5	0.0	0.0	75.8	14.0	5.3	5.7	12.9	-1.9	-3.9	-5.4	-2.6
S10	19 015 3C	MNPM	Granodiorite	130	40	58				parallel	5	-2.6	0.1	-14.4	0.0	16.1	0.5	0.0	0.0	74.8	7.6	3.4	3.8	9.4	-3.4	-5.4	-6.9	-4.1
S11	19 019 02A	MNPM	Granodiorite	217	127	70	54	28	N	parallel	12	-10.0	0.0	-13.3	0.1	17.2	0.6	0.0	0.0	38.5	8.5	2.5	2.6	5.4	-8.3	-10.1	-11.4	-8.6
S12	19 019 02B	MNPM	Granodiorite	217	127	70	54	28	N	parallel	4	-9.2	0.1	-11.3	0.1	19.3	0.5	0.0	0.0	62.2	1.6	0.8	0.9	2.5	-2.2	-4.1	-4.5	-2.7
S13	19 023 01	MNPM	Arkose	236	146	76				parallel	7	-11.4	0.0	-19.2	0.1	11.1	0.5	0.0	0.0	44.6	13.4	5.1	5.5	12.4	-13.2	-15.0	-16.3	-13.5
S14	19 025 01A	MNPM	Granite	127	37	82				parallel	13	-9.2	0.2	-11.9	0.2	18.7	0.5	0.0	0.0	45.4	13.3	3.7	3.8	8.0	-5.7	-7.5	-8.8	-6.0
S15	19 025 01B	MNPM	Granite	127	37	82				matrix	8	-16.5	0.1	-8.5	0.1	22.2	0.5	0.0	0.0	64.3	13.0	4.6	4.9	10.9	0.9	-1.0	-2.4	0.4
S16	19 030D 1	MNPM	Granite	216	126	50				parallel	5	-9.1	0.1	-11.7	0.1	18.9	0.5	0.0	0.0	64.1	5.7	2.6	2.9	7.1	-2.3	-4.3	-5.7	-2.8
S17	19 030D 2	MNPM	Granite	216	126	50				parallel	4	-11.5	0.0	-11.4	0.0	19.2	0.5	0.0	0.0	65.3	9.1	4.6	5.4	14.5	-1.9	-3.8	-5.2	-2.4
S18	19 039 01	MNPM	Migmatite	317	227	79	142	22	D	parallel	4	-1.1	0.1	-20.9	0.1	9.4	0.4	0.0	0.0	117.6	19.4	9.7	11.5	30.8	-4.4	-6.5	-8.1	-5.9
S19	19 046 01A	MNPM	Migmatite	355	265	71				randomly oriented	11	-5.6	2.6	-16.5	1.8	13.9	0.5	0.1	0.0	84.8	33.2	10.0	10.5	22.3	-4.1	-6.1	-7.7	-5.0
S20	19 046 01B	MNPM	Migmatite	355	265	71			X	fibrous	4	-13.3	0.4	-11.3	0.4	19.3	0.6	0.0	0.0	28.5	9.6	4.8	5.7	15.3	-8.2	-9.9	-11.2	-8.5
S21	19 046 02	MNPM	Migmatite	358	268	65				parallel	3	-14.7	0.1	-11.2	0.4	19.4	0.5	0.0	0.0	53.4	16.7	9.7	12.7	41.5	-3.6	-5.4	-6.8	-3.9
S22	19 046 03	MNPM	Migmatite	334	244	65				parallel	9	-22.8	0.1	-7.1	0.0	23.6	0.6	0.0	0.0	32.7	8.1	2.7	2.9	6.2	-3.2	-5.0	-6.2	-3.5
S23	19 049 01	MNPM	Migmatite	324	234	75			N	parallel	8	-1.2	0.0	-22.0	0.1	8.3	0.4	0.0	0.0	128.3	20.7	7.3	7.8	17.3	-4.3	-6.4	-8.1	-6.1
S24	19 050 01	MNPM	Migmatite	205	115	80			X	fibrous	4	-11.9	0.7	-13.9	0.2	16.6	0.6	0.0	0.0	25.5	10.8	5.4	6.4	17.2	-11.4	-13.1	-14.3	-11.7
S25	19 050 02	MNPM	Migmatite	47	317	87				parallel	10	-13.1	0.1	-9.4	0.1	21.3	0.5	0.0	0.0	50.9	9.6	3.0	3.2	6.9	-2.2	-4.0	-5.4	-2.5
S26	19 052 01	MNPM	Gneiss	54	324	79				parallel	11	-19.7	0.6	-15.0	0.2	15.5	0.5	0.0	0.0	45.4	6.7	2.0	2.1	4.5	-8.8	-10.6	-11.9	-9.1
S27	19 052 02	MNPM	Gneiss	54	324	79				parallel	4	-12.9	0.1	-14.7	0.1	15.7	0.5	0.0	0.0	58.6	11.9	6.0	7.1	19.0	-6.3	-8.2	-9.6	-6.7
S28	19 052 03	MNPM	Gneiss	16	286	73				parallel	4	-1.4	0.0	-24.2	0.0	6.0	0.3	0.0	0.0	185.5	14.6	7.3	8.7	23.3	-0.9	-3.2	-5.1	-4.3
S29	19 052 04	MNPM	Gneiss	46	316	63				randomly oriented	8	-21.4	0.7	-13.0	0.1	17.5	0.6	0.0	0.0	34.0	8.1	2.9	3.1	6.8	-8.9	-10.7	-11.9	-9.2
S30	19 060 01	MNPM	Migmatitic gneiss	80	350	87	270	3	X	fibrous	4	-15.2	0.3	-17.9	1.0	12.5	0.5	0.0	0.0	55.4	11.1	5.6	6.6	17.7	-10.0	-11.9	-13.3	-10.4
S31	19 060 02	MNPM	Migmatitic gneiss	80	350	87	258	15	S	parallel	11	-13.9	0.0	-22.1	0.1	8.1	0.5	0.0	0.0	48.5	10.0	3.0	3.2	6.7	-15.4	-17.3	-18.6	-15.8
S32	19 062 01	MNPM	Orthogneiss	148	58	51	99	41	N	fibrous	11	-14.5	0.1	-15.0	0.1	15.5	0.5	0.0	0.0	44.7	11.1	3.4	3.5	7.5	-8.9	-10.7	-12.1	-9.2

S33	19 063 01	MNPM	Migmatitic gneiss	179	89	88	171	17	X	parallel	4	-13.5	0.2	-14.3	0.4	16.2	0.5	0.0	0.0	43.8	6.9	3.5	4.1	11.0	-8.4	-10.2	-11.5	-8.7
S34	19 068 01	MNPM	Migmatitic gneiss	95	5	78	81	55	N	parallel	11	-15.3	0.3	-17.5	0.2	12.9	0.5	0.0	0.0	67.1	15.2	4.6	4.8	10.2	-7.7	-9.6	-9.9	-8.2
S35	19 068 02	MNPM	Migmatitic gneiss	97	7	75				parallel	10	-12.6	0.1	-17.9	0.1	12.5	0.5	0.0	0.0	62.5	6.8	2.2	2.3	4.9	-8.8	-10.8	-12.2	-9.3
S36	19 070 02	MNPM	Gneiss	311	221	79				parallel	11	-13.3	0.0	-18.4	0.1	12.0	0.5	0.0	0.0	59.0	9.7	2.9	3.1	6.5	-9.9	-11.8	-13.2	-10.3
S37	19006 A	MNPM	Granite	103	13	21	344	27	N	blocky	7	-3.7	0.0	-15.1	0.0	15.3	0.4	0.0	0.0	91.7	22.0	8.3	9.0	20.3	-1.8	-3.8	-5.4	-2.8
S38	19064 01	MNPM	Migmatitic gneiss	217	127	83	41	5	S	fibrous	10	-8.6	0.4	-17.7	0.1	12.6	0.4	0.0	0.0	98.6	31.4	9.9	10.5	22.5	-3.5	-5.6	-5.2	-4.7
S39	19072 01	MNPM	Gneiss	195	105	78				randomly oriented	8	-3.6	0.0	-21.3	0.1	8.9	0.4	0.0	0.0	156.6	9.4	3.3	3.6	7.8	-0.7	-2.9	-4.7	-3.3
S40	TSC 20 01	Bømlo	Granodiorite	355	85	60	143	36	N	parallel	9	-7.0	0.1	-11.8	0.0	18.7	0.5	0.0	0.0	67.8	14.2	4.7	5.0	10.9	-1.9	-3.8	-5.3	-2.5
S41	TSC 20 02	Bømlo	Granodiorite	355	85	60	143	36	N	parallel	10	-6.9	0.0	-12.4	0.0	18.1	0.5	0.0	0.0	77.1	13.6	4.3	4.5	9.7	-1.1	-3.0	-4.5	-1.8
S42	TSC 25	Bømlo	Granodiorite	27	117	58	ENE	ENE	N	parallel	10	-6.4	0.4	-12.2	0.3	18.4	0.5	0.0	0.0	56.6	6.7	2.1	2.2	4.8	-4.0	-5.9	-7.3	-4.4
S43	TSC 25 1	Bømlo	Granodiorite	27	117	58	ENE	ENE	N	parallel	12	-5.6	0.8	-13.1	0.7	17.4	0.5	0.0	0.0	56.3	12.6	3.6	3.8	8.0	-5.1	-6.9	-8.3	-5.5
S44	TSC 25 2	Bømlo	Granodiorite	27	117	58	ENE	ENE	N	parallel	13	-6.6	0.9	-12.2	0.6	18.3	0.5	0.0	0.0	56.0	13.9	3.9	4.0	8.4	-4.2	-6.1	-7.4	-4.6
S45	TSC 25 3	Bømlo	Granodiorite	27	117	58	ENE	ENE	N	parallel	16	-4.5	0.2	-14.0	0.1	16.5	0.5	0.0	0.0	70.4	12.9	3.2	3.3	6.9	-3.7	-5.6	-7.1	-4.3
S47	TSC 52	Bømlo	Granodiorite	25	115	82				parallel	12	-2.8	1.9	-15.4	3.2	15.0	0.5	0.0	0.0	69.5	11.4	3.3	3.4	7.3	-5.3	-7.2	-8.7	-5.9
S48	TSC 53	Bømlo	Granodiorite	25	115	82				parallel	4	-4.5	0.2	-14.0	0.1	16.5	0.5	0.0	0.0	63.9	16.6	8.3	9.9	26.5	-4.7	-6.6	-8.0	-5.2
S49	TSC 56	Bømlo	Granodiorite	27	117	58	ENE	ENE	N	parallel	12	-1.9	0.0	-16.2	0.1	14.2	0.5	0.0	0.0	77.2	18.9	5.4	5.7	12.0	-4.9	-6.9	-8.4	-5.6
S50	TSC 56 2	Bømlo	Granodiorite	27	117	58	ENE	ENE	N	parallel	9	-2.3	0.1	-14.8	0.2	15.6	0.5	0.1	0.0	65.9	28.7	9.6	10.2	22.1	-5.2	-7.1	-8.6	-5.8
S51	TSC 56 3	Bømlo	Granodiorite	27	117	58	ENE	ENE	N	parallel	8	-2.1	0.1	-15.5	0.1	14.9	0.4	0.0	0.0	91.6	12.8	4.5	4.8	10.7	-2.2	-4.3	-5.8	-3.2
S52	TSC 56 4	Bømlo	Granodiorite	27	117	58	ENE	ENE	N	parallel	10	-2.5	0.0	-15.6	0.1	14.8	0.4	0.0	0.0	114.3	22.1	7.0	7.3	15.8	0.6	-1.5	-3.2	-0.9
S53	TSC 62	Bømlo	Gabbro	355	85	44	125	33	N	matrix	15	-6.5	0.0	-14.3	0.1	16.2	0.5	0.0	0.0	85.6	11.9	3.1	3.2	6.6	-1.8	-3.8	-5.3	-2.6
S54	TSC 64_1	Bømlo	Gabbro	0	270	85	270	85	X	matrix	2	-3.7	0.0	-16.3	0.1	14.1	0.5	0.0	0.0	61.4	0.7	0.5	0.9	6.5	-7.4	-9.3	-10.7	-7.9
S55	TSC 64_2	Bømlo	Gabbro	0	270	85	270	85	X	matrix	14	-3.9	0.0	-16.4	0.0	14.0	0.4	0.0	0.0	127.1	26.2	7.0	7.3	15.2	1.2	-0.9	-2.6	-0.6
S56	TSC 67 1	Bømlo	Gabbro	5	95	50	123	40	N	parallel	7	-2.9	0.1	-14.5	0.1	16.0	0.4	0.0	0.0	101.1	17.9	6.8	7.3	16.5	0.1	-2.0	-3.6	-1.1
S57	TSC 67 2	Bømlo	Gabbro	5	95	50	123	40	N	parallel	7	-2.9	0.0	-14.6	0.1	15.8	0.5	0.0	0.0	80.0	23.7	9.0	9.7	21.9	-2.9	-4.9	-6.4	-3.7
S58	TSC 67 3	Bømlo	Gabbro	5	95	50	123	40	N	parallel	6	-4.1	0.1	-13.3	0.1	17.2	0.5	0.0	0.0	74.7	7.3	3.0	3.3	7.7	-2.4	-4.3	-5.8	-3.0
S59	TSC 67 4	Bømlo	Gabbro	5	95	50	123	40	N	parallel	13	-3.8	0.0	-14.5	0.1	15.9	0.4	0.0	0.0	117.3	24.1	6.7	6.9	14.6	2.1	-0.1	-1.7	0.5
S60	TSC 67 5	Bømlo	Gabbro	5	95	50	123	40	N	parallel	8	-3.5	0.0	-14.7	0.0	15.8	0.4	0.0	0.0	119.1	25.5	9.0	9.6	21.3	2.1	0.0	-1.7	0.5
S61	TSC 68	Bømlo	Gabbro	0	90	60				matrix	4	-5.6	0.1	-15.1	0.1	15.3	0.5	0.0	0.0	82.0	17.0	8.5	10.1	27.0	-3.1	-5.1	-6.7	-4.0
S62	TSC 69 1	Bømlo	Gabbro	325	55	45	25	38	X	parallel	4	-5.4	0.2	-14.1	0.2	16.4	0.5	0.0	0.0	74.9	5.9	3.0	3.5	9.4	-3.1	-5.1	-6.6	-3.8
S63	TSC 70	Bømlo	Gabbro	45	315	78	45	79	X	parallel	13	-2.7	0.1	-15.7	0.1	14.7	0.4	0.0	0.0	98.2	22.0	6.1	6.3	13.3	-1.5	-3.5	-5.1	-2.6
S64	TSC 70 2	Bømlo	Gabbro	45	315	78	45	79	X	parallel	9	-3.4	0.1	-16.5	0.3	13.9	0.5	0.1	0.0	53.8	34.7	11.6	12.3	26.7	-8.9	-10.8	-12.2	-9.3
S65	TSC 72	Bømlo	Granodiorite	16	106	77	180	23	X	fibrous	4	-1.0	0.0	-10.3	0.0	20.3	0.5	0.0	0.0	53.6	4.7	2.3	2.8	7.5	-2.7	-4.6	-5.9	-3.1
S66	TSC 73	Bømlo	Granodiorite	280	190	74			X	fibrous	12	-6.7	0.0	-15.6	0.0	14.8	0.5	0.0	0.0	84.3	12.5	3.6	3.8	7.9	-3.3	-5.3	-6.8	-4.2
S67	TSC 75	Bømlo	Granodiorite	342	72	67	153	22	X	parallel	8	-9.9	0.0	-13.3	0.0	17.2	0.5	0.0	0.0	66.4	18.6	6.6	7.0	15.6	-3.6	-5.5	-7.0	-4.1
S68	TSC 77	Bømlo	Granodiorite	319	229	88	137	3	X	fibrous	8	10.2	0.2	2.1	0.4	33.1	0.6	0.0	0.0	20.6	11.1	3.9	4.2	9.2	3.6	1.9	0.7	3.2
S69	TSC 78	Bømlo	Granodiorite	308	218	85	130	24	S	fibrous	9	-6.7	0.1	-9.3	0.1	21.4	0.6	0.0	0.0	27.4	6.2	2.1	2.2	4.8	-6.4	-8.2	-9.4	-6.7
S70	TSC 79	Bømlo	Granodiorite	45	135	60	082	42	N	fibrous	10	-5.6	0.0	-12.2	0.0	18.4	0.5	0.0	0.0	72.3	14.3	4.5	4.7	10.2	-1.6	-3.5	-5.0	-2.2
S71	TSC 80	Bømlo	Granodiorite	10	100	84	035	55	X	parallel	4	-7.9	0.0	-14.0	0.0	16.4	0.5	0.0	0.0	78.5	18.4	9.2	10.9	29.3	-2.5	-4.5	-6.0	-3.3
S72	TSC 81	Bømlo	Granodiorite	342	072	136				blocky	2	-6.9	0.0	-12.2	0.0	18.3	0.5	0.0	0.0	61.5	4.1	2.9	5.2	36.7	-3.3	-5.2	-6.6	-3.8
S73	TSC 82	Bømlo	Granodiorite	297	207	56	289	24	D	fibrous	13	-8.0	0.0	-13.4	0.0	17.1	0.5	0.0	0.0	85.2	15.1	4.2	4.3	9.1	-0.9	-2.9	-4.5	-1.8
S74	TSC 83	Bømlo	Granodiorite	46	316	85	229	27	S	fibrous	6	-6.8	0.2	-13.6	0.1	16.9	0.5	0.0	0.0	57.0	11.8	4.8	5.3	12.3	-5.4	-7.3	-8.7	-5.8
S75	TSC 84	Bømlo	Granodiorite	336	246	88				parallel	6	-4.0	0.1	-16.4	0.1	14.0	0.4	0.0	0.0	94.2	12.0	4.9	5.4	12.6	-2.7	-4.7	-4.5	-3.8
S76	TSC 85	Bømlo	Granodiorite	350	260	68	338	41	X	fibrous	5	-6.4	0.1	-14.8	0.2	15.6	0.5	0.0	0.0	71.3	10.3	4.6	5.2	12.7	-4.4	-6.3	-7.8	-5.0
S77	TSC 86	Bømlo	Granodiorite	343	073	53	93	45	N	parallel	9	-5.7	0.1	-14.2	0.2	16.3	0.5	0.0	0.0	75.3	21.0	7.0	7.4	16.1	-3.2	-5.1	-6.6	-3.9
S78	TSC 87	Bømlo	Granodiorite	345	075	55	075	55	N	parallel	4	-6.9	0.4	-13.8	0.5	16.7	0.5	0.0	0.0	52.8	7.8	3.9	4.6	12.4	-6.3	-8.2	-9.6	-6.7
S79	TSC 88	Bømlo	Granodiorite	348	258	80				parallel	4	-2.7	0.0	-14.8	0.0	15.7	0.5	0.0	0.0	71.9	4.1	2.1	2.4	6.5	-4.3	-6.2	-6.4	-4.9
S80	TSC 89	Bømlo	Granodiorite	354	264	88	010	71	X	fibrous	3	-3.9	0.0	-13.7	0.1	16.8	0.5	0.0	0.0	81.6	15.8	9.1	11.9	39.2	-1.7	-3.7	-5.2	-2.5
S81	TSC 90	Bømlo	Granodiorite	15	285	60			N	fibrous	4	-2.7	0.0	-7.3	0.0	23.4	0.5	0.0	0.0	48.0	17.6	8.8	10.4	27.9	-0.6	-2.4	-3.8	-0.9
S82	TSC 91	Bømlo	Granodiorite	9	99	28	70	25	N	matrix	13	-4.3	0.0	-13.4	0.0	17.1	0.5	0.0	0.0	74.0	10.8	3.0	3.1	6.5	-2.5	-4.5	-6.0	-3.2